frontiers | Research Topics

Multiscale characterization of advanced pavement materials

Edited by
Dawei Wang, Hui Yao, Qingli Dai and Markus Oeser

Published in
Frontiers in Materials

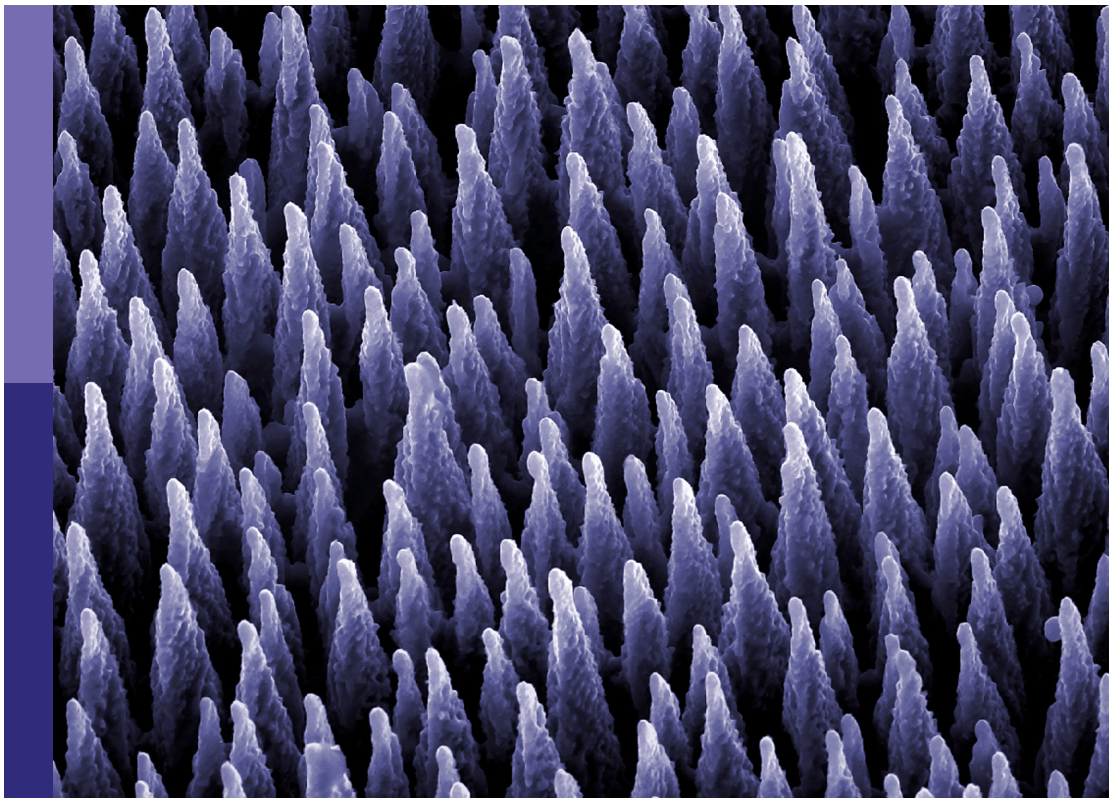

ISSN 1664-8714
ISBN 978-2-8325-3662-9
DOI 10.3389/978-2-8325-3662-9

About Frontiers

Frontiers is more than just an open access publisher of scholarly articles: it is a pioneering approach to the world of academia, radically improving the way scholarly research is managed. The grand vision of Frontiers is a world where all people have an equal opportunity to seek, share and generate knowledge. Frontiers provides immediate and permanent online open access to all its publications, but this alone is not enough to realize our grand goals.

Frontiers journal series

The Frontiers journal series is a multi-tier and interdisciplinary set of open-access, online journals, promising a paradigm shift from the current review, selection and dissemination processes in academic publishing. All Frontiers journals are driven by researchers for researchers; therefore, they constitute a service to the scholarly community. At the same time, the *Frontiers journal series* operates on a revolutionary invention, the tiered publishing system, initially addressing specific communities of scholars, and gradually climbing up to broader public understanding, thus serving the interests of the lay society, too.

Dedication to quality

Each Frontiers article is a landmark of the highest quality, thanks to genuinely collaborative interactions between authors and review editors, who include some of the world's best academicians. Research must be certified by peers before entering a stream of knowledge that may eventually reach the public - and shape society; therefore, Frontiers only applies the most rigorous and unbiased reviews. Frontiers revolutionizes research publishing by freely delivering the most outstanding research, evaluated with no bias from both the academic and social point of view. By applying the most advanced information technologies, Frontiers is catapulting scholarly publishing into a new generation.

What are Frontiers Research Topics?

Frontiers Research Topics are very popular trademarks of the *Frontiers journals series*: they are collections of at least ten articles, all centered on a particular subject. With their unique mix of varied contributions from Original Research to Review Articles, Frontiers Research Topics unify the most influential researchers, the latest key findings and historical advances in a hot research area.

Find out more on how to host your own Frontiers Research Topic or contribute to one as an author by contacting the Frontiers editorial office: frontiersin.org/about/contact

Multiscale characterization of advanced pavement materials

Topic editors

Dawei Wang — RWTH Aachen University, Germany
Hui Yao — Beijing University of Technology, China
Qingli Dai — Michigan Technological University, United States
Markus Oeser — RWTH Aachen University, Germany

Citation

Wang, D., Yao, H., Dai, Q., Oeser, M., eds. (2023). *Multiscale characterization of advanced pavement materials*. Lausanne: Frontiers Media SA.
doi: 10.3389/978-2-8325-3662-9

Table of contents

frontiers | Frontiers in Materials

TYPE Editorial
PUBLISHED 25 September 2023
DOI 10.3389/fmats.2023.1295653

OPEN ACCESS

EDITED AND REVIEWED BY
John L. Provis,
Paul Scherrer Institut (PSI), Switzerland

*CORRESPONDENCE
Hui Yao,
huiyao@mtu.edu

RECEIVED 17 September 2023
ACCEPTED 19 September 2023
PUBLISHED 25 September 2023

CITATION
Yao H, Wang D, Dai Q and Oeser M (2023), Editorial: Multiscale characterization of advanced pavement materials.
Front. Mater. 10:1295653.
doi: 10.3389/fmats.2023.1295653

Editorial: Multiscale characterization of advanced pavement materials

Hui Yao[1]*, Dawei Wang[2,3], Qingli Dai[4] and Markus Oeser[2]

[1]Faculty of Architecture, Civil and Transportation Engineering, Beijing University of Technology, Beijing, China, [2]Institute of Highway Engineering, RWTH Aachen University, Aachen, Germany, [3]School of Transportation Science and Engineering, Harbin Institute of Technology, Harbin, China, [4]Civil, Environmental, and Geospatial Engineering, Michigan Technological University, Houghton, MI, United States

KEYWORDS

civil engineering, pavement materials, pavement performance, characterization method, technical optimization method

Editorial on the Research Topic
Multiscale characterization of advanced pavement materials

The improvement of pavement materials and performance has always been a main direction for researchers. Whether the road performance of pavement materials is fine or not produces a decisive influence on service life and driving comfort of pavement. Therefore, the exploration and innovation of pavement materials and technologies are extremely important to enhance pavement performance in engineering construction.

"Frontiers in Materials" is a very highly renowned international journal, which publishes rigorously peer-reviewed research in the fields of materials science and engineering. This Research Topic "*Multiscale Characterization of Advanced Pavement Materials*" reports the emerging technologies in the field of pavement engineering that have been developing. This special Research Topic concentrates on the following aspects: advanced pavement materials, advanced road performance characterization methods, and technical optimization methods.

1) Advanced Pavement Materials: The Redundant wind turbine blades (WTBs) powders and fibers were prepared and added to the asphalt mixture to prepare WTBs asphalt concrete. The road performance of WTBs asphalt concrete was investigated by wheel tracking tests, three-point bending tests, and Marshall immersion tests. The results showed that the synergistic effect of WTBs powders and fibers could comprehensively improve the road performance of asphalt concrete (Lan et al.). The effects of different chloride deicing agents on the performance of asphalt and mixture were also completely researched. The three deicing agents (NaCl, KHF-1A, and NW056) were selected, and their influence on the performance of asphalt and asphalt mixture through the DSR test, BBR test, indirect tensile test, the bending test of the small beam and freeze-thaw splitting test were examined. The results indicated that the NW056 deicing agent had minimal effect on the performance of airport pavement, which could replace traditional chloride deicing agents to extend the service life of airport asphalt pavement (Li et al.).
2) Advanced road performance characterization methods: The high-temperature properties of rubberized asphalt and mixture were evaluated by a series of laboratory experiments, including frequency scanning, repeated creep recovery test, temperature sweep test, and Hamburg wheel tracking test. The evaluation indexes of the high-temperature properties

of rubberized asphalt and mixture were analyzed through the gray correlation theory (Xie et al.). Recently, the bibliometric analysis method was conducted to study the effects of physical and chemical properties of polymer and matrix asphalt on the road performance of polymer-modified asphalt (Alnadish et al.). In addition, in order to reveal the damage mechanism of cement concrete pavement by weakened subgrade modulus, a meshless finite block method was invented, and a normal distribution function was used to study the distribution of subgrade modulus at the bottom of cement concrete pavement panel (Wei et al.). Based on the traffic data of a steel deck strengthened with the ultra-high-performance concrete (UHPC) layer for 1 week, the Monte Carlo method was used to simulate the fatigue life of the bridge deck under random traffic loads, a fatigue life analysis model including traffic load simulation, a refined finite element model, the S-N curve and Miner linear cumulative damage criterion had been established to predict the service life of bridge deck (Deng and Yi). The changes in capillary water absorption and pore distribution would lead to a decrease in the durability of steam-cured concrete, reducing the bonding performance between concrete and GFRP bars. The method of steam curing was used to simulate the damage of the actual steam curing environment to components. The influence of pore characteristics on the bonding performance between steam-cured concrete and GFRP steel bars was deliberated through SEM, mercury intrusion test, and three-point beam test (Zhang et al.).

3) Technical optimization methods: In order to diminish the destructive rate of the pavement and extend the service life of the road, fog seal technology has been widely applied in pavement maintenance. However, based on the deficiency of the existing fog seal test methods, the road performance of different types of fog seals was measured through improved Wet Track Abrasion Test (WTAT), improved Cantabro test, improved Water seepage test, and improved Pendulum instrument tester pavement friction coefficient test (Li et al.). The grafting-activated crumb rubber (GACR) was incorporated into the terminal blend rubber asphalt (TB) to prepare the terminal blend/grafting activated crumb rubber composite modified asphalt, the response surface methodology was used to investigate the effects of shear temperature, shear time, and grafting active rubber powders content on the performance of composite modified asphalt so as to optimize the preparation process of composite modified asphalt. The experiment results showed that the composite-modified asphalt had good high-temperature stability and storage stability under the conditions of a shearing temperature of 190°C, shearing time of 90 min, and GACR content of 15% (Xie et al.).

Nine manuscripts were invited and received as possible publications in the Research Topic. All manuscripts were rigorously, fairly, and anonymously reviewed. Both the quality and originality of these papers were thoroughly examined and checked. Finally, nine research articles were accepted and approved for publication.

Author contributions

HY: Conceptualization, Writing–original draft, Writing–review and editing. DW: Conceptualization, Writing–original draft, Writing–review and editing. QD: Conceptualization, Writing–review and editing. MO: Conceptualization, Writing–review and editing.

Acknowledgments

Our editorial team members thank all reviewers for their professional and dedicated support and help, and also, appreciate all the authors for their efforts and contributions to this Research Topic. In addition, we all are grateful to the editorial and support teams from Frontiers in Materials, especially Prof. John L. Provis, Elie Abdel Ahad, and Tanya Grenade.

Conflict of interest

The authors declare that the research was conducted in the absence of any commercial or financial relationships that could be construed as a potential conflict of interest.

Publisher's note

frontiers | Frontiers in Materials

ORIGINAL RESEARCH
published: 20 May 2022
doi: 10.3389/fmats.2022.904087

Research on Evaluation Index of High Temperature Performance of Rubberized Asphalt Binder

Cheng Xie[1]*, *Junhui Luo*[1], *Lihao Zeng*[2], *Tianzeng Ren*[1], *Haobin Liu*[1] and *Jiangcai Chen*[1]

[1]Guangxi Beitou Transportation Maintenance Technology Group Co.,LTD, Nanning, China, [2]Guangxi Transportation Science and Technology Group CO., LTD., Nanning, China

The high-temperature rheological properties of rubberized asphalt and mixture were evaluated by frequency scanning, repeated creep recovery (RCR) test, temperature sweep test, Hamburg wheel tracking test (HWTT). Based on the Pearson correlation coefficient, the correlation of the mixture gradation and asphalt characteristics with the high-temperature stability of the mixture was analyzed. Finally, the gray correlation theory was applied to analyze the evaluation indexes of the high-temperature rheological properties of rubberized asphalt and mixture. The results show that the asphalt-stone ratio and the fractal dimension (Dc) of coarse aggregate have a significant correlation with the high-temperature performance of the mixture, and the mixture with a smaller asphalt-stone ratio and a higher percentage of coarse aggregate has a better high-temperature performance. The correlation degree of softening point, viscous stiffness modulus and permanent deformation with rubber-asphalt mixture is higher than 0.7, and are significantly higher than those of rotational viscosity at 180°C. Therefore, we recommend the use of permanent deformation, softening point, and viscous stiffness modulus to evaluate the high-temperature performance of rubberized asphalt mixture.

Keywords: rubberized asphalt, high-temperature performance, rheological property, correlation analysis, gray correlation analysis

OPEN ACCESS

Edited by:
Hui Yao,
Beijing University of Technology, China

Reviewed by:
Tao Ma,
Southeast University, China
Siyu Chen,
Southeast University, China
Jue Li,
Chongqing Jiaotong University, China

***Correspondence:**
Cheng Xie
45902900@qq.com

Specialty section:
This article was submitted to Structural Materials, a section of the journal Frontiers in Materials

Received: *25 March 2022*
Accepted: *20 April 2022*
Published: *20 May 2022*

Citation:
Xie C, Luo J, Zeng L, Ren T, Liu H and Chen J (2022) Research on Evaluation Index of High Temperature Performance of Rubberized Asphalt Binder. Front. Mater. 9:904087. doi: 10.3389/fmats.2022.904087

1 INTRODUCTION

As a mature environmentally-friendly pavement material, rubber modified asphalt has been widely used in China for decades. It shows advantages in noise reduction and skid resistance and boosts excellent high and low temperature performances, especially high-temperature performance, and anti-fatigue property (He et al., 2014; Zhou et al., 2014; Ma et al., 2021). At present, the evaluation indexes for the high-temperature performance of rubber modified asphalt are still similar to those for matrix asphalt and conventional polymer modified asphalt. South Africa, the United States, and Chile all use rotational viscosity at 177 °C (He, 2019) and China adopts rotational viscosity at 180 °C stipulated in *crumb rubber modified Asphalt for Highway Engineering* (JT/T 798–2019) (Industry standards of Transportation Department of the People ' s Republic of China, 2011a). However, 177°C–180°C is a range of mixing temperature during construction and does not fit the actual pavement operating temperature. When the rubberized asphalt is at 180°C, a solid-liquid two-phase separation state is formed inside, which is quite different from the phase structure of rubberized asphalt in the working temperature range. Therefore, it is difficult to evaluate the high-temperature rutting resistance of the road surface. In addition, in the high-content rubber modified asphalt, the rotor movement may be blocked due to rubber powder accumulation, resulting in large result

variability (He, 2019). To sum up, it is necessary to compare the evaluation indexes of high-temperature performance of rubber modified asphalt and propose an evaluation index that is highly correlated to the rutting resistance of the road surface to guide the construction.

At present, high-temperature performance evaluation indexes of rubberized asphalt have been extensively studied. Navarro (Navarro et al., 2005) studied the high-temperature performance of rubberized asphalt through dynamic shear rheometer (DSR) frequency scanning and rotational viscosity test and found that mixing rubber powder could significantly improve the temperature sensitivity and then the high-temperature performance of asphalt. Ding et al. (2019) and Hu et al. (2022) studied the performance of recycled asphalt concrete with stable crumb rubberized asphalt (SCRA) binder and foamed warm mix asphalt with crumb rubber, and found that the high and low temperature properties of the test samples were significantly improved after adding rubber. Shenoy (2001) concluded that the DSR rutting factor proposed in the SHRP plan was not an applicable index for grading evaluation of modified asphalts after high-temperature performance research on different polymer modified asphalts. They proposed an improved rutting factor $G^*(\sin\delta)^{-9}$ to avoid the influence of the small phase angle of the modified asphalt on its high-temperature performance. Yang et al. (2010) studied the correlation between the dynamic stability of rubberized asphalt mixture and indicators of the corresponding modified asphalt, such as the rotational viscosity at 177°C, softening point, and penetration. It was found that the rotational viscosity at 177°C of the modified asphalt was significantly correlated to the dynamic stability of the mixture. Hu et al. (2018) tested the four components of different rubber modified asphalt based on multivariate regression analysis and gray correlation analysis to analyze the correlation between the proportion of the four components and each index. The results showed that the 60°C complex elastic modulus and the zero shear viscosity (ZSV) obtained by the DSR testing had a correlation coefficient as high as 0.99 with four components of asphalt. Li et al. (2015) studied the influence of rubber powder content and matrix asphalt type on the performance of rubber modified asphalt through conventional performance tests and DSR testing. Li also analyzed the applicability of evaluation indexes and concluded that penetration degree is not appropriate for the performance evaluation of rubber modified asphalt while the softening point is suitable. Huang et al. (2010) investigated the influence of rubber powder property, asphalt-stone ratio, porosity, etc., on the high-temperature performance of mixture through the wheel rutting test and found that rubber powder content and asphalt-stone ratio had more significant impacts.

In previous studies, various indexes were used to evaluate the high-temperature performance of rubberized asphalt and mixture. However, consistent results of asphalt and mixture have rarely been reported, making it difficult to characterize the high-temperature performance of actual road surfaces with asphalt evaluation indexes used in engineering. Therefore, in this paper, rubberized asphalt and mixtures with different viscosity grades were prepared based on the rotational viscosity at 180°C and their high-temperature rheological properties were analyzed using frequency scanning, repeated creep recovery (RCR), and temperature sweep tests. Furthermore, the correlation between indicators, including the fractal dimension of rubberized asphalt and mixture and high-temperature stability of three types of asphalt mixtures (SMA, ARAC, and AC) was analyzed by Pearson correlation. Finally, the gray correlation degree of the high-temperature performance evaluation index of asphalt and mixture was analyzed. It is expected that this study can guide the selection of reasonable evaluation indexes for rubberized asphalt pavement construction in the future.

2 RAW MATERIAL AND TESTS

2.1 Raw Materials

The rubberized asphalt with different viscosity grades (about 1 Pa·s, 3 Pa·s, 5 Pa·s, and 7 Pa·s) was prepared according to rotational viscosity at 180°C. Esso matrix asphalt and Maoming matrix asphalt (referred to as A and B) were selected as raw materials, and 30–100 mesh rubber powder under different dosing regimens was used as the modifier. For simplification, asphalt samples were expressed in the form of asphalt type-rubber powder content-rotational viscosity at 180°C. For example, A-20%-1 represents the Esso modified rubberized asphalt with a rubber powder content of 20% and a rotational viscosity of 1 Pa·s at 180°C. The performance indexes of raw materials, rubber powder, and modified asphalt are shown in **Tables 1–3**.

2.2 Test Methods

2.2.1 Rheological Property Test

In this paper, the Bohlin cvo100D-ADS type DSR produced by Malvern, United Kingdom, was used to study the rheological properties of asphalt samples. The test temperature range of this instrument is 5°C–95 °C, the frequency range is 10 μHz–100 Hz, and the shear rate range is 0.1 μrad/s-320 rad/s, and the strain range is 1%–100%. In this paper, frequency scanning, temperature sweep, and RCR tests were conducted to evaluate the rheological properties.

2.2.1.1 Frequency Scanning Test.

The DSR frequency scanning was performed to explore the stress-resistant behavior of asphalt when vehicle loads were moving on the asphalt pavement at different speeds. In this paper, the change of complex viscosity with stress frequency from 0.001 to 10 Hz at 60°C was used to indicate the anti-deformation ability of rubber modified asphalt. Additionally, based on the Carreau model and the Cross model (He, 2019), ZSV of different asphalt samples was derived for subsequent correlation evaluation of asphalt indexes.

2.2.1.2 Repeated Creep Recovery Test.

The RCR test was proposed by Bahia et al. (2001). It aims to simulate the behavior of asphalt in the development of permanent deformation of the mixture when the pavement is under the traffic load. In this paper, the DSR instrument was applied to load the sample for 1 s and unload the sample for 9 s under a stress of

TABLE 1 | Main performance indexes of matrix asphalt.

Performance Index	Test method (Industry standards of Transportation Department of the People ' s Republic of China, 2011b)	Test result	
		A	B
Penetration degree (25 °C, 100 g, 5 s)/0.1 mm	T0604	62.2	68.2
Penetration Index (PI)	T0604	0.1	-0.1
Ductility (5 cm/min, 15 °C)/cm	T0605	135	120
Softening point/°C	T0606	48.6	48.8
Flashing point/°C	T0611	279	289

TABLE 2 | Main performance indexes of rubber powder.

Performance Index	Test method	Test result
Sieve residue/%	GB/T19208	5.6
Relative density	JT/T797	1.11
Moisture content/%	GB/T19208	0.5
Metal content/%	JT/T797	0.029
Fiber content/%	GB/T19208	0.01

30 Pa and the cycle was repeated 100 times. The stress change of the sample was recorded. Finally, the Burgers model (Lin and Fan, 2018) was used to fit the obtained stress and deformation data, and the viscous stiffness modulus (G_v) and permanent deformation (ε_L) were applied for performance evaluation.

2.2.1.3 Temperature Sweep Test.

The rutting factor $G^*/\sin\delta$ in the DSR temperature sweep is one of the important indexes to evaluate the high-temperature performance of asphalt. Since the phase angle of rubber modified asphalt has a low phase angle, its temperature sweep test was carried out at 64°C–82°C. Furthermore, the improved rutting factor $G^*(\sin\delta)^{-9}$ based on the study of Shenoy (2001) was compared with the conventional rutting factor.

2.2.2 Hamburg Wheel Tracking Test

Hamburg wheel tracking test (HWTT) reflects the high-temperature rutting resistance of asphalt mixture through the stress-strain behavior of the mixture sample against deformation under repeated load. The rutting deformation rate (RDr) and the creep slope (CS) were used to evaluate the results of the HWTT. The physical meaning of RDr is the amount of rutting deformation per hour and a larger RDr indicates worse high-temperature rutting resistance. The RDr index includes the maximum rutting depth, which can compare the high-temperature rutting resistance among asphalt mixtures simply and effectively. CS represents the rutting development speed, which is reflected in the rut development curve as the reciprocal of the slope in a certain stage, and its physical meaning is the number of loadings to produce 1 mm deformation.

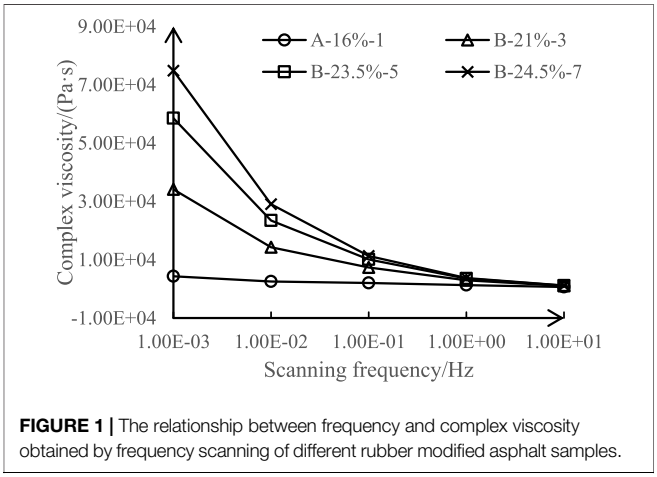

FIGURE 1 | The relationship between frequency and complex viscosity obtained by frequency scanning of different rubber modified asphalt samples.

3 TEST RESULTS

3.1 Rheological Property Test Results

3.1.1 Frequency Scanning Test Results

The relationship between frequency and complex viscosity obtained by frequency scanning of different rubber modified asphalt samples at 60 °C is shown in **Figure 1**.

As shown in **Figure 1**, the increase of the complex viscosity gradually slows down with the progressive increase in rotational

TABLE 3 | Main performance indexes of rubber modified asphalt.

Performance Index	Test method	Test result			
		A-16%	B-20%	B-23.5%	B-24.5%
Penetration (25 °C, 100 g, 5 s)/0.1 mm	GB/T19208	39.8	35.7	32.4	31.7
Softening point/°C	JT/T797	66.9	72.8	77.2	78.5
Rotational viscosity at 180 °C/Pa·s	GB/T19208	0.97	3.21	5.14	7.21

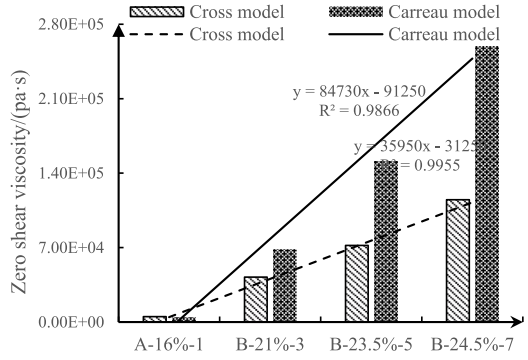

FIGURE 2 | ZSV of modified asphalt under different calculation models.

viscosity. When the frequency is 0.001 Hz, the complex viscosity of the B-21%-3 sample is 686.4% higher than that of the A-16%-1 sample, while the complex viscosity of the B-24.5%-7 sample is only 27.8% higher than that of the B-23.5%-5 sample. However, the gap decreases significantly as the scanning frequency increases. When the scanning frequency is 10 Hz, the complex viscosity of the B-21%-3 sample is 56.9% higher than that of the A-16%-1 sample, while the complex viscosity of the B-24.5%-7 sample is only 6.4% higher than that of the B-23.5%-5 sample. It is shown that under low-frequency stress scanning, the complex viscosity and the rotational viscosity have large evaluation differences.

Since rubberized asphalt is easily affected by stress frequency, its viscosity evaluation index is also susceptible to the interference of stress frequency. In this paper, ZSV derived based on the Carreau model and the Cross model (He, 2019) was adopted as an evaluation index of rubberized asphalt. The variation of ZSV of different modified asphalt samples is shown in **Figure 2**.

ZSV increases with the progressive increase of rotational viscosity. The linear fitting shows that the correlation coefficient between ZSV derived based on the two models and rotational viscosity are 0.9866 and 0.9955, respectively, indicating strong correlations. Furthermore, the fitting slope of the Carreau model is greater than that of the Cross model, indicating that the Carreau model is more sensitive to asphalt viscosity changes.

3.1.2 Repeated Creep Recovery Test Results

The trends of the viscous stiffness modulus (G_v) and permanent deformation (ε_L) of different modified asphalt under the stress of 30 Pa in the RCR test are shown in **Figure 3**.

It can be seen from **Figure 3** that as the rotation viscosity progressively increases, the viscous stiffness modulus (G_v) of asphalt samples increases, and the permanent deformation (ε_L) decreases, suggesting that asphalt samples with higher viscous stiffness modulus (G_v) have a better permanent deformation (ε_L) resistance ability. This finding is consistent with the previous conclusion. The linear fitting of rotational viscosity and viscous stiffness modulus (G_v) show that the R^2 = 0.7582, which indicates a strong correlation, but the correlation is weaker than that between ZSV and rotational viscosity.

3.1.3 Temperature Sweep Test

In this paper, the rutting factor $G^*/\sin\delta$ and the improved rutting factor $G^*(\sin\delta)^{-9}$ were used to evaluate the asphalt samples. The results are shown in **Figure 4**.

As shown in **Figure 4**, the basic trends of the two indexes are the same. However, the difference among improved rutting factor $G^*(\sin\delta)^{-9}$ is larger than that among conventional rutting factor $G^*/\sin\delta$. The temperature sweep curves of B-24.5%-7 and B-23.5%-5 in **Figure 4A** almost overlap while curves in **Figure 4B** do not. With the rising temperature, the decrease in the improved rutting factor $G^*(\sin\delta)^{-9}$ is more significant than that of the conventional rutting factor $G^*/\sin\delta$. For example, the improved rutting factor of B-24.5%-7 sample at 82°C decreases by 95.8% compared with that at 64°C. In contrast, the conventional rutting factor $G^*/\sin\delta$ decreases by 83.4%, suggesting that the improved rutting factor $G^*(\sin\delta)^{-9}$ is more sensitive to changes in temperature and asphalt rotational viscosity.

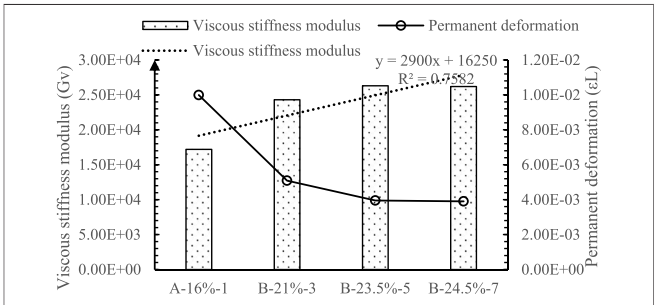

FIGURE 3 | RCR test results of modified asphalt with different rotational viscosities.

3.2 Hamburg Wheel Tracking Test

In this paper, RDr and CS were adopted to evaluate the high-temperature rutting resistance of different modified rubberized asphalt mixtures with three gradations (SMA-13, ARAC-13, and AC-13). The sieve passing rates of these gradations are shown in **Table 4**, and the performance index of the mixture is shown in **Table 5**.

4 TEST RESULT ANALYSIS

4.1 Correlation Analysis of Factors Affecting the High-Temperature Performance of the Mixture

4.1.1 Analysis of Gradation Characteristics Based on Fractal Theory

The correlations between factors including gradation type, rotational viscosity, rubber powder content, asphalt-stone ratio, and porosity, and two indexes (RDr and CS) in HWTT were analyzed. In this way, the influencing factors for the high-

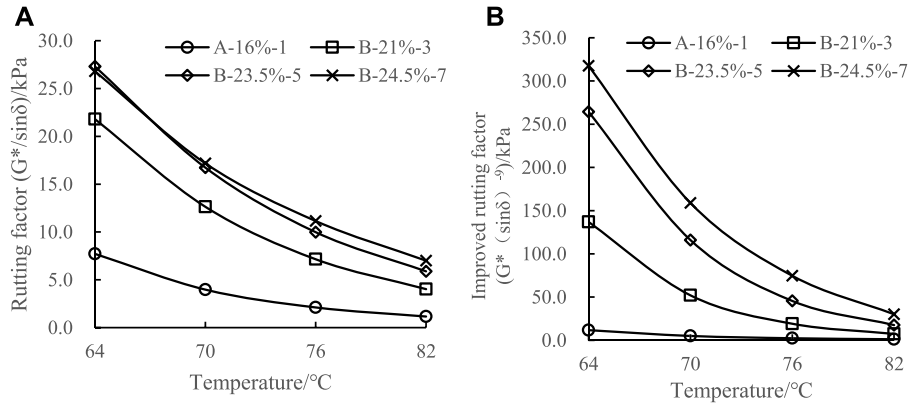

FIGURE 4 | The trend of two rutting factors of different modified asphalt. **(A)** Conventional rutting factor **(B)** Improved rutting factor.

TABLE 4 | Sieve passing rates of the three gradations.

Gradation type	Sieve (mm) passing rate/%									
	16	**13.2**	**9.5**	**4.75**	**2.36**	**1.18**	**0.6**	**0.3**	**0.15**	**0.075**
SMA-13	100	94.5	61	25.5	19.5	16	13	11	9	6
ARAC-13	100	93.2	68.8	30.2	19.8	13.2	9.2	5.9	3.8	2.5
AC-13	100	96.5	73.5	45	29	19.5	13	9	6.5	4.5

TABLE 5 | Asphalt-stone ratio and performance indexes of different modified asphalt mixtures.

Gradation type	Asphalt type	Asphalt-Stone ratio/%	Porosity/%	RDr/(mm/h)	CS/(times/mm)
SMA-13	A-16%-1	5.8	3.8	4.879	0.118
	B-21%-3	6.6	4.1	1.278	0.025
	B-23.5%-5	6.9	4.0	0.924	0.0162
	B-24.5%-7	7.1	3.8	0.707	0.0116
ARAC-13	A-16%-1	6.7	4.0	6.524	0.167
	B-21%-3	7.1	4.2	1.285	0.0251
	B-23.5%-5	7.2	3.8	1.087	0.0209
	B-24.5%-7	7.3	4.0	1.047	0.016
AC-13	A-16%-1	4.9	4.1	1.658	0.0323
	B-21%-3	5.4	3.9	0.536	0.0082
	B-23.5%-5	5.5	4.2	0.516	0.0086
	B-24.5%-7	5.7	4.0	0.484	0.0067

temperature performance of the mixture were ranked to guide the engineering construction. For the simplicity of the characteristics analysis of the overall gradation and coarse and fine gradations, the gradation was described based on the fractal dimension theory. Fractal dimension theory is an emerging subject that quantitatively describes the complexity and space-filling capacity of geometry. In addition, the theory can describe the asphalt mixtures, which are characterized by heterogeneity, nonlinearity, irregularity, and ambiguity, especially aggregate gradation with self-similarity (Yang et al., 2006).

The double logarithmic scatter plots of three gradation curves are drawn based on the fractal theory, as shown in **Figure 5**. The least square method was applied to perform linear regression to obtain the overall fractal dimension (D) of the gradation. Then, only the parts of the gradation curve with a value above or below 4.75 mm were taken to calculate the gradation fractal dimensions of coarse and fine aggregates (Dc and Df), respectively. The fractal indexes of the three degradations are shown in **Table 6**, and the changing trend is shown in **Figure 6**.

1) R^2 in the regression equation represents the fitting degree between the actual gradation and the gradation modeled based on the fractal theory. **Figure 6** shows that the fractal characteristics of the three types of gradation are all strongly correlated. AC has the strongest correlation, and SMA has the weakest correlation. This phenomenon is because SMA gradation is discontinuous and its continuous granular material system with fractal characteristics breaks into multiple small fractal systems due to the lack of aggregates in a certain particle size range.

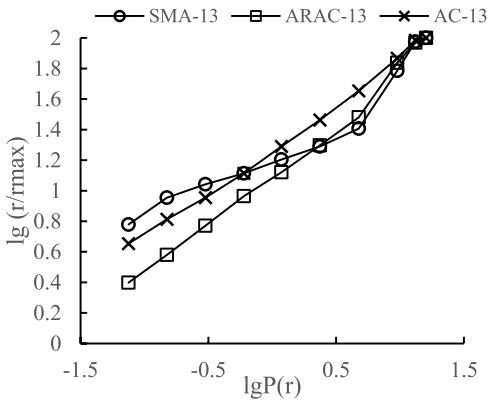

FIGURE 5 | Double logarithmic scatter plot of three gradation curves.

TABLE 6 | Calculation results of the fractal dimension of three gradations.

Gradation type	D		Df		Dc	
	Value	R^2	Value	R^2	Value	R^2
SMA-13	2.5042	0.919	2.676	0.9849	1.8248	0.9866
ARAC-13	2.3121	0.9885	2.4007	0.9995	1.9801	0.9823
AC-13	2.41	0.9962	2.4478	0.9979	2.3133	0.9882

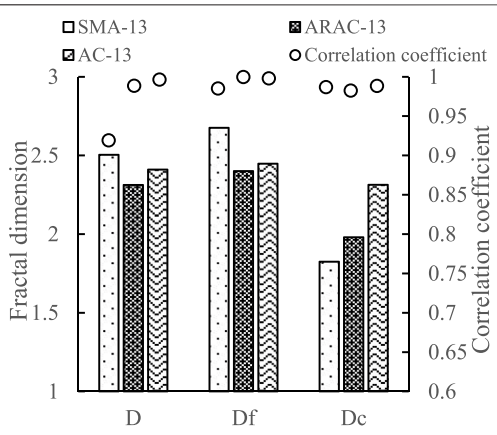

FIGURE 6 | Three fractal dimensions with different gradations and their correlation coefficients.

2) **Figure 6** shows that the D and Df values of SMA are higher than those of ARAC and AC, which are continuous gradations. **Figure 6** and the aggregate proportion of each gradation in **Table 5** indicate that as the proportion of the coarse aggregate in the gradation increases, the D and Df values increase while the Dc value decreases. This result suggests that the fractal dimension can effectively characterize the difference in the proportion of particle size of different gradations. Therefore, in the following part, the Pearson correlation analysis between the characteristics of the overall gradation and coarse and fine aggregates represented by D, Df, and Dc, and the rutting performance indexes of the mixture in HWTT were conducted.

4.1.2 Correlation Analysis

The Pearson correlation analysis between fractal dimensions, rubber powder content, asphalt-stone ratio, and porosity of the three gradation types and RDr and CS obtained from HWTT was performed. The results are shown in **Table 7**.

It can be seen from **Table 7** that.

1) Among the influencing factors, asphalt-stone ratio, porosity, and Df are all positively correlated with RDr and CS, indicating that the larger the three factors, the worse the high-temperature performance of the mixture. While the other influencing factors are all negatively correlated with the two indexes in HWTT, indicating that when their values are large, the high-temperature performance of the mixture is excellent.

2) The asphalt-stone ratio and Dc have significant effects on the high-temperature performance of the mixture, and the absolute values of the correlation coefficients are higher than 0.7. The remaining factors in the order of influence are the rubber powder content, rotational viscosity at 180°C, porosity, D, and Df. The asphalt-stone ratio of the mixture needs to be determined by aggregate characteristics and gradation characteristics together and cannot be controlled artificially. Therefore, to improve the high-temperature performance of the mixture, the priority is controlling the proportion of the coarse aggregate in the gradation. Then the rubber powder content needs to be controlled to enhance the asphalt viscosity.

4.2 Gray Correlation Analysis for Performance Index of Asphalt and Index of Hamburg Wheel Tracking Test

4.2.1 Calculation Method for Gray Correlation Analysis

The gray correlation analysis of indexes of general performance and rheological performance and the indicators of HWTT was performed to obtain the index which has the strongest correlation with the indicator.

Gray correlation analysis theory (Tan and Deng, 1995), proposed by Chinese scholar Prof. Deng Julong in 1982, is an important part of gray system theory. It has been widely used in many scientific research fields. The basic idea of gray correlation analysis theory is to judge whether the relationship is close according to the similarity of the geometry of the sequence curve. Curves close to each other indicate a strong correlation between the corresponding sequences. Gray relational analysis theory is applicable whether the sample size has regularity or not. The calculation is easy, and the quantitative results agree with the qualitative analysis results. In practical applications, the degree of the influence of factors on the results is generally represented by the gray correlation degree. A value closer to 1 indicates a higher influence degree. The calculation process is as follows:

1 The reference sequence that characterizes the system (i.e., the result)and the comparison sequence that affects the system features (i.e., the influencing factor) are determined. The two sequences are characterized by $X_0(k)$,k = 1,2 . . . m and $X_i(k)$,k

TABLE 7 | Correlation analysis of mixture performance and influencing factors.

Performance Index		Influencing factors						
		D	Df	Dc	Rotational viscosity	Rubber content	Asphalt-Stone ratio	Porosity
RDr	R^2	-0.238	0.085	-0.728	-0.385	-0.392	0.764	0.195
	SIG	0.538	0.827	0.026*	0.306	0.297	0.017*	0.615
CS	R^2	-0.195	0.107	-0.696	-0.486	-0.476	0.695	0.225
	SIG	0.615	0.783	0.037*	0.184	0.196	0.038*	0.561

Note: sig value ≤0.05 indicates a significant correlation.

= 1,2 . . . m,i = 1,2 . . . n, respectively, where m is the number of results corresponding to one factor, and n is the number of factors.

2 According to **Eq. 1**, the original data are non-dimensionalized:

$$X_i^{'}(k) = X_i(k) \Big/ X_i(1), k = 1, 2, \ldots m; i = 0, 1, \ldots n \quad (1)$$

where $X_i^{'}(k)$ is the non-dimensionalization result of the k th number of the i th factor (result).

3 The difference sequence is calculated according to **Eq. 2**:

$$\Delta_{0i}(k) = \left|X_0^{'}(k) - X_i^{'}(k)\right|, k = 1, 2, \ldots m; i = 1, 2, \ldots n \quad (2)$$

Where $\Delta_{0i}(k)$ is the absolute value of the difference between the k th number of the i th factor and the k th result in the reference sequence after non-dimensionalization.

4 The gray correlation number is calculated according to **Eq. 3**:

$$\xi_{0i}(k) = \frac{\Delta_{\min} + \rho\Delta_{\max}}{\Delta_{0i}(k) + \rho\Delta_{\max}} \quad (3)$$

where $\xi_{0i}(k)$ is the correlation number between the k th number of the i th factor and the k th result in the reference sequence; $\Delta_{\min}$ and $\Delta_{\max}$ are the minimum and maximum values in the difference sequence, respectively; ρ is the correlation resolution coefficient, which is usually set at 0.5.

5 The gray correlation degree is calculated according to **Eq. 4**:

$$\gamma_{0i} = \frac{1}{m}\sum_{k=1}^{m}\xi_{0i}(k) \quad (4)$$

where γ_{0i} is the gray correlation degree between the i th factor and the reference sequence.

4.2.2 Gray Correlation Analysis

The data of the same kind of modified asphalt with different gradations in **Table 5** are equalized (since the deformation of the A-16%-1 asphalt mixture reaches 1,000 mm, resulting in the abnormal indexes, this set of data is excluded from the analysis). RDr and CS in HWTT are taken as reference sequences. The softening point, rotational viscosity at 180 ˚C in the conventional test, the ZSV of the Cross model and Carreau model obtained by frequency scanning in the rheological property test, the viscous stiffness modulus (G_v) and permanent deformation (ε_L) obtained in the RCR test, and the rutting factor G*/sinδand the improved rutting factor $G^*(\sin\delta)^{-9}$ at 64 ˚C in the temperature sweep test are taken as the comparison sequences. The gray correlation degree is calculated according to **Eqs 1–4**. The initial values of the reference sequence and the comparison sequence are shown in **Table 8**.

The correlation analysis is performed on the data in **Table 8**. The correlation between the two reference sequences is shown in **Table 9**.

As shown in **Table 9**, the ranking of asphalt performance indexes in terms of the gray correlation degree with RDr and CS in HWTT is the same: permanent deformation > softening point > viscous stiffness modulus > rutting factor > rotational viscosity > ZSV (Cross model) > improved rutting factor > ZSV (Caren model). The permanent deformation has a correlation degree larger than 0.8 with both RDr and CS, indicating that it is strongly correlated with the high-temperature rutting resistance of the asphalt mixture. Additionally, the correlations between the softening point and viscous stiffness modulus and the two indexes in HWWT are all higher than 0.7, which indicates a strong correlation. Therefore, the use of the permanent deformation and viscous stiffness modulus in the repeated creep test is recommended for the evaluation of the high-temperature performance of rubberized asphalt mixture. Compared with rotational viscosity in conventional tests, they correlate better with the high-temperature stability of the mixture. The softening point also shows an excellent correlation with the high-temperature performance in conventional tests and has a priority over rotational viscosity.

5 CONCLUSION

1) The correlation coefficients of eigenvalues based on fractal dimension theory are all greater than 0.9, which indicates that fractal dimension theory is suitable for characterization of gradation characteristics. Based on the correlation analysis of the influencing factors of the high temperature performance of the mixture, it can be seen that the asphalt-stone ratio and the fractal dimension of coarse aggregate Dc have significant indigenous effects on the high temperature performance of the

TABLE 8 | Initial values of the reference sequence and comparison sequence.

Index			Asphalt type		
			B-21%-3	B-23.5%-5	B-24.5%-7
CS		Reference sequence	0.019	0.015	0.011
RDr			1.033	0.842,333	0.746
Softening point		Comparison sequence	72.8	77.2	78.5
Rotational viscosity			3.212	5.143	7.248
ZSV	Cross model		4.23E+04	7.21E+04	1.15E+05
	Carreau model		6.81E+04	1.51E+05	2.59E+05
Viscous stiffness modulus (G_v)			2.43E+04	2.63E+04	2.62E+04
Permanent deformation (ε_L)			5.09E-03	3.95E-03	3.90E-03
Rutting factor			21.795	27.297	26.799
Improved rutting factor			137.017	264.307	317.619

TABLE 9 | Gray correlation degree of each asphalt index and the index in HWTT.

Reference sequence	Comparison sequence							
	Softening point	Rotational viscosity	ZSV		Viscous stiffness modulus (G_v)	Permanent deformation (ε_L)	Rutting factor	Improved rutting factor
			Cross model	Caren model				
RDr	0.738	0.591	0.570	0.547	0.730	0.928	0.660	0.527
Correlation ranking	②	⑤	⑥	⑧	③	①	④	
CS	0.719	0.605	0.553	0.532	0.710	0.813	0.650	0.542
Correlation ranking	②	⑤	⑥	⑧	③		④	

mixture. Therefore, gradation has the greatest impact on the high temperature stability of rubberized asphalt mixture.

2) The grey correlation degree was used to analyze the indexes of rubberized asphalt binder and hamburger rutting test results. It was found that there was no significant correlation between rotational viscosity and other high temperature rheological indexes and rubberized asphalt mixture. The correlation coefficient between the permanent deformation, viscous stiffness modulus and softening of the repeated creep test and the results of the Hamburg rutting test is greater than 0.7, showing a significant indigenous correlation, which can effectively characterize the high-temperature performance of rubberized asphalt binder. These three indicators are recommended as high-temperature evaluation indexes of rubberized asphalt binder.

DATA AVAILABILITY STATEMENT

The raw data supporting the conclusion of this article will be made available by the authors, without undue reservation.

AUTHOR CONTRIBUTIONS

CX is the experimental designer and executor of this research, completing data analysis and writing the first draft of the paper; JL guides data analysis, thesis writing and revision; LZ, TR, HL, and JC participated in the experimental design and analysis of experimental results, and the paper was revised. All authors have read and agreed to the final text.

REFERENCES

Bahia, H. U., Hanson, D. I., and Zeng, M. (2001). *Characterization of Modified Asphalt Binders in Superpave Mix Design[R]*. Washington DC, United States: Transportation Research Board.

Ding, X., Chen, L., Ma, T., Ma, H., Gu, L., Chen, T., et al. (2019). Laboratory Investigation of the Recycled Asphalt Concrete with Stable Crumb Rubber Asphalt Binder. *Constr. Build. Mater.* 203 (APR.10), 552–557. doi:10.1016/j.conbuildmat.2019.01.114

He, L. P., Shen, A. Q., and Xie, C. (2014). Orthogonal Test of Rubber Asphalt Binder Performance[J]. *J. Chang'an University:Natural(Science Ed.* 34 (1), 7–12. doi:10.19721/j.cnki.1671-8879.2014.01.002

He, L. P. (2019). *Study on Viscoelastic Properties and High Temperature Performance of Rubber Asphalt Based on DMA method[D]*. Xi'an, China: Chang'an University.

Hu, J., Ma, T., Yin, T., and Zhou, Y. (2022). Foamed Warm Mix Asphalt Mixture Containing Crumb Rubber: Foaming Optimization and Performance Evaluation. *J. Clean. Prod.* 333, 130085. doi:10.1016/j.jclepro.2021.130085

Hu, S. S., Qin, R. P., and Li, H. (2018). Application of Rubber Asphalt Performance Testing Technology[J]. *Acta Mater. Compos. Sin.* 35 (8), 14. doi:10.13801/j.cnki.fhclxb.20170905.002

Huang, W. D., Wang, W., and Huang, Y. (2010). Test on Influencing Factors of High Temperature Stability of Rubber Asphalt Mixture[J]. *J. Tongji Univ. Sci.* 38 (7). doi:10.3969/j.issn.0253-374x.2010.07.015

Industry standards of Transportation Department of the People ' s Republic of China (2011). *Asphalt Rubber for Highway Engineering: JT/T 798-2019 [S]*. Beijing, China: china communications press.

Industry standards of Transportation Department of the People ' s Republic of China (2011). *Standard Test Methods of Bitumen and Bituminous Mixtures for Highway Engineering: JTG E20-2011[S]*. Beijing, China: china communications press.

Li, X. Y., Ping, L., and Wang, H. N. (2015). Performance Test of Rubber Asphalt Based on Domestic and Foreign Test Methods[J]. *J. Transp. Eng.* 15 (1), 8. doi:10.3969/j.issn.1671-1637.2015.01.002

Lin, J. T., and Fan, L. (2018). High Temperature Performance Evaluation of Asphalt Based on MSCR Test and Burgers Model Analysis[J]. *J. Highw. Transp. Res. Dev.* 35 (6), 8. doi:10.3969/j.issn.1002-0268.2018.06.004

Ma, T., Chen, C. L., and Zhang, Y. (2021). Development of Rubber Powder Used in Asphalt Modification Technology[J]. *China J. Highw. Transp.* 34 (10), 16. doi:10.19721/j.cnki.1001-7372.2021.10.001

Navarro, F. J., Partal, P., Martínez-Boza, F., and Gallegos, C. (2005). Influence of Crumb Rubber Concentration on the Rheological Behavior of a Crumb Rubber Modified Bitumen. *Energy fuels.* 19 (5), 1984–1990. doi:10.1021/ef049699a

Shenoy, A. (2001). Unifying Asphalt Rheological Data Using the Material's Volumetric-Flow Rate. *J. Mat. Civ. Eng.* 13 (4), 260–273. doi:10.1061/(asce)0899-1561(2001)13:4(260)

Tan, X. R., and Deng, J. L. (1995). Grey Correlation Analysis : a New Method for Multivariate Statistical Analysis[J]. *Stat. Res.* 3, 3. doi:10.19343/j.cnki.11-1302/c.1995.03.011

Yang, G., Huang, W. D., and Li, Y. W. (2010). Experimental Study on High Temperature Performance Evaluation Index of Rubber Asphalt Mixture[J]. *J. Build. Mater.* 13 (6), 6. doi:10.3969/j.issn.1007-9629.2010.06.010

Yang, Q., Guo, Z. Y., and Chen, L. P. (2006). Fractal Characteristics Analysis of Graded Crushed Stone and its Application in Pavement Engineering[J]. *J. Build. Mater.* 9 (4), 5. doi:10.3969/j.issn.1007-9629.2006.04.008

Zhou, H., Holikatti, S., and Vacura, P. (2014). Caltrans Use of Scrap Tires in Asphalt Rubber Products:a Comprehensive Review[J]. *J. Traffic Transp. Eng. Ed.* 12 (2), 23–34.

Conflict of Interest: Authors CX, JL, TR, HL, and JC were employed by Guangxi Beitou Transportation Maintenance Technology Group Co., LTD. Author LZ was employed by Guangxi Transportation Science and Technology Group CO., LTD.

frontiers | Frontiers in Materials

TYPE Original Research
PUBLISHED 14 March 2023
DOI 10.3389/fmats.2023.1157529

OPEN ACCESS

EDITED BY
Hui Yao,
Beijing University of Technology, China

REVIEWED BY
Hao Wu,
Central South University, China
Dong Lu,
Hong Kong Polytechnic University, Hong Kong SAR, China

*CORRESPONDENCE
Jue Li,
lijue1207@cqjtu.edu.cn

SPECIALTY SECTION
This article was submitted to Structural Materials, a section of the journal Frontiers in Materials

RECEIVED 02 February 2023
ACCEPTED 28 February 2023
PUBLISHED 14 March 2023

CITATION
Wei H, Zhou Y, Huang W, Wen P and Li J (2023), Fracture characteristics of a cement concrete pavement plate considering subgrade modulus decay based on a meshless finite block method. *Front. Mater.* 10:1157529. doi: 10.3389/fmats.2023.1157529

Fracture characteristics of a cement concrete pavement plate considering subgrade modulus decay based on a meshless finite block method

Hui Wei[1,2], Yu Zhou[2], Wang Huang[2], Pihua Wen[3] and Jue Li[4]*

[1]Engineering Research Center of Catastrophic Prophylaxis and Treatment of Road and Traffic Safety of Ministry of Education, Changsha University of Science and Technology, Changsha, China, [2]School of Traffic and Transportation Engineering, Changsha University of Science and Technology, Changsha, China, [3]Institute of Aerospace, Nanchang University, Nanchang, China, [4]College of Traffic and Transportation, Chongqing Jiaotong University, Chongqing, China

The decrease in the subgrade modulus immersed in rainwater can significantly increase the fracture risk of a cement concrete pavement plate. The aim of this study was to develop a meshless finite block method (MFBM) to reveal the failure mechanism of a cement concrete pavement due to the weakening of the subgrade modulus. A normal distribution function was adopted in this study to represent the distribution of the subgrade modulus at the bottom of the cement concrete pavement plate. The settlement results show that the progressive softening model of soil subgrade is more suitable to represent subgrade modulus decay. The maximum stress of the cement concrete pavement mainly concentrates at 1.05–1.15 m of the plate edge. The weak fracture position is influenced by the subgrade modulus reduction, the size of the immersion range, and the pavement and subgrade thickness. When improving the subgrade modulus, adding plate thickness appropriately can effectively control the cracking of the cement concrete pavement. Compared with the finite element model, it is proved that the proposed MFBM has an advantage in the solution of pavement fracture with high accuracy and less computation time. In addition, findings in this study may provide evidence for understanding the effect of the subgrade modulus on the durable pavement design.

KEYWORDS

concrete pavement, meshless finite block method, progressive softening model, finite element method, subgrade modulus decay

1 Introduction

Generally, a cement concrete pavement is regarded as a small deflection elastic plate supported on an elastic foundation, and the theory of the elastic foundation plate is used for analysis and calculation. This theory assumes that the contact surface between the elastic thin plate and the elastic half-space body is completely contact, continuous, and uniform, with no void (Rahim and George, 2005; Lin and Karadelis, 2019). However, it is interesting to note that the phenomenon of scouring and disengaging is very common in reality for a pavement base composed of semi-rigid materials (Wang et al., 2019). These common defects result in a great difference between the actual support condition at the

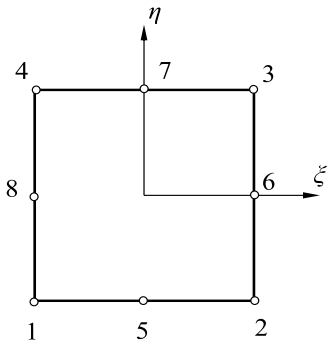

FIGURE 1
Geometry mapping technique in the FEM.

concrete plate bottom and the complete contact assumption of continuous uniform support (Liu et al., 2020). In addition, the cavity beneath the concrete plate can be exacerbated over time, making the surface layer lose its support of foundation (Qu et al., 2017). The soil subgrade is also affected by scouring and disengaging issues, which leads to obvious changes in soil subgrade conditions in different periods (Peng et al., 2020). In particular, water is one of the environmental media that significantly affects the subgrade modulus. The decay of the subgrade modulus results in the uneven settlement of the base layer (Zhao et al., 2019). Since the bearing mode of the concrete surface plate becomes a cantilever mode with a single support, the corner of the plate is easily prone to fracture failure. However, currently, experimental studies find it difficult to measure the fracture behavior of the pavement plate, considering the effect of moisture on the subgrade modulus. The fracture characteristics of a cement concrete pavement plate are still a necessary issue in pavement structure design.

In engineering applications, numerical techniques have become an effective and efficient tool for analyzing the mechanical strength of continuum and dis-continuum structures (Wen et al., 1997; Wen et al., 1998; Wei et al., 2022). Nowadays, the most popular numerical research method of cement concrete pavement failure is the finite element method (FEM) (Li et al., 2019). However, the FEM often lacks the precision and convergence for calculated results for discontinuous physical domains. Due to the restriction of the FEM on discontinuous mechanics, some novel computational methods have been formulated in recent years (Li et al., 2023). For example, Lian et al. (2011) developed a material point (MP) model of a reinforced concrete structure by incorporating the FEM element of steel reinforcement. The results suggest that the MP method can take into account the advantages of different FEM elements. Combining the crack propagation of a specific loading zone, Mahmoud et al. (2014) investigated the fracture characteristics of seven paving materials through an extended FEM. Nayroles et al. (1992) reported that meshless approximation is applicable in a simulating discontinuous medium since it takes discrete points as calculation elements. The meshless method has a unique advantage in adaptive, large deformation, and structural failure analysis (Atluri and Zhu, 1998). In addition, the numerical model is independent of meshing elements due to neither domain nor boundary meshes required in the numerical procedure (Sladek et al., 2005; Sladek et al., 2006). Based on the meshless method, Yu et al. (2023) established a microstructure of cement concrete to analyze the impact of drying shrinkage on mechanical behavior. The result suggested that the meshless method is more flexible and applicable in the adaptive analysis and the global stress smoothness than in the traditional FEM. Therefore, the meshless method provides a scientific solution to evaluate fracture characteristics of a dis-continuum structure under load and other external conditions (Huang et al., 2023). Furthermore, to improve the efficiency and accuracy of calculation, a finite block method (FBM) was proposed for solving practical problems over unbounded regions by Lagrange series interpolation (Li and Wen, 2014; Wen et al., 2014). Huang et al. (2018) established the FBM to determine the stress and fracture characteristics of an elastoplastic structure with excellent accuracy. Ahmad et al. (2020) applied a local meshless method to solve the sparse system of 3D problems and demonstrated the high degree of accuracy with rectangular domains. These numerical studies demonstrated that the meshless finite block method is effective for solving fracture problems of a cement concrete plate.

The aim of this paper was to establish a meshless finite block method (MFBM) model of a cement concrete pavement structure for evaluating the stress change of the pavement plate with the weakening of the subgrade modulus. The MFBM developed in this study can eliminate the limitation with a mesh technique with high accuracy and less computation time. The subgrade material drenched by rainwater was assumed as a functionally graded material in this study. A progressive softening model of soil subgrade was established to characterize the subgrade modulus decay. The FEM analysis software application Abaqus was used to verify the validity and accuracy of the results calculated by the MFBM.

2 Lagrange interpolation and mapping technique

An MFBM interpolated by the Lagrange series has been proposed on the mapping technique according to the research of Li et al. (2016). A brief introduction about the technique is described in this section. Specifically, for 2D problems, a set of nodes is used in the normalized space $P(\xi_k, \eta_k)$, $k = (j-1) \times N_\xi + i$, $i = 1, 2, \cdots, N_\xi$, and $j = 1, 2, \cdots, N_\eta$, as shown in Figure 1. The field function $u(Q)$ at a mapped domain $Q(\xi, \eta)$ can be approximately expressed by Eq. (1).

$$u(Q) = \sum_{i=1}^{N_\xi}\sum_{j=1}^{N_\eta} F(\xi, \xi_i) G\left(\eta, \eta_j\right) u^{(k)} = \sum_{k=1}^{M} \varphi_k(Q) u^{(k)}, \qquad (1)$$

where N_ξ and N_η indicate the numbers of nodes along ξ and η axes, respectively; M is the total number of nodes for each block; $\varphi_k(Q)$ is the shape function; ξ and η represent coordinates in $Q(\xi, \eta)$; and $F(\xi, \xi_i)$ and $G(\eta, \eta_i)$ are the polynomial functions, as shown in Eq. (2).

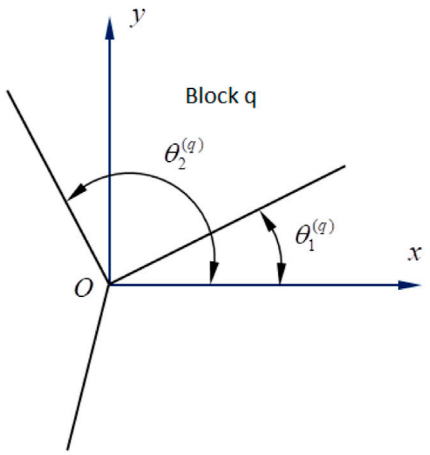

FIGURE 2
Starting and ending angles for block q at joint O.

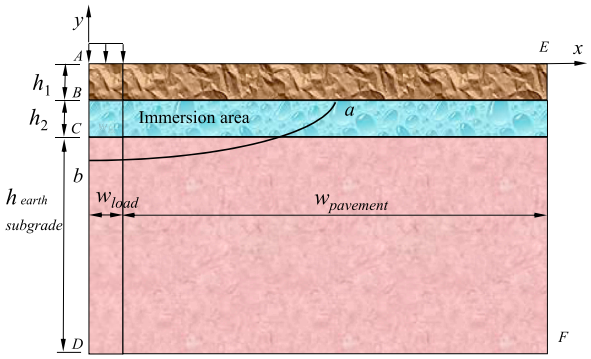

FIGURE 4
Mechanical model of the cement concrete pavement.

$$F(\xi,\xi_i)=\prod_{\substack{m=1\\m\neq i}}^{N_\xi}\frac{(\xi-\xi_m)}{(\xi_i-\xi_m)},G(\eta,\eta_j)=\prod_{\substack{n=1\\n\neq j}}^{N_\eta}\frac{(\eta-\eta_n)}{(\eta_j-\eta_n)}. \tag{2}$$

Combined with Eq. 1, 2, the shape function can be calculated by Eq. (3).

$$\varphi_k(Q)=F(\xi,\xi_i)G(\eta,\eta_j)=\prod_{\substack{m=1\\m\neq i}}^{N_\xi}\frac{(\xi-\xi_m)}{(\xi_i-\xi_m)}\prod_{\substack{n=1\\n\neq j}}^{N_\eta}\frac{(\eta-\eta_n)}{(\eta_j-\eta_n)}. \tag{3}$$

Therefore, the first-order partial differentials (FOPDs) of the shape function $\varphi_k(Q)$ directly with respect to Q can be derived, as shown in Eq. (4).

$$\frac{\partial\varphi_k(Q)}{\partial\xi}=\frac{\partial F(\xi,\xi_i)}{\partial\xi}G(\eta,\eta_j),\frac{\partial\varphi_k(Q)}{\partial\eta}=F(\xi,\xi_i)\frac{\partial G(\eta,\eta_j)}{\partial\eta}. \tag{4}$$

The nodal value of the FOPDs is arranged by a vector form, as shown in Eq. (5).

$$\mathbf{u}_{,\alpha}=\mathbf{D}_\alpha\mathbf{u},\mathbf{D}_\alpha=\left\{\varphi_{kl,\alpha}\right\}_{M\times M}\ (k,l=1,2,\cdots,M;\alpha=\xi,\eta), \tag{5}$$

where $\mathbf{u}$ is the nodal value, expressed by Eq. (6). $\mathbf{D}$ represents the partial differential matrices.

$$\mathbf{u}_{,\alpha}=\left\{\frac{\partial u(P_1)}{\partial\alpha},\frac{\partial u(P_2)}{\partial\alpha},\cdots,\frac{\partial u(P_M)}{\partial\alpha}\right\}^{\mathrm{T}},\mathbf{u}=\{u(P_1),u(P_2),\cdots,u(P_M)\}^{\mathrm{T}} \tag{6}$$

.

Its L-order partial differential function is calculated, as shown in Eq. (7).

$$\mathbf{u}_{,mn}(\xi,\eta)=\frac{\partial^{m+n}u}{\partial\xi^m\partial\eta^n},m+n=L. \tag{7}$$

Therefore, the aforementioned expression can be approximated, as shown in Eq. (8).

$$\mathbf{u}_{,mn}\approx\mathbf{D}_\xi^m\mathbf{D}_\eta^n\mathbf{u}. \tag{8}$$

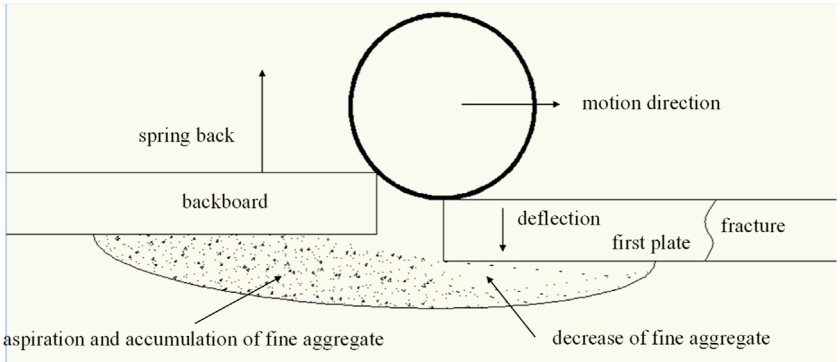

FIGURE 3
Disengaging of the cement concrete pavement plate.

TABLE 1 Calculation parameters of the MFBM model.

Horizon	Thickness/cm	Modulus/MPa	Poisson ratio
Pavement	20/25	31,000	0.3
Subgrade	20	1,200	0.3
Foundation	—	50	0.3

In Figure 1, a quadratic block with eight seeds can be mapped into a space $Q(\xi,\eta)$ by Eq. (9).

$$\begin{aligned} N_i &= \frac{1}{4}\left(1+\bar{\xi}_i\xi\right)\left(1+\bar{\eta}_i\eta\right)\left(\bar{\xi}_i\xi+\bar{\eta}_i\eta-1\right) \text{ for } i=1,2,3,4,\\ N_i &= \frac{1}{2}\left(1-\xi^2\right)\left(1+\bar{\eta}_i\eta\right) \text{ for } i=5,7,\\ N_i &= \frac{1}{2}\left(1-\eta^2\right)\left(1+\bar{\xi}_i\xi\right) \text{ for } i=6,8, \end{aligned} \tag{9}$$

where $(\bar{\xi}_i,\bar{\eta}_i), i=1,2,\cdots,8$ are coordinates of seeds, as shown in Figure 1.

Then, the coordinate (mapping) can be transferred from the coordinate of the real system into that of the normalized space by Eq. (10).

$$x=\sum_{k=1}^{8}N_k(\xi,\eta)x_k,\ y=\sum_{k=1}^{8}N_k(\xi,\eta)y_k\,. \tag{10}$$

The FOPDs of $u(x,y)$ are given by Eq. (11) in Cartesian coordinates.

$$\frac{\partial u}{\partial x}=\frac{1}{J}\left(\beta_{11}\frac{\partial u}{\partial \xi}+\beta_{12}\frac{\partial u}{\partial \eta}\right),\ \frac{\partial u}{\partial y}=\frac{1}{J}\left(\beta_{21}\frac{\partial u}{\partial \xi}+\beta_{22}\frac{\partial u}{\partial \eta}\right), \tag{11}$$

where these parameters are defined by Eq. (12).

$$J=\beta_{22}\beta_{11}-\beta_{21}\beta_{12},\beta_{11}=\frac{\partial y}{\partial \eta},\quad \beta_{12}=-\frac{\partial y}{\partial \xi},\quad \beta_{21}=-\frac{\partial x}{\partial \eta},\beta_{22}=\frac{\partial x}{\partial \xi}. \tag{12}$$

Therefore, the matrices of FOPDs are introduced by Eq. (13).

$$\begin{aligned} \mathbf{u}_{,x} &= \mathbf{\Delta}_{11}\mathbf{U}_\xi+\mathbf{\Delta}_{12}\mathbf{U}_\eta=\left(\mathbf{\Delta}_{11}\mathbf{D}_\xi+\mathbf{\Delta}_{12}\mathbf{D}_\eta\right)\mathbf{u}=\mathbf{D}_x\mathbf{u},\\ \mathbf{u}_{,y} &= \mathbf{\Delta}_{21}\mathbf{U}_\xi+\mathbf{\Delta}_{22}\mathbf{U}_\eta=\left(\mathbf{\Delta}_{21}\mathbf{D}_\xi+\mathbf{\Delta}_{22}\mathbf{D}_\eta\right)\mathbf{u}=\mathbf{D}_y\mathbf{u}, \end{aligned} \tag{13}$$

where matrices $\mathbf{\Delta}_{ij}$ are defined as follows:

$$\mathbf{\Delta}_{ij}=\begin{pmatrix} \left(\beta_{ij}^{(1)}/J^{(1)}\right) & 0 & \cdots & 0\\ 0 & \left(\beta_{ij}^{(2)}/J^{(2)}\right) & \cdots & 0\\ \cdots & \cdots & \cdots & \cdots\\ 0 & 0 & \cdots & \left(\beta_{ij}^{(M)}/J^{(M)}\right) \end{pmatrix}, \tag{14}$$

where $(\beta_{ij}^{(k)}/J^{(k)}), k=1,2,\cdots,M$ is at each collocation point $P(\xi_k,\eta_k)$.

It is obvious that the nodal values of the FOPDs in the physical domain can be obtained by the FOPDs in the normalized space $|\xi|\le 1;|\eta|\le 1$.

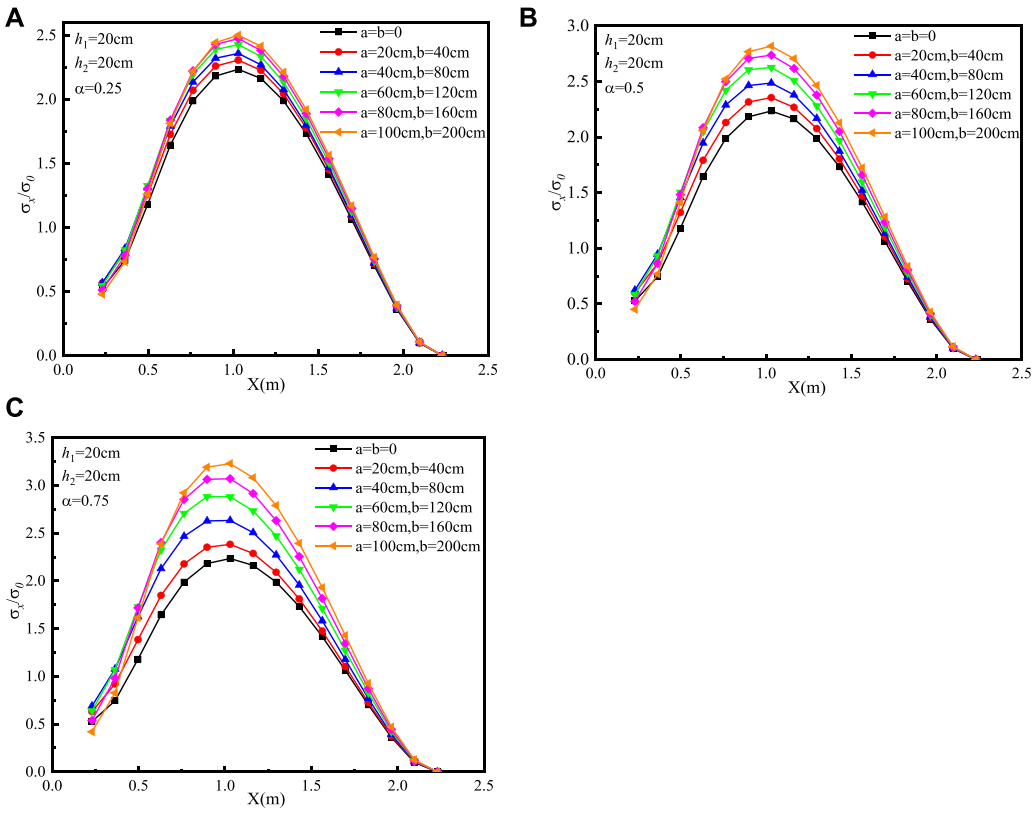

FIGURE 5
Dimensionless tensile stress distribution of the pavement using the MFBM with $h_1 = h_2 = 20$ cm: **(A)** $\alpha = 0.25$, **(B)** $\alpha = 0.5$, and **(C)** $\alpha = 0.75$.

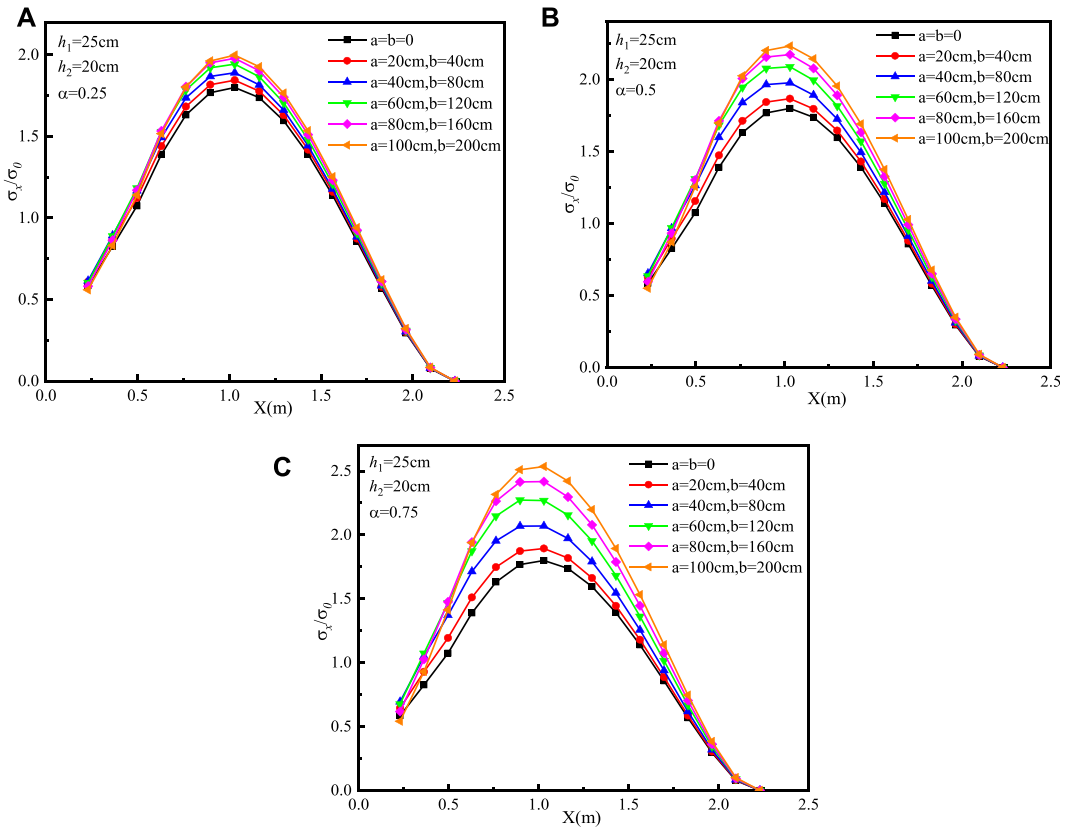

FIGURE 6
Dimensionless tensile stress distribution of the pavement using the MFBM with h_1 = 25 cm and h_2 = 20 cm: **(A)** α = 0.25, **(B)** α = 0.5, and **(C)** α = 0.75.

3 Finite block method in elasticity

First, this study makes a basic assumption that the parameters of non-homogeneous materials are closely related to the coordinates in space, and in Cartesian coordinates, the relationships between displacements $(u_\alpha, \alpha = x, y)$ and stress $(\sigma_x, \sigma_y, \tau_{xy})$ are given in Eq. (15).

$$\sigma_x = Q_1\frac{\partial u_x}{\partial x} + Q_2\frac{\partial u_y}{\partial y}, \sigma_y = Q_2\frac{\partial u_x}{\partial x} + Q_1\frac{\partial u_y}{\partial y}, \tau_{xy} = Q_3\left(\frac{\partial u_x}{\partial y} + \frac{\partial u_y}{\partial x}\right). \tag{15}$$

For plane-stress elasticity, isotropic homogenous material mechanical coefficients are given, as shown in Eq. (16).

$$Q_1 = \frac{E(\mathbf{x})}{1-\nu^2(\mathbf{x})}, Q_2 = \frac{\nu(\mathbf{x})E(\mathbf{x})}{1-\nu^2(\mathbf{x})}, Q_3 = G(\mathbf{x}), \tag{16}$$

where $E, \nu,$ and G are the Young's modulus, Poisson's ratio, and shear modulus, respectively, and $\mathbf{x}$ indicates the coordinate (x, y).

The equilibrium equations are expressed in Eq. (17).

$$\frac{\partial \sigma_x}{\partial x} + \frac{\partial \tau_{xy}}{\partial y} + b_x = 0, \frac{\partial \tau_{xy}}{\partial x} + \frac{\partial \sigma_y}{\partial y} + b_y = 0, \tag{17}$$

where b_x and b_y are body forces in two directions.

Considering the matrix forms of Eqs. 13, 15, 16, the differential matrices' form $(\mathbf{D}_\alpha, \alpha = x, y)$ of Eq. (17) is shown in Eq. (18).

$$\begin{aligned}\left(\mathbf{D}_x\mathbf{Q}_1\mathbf{D}_x + \mathbf{D}_y\mathbf{Q}_3\mathbf{D}_y\right)\mathbf{u}_x + \left(\mathbf{D}_x\mathbf{Q}_2\mathbf{D}_y + \mathbf{D}_y\mathbf{Q}_3\mathbf{D}_x\right)\mathbf{u}_y + \mathbf{b}_x = \mathbf{0},\\ \left(\mathbf{D}_y\mathbf{Q}_2\mathbf{D}_x + \mathbf{D}_x\mathbf{Q}_3\mathbf{D}_y\right)\mathbf{u}_x + \left(\mathbf{D}_x\mathbf{Q}_3\mathbf{D}_x + \mathbf{D}_y\mathbf{Q}_1\mathbf{D}_y\right)\mathbf{u}_y + \mathbf{b}_y = \mathbf{0},\end{aligned} \tag{18}$$

where u_β stands for vectors of nodal displacement; $\mathbf{b}_\beta(\beta = x, y)$ stands for body force vectors; $\mathbf{Q}_l = \mathbf{diag}[Q_l^{(k)}]$ represents diagonal matrices; and $Q_l^{(k)}(l = 1, 2, \text{and } 3)$ represents the elasticity coefficient at node k.

For 2D elasticity, there are two kinds of boundary conditions shown as follows:

$$\begin{aligned}u_\beta(\mathbf{x}) = u_\beta^0(\mathbf{x}),\ \mathbf{x} \in \Gamma_u,\\ t_\beta(\mathbf{x}) = t_\beta^0(\mathbf{x}),\ \mathbf{x} \in \Gamma_t,\end{aligned} \tag{19}$$

where u_β^0 and t_β^0 are specified displacements and tractions on the boundaries Γ_u and Γ_u, respectively.

There are $2M$ linear algebraic equations in Eqs 18, 19, respectively. Therefore, all nodal values of displacement should be determined. The physical domain is divided into few blocks by using the finite block method, which is unlike the traditional meshless method. In this case, the continuous condition for displacements u_β and tractions t_β on the smooth interface except two ends (joints) between blocks I and II is given in Eq. 20

$$u_\beta^I(\mathbf{x}) - u_\beta^{II}(\mathbf{x}) = 0, t_\beta^I(\mathbf{x}) + t_\beta^{II}(\mathbf{x}) = 0, \mathbf{x} \in \Gamma_{\text{int}}. \tag{20}$$

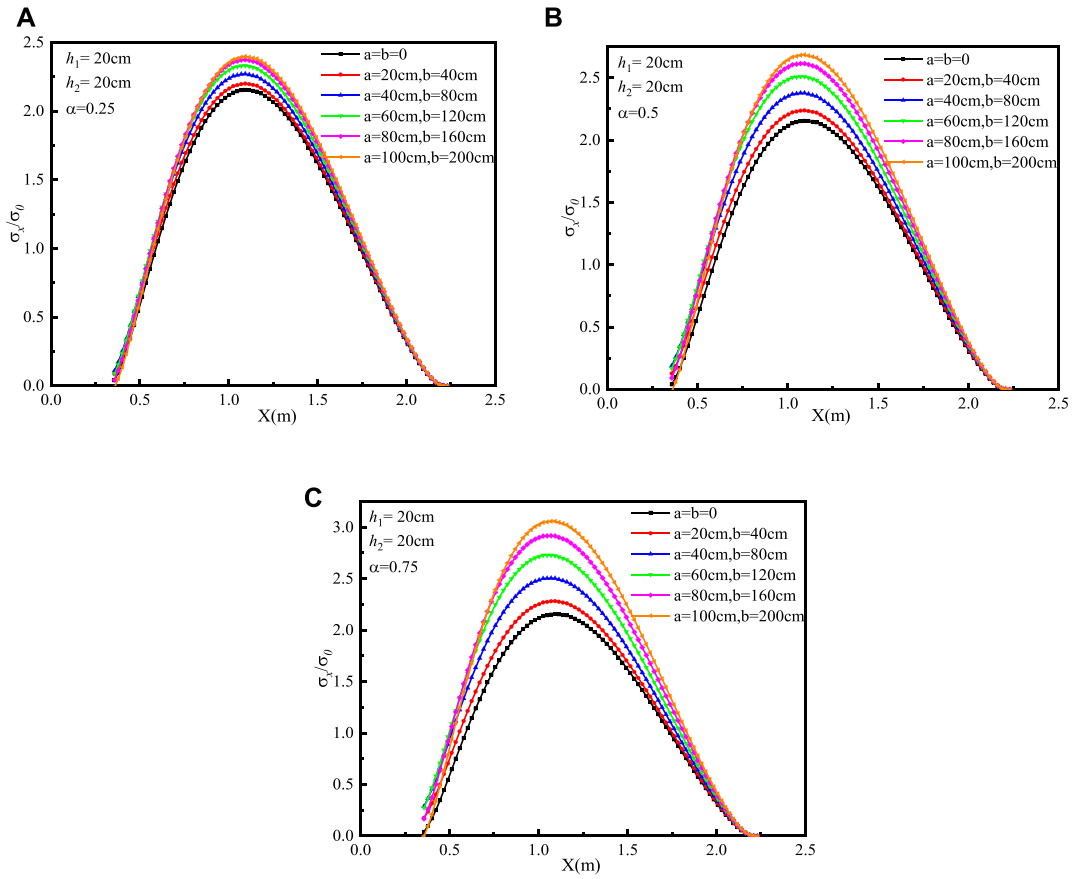

FIGURE 7
Dimensionless tensile stress distribution of the pavement using the FEM with $h_1 = h_2 = 20$ cm: **(A)** $\alpha = 0.25$, **(B)** $\alpha = 0.5$, and **(C)** $\alpha = 0.75$.

However, at a corner joint, both the point equilibrium equations and displacement continuity conditions should be considered, as shown in Eqs 21, 22.

$$u_\beta^I(\mathbf{x}) = u_\beta^{II}(\mathbf{x}) = \cdots = u_\beta^X(\mathbf{x}), \tag{21}$$

$$\sum_{q=I}^{X}\left(\sigma_x^{(q)}\left[\sin\theta_2^{(q)} - \sin\theta_1^{(q)}\right] - \tau_{xy}^{(q)}\left[\cos\theta_2^{(q)} - \cos\theta_1^{(q)}\right]\right) = 0,$$
$$\sum_{q=I}^{X}\left(\tau_{xy}^{(q)}\left[\sin\theta_2^{(q)} - \sin\theta_1^{(q)}\right] - \sigma_y^{(q)}\left[\cos\theta_2^{(q)} - \cos\theta_1^{(q)}\right]\right) = 0, \tag{22}$$

where $\theta_2^{(q)}$ and $\theta_1^{(q)}$ are starting and ending angles, respectively, at the joint for block q at the joint, as shown in Figure 2.

4 Case studies

The aforementioned method has been applied in the fields of computational solid mechanics and fluid mechanics. It can avoid grid reconstruction and effectively solve the numerical simulation problems that are difficult to analyze using the grid algorithm. It is extremely beneficial to solve large deformations such as stamping deformation, crack propagation, and fluid–solid coupling problems.

A cement concrete pavement is an important structural form of high-grade pavement. The cement concrete pavement is a multi-layer structure. The surface layer is divided into rectangular plates of finite size by joints. The scale in the plane direction is much larger than that in the thickness direction. In the analysis of the pavement structure, it is necessary to establish a reasonable mechanical model for the actual pavement structure and the stress–strain relationship of each structural layer material. At present, the pavement structure is mainly modeled by two schemes. One is the plate model, which regards the concrete surface layer as a single plate or multiple plates supported by the foundation. The other is that the three-dimensional model can consider the actual geometric shape and structural level of the pavement structure, which is an ideal model. However, under the repeated action of temperature change, humidity change, and vehicle load, the cement concrete pavement can warp and deform. The bottom surface of the edge, middle, or corner part of the panel may be separated from the top surface of the foundation and form a void beneath the slab. At the same time, the plastic deformation accumulates when the base material is pressed, which also leads to a void beneath the slab. This is similar to the problem of large deformation such as stamping deformation and crack extension. Therefore, it is feasible to analyze the fracture

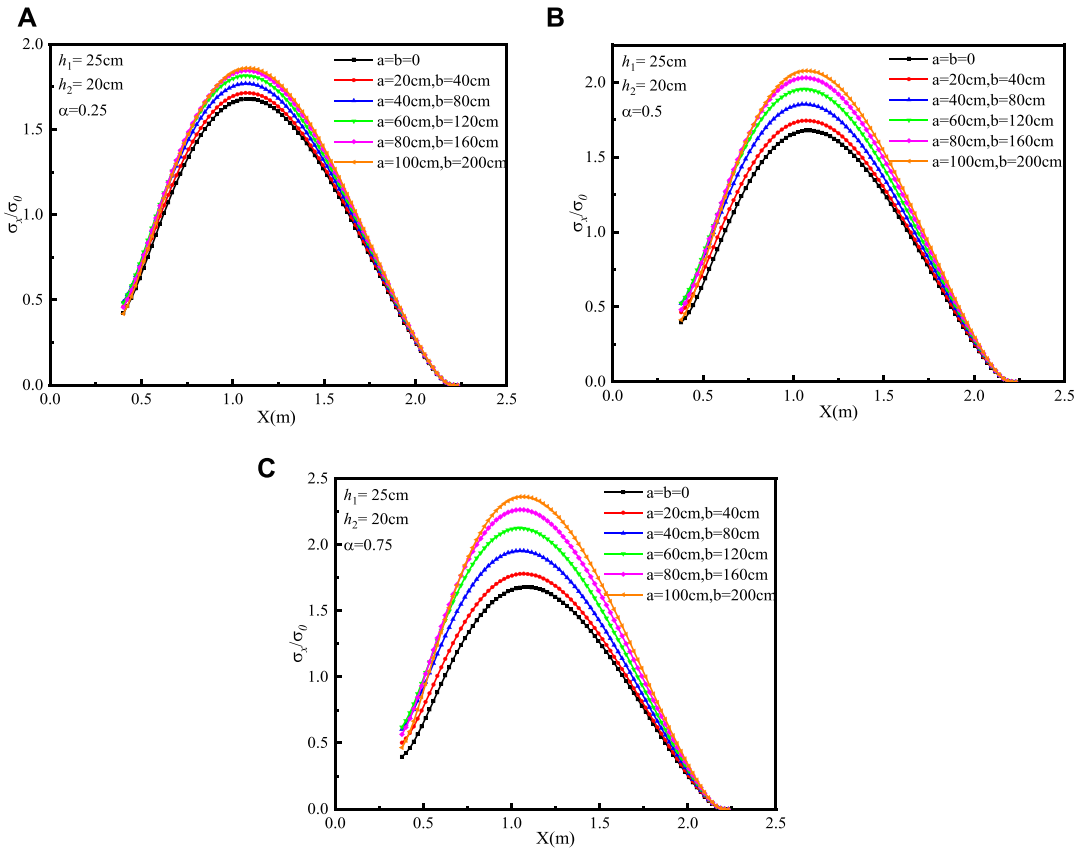

FIGURE 8
Dimensionless tensile stress distribution of the pavement using the FEM with h_1 = 25 cm and h_2 = 20 cm: **(A)** α = 0.25, **(B)** α = 0.5, and **(C)** α = 0.75.

characteristics of the slab at the edge of the cement pavement using the aforementioned method. In this study, all codes of the MFBM were written in Fortran. The commercialized package Abaqus with subroutine UMAT was used for FEM simulation.

First, a square domain was divided into 10 × 10 cells in the model. In addition, each cell was divided into 4 × 4 Gauss points. In the normalized domain (ξ, η), the coordinates of the node are calculated by Eq. (23). The number of nodes in total is $M = N_\xi \times N_\eta$ for each block.

$$\xi_i = -\cos\frac{\pi(i-1)}{N_\xi - 1}, i = 1, 2, \cdots, N_\xi,$$
$$\eta_j = -\cos\frac{\pi(j-1)}{N_\eta - 1}, j = 1, 2, \cdots, N_\eta. \tag{23}$$

4.1 Mechanical model of the cement concrete pavement plate

There are two kinds of voids beneath the slab. One is the structural void, which is caused by temperature and humidity warping deformation and plastic deformation accumulation of the base. The other is the squirt mud void. Rainwater percolates into the panel bottom through joints and edges of cement concrete plates. The hydrodynamic pressure scours the top surface of the base course and then forms, disengaging under the action of traffic load. Because of the disengaging of the foundation and the traffic load, the stress state of the cement concrete pavement is extremely disadvantageous (Figure 3). In this case, the cement pavement plate is similar to a cantilever beam and produces excessive deflection and stress, resulting in the cracking of the cement concrete plate. The structural void is the origin of the squirt mud void, and the squirt mud void further develops the structural void. The two types of voids alternately or jointly drive the evolution and development of the void at the bottom of the slab. It can be seen that squirt mud is one of the main factors leading to the void and fracture of the cement concrete pavement. The most direct manifestation of the phenomenon of squirt mud is the attenuation of the subgrade modulus, which, in turn, affects the deformation of the cement concrete pavement.

Based on the aforementioned situation, the progressive softening model of subgrade was established, as shown in Figure 4. The calculation parameters are shown in Table 1. The boundary conditions are as follows: AB and EF are free edges, BC and CD are simply supported edges, and DF is a fixed boundary. Assuming that the load acts on the upper edge of the first plate, the width of the load is 23 cm and the width of the pavement is 200 cm. At the same time, the immersed area is

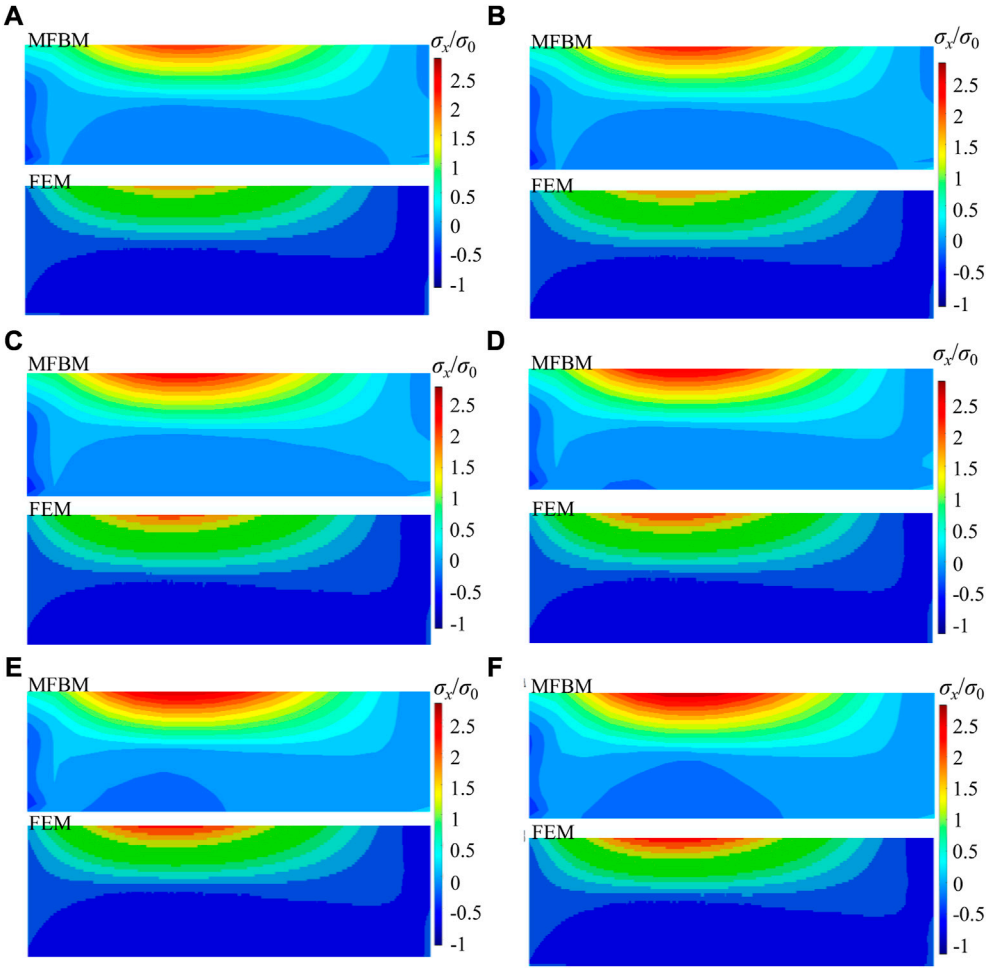

FIGURE 9
Maximum principal stress/load gradient distributions with h_1 = 20 cm and h_2 = 20 cm (A: the MFBM; B: the FEM): **(A)** a = b = 0 cm; **(B)** a = 20 cm and b = 40 cm; **(C)** a = 40 cm and b = 80 cm; **(D)** a = 60 cm and b = 120 cm; **(E)** a = 80 cm and b = 160 cm; **(F)** a = 100 cm and b = 200 cm.

assumed to be an ellipse, which should satisfy the requirement of Eq. 24.

$$\frac{x^2}{a^2} + \frac{(y + h_1 + h_2)^2}{b^2} = 1, \tag{24}$$

where a and b are the principal axis radii of the ellipse ($b = 2a$ for this example), and x and y are the coordinates, h_1 and h_2 are the thicknesses of the pavement, respectively, as shown in Figure 4.

The soaking subgrade materials can be regarded as a functionally graded material. The minimum value at the center position is taken, and the subgrade modulus (E) is described as a function of coordinates in Eq. (25).

$$E = E_n\left(1 - \alpha e^{-\beta\left(x^2/a^2 + y'^2/b^2\right)}\right), \quad y' = y + h_1 + h_2, \tag{25}$$

where E_n is the subgrade modulus under an anhydrous state; α is the maximum reduced value of the subgrade modulus; and $0 \le a \le 1$; β is a control parameter, which is the gradient of soil subgrade softening.

Parameters α and β can be determined by two points of the subgrade modulus, such as E_0 (located at the central point) and $E_1\,(y = y_1)$ (located at a certain depth). In this example, the value of α is 0.25, 0.5, and 0.75, respectively; $\beta = \ln(100\alpha)$. Six groups of different immersion conditions were selected for calculation, i.e., $a = b = 0$, $a = 20$ cm and $b = 40$ cm, $a = 40$ cm and $b = 80$ cm, $a = 60$ cm and $b = 120$ cm, $a = 80$ cm and $b = 160$ cm, and $a = 100$ cm and $b = 200$ cm.

4.2 Result analysis

4.2.1 Dimensionless tensile stress distribution

Figures 5, 6 present the dimensionless tensile stress distribution of the pavement. The dimensionless tensile stress is the ratio of surface stress to tire stress. In Figure 5, $h_1 = h_2 = 20$ cm and α is 0.25, 0.5, and 0.75. With the increase of the distance from the edge of the plate, the stress first increases and then decreases. The stress reaches the peak value at about 1.1 m from the edge of the plate, which presents the weak position of the cement concrete plate fracture. The subgrade modulus decay has an important influence on the force

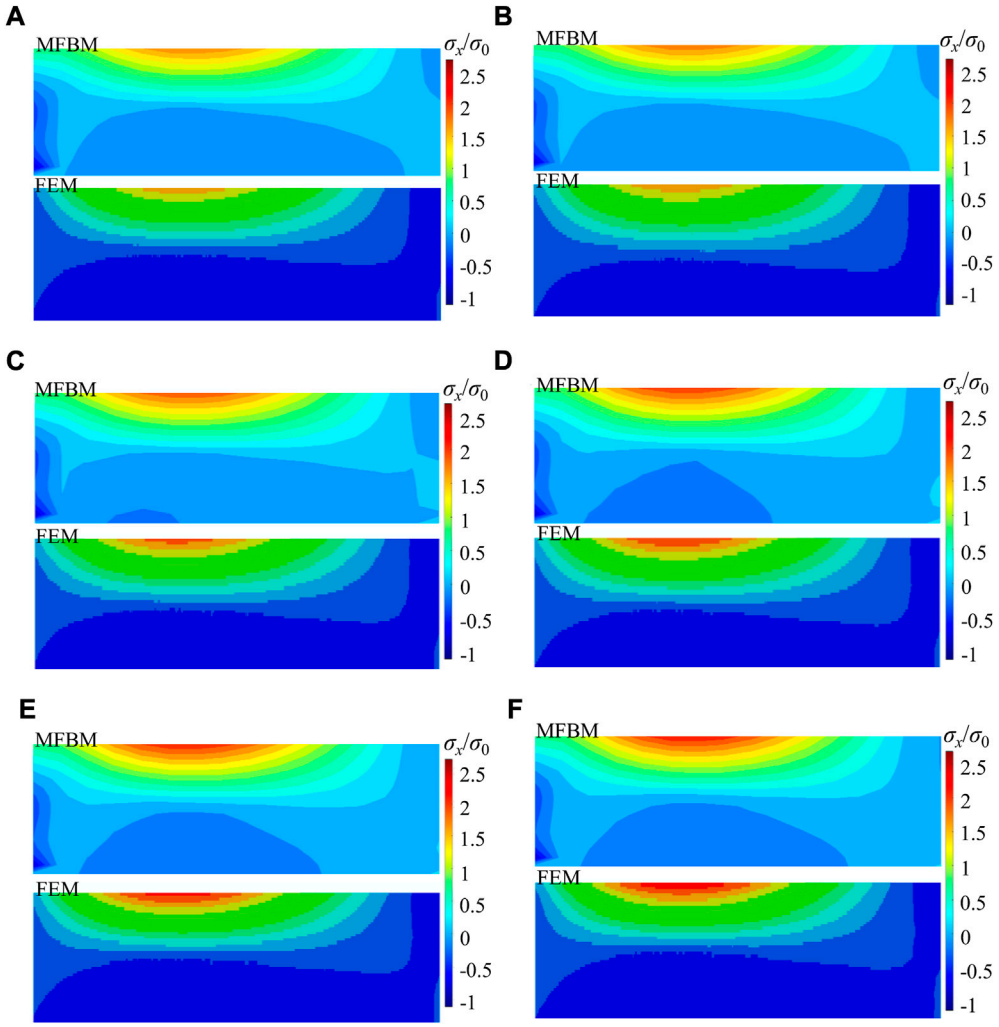

FIGURE 10
Maximum principal stress/load gradient distributions with h1 = 25 cm and h2 = 20 cm: **(A)** a = b = 0 cm; **(B)** a = 20 cm and b = 40 cm; **(C)** a = 40 cm and b = 80 cm; **(D)** a = 60 cm and b = 120 cm; **(E)** a = 80 cm and b = 160 cm; **(F)** a = 100 cm and b = 200 cm.

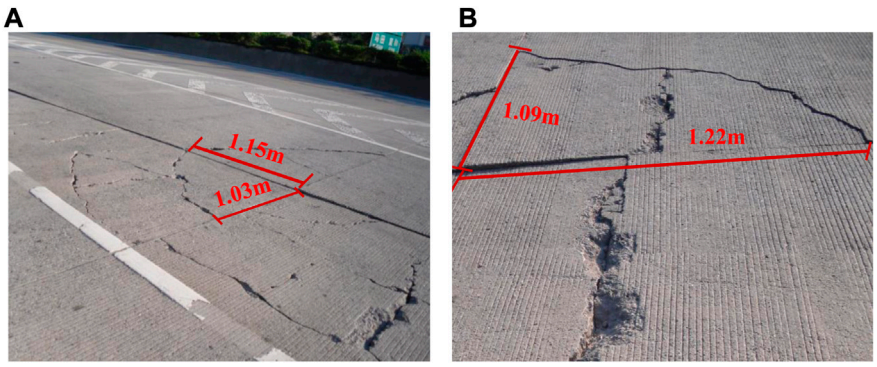

FIGURE 11
Field cracking investigation of the concrete pavement: **(A)** point 1; **(B)** point 2.

condition of the cement concrete plate. The peak stress reaches the maximum when α is 0.75, and the cement concrete plate is more likely to break. When α is a fixed value, the larger the size of the immersion range, the greater the peak stress. In Figure 6, $h_1 = 25$ cm, $h_2 = 20$ cm, and α is 0.25, 0.5, and 0.75. The change trend shown in Figure 6 is similar to that shown in Figure 5, and the stress value under the condition $h_1 = 0.25$ m and $h_2 = 0.2$ m is lower than that under the condition $h_1 = h_2 = 0.2$ m. With the increase of α, the stress value decreases. When α is 0.75, the reduction of the stress value reaches 27%. Figure 6 shows that increasing pavement thickness can reduce the risk of cement concrete plate fracture.

In other words, all the reduction of the subgrade modulus, the size of the immersion range, and the thicknesses of the pavement and subgrade can affect the cement concrete plate fracture. The smaller subgrade modulus reduced ratio, broader immersion ranges of earth subgrade, and thinner pavement and subgrade thickness are extremely disadvantageous to the force acting on the pavement plate. The maximum stress of the cement concrete pavement mainly concentrates in the range 1.05–1.15 m from the plate edge. When the stress changes to a certain extent, the pavement plate may be prone to fracture damage.

4.2.2 Comparison between results of the MFBM and FEM

In order to verify the validity and accuracy of the MFBM, the FEM was used as a benchmark for comparative analysis. The material parameters, geometry, and boundary of the FEM are the same as those of the MFBM. Six sets of the same situations were discussed. The results of the FEM are shown in Figures 7, 8.

The trend of solutions of the MFBM is the same as the FEM results, and the positions of the maximum stress determined by the two methods are basically consistent. The positions of the maximum stress of the cement concrete pavement determined by the FEM are around 1.1 m from the plate edge. The relationship between the maximum reduction of the subgrade modulus and the tendency of stress change can be identified using the FEM. The larger the maximum reduced value of the subgrade modulus, the higher the stress of the cement concrete pavement. The difference between the maximum stress values of the two methods is below 5%. With the thickness increase of the pavement plate, the position of the maximal stress is still in the same place, but the value of the stress reduces. The simulation results of the MFBM and FEM confirm that increasing the thickness of the pavement plate can decrease the degree of the plate fracture.

For further explanation, the (σ_x/σ_0) gradient distributions of the two methods are compared when the maximum reduction of the subgrade modulus is 0.5, as shown in Figure 9 and Figure 10, respectively. As the maximum principal stress fluctuation mainly occurs in the upper part of the road structure, this paper selects the pavement layer of the structure and analyzes six groups of different immersion conditions. The positions and magnitudes of the principal stress of the two methods are basically the same. As the immersion range increases, the magnitude of the principal stress also increases. Meanwhile, the principal stress decreases as the thickness of the pavement layer increases.

The subgrade modulus is an important characterization for the performance of the pavement structure. When the cement concrete pavement is in the process of scouring and disengaging, the subgrade modulus changes with the position. The progressive softening model of earth subgrade is more suitable to represent the changes in the subgrade modulus, and the MFBM model is suitable for the cement concrete pavement. Compared to the FEM, the MFBM offers advantages such as the elimination of mesh or element limitations, accurate solutions with reduced computation time, and convenience in analyzing non-homogeneous softening models.

In order to further verify the effectiveness and rationality of the proposed calculation method, we conducted a large number of road condition surveys on cement concrete pavements in Hunan, Guangxi, Guangdong, and other provinces and cities in China. The on-site cracking investigation was carried out in combination with the Highway Performance Assessment Standards by the Chinese traffic management department (JTG 5210-2018). We randomly investigated the corner fracture in different areas and traffic load sections. In addition, from the field investigation of the cement pavement plate fracture, the position of the pavement plate fracture is basically consistent with the calculated range, as shown in Figure 11. Therefore, the numerical and field results indicate that the MFBM is feasible and effective. By measuring the distance between the crack position of the corner fracture of the cement concrete pavement slab and the intersection of the longitudinal and transverse joints, it is easy to observe that the maximum stress positions of the cement concrete pavement obtained by numerical simulation agree with the measurements very well.

5 Conclusion

A novel MFBM was extended to cement concrete pavement engineering in this study. Compared with the FEM, the MFBM is convenient and suitable for non-homogeneous softening model analysis. The main findings are as follows:

(1) A progressive softening model established by the MFBM is capable of describing the response of a cement concrete plate with the decrease of the subgrade modulus. The proposed MFBM model is suitable for the cement concrete pavement. The position of the pavement plate fracture in the field is consistent with the range calculated by the MFBM. The FEM is one of the most powerful numerical tools for complicated problems in engineering and science. As an alternative, the meshless finite block method provides a new approach with many advantages such as efficiency and simplicity.
(2) The subgrade modulus reduction, the size of the immersion zone, and the thickness of the pavement and subgrade can affect the cement concrete plate fracture. The larger the subgrade modulus decay, the higher the stress. With the increase in the thickness of the pavement plate, the position of the maximum stress remains at the same place but the value of the stress decreases. The maximum stress of the cement concrete pavement mainly concentrates at 1.05–1.15 m of the plate edge.

However, the selection of a Lagrange series polynomial order is one issue in the MFBM. At present, meshing of the block is still a manual process in the MFBM, and the versatility needs to be further

improved with complex regional models. In future works, the FBM is to be extended to apply to more complicated problems, such as elastoplasticity, thermoelasticity, and elastodynamics.

Data availability statement

The original contributions presented in the study are included in the article/Supplementary Material; further inquiries can be directed to the corresponding author.

Author contributions

HW, WH, and PW contributed to the conception and design of the study. HW, WH, and YZ organized the database. PW and JL performed the statistical analysis. HW, PW, and JL wrote the first draft of the manuscript. HW, YZ, WH, and JL wrote sections of the manuscript. All authors contributed to manuscript revision, and read and approved the submitted version.

Funding

This research was funded by the National Natural Science Foundation of China, grant numbers 52278436 and 52208426, the Science and Technology Innovation Program of Hunan Province, grant number 2022RC1024, the Scientific Research Project of Hunan Provincial Department of Education for Excellent Young Scholars, grant number 20B039, the Foundation of Engineering Research Center of Catastrophic Prophylaxis and Treatment of Road and Traffic Safety of Ministry of Education, grant number kfj220402, and the National Key R&D Program of China, grant number 2021YFB2601200.

Conflict of interest

The authors declare that the research was conducted in the absence of any commercial or financial relationships that could be construed as a potential conflict of interest.

Publisher's note

All claims expressed in this article are solely those of the authors and do not necessarily represent those of their affiliated organizations, or those of the publisher, the editors, and the reviewers. Any product that may be evaluated in this article, or claim that may be made by its manufacturer, is not guaranteed or endorsed by the publisher.

References

Ahmad, I., Ahmad, H., Thounthong, P., Chu, Y. M., and Cesarano, C. (2020). Solution of multi-term time-fractional PDE models arising in mathematical biology and physics by local meshless method. *Symmetry* 12 (7), 1195. doi:10.3390/sym12071195

Atluri, S., and Zhu, T. (1998). A new meshless local Petrov-Galerkin (MLPG) approach to nonlinear problems in computer modeling and simulation. *Comput. Model. Simul. Eng.* 3, 187–196.

Huang, T., Yang, J., Jin, J., Wen, P., and Aliabadi, M. (2018). Evaluation of stress intensity factors and T-stress by finite block method: Static and dynamic. *Theor. Appl. Fract. Mech.*, 93, 222–232. doi:10.1016/j.tafmec.2017.08.009

Huang, W., Yang, J., Sladek, J., Sladek, V., and Wen, P. (2023). Meshless finite block method with infinite elements for axisymmetric cracked solid made of functionally graded materials. *Eur. J. Mechanics-A/Solids*, 97, 104852. doi:10.1016/j.euromechsol.2022.104852

Li, J., Zhang, J., Yang, X., Zhang, A., and Yu, M. (2023). Monte Carlo simulations of deformation behaviour of unbound granular materials based on a real aggregate library. *Int. J. Pavement Eng.* 24 (1), 2165650. doi:10.1080/10298436.2023.2165650

Li, J., Zheng, J., Yao, Y., Zhang, J., and Peng, J. (2019). Numerical method of flexible pavement considering moisture and stress sensitivity of subgrade soils. *Adv. Civ. Eng.* 2019, 7091210, 10. doi:10.1155/2019/7091210

Li, M., Meng, L., Hinneh, P., and Wen, P. (2016). Finite block method for interface cracks. *Eng. Fract. Mech.* 156, 25–40. doi:10.1016/j.engfracmech.2016.02.015

Li, M., and Wen, P. (2014). Finite block method for transient heat conduction analysis in functionally graded media. *Int. J. Numer. Methods Eng.* 99 (5), 372–390. doi:10.1002/nme.4693

Lian, Y., Zhang, X., Zhou, X., and Ma, Z. (2011). A FEMP method and its application in modeling dynamic response of reinforced concrete subjected to impact loading. *Comput. Methods Appl. Mech. Eng.* 200 (17-20), 1659–1670. doi:10.1016/j.cma.2011.01.019

Lin, Y., and Karadelis, J. N. (2019). Interfacial fracture toughness of composite concrete beams. *Constr. Build. Mater.* 213, 413–423. doi:10.1016/j.conbuildmat.2019.04.066

Liu, B., Zhou, Y., Gu, L., and Huang, X. (2020). Finite element simulation and multi-factor stress prediction model for cement concrete pavement considering void under slab. *Materials* 13 (22), 5294. doi:10.3390/ma13225294

Mahmoud, E., Saadeh, S., Hakimelahi, H., and Harvey, J. (2014). Extended finite-element modelling of asphalt mixtures fracture properties using the semi-circular bending test. *Road Mater. Pavement Des.* 15 (1), 153–166. doi:10.1080/14680629.2013.863737

Nayroles, B., Touzot, G., and Villon, P. (1992). Generalizing the finite element method: Diffuse approximation and diffuse elements. *Comput. Mech.* 10 (5), 307–318. doi:10.1007/bf00364252

Peng, J., Zhang, J., Li, J., Yao, Y., and Zhang, A. (2020). Modeling humidity and stress-dependent subgrade soils in flexible pavements. *Comput. Geotechnics* 120, 103413. doi:10.1016/j.compgeo.2019.103413

Qu, B., Weng, X. Z., Zhang, J., Mei, J., Guo, T. X., Li, R. F., et al. (2017). Analysis on the deflection and load transfer capacity of a prefabricated airport prestressed concrete pavement. *Constr. Build. Mater.* 157, 449–458. doi:10.1016/j.conbuildmat.2017.09.124

Rahim, A., and George, K. (2005). Models to estimate subgrade resilient modulus for pavement design. *Int. J. Pavement Eng.* 6 (2), 89–96. doi:10.1080/10298430500131973

Sladek, J., Sladek, V., Wen, P., and Aliabadi, M. (2006). Meshless local Petrov-Galerkin (MLPG) method for shear deformable shells analysis. *Comput. Model. Eng. Sci.* 13 (2), 103–117.

Sladek, V., Sladek, J., Tanaka, M., and Zhang, C. (2005). Local integral equation method for potential problems in functionally graded anisotropic materials. *Eng. analysis Bound. Elem.* 29 (9), 829–843. doi:10.1016/j.enganabound.2005.04.009

Wang, W., Wang, L., Xiong, H., and Luo, R. (2019). A review and perspective for research on moisture damage in asphalt pavement induced by dynamic pore water pressure. *Constr. Build. Mater.*, 204, 631–642. doi:10.1016/j.conbuildmat.2019.01.167

Wei, H., Li, J., Wang, F., Zheng, J., Tao, Y., and Zhang, Y. (2022). Numerical investigation on fracture evolution of asphalt mixture compared with acoustic emission. *Int. J. Pavement Eng.*, 23 (10), 3481–3491. doi:10.1080/10298436.2021.1902524

Wen, P., Aliabadi, M., and Rooke, D. (1997). A contour integral method for dynamic stress intensity factors. *Theor. Appl. Fract. Mech.* 27 (1), 29–41. doi:10.1016/s0167-8442(97)00005-0

Wen, P., Aliabadi, M., and Rooke, D. (1998). A variational technique for boundary element analysis of 3D fracture mechanics weight functions: Static. *Int. J. Numer. methods Eng.* 42 (8), 1409–1423. doi:10.1002/(sici)1097-0207(19980830)42:8<1409:aid-nme426>3.0.co;2-z

Wen, P., Cao, P., and Korakianitis, T. (2014). Finite block method in elasticity. *Eng. Analysis Bound. Elem.* 46, 116–125. doi:10.1016/j.enganabound.2014.05.006

Yu, S., Sun, Z., Qian, W., Yu, J., and Yang, J. (2023). A meshless method for modeling the microscopic drying shrinkage cracking processes of concrete and its applications. *Eng. Fract. Mech.* 277, 109014. doi:10.1016/j.engfracmech.2022.109014

Zhao, H., Wu, D., Zeng, M., and Ling, J. (2019). Support conditions assessment of concrete pavement slab using distributed optical fiber sensor. *Transp. A Transp. Sci.* 15 (1), 71–90. doi:10.1080/23249935.2018.1457733

frontiers | Frontiers in Materials

TYPE Original Research
PUBLISHED 03 May 2023
DOI 10.3389/fmats.2023.1193225

OPEN ACCESS

EDITED BY
Hui Yao,
Beijing University of Technology, China

REVIEWED BY
Yue Xiao,
Wuhan University of Technology, China
Shifeng Wang,
Shanghai Jiao Tong University, China

*CORRESPONDENCE
Juan Xie,
xiejuan08@126.com

RECEIVED 24 March 2023
ACCEPTED 21 April 2023
PUBLISHED 03 May 2023

CITATION
Xie J, Zhao X, Zhang Y, Yu F, Luo H, Chen X and He W (2023), Preparation of terminal blend/ grafting activated crumb rubber composite modified asphalt based on response surface methodology . *Front. Mater.* 10:1193225. doi: 10.3389/fmats.2023.1193225

Preparation of terminal blend/ grafting activated crumb rubber composite modified asphalt based on response surface methodology

Juan Xie[1,2]*, Xucheng Zhao[1], Yongning Zhang[3], Fan Yu[1], Haochen Luo[1], Xueru Chen[1] and Wen He[1]

[1]School of Traffic and Transportation Engineering, Changsha University of Science and Technology, Changsha, China, [2]National Engineering Research Center of Highway Maintenance Technology, Changsha University of Science and Technology, Changsha, China, [3]Shanghai Municipal Engineering Design Institute (Group) Co., Ltd., Shanghai, China

Recycling waste tires, crushing them into crumb rubber (CR) and adding them to asphalt can effectively improve the performance and prolong the service life of asphalt pavement. However, the crumb rubber modified asphalt (CRMA) prepared by aforementioned process is prone to segregation during storage and transportation. The terminal blend rubber asphalt (TB) prepared with fine rubber powder by high-speed shearing at high temperature for long time, which effectively improves the storage stability and working performance of crumb rubber modified asphalt, but reduces the high-temperature performance. In this study, grafting activated crumb rubber (GACR) was incorporated into TB to improve its high temperature performance without impairing storage stability. Using shearing temperature, shearing time and grafting activated crumb rubber content as influencing factors, the response surface method (RSM) was carried out to optimize the preparation process. The results indicated that 180°C was a critical temperature, and the swelling of crumb rubber dominated with the temperature below it, but the desulfurization prevailed with the temperature above it. The extension of time favored the swelling of crumb rubber at low temperature but promoted desulfurization at high temperature. With the increase of crumb rubber content, the high temperature performance of modified asphalt improved whereas the storage stability deteriorated. According to the determination of response values and the prediction of optimal values, the suitable preparation conditions and parameters were recommended as shearing temperature of 190°C, shearing time of 90 min, and GACR content of 15%. The composite modified asphalt prepared through the optimized process showed good high temperature stability and storage stability.

KEYWORDS

modified asphalt, terminal blend, grafting activated crumb rubber, response surface methodology, high temperature performance, storage stability

1 Introduction

At present, the concept of sustainable development and the principles based on the "4R" (reclaim, recycle, reuse, and reduce) have attracted widespread attention (Jamshidi et al., 2016). As a sustainable low-cost composite material, crumb rubber has been widely used in industries such as roads, construction, electricity, and power sources (Khaloo et al., 2015; Xu

et al., 2020; Phiri et al., 2021; Zhang et al., 2021). Adding crumb rubber (CR) to asphalt can not only improve various performances of asphalt but also provide an environmentally friendly way for the recycling of waste tires. Studies have found that crumb rubber modified asphalt (CRMA) has the advantages of excellent high temperature stability, low temperature crack resistance, fatigue resistance, anti-aging performance and less traffic noise (Yu et al., 2020). However, the storage stability is poor due to the "solid-liquid" two-phase system of rubber powder and asphalt and the density difference between them, which greatly hinders the use of rubber asphalt in actual engineering (Han et al., 2016; Ma et al., 2021a).

In order to solve the above problems, the rubber powder is pretreated before being added to the base asphalt to improve its compatibility with the asphalt, which in turn improves the storage stability of the CRMA. Wang et al. (2020) introduced tetraethyl orthosilicate (TEOS) to modify the surface of CR, and determined the optimal amount of TEOS. This research has a positive effect on improving the storage stability of CRMA. Hosseinnezhad et al. (2019) pretreated CR by the combination of microwave radiation and bio-modification. The results showed that the storage stability of CRMA was significantly improved, and its performance was also improved. It is worth mentioning that Xiao et al. innovatively applied a cold plasma surface treatment technology to the surface treatment of CR, which enhanced the compatibility of CR and base asphalt and thus improved the storage stability of CRMA (Li et al., 2020). At the same time, our group's previous research also found that graft activation of rubber powder could improve the storage stability of modified asphalt (Xie et al., 2019a; Xie et al., 2019b; Xie et al., 2020a). But generally speaking, the incorporation of CR leads to high viscosity of CRMA and decreases its workability (Yu et al., 2021). In addition, adding admixtures has been proven to improve the storage stability of CRMA, but which made the factors affecting the performance more complicated and the preparation process more difficult to control (Liu et al., 2014; Fini et al., 2017; Ma et al., 2021b).

Moreover, some existing studies indicated the storage stability of CRMA could be increased by adjusting the preparation process (Sienkiewicz et al., 2017). It has been confirmed that the solubility of CR in asphalt could be improved under strict shearing conditions (such as high temperature, high pressure and long-time), and when it is up to 97% (Huang et al., 2017), CRMA will not segregate during storage. Terminal Blend rubber asphalt (TB) is developed on this basis and solves the defects of poor storage stability and high viscosity of traditional rubber asphalt (Han et al., 2016). TB is usually prepared with 40–80 mesh rubber powder through high-speed shearing for a long time at temperature above 220°C (Huang et al., 2017; Xie et al., 2020b). During the process the rubber powder conducts desulfurization and degradation, its molecular chains gradually break into small molecules and dissolve in asphalt (Ragab and Abdelrahman, 2018). On the one hand, this preparation process reduces the viscosity of the rubber asphalt and improves the storage stability significantly (Huang et al., 2016). But on the other hand, this process decreases the high temperature performance of modified asphalt and keeps it from being used alone (Polacco et al., 2015). Compounding with other modifiers is considered to be an effective way to solve this problem, and the most common modifiers include SBS (Lin et al., 2017; Tang et al., 2017), nano-materials (Han et al., 2017; Zheng et al., 2018), polyphosphoric acid (PPA) (Niu, 2017), rock asphalt (Zhong et al., 2017) and other chemical modifiers (Wen et al., 2018). But the high cost of SBS and nano-materials, and the deterioration of low temperature performance caused by rock asphalt and PPA are issues for composite modification (Huang et al., 2016; Lin et al., 2018).

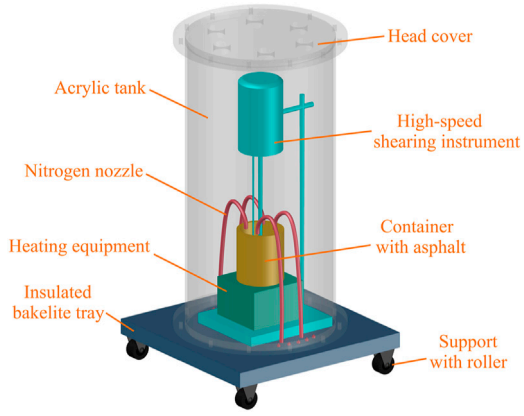

FIGURE 1
Schematic diagram of high-speed shearing instrument with nitrogen protective device.

Therefore, the research objectives of this article are as follows.

- Attempt to composite the acrylamide grafted activated crumb rubber prepared earlier with TB to improve its high-temperature performance. Simultaneously utilizing the unique advantages of GACR (Xie et al., 2020a), ensuring the excellent storage stability and other performance of TB will not be affected.
- Based on response surface methodology (RSM), to determine the optimal preparation for TB/GACR modified asphalt (TB/GACR). Shearing temperature, shearing time and crumb rubber content were selected as influencing factors, and their effects on the penetration, ductility, storage stability and viscosity of modified asphalt were explored.
- To study the synergistic effect of GACR and terminal blend technology on the high temperature performance and storage stability of composite modified asphalt, GACR modified asphalt (GACR-MA) and TB asphalt were also prepared as the reference via the optimized process.

2 Materials and methods

2.1 Materials

Base asphalt of PG 64-22, 70#A grade was supplied by Hunan Poly Company (Hunan, China), crumb rubber of 80 mesh was purchased from Sichuan Lubaotong Company (Chengdu, China), and all other reagents were purchased from Sinopharm Chemical Reagent Co., Ltd. (Shanghai, China).

TABLE 1 Test methods.

Items	Test instruments	Manufacturers	Test conditions
Penetration	PNR12 penetration meter	Antongpa, Austria	Test temperature: 25°C
Softening point	RKA 4 softening point meter	Antongpa, Austria	Initial temperature: 5°C
Ductility	The digital ductility tester	Infra Test, Germany	Test temperature: 15°C, tensile speed: 50 mm/min
Viscosity	Brookfield rotary viscometer	Shanghai Changji, China	Test temperature: 175°C
High temperature rheology	Dynamic shear rheometer- MCR 302	Antongpa, Austria	Test temperature: 52°C–82°C, Load frequency: 10 rad/s
Low temperature rheology	TE-Bending beam rheometer	Cannon, United States	Test temperature: −12°C, −18°C

2.2 Preparation of TB/GACR

GACR was prepared according to the literature (Xie et al., 2020a), and the process was sketched as follows: crumb rubber, potassium persulfate and acrylamide were mixed at a certain ratio and stirred for 4 h at 65°C. Through grafting action, amide groups were introduced into the molecular chains of crumb rubber, which could improve the compatibility between rubber powder and base asphalt.

TB asphalt was prepared by homemade high-speed shearing instrument with nitrogen protective device (Figure 1). The steps of preparation were as follows:15% (by the weight of base asphalt, the same hereinafter) untreated crumb rubber and base asphalt were mixed and swelled in an oven for 30 min at 180°C, followed by being sheared at a rate of 4,000 r/min for 3 h at 220°C (Xie et al., 2020c). During the preparation process, nitrogen protection was adopted to alleviate the aging of asphalt.

The wet process was employed to prepare TB/GACR and was illustrated as below. TB asphalt was heated at 145°C–165°C to fluid state and then mixed with dried GACR (10%–20% dosages). The mixture was sheared at 160°C–200°C for 30–90 min, followed by being placed in an oven at 165°C for 1 h.

2.3 Test methods

Detailed physical performance test methods are listed in Table 1.

In addition, the storage stability was tested according to the "Standard Test Methods of Bitumen and Bituminous Mixtures for Highway Engineering" (JTG E20-2011). A standard aluminium tube (diameter 25 mm, height 140 mm) was filled with the obtained asphalt and sealed. Then it was placed vertically in the oven at 163°C for 48 h to simulate the segregation during high temperature storage. Afterwards the aluminium tube was taken out and frozen for 240 min at 4°C, followed by being divided into 3 sections to measure the softening point of the upper and lower sections. The softening point difference and rutting factor separation index (*SI*) of the upper and lower sections of modified asphalt were measured to appraise storage stability. The value of *SI* was calculated by the following formula:

$$SI = \left(G^*/\sin\delta\right)_{\text{bottom}} / \left(G^*/\sin\delta\right)_{\text{top}} \quad (1)$$

where $(G^*/\sin\delta)_{\text{bottom}}$ and $(G^*/\sin\delta)_{\text{top}}$ are the rutting resistance factor of modified asphalt at the bottom and top of tube, respectively.

2.4 Analytical methods

Response surface methodology (RSM) is a method that combines experimental design and mathematical modeling for optimization, whose advantage is that it can continuously analyze various levels of the experiment, more intuitively reflecting the optimal value of the dependent variable (Chelladurai et al., 2021). There are two main types of design in RSM: Central Composite Design (CCD) and Box-Behnken Design (BBD). By comparison, the latter can provide more accurate responses with fewer combination schemes (Goo et al., 2020). So, BBD was used to optimize the preparation process of TB/GACR through a three-factor composite design. In this study, shearing temperature (160°C–200°C), shearing time (30–90 min) and GACR content (10%–20%) were chosen as influencing factors, and the penetration (25°C), softening point, ductility (15°C), softening point difference and viscosity were defined as response values.

3 Results and discussion

3.1 Influence of different factors on the properties of TB/GACR

The experimental schemes and performance test results obtained through RSM were shown in Table 2. The results of simulation showed that the values obtained by the quadratic equation were close to the actual values. Therefore, the quadratic equation was used to simulate the response values and influencing factors, so as to estimate the significance of the variables. The three influencing factors: shearing temperature, shearing time, and GACR content were recorded as *A*, *B*, and *C*, respectively. Analysis of variance of the experimental data in Table 4 was performed and the results are described below. Therein *F* represents the significance of the whole fitting equation, and *P* represents the correlation between the control group and the experimental group. Generally, the larger the value of *F*, the higher the fitting degree, and the smaller the value of *P*, the more significant the analysis result.

TABLE 2 Experimental schemes and various performance test results of TB/GACR.

Experimental program			Experimental results				
Shearing temperature (°C)	Shearing time (min)	GACR content (%)	Penetration (0.1 mm)	Softening point (°C)	Ductility (mm)	Softening point difference (°C)	Viscosity (mPa·s)
160	90	15	57.7	54.6	102	3.1	750
160	60	20	51.0	53.7	60	12.4	2,100
160	30	15	55.0	51.7	69	12.7	610
160	60	10	62.0	48.2	127	6.6	410
180	60	15	55.0	58.8	99	3.4	875
180	90	10	61.3	55.1	166	3.1	430
180	30	10	53.0	57.7	97	8.9	420
180	60	15	54.0	65.3	86	4.2	840
180	90	20	49.0	69.4	79	3.4	1825
180	60	15	54.3	58.8	96	2.5	800
180	60	15	56.0	59.7	125	3.7	705
180	60	15	55.3	62.2	128	3.0	985
180	30	20	51.3	67.7	97	9.3	2,250
200	60	10	63.3	57.3	117	2.4	430
200	90	15	64.7	58.2	144	0.3	720
200	30	15	54.3	65.4	94	5.2	860
200	60	20	55.7	64.4	110	3.0	1,420

TABLE 3 The analysis of variance results of penetration.

Factor	Sum of squares	*df*	Mean square	*F*	*P*	
Model	301.86	9	33.54	20.41	0.0003	Significant
A	18.91	1	18.91	11.51	0.0116	Significant
B	45.60	1	45.60	27.74	0.0012	Significant
C	132.85	1	132.85	80.82	<0.0001	Significant
AB[a]	14.82	1	14.82	9.02	0.0199	Significant
AC	2.89	1	2.89	1.76	0.2265	
BC	28.09	1	28.09	17.09	0.0044	Significant
A^2	56.94	1	56.94	34.64	0.0006	Significant
B^2	1.90	1	1.90	1.16	0.3175	
C^2	1.50	1	1.50	0.91	0.3708	
R^2	96%	Adjusted R^2	91%			

[a]AB, represents the interaction effect between variables A and B, and A2 represents the quadratic effect of variable A.

3.1.1 Penetration

The results of analysis of variance on penetration are shown in Table 3. It can be seen that this model had a high degree of fitting with small error and could be used to predict and analyze the variation law of penetration. The significant variables of the model were *A*, *B*, *C*, *AB*, *BC* and A^2, which meant in the single effect, the influence of shearing temperature, shearing time and GACR content were significant. But in the quadratic effects, the interaction between shearing temperature and shearing time, and the interaction between shearing time and GACR content were significant. Moreover, in the quadratic effect, the influence of shearing temperature was significant.

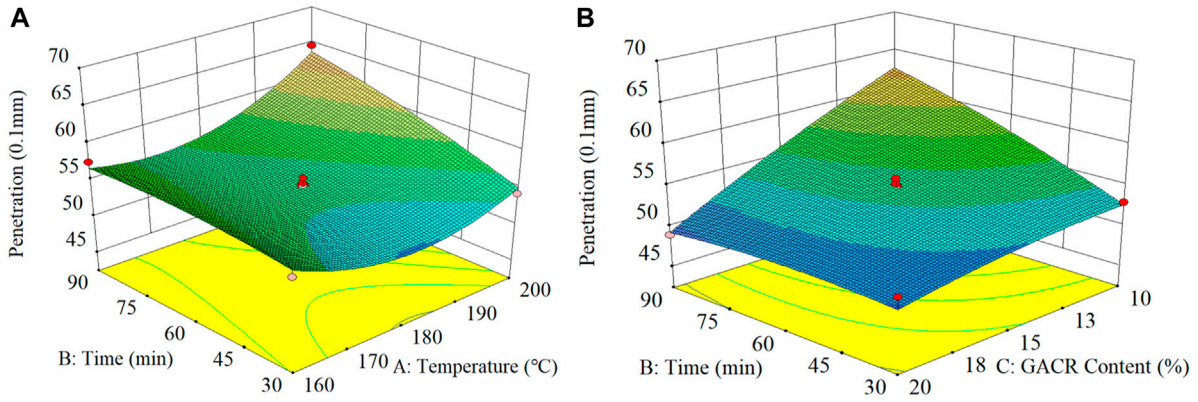

FIGURE 2
Response surface plot of penetration **(A)** Under the interaction of temperature and time; **(B)** Under the interaction of time and GACR content.

The fitting equation of penetration based on significant variables is.

$$R_1 = 54.92 + 1.54A + 2.39B - 4.08C + 1.92AB - 2.65BC + 3.68A^2 \quad (2)$$

where: R_1 is the penetration value of TB/GACR.

The RSM models of GACR content, shearing temperature and shearing time on penetration were obtained according to Eq. 2, as shown in Figure 2. With the increase of shearing temperature, the penetration of TB/GACR decreased first and increased afterwards, which may be due to the swelling and desulfurization of crumb rubber during the shearing process (Xie et al., 2019b). In the range of 160°C–180°C, GACR absorbed the light component and swelled. With the increase of temperature, the swell degree increased and a network structure was gradually formed, leading to the rise in viscosity and the reduction in penetration. When the shearing temperature exceeded 180°C, the network was broken and the solubility of GACR improved because of the desulfurization and degradation, causing the increase in penetration (Navarro et al., 2007; Nanjegowda and Biligiri, 2020).

The penetration increased with time in the whole temperature range. But interestingly, the extent of increase was slight when the temperature was below 180°C and was remarkable when the temperature was above 180°C. Similarly, that was ascribed to the swelling and desulfurization of GACR.

The effect of GACR content on the penetration of TB/GACR showed obvious regularity, that is, the penetration declined with the increase of GACR content. It can be illustrated by volume expansion of crumb rubber caused by swelling (Ghavibazoo et al., 2013; Pais et al., 2019) and enhanced interaction between GACR and base asphalt due to the grafting activation (Xie et al., 2019a; Xie et al., 2019b).

3.1.2 Softening point

The analysis of variance of softening point (shown in Table 4) indicated that the model was significant with small P (<0.05) and the correlation coefficient was high. The fitting effect of the model was accurate, so it could be used to predict the variation law of softening point. The significant variables were A, C, A^2 and C^2 when variables with non-significant effects were removed. Among the single effect, the shearing time and GACR content were significant, but among the quadratic effects, the significant variables turned to be shearing temperature and GACR content.

The response surface fitting equation of softening point according to the significant variables is:

$$R_2 = 60.96 + 4.64A + 4.61C - 5.03A^2 - 0.03C^2 \quad (3)$$

where: R_2 is the softening point value of TB/GACR.

From Eq. 3, the RSM models of GACR content, shearing temperature and shearing time with softening point were obtained, as shown in Figure 3.

As illustrated in Figure 3A, with the temperature increasing, the softening point rose at first and then declined. Meanwhile, the effect of shearing time on the softening point was a little bit complicated. Under the temperature condition of 160°C the softening point gradually increased with the increase of shearing time. When the shearing temperature increased to 200°C, the opposite trend appeared. The above results can be explained by the swelling and desulfurization of crumb rubber as mentioned before.

It can be seen from Figure 3B that the addition of GACR improved the softening point of TB/GACR, which could be explained from two aspects: one is that the increased GACR absorbed more light components; the other is that the chemical reaction between the basic groups on the molecular chains of GACR and the acidic groups in the asphalt reinforced the interfacial bonding between them (Xie et al., 2019a).

3.1.3 Ductility

The results of analysis of variance on ductility are listed in Table 5. It is observed that the fitting effect of the model was good and the correlation coefficient between predicted values and actual values was high.

The significant variables were determined as A, B, C, AC and BC. And the fitting equation of this model based on the significant variables is:

$$R_3 = 105.65 + 13.38A + 16.75B - 20.13C + 15AC - 21.75BC \quad (4)$$

TABLE 4 The analysis of variance results of softening point.

Factor	Sum of squares	df	Mean square	F	P	
Model	490.06	9	54.45	7.53	0.0072	Significant
A	172.05	1	172.05	23.79	0.0018	Significant
B	3.38	1	3.38	0.47	0.5162	
C	170.20	1	170.20	23.53	0.0019	Significant
AB	25.50	1	25.50	3.53	0.1025	
AC	0.64	1	0.64	0.088	0.7747	
BC	4.62	1	4.62	0.64	0.4503	
A^2	106.53	1	106.53	14.73	0.0064	Significant
B^2	10.05	1	10.05	1.39	0.2770	
C^2	3.789E-003	1	3.789E-003	5.239E-004	0.9824	
R^2	90%	Adjusted R^2	79%			

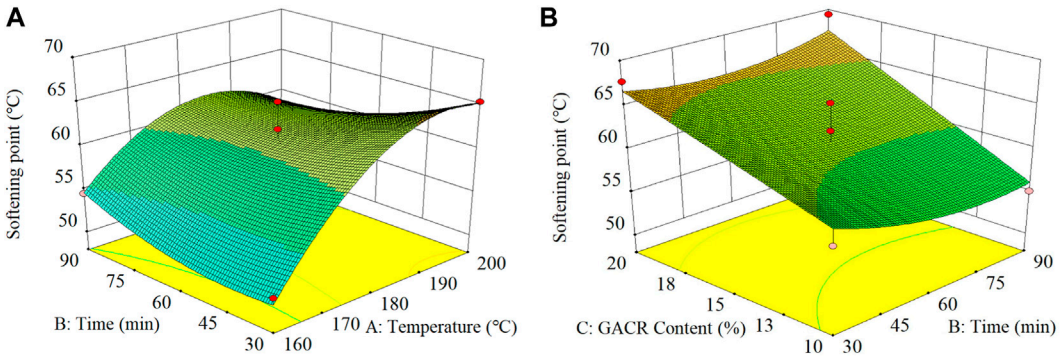

FIGURE 3
Response surface plot of softening point **(A)** Under the interaction of temperature and time; **(B)** Under the interaction of time and GACR content.

TABLE 5 The analysis of variance results of ductility.

Factor	Sum of squares	df	Mean square	F	P	
Model	9,780.25	6	1,630.04	9.21	0.0014	Significant
A	1,431.13	1	1,431.13	8.09	0.0174	Significant
B	2,244.50	1	2,244.50	12.68	0.0052	Significant
C	3,240.13	1	3,240.13	18.31	0.0016	Significant
AB	72.25	1	72.25	0.41	0.5372	
AC	900.00	1	900.00	5.09	0.0478	Significant
BC	1892.25	1	1892.25	10.69	0.0084	Significant
R^2	84%	Adjusted R^2	75%			

where: R_3 is the ductility value of TB/GACR.

According to Eq. 4, the RSM models of shearing temperature, shearing time and GACR content with respect to ductility were obtained, as shown in Figure 4.

Raising temperature not only favored the swelling of the GACR and the generation of the network structure in modified asphalt but also accelerated the chemical reaction between acrylamide groups of GACR and anhydride groups of base asphalt (Xie et al., 2019a; Xie

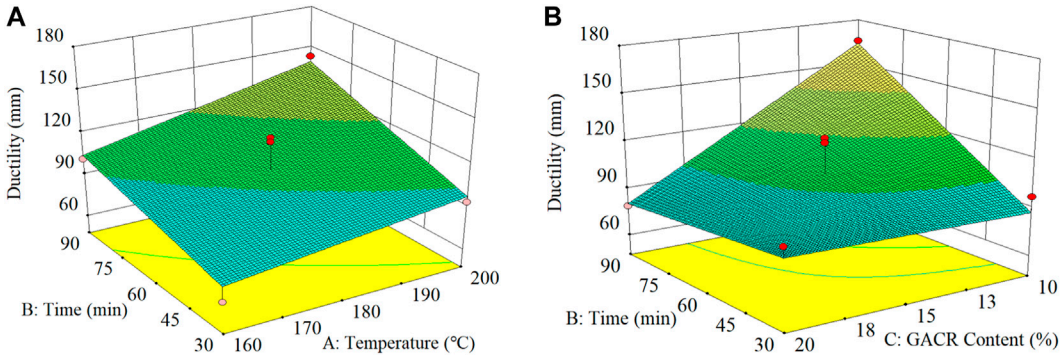

FIGURE 4
Response surface plot of ductility **(A)** Under the interaction of temperature and time; **(B)** Under the interaction of time and GACR content.

TABLE 6 The analysis of variance results of softening point difference.

Factor	Sum of squares	df	Mean square	F	P	
Model	199.74	9	22.19	19.19	0.0004	Significant
A	71.40	1	71.40	61.75	0.0001	Significant
B	85.80	1	85.80	74.20	<0.0001	Significant
C	6.30	1	6.30	5.45	0.0523	
AB	5.52	1	5.52	4.78	0.0651	
AC	6.76	1	6.76	5.85	0.0462	Significant
BC	2.500E-003	1	2.500E-003	2.162E-003	0.9642	
A^2	3.76	1	3.76	3.25	0.1143	
B^2	4.38	1	4.38	3.79	0.0927	
C^2	13.57	1	13.57	11.73	0.0111	Significant
R^2	96%	Adjusted R^2	91%			

et al., 2019b). To sum up, the homogeneity of TB/GACR increased with temperature, which improved the ductility consequently.

Even GACR has higher compatibility with asphalt and dispersed more uniformly compared with original crumb rubber (Li et al., 2021), the ductility still gradually decreased with the increase of its content. This is because that GACR cannot dissolve in asphalt and the particles aggregate easily with the increase of content. Hence the homogeneity of TB/GACR got worse and the stress concentration formed, resulting in a fall in ductility.

3.1.4 Softening point difference

The results of analysis of variance on storage stability are shown in Table 6. It can be seen that the fitting model of quadratic equation was significant (p = 0.0004). After correction, the correlation coefficient between predicted values and measured values was 91%, indicating that this model was reasonable to predict and analyze the softening point difference.

The significant variables were A, B, AC, C2, and the response surface fitting equation obtained based on the variables is:

$$R_4 = 3.36 - 2.99A - 3.28B - 1.3AC + 1.8C^2 \quad (5)$$

where: R_4 is the softening point difference value of TB/GACR.

From Eq. 5, the RSM models of shearing temperature, shearing time and GACR content on softening point difference can be obtained, as shown in Figure 5.

It can be seen from Figure 5A that with the increase of shearing temperature, the softening point difference of TB/GACR decreased, indicating that the storage stability improved. However, the way temperature affected storage stability was not same in different range. When the temperature was raised from 160°C to 180°C, the swelling degree of GACR increased and a gel film formed on the surface of GACR, which led to the semi-solid continuous phase of TB/GACR (Xie et al., 2019a; Xie et al., 2019b). When the temperature exceeded 180°C, GACR conducted desulfurization and degradation to generate small molecules. According to Stokes' law, the reduction of particle size helps to reduce the speed of its falling (Wen et al., 2018). Therefore, the generation of small molecules improved the storage stability.

With the increase of shearing time, the softening point difference showed a downward trend, indicating that the longer

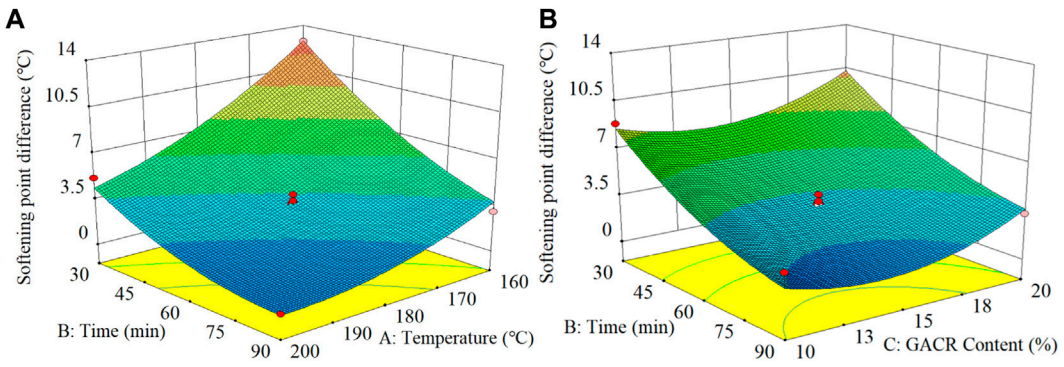

FIGURE 5
Response surface plot of softening point difference **(A)** Under the interaction of temperature and time; **(B)** Under the interaction of time and GACR content.

TABLE 7 The analysis of variance results of viscosity.

Factor	Sum of squares	df	Mean square	F	P	
Model	5.228E+006	9	5.809E+005	20.59	0.0003	Significant
A	24,200.00	1	24,200.00	0.86	0.3852	
B	21,528.13	1	21,528.13	0.76	0.4114	
C	4.359E+006	1	4.359E+006	154.46	<0.0001	Significant
AB	19,600.00	1	19,600.00	0.69	0.4321	
AC	1.225E+005	1	1.225E+005	4.34	0.0757	
BC	47,306.25	1	47,306.25	1.68	0.2365	
A^2	64,350.07	1	64,350.07	2.28	0.1748	
B^2	1,307.96	1	1,307.96	0.046	0.8357	
C^2	5.846E+005	1	5.846E+005	20.72	0.0026	Significant
R^2	96%	Adjusted R^2	92%			

the shearing time, the better the dispersion of GACR and the better the storage stability of TB/GACR.

The grafting activation of crumb rubber strengthened the interaction between it and base asphalt but not improved its solubility in base asphalt very much, and so the aggregation of GACR could not be avoided when the content was high. That's why the storage stability dropped with the increase of GACR content.

3.1.5 Viscosity

The results of analysis of variance on viscosity are shown in Table 7.

It can be seen that the model had high correlation and fitting degree to predict and analyze the change law of viscosity. The response surface fitting equation of viscosity based on significant variables is:

$$R_5 = 841 + 738.13C + 372.63C^2 \quad (6)$$

where: R_5 is the viscosity value of TB/GACR.

From Eq. 6, the RSM models of GACR content, shearing temperature and shearing time on viscosity were obtained, as shown in Figure 6.

The change trend of viscosity with temperature was the same with that of softening point, namely, first rose then descended. Also, the prolongation of shearing time raised viscosity at lower temperature (160°C–180°C) but reduced it at higher temperature (>180°C). Simultaneously, the reason causing this phenomenon was identical to that discussed in the softening point section.

When talking about GACR content, it increased the viscosity TB/GACR regardless of temperature and time. This could be attributed to the decrease in light components because of GACR swelling and the reinforcement in interaction between GACR and base asphalt.

3.2 Optimized process parameters of TB/GACR

On the basis of the analysis and discussion of the influence of GACR content, shearing temperature, and shearing time on the performance of TB/GACR, using the desired goal values as control, the optimal process parameters were predicted through

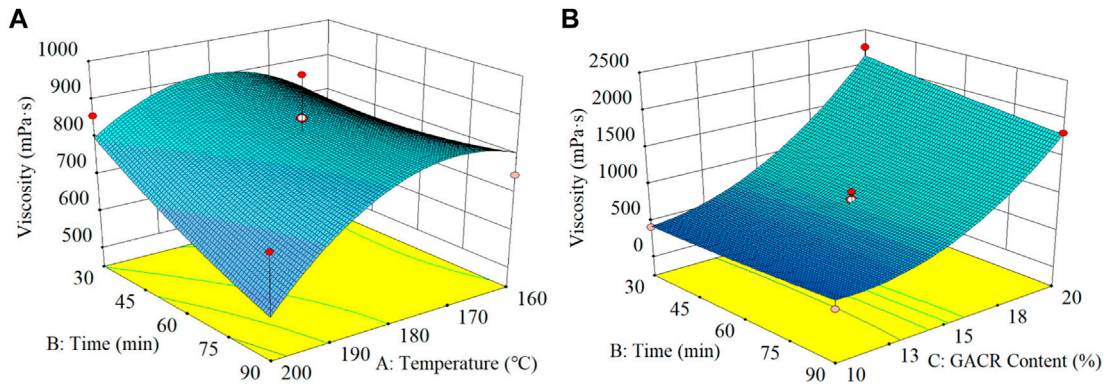

FIGURE 6
Response surface plot of viscosity. **(A)** Under the interaction of temperature and time; **(B)** Under the interaction of time and GACR content.

TABLE 8 Determination of Optimal values.

Constrained condition of response values		Optimal values of preparation parameters	
Items	Desired goal	Items	Solutions
Penetration (0.1 mm)	Min	Shearing temperature (°C)	187
Softening point (°C)	Max		
Ductility (mm)	Max	Shearing time (min)	90
Softening point difference (°C)	Min	GACR content (%)	18
Viscosity (mPa·s)	1,000–2,500		

*Min means that the target value of response is the smaller the better, and Max means the bigger the better.

Optimization module of RSM and listed in Table 8. Since TB system contained 15% rubber powder, in view of operation convenience and comprehensive properties of TB/GACR, the process parameters were proposed as shearing temperature of 190°C, shearing time of 90min and GACR content of 15%.

3.3 High and low temperature performance

Three kinds of modified asphalts: TB, GACR-MA, and TB/GACR, were prepared by the optimal process parameters, and the penetration, softening point, viscosity and rheological properties of the modified asphalts were tested to evaluate the high-temperature performance. As shown in Figure 7, the penetration of TB, GACR-MA and TB/GACR decreased and the softening point increased sequentially. Compared with TB, the penetration of TB/GACR decreased by 28.4%, and the softening point increased by 20.5%. Meanwhile, the high temperature rheological properties of modified asphalts were measured and the rutting factor ($G^*/\sin\delta$) was used to characterize the abilities of resistance to rutting and permanent deformation. As shown in Figure 8, the rutting factor of TB was the smallest and that of TB/GACR was the largest at the same temperature.

The creep stiffness (S) and creep rate (m-value) measured by bending beam rheometer (BBR) are used to evaluate the

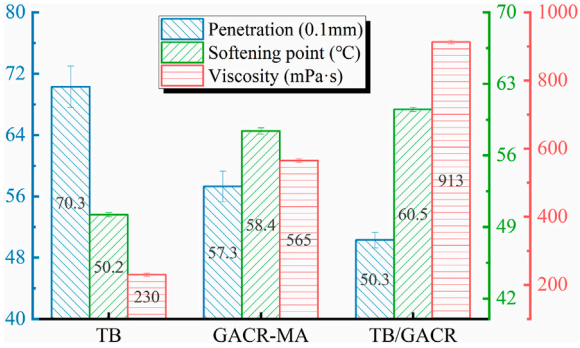

FIGURE 7
Penetration, Softening point and Viscosity of modified asphalts.

performance of TB/GACR under low temperature environment. The test results were listed in Table 9. At the same temperature, the smaller the S and the greater the m-value of the modified asphalt, the better its low-temperature performance. It is obvious that under the low temperature environment of −12°C and −18°C, the S of TB/GACR was significantly lower than that of TB and GACR, and TB/GACR had the smallest S and the largest m-value among the three modified asphalt.

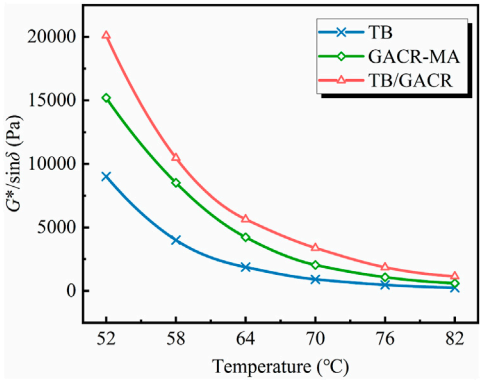

FIGURE 8
The $G^*/\sin\delta$ of modified asphalt.

TABLE 9 *S* **and** *m*-**value of modified asphalts.**

Asphalt types	−12°C		−18°C	
	S(MPa)	*m*-value	*S*(MPa)	*m*-value
TB	41.8	0.438	96.8	0.36
GACR-MA	45.1	0.425	99.6	0.358
TB/GACR	31.2	0.462	69.4	0.372

To sum up, TB/GACR had the best high and low temperature properties among these three kinds of modified asphalts. It could be explained that GACR had a positive effect on improving high temperature performance of TB asphalt, and the addition of GACR did not affect its low-temperature performance.

3.4 Storage stability

Segregation tests were carried out on the three kinds of modified asphalts, and the results of softening point difference are shown in Figure 9A. The softening point difference was greater for TB/GACR compared to TB because the addition of the rubber powder disrupted the homogeneous structure of the asphalt, thus increasing the possibility of segregation. In comparison to GACR asphalt, the softening point difference of TB/GACR was reduced by 38%, indicating that TB/GACR still maintained the excellent storage stability of TB and further reduced the segregation phenomenon of GACR in modified asphalt.

To further evaluate the storage stability of modified asphalts, the *SI*s were calculated from the temperature sweep test (Figure 9B). It could be seen that the *SI* of TB asphalt was stable at about 1.0 within the scanning temperature range. Among the three kinds of modified asphalts, GACR-MA had the largest *SI*, which indicating the poorest storage stability. Compared with TB asphalt, the *SI* of TB/GACR increased slightly but obviously lower than that of GACR-MA. The results of *SI* are consistent with the results of softening point difference, which fully indicates that the storage stability of TB/GACR is slightly inferior to that of TB bitumen, but superior to that of GACR-MA.

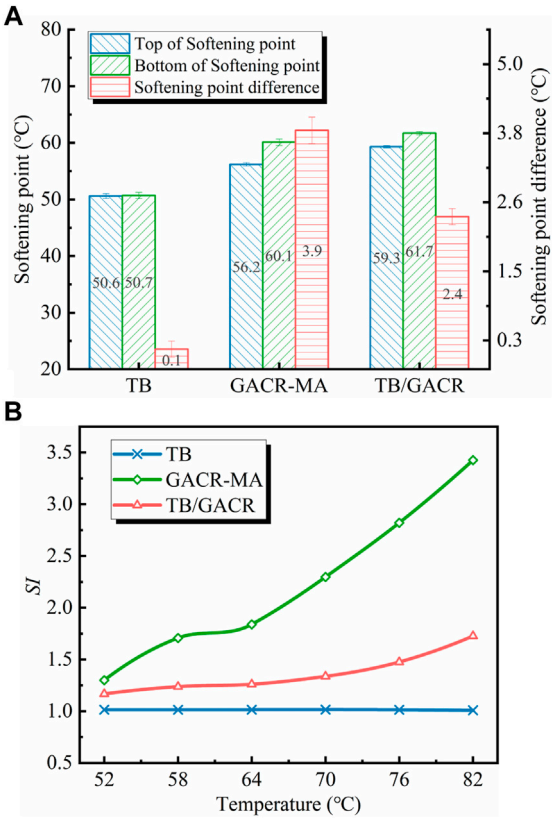

FIGURE 9
Softening point difference **(A)** and *SI* **(B)** of modified asphalts.

4 Conclusion

GACR and TB asphalt were compounded to prepare rubber asphalt with good storage stability and high temperature performance. With the penetration, softening point, ductility, storage stability and viscosity as indexes, RSM was adopted to optimize the process parameters. The main conclusions were summarized as follow.

(1) In the range of 160°C–180°C, GACR mainly swelled in TB asphalt by absorbing the light components. Both the increase of temperature and prolongation of time facilitated the swelling degree and thus improved the high temperature performance and storage stability of TB/GACR asphalt.
(2) In the range of 180°C–200°C, GACR degraded obviously. The crosslink bonds tended to break easily with increasing temperature and time, and consequently, the low temperature property and storage stability of compound modified asphalt were further improved but the high temperature property decreased.

(3) The increase of GACR content was beneficial to the high temperature performance of TB/GACR asphalt. But at the same time the aggregation possibility of the insoluble crumb rubber also increased, which reduced the storage stability and low temperature performance.
(4) According to the experiment results and the operation convenience, the optimum preparation parameters of TB/GACR asphalt were suggested as follows: shearing temperature of 190°C, shearing time of 90min and GACR content of 15%.

Data availability statement

The original contributions presented in the study are included in the article/supplementary material, further inquiries can be directed to the corresponding author.

Author contributions

JX is the supervisor of this research work and responsible for experimental design, the editing and writing of manuscript. XZ completing data analysis and writing the first draft of the paper. YZ helped in software support and data analysis. FY, HL, XC, and WH participated in the testing of experimental samples. All authors reviewed the results and approved the final version of the manuscript.

Funding

This work was supported by the National Natural Science Foundation of China (52178411 and 51608056), the Education Department of Hunan Province (22A0209), Changsha Municipal Natural Science Foundation (kq2014108), Postgraduate Scientific Research Innovation Project of Hunan Province (CX20210757), and Graduate Research Innovation Project of Changsha University of Science and Technology (CXCLY2022016).

Conflict of interest

Author YZ was employed by Shanghai Municipal Engineering Design Institute (Group) Co., Ltd.

The remaining authors declare that the research was conducted in the absence of any commercial or financial relationships that could be construed as a potential conflict of interest.

Publisher's note

References

Chelladurai, S. J. S., Murugan, K., Ray, A. P., Upadhyaya, M., and Narasimharaj, V. (2021). Optimization of process parameters using response surface methodology: A review. *Mater. Today Proc.* 37 (2), 1301–1304. doi:10.1016/j.matpr.2020.06.466

Fini, E. H., Hosseinnezhad, S., Oldham, D., McLaughlin, Z., Alavi, Z., and Harvey, J. (2017). Bio-modification of rubberised asphalt binder to enhance its performance. *Int. J. Pavement Eng.* 20 (10), 1216–1225. doi:10.1080/10298436.2017.1398548

Ghavibazoo, A., Abdelrahman, M., and Ragab, M. (2013). Mechanism of crumb rubber modifier dissolution into asphalt matrix and its effect on final physical properties of crumb rubber–modified binder. *Transp. Res. Rec.* 2370 (1), 92–101. doi:10.3141/2370-12

Goo, Y. T., Park, S. Y., Chae, B. R., Yoon, H. Y., Kim, C. H., Choi, J. Y., et al. (2020). Optimization of solid self-dispersing micelle for enhancing dissolution and oral bioavailability of valsartan using Box-Behnken design. *Int. J. Pharm.* 585, 119483. doi:10.1016/j.ijpharm.2020.119483

Han, L., Han, H., and Zheng, L. (2017). Viscosity-temperature relationship and low temperature toughness of terminal blend crumb rubber-nano SiO_2 modified asphalt. *J. Mater. Sci. Eng.* 35 (6), 902–920. doi:10.14136/j.cnki.issn1673-2812.2017.06.009

Han, L., Zheng, M., and Wang, C. (2016). Current status and development of terminal blend tyre rubber modified asphalt. *Constr. Build. Mater.* 128, 399–409. doi:10.1016/j.conbuildmat.2016.10.080

Hosseinnezhad, S., Kabir, S. F., Oldham, D., Mousavi, M., and Fini, E. H. (2019). Surface functionalization of rubber particles to reduce phase separation in rubberized asphalt for sustainable construction. *J. Clean. Prod.* 225, 82–89. doi:10.1016/j.jclepro.2019.03.219

Huang, W., Lin, P., Tang, N., Hu, J., and Xiao, F. (2017). Effect of crumb rubber degradation on components distribution and rheological properties of Terminal Blend rubberized asphalt binder. *Constr. Build. Mater.* 151, 897–906. doi:10.1016/j.conbuildmat.2017.03.229

Huang, W., Lv, Q., and Chai, C. (2016). Research on composite modification by terminal blend asphalt. *J. Build. Mater.* 19 (1), 111–118. doi:10.3969/j.issn.1007-9629.2016.01.019

Jamshidi, A., Kurumisawa, K., Nawa, T., and Igarashi, T. (2016). Performance of pavements incorporating waste glass: The current state of the art. *Renew. Sustain. Energy Rev.* 64, 211–236. doi:10.1016/j.rser.2016.06.012

Khaloo, A. R., Esrafili, A., Kalani, M., and Mobini, M. H. (2015). Use of polymer fibres recovered from waste car timing belts in high performance concrete. *Constr. Build. Mater.* 80, 31–37. doi:10.1016/j.conbuildmat.2015.01.011

Li, J., Chen, Z., Xiao, F., and Amirkhanian, S. N. (2021). Surface activation of scrap tire crumb rubber to improve compatibility of rubberized asphalt. *Resour. Conservation Recycl.* 169, 105518. doi:10.1016/j.resconrec.2021.105518

Li, J., Xiao, F., and Amirkhanian, S. N. (2020). High temperature rheological characteristics of plasma-treated crumb rubber modified binders. *Constr. Build. Mater.* 236, 117614. doi:10.1016/j.conbuildmat.2019.117614

Lin, P., Huang, W., Tang, N., Xiao, F., and Li, Y. (2018). Understanding the low temperature properties of Terminal Blend hybrid asphalt through chemical and thermal analysis methods. *Constr. Build. Mater.* 169, 543–552. doi:10.1016/j.conbuildmat.2018.02.060

Lin, P., Huang, W., Tang, N., and Xiao, F. (2017). Performance characteristics of Terminal Blend rubberized asphalt with SBS and polyphosphoric acid. *Constr. Build. Mater.* 141, 171–182. doi:10.1016/j.conbuildmat.2017.02.138

Liu, H., Chen, Z., Wang, W., Wang, H., and Hao, P. (2014). Investigation of the rheological modification mechanism of crumb rubber modified asphalt (CRMA) containing TOR additive. *Constr. Build. Mater.* 67, 225–233. doi:10.1016/j.conbuildmat.2013.11.031

Ma, T., Chen, C., Zhang, Y., and Zhang, W. (2021). Development of using crumb rubber in asphalt modification: A review. *China J. Highw. Transp.* 34 (10), 1–16. doi:10.19721/j.cnki.1001-7372.2021.10.001

Ma, Y., Wang, S., Zhou, H., Hu, W., Polaczyk, P., Zhang, M., et al. (2021). Compatibility and rheological characterization of asphalt modified with recycled rubber-plastic blends. *Constr. Build. Mater.* 270, 121416. doi:10.1016/j.conbuildmat.2020.121416

Nanjegowda, V. H., and Biligiri, K. P. (2020). Recyclability of rubber in asphalt roadway systems: A review of applied research and advancement in technology. *Resour. Conservation Recycl.* 155, 104655. doi:10.1016/j.resconrec.2019.104655

Navarro, F. J., Partal, P., Martínez-Boza, F. J., and Gallegos, C. (2007). Influence of processing conditions on the rheological behavior of crumb tire rubber-modified bitumen. *J. Appl. Polym. Sci.* 104 (3), 1683–1691. doi:10.1002/app.25800

Niu, W. (2017). Rheological properties of polyphosphoric acid composite TB crumb rubber modified asphalt and pavement performance of its asphalt mixture. *Highway* 62 (8), 234–243.

Pais, J., Lo Presti, D., Santos, C., Thives, L., and Pereira, P. (2019). The effect of prolonged storage time on asphalt rubber binder properties. *Constr. Build. Mater.* 210, 242–255. doi:10.1016/j.conbuildmat.2019.03.155

Phiri, M. M., Phiri, M. J., Formela, K., and Hlangothi, S. P. (2021). Chemical surface etching methods for ground tire rubber as sustainable approach for environmentally-friendly composites development– a review. *Compos. Part B Eng.* 204, 108429. doi:10.1016/j.compositesb.2020.108429

Polacco, G., Filippi, S., Merusi, F., and Stastna, G. (2015). A review of the fundamentals of polymer-modified asphalts: Asphalt/polymer interactions and principles of compatibility. *Adv. Colloid Interface Sci.* 224, 72–112. doi:10.1016/j.cis.2015.07.010

Ragab, M., and Abdelrahman, M. (2018). Enhancing the crumb rubber modified asphalt's storage stability through the control of its internal network structure. *Int. J. Pavement Res. Technol.* 11 (1), 13–27. doi:10.1016/j.ijprt.2017.08.003

Sienkiewicz, M., Borzędowska-Labuda, K., Wojtkiewicz, A., and Janik, H. (2017). Development of methods improving storage stability of bitumen modified with ground tire rubber: A review. *Fuel Process. Technol.* 159, 272–279. doi:10.1016/j.fuproc.2017.01.049

Tang, N., Huang, W., Hu, J., and Xiao, F. (2017). Rheological characterisation of terminal blend rubberised asphalt binder containing polymeric additive and sulphur. *Road Mater. Pavement Des.* 19 (6), 1288–1300. doi:10.1080/14680629.2017.1305436

Wang, Z., Xu, X., Wang, X., Jinyang, H., Guo, H., and Yang, B. (2020). Performance of modified asphalt of rubber powder through tetraethyl orthosilicate (TEOS). *Constr. Build. Mater.* 267, 121032. doi:10.1016/j.conbuildmat.2020.121032

Wen, Y., Wang, Y., Zhao, K., Chong, D., Huang, W., Hao, G., et al. (2018). The engineering, economic, and environmental performance of terminal blend rubberized asphalt binders with wax-based warm mix additives. *J. Clean. Prod.* 184, 985–1001. doi:10.1016/j.jclepro.2018.03.011

Xie, J., Yang, Y., Lv, S., Peng, X., and Zhang, Y. (2019). Investigation on preparation process and storage stability of modified asphalt binder by grafting activated crumb rubber. *Mater. (Basel)* 12 (12), 2014. doi:10.3390/ma12122014

Xie, J., Yang, Y., Lv, S., Zhang, Y., Zhu, X., and Zheng, C. (2019). Investigation on rheological properties and storage stability of modified asphalt based on the grafting activation of crumb rubber. *Polym. (Basel)* 11 (10), 1563. doi:10.3390/polym11101563

Xie, J., Zhang, Y., and Yang, Y. (2020). Development trends of terminal blend rubber modified asphalt. *Plastics* 49 (04), 124–130+140.

Xie, J., Zhang, Y., Yang, Y., Ma, Y., Li, J., and Huang, M. (2020). The effect of activation method of rubber on the performance of modified asphalt binder. *Mater. (Basel)* 13 (17), 3679. doi:10.3390/ma13173679

Xie, J., Zhang, Y., and Yang, Y. (2020). Study on preparation method of terminal blend rubberized asphalt binder. *Front. Mater.* 7, 279. doi:10.3389/fmats.2020.00279

Xu, J., Yu, J., Xu, J., Sun, C., He, W., Huang, J., et al. (2020). High-value utilization of waste tires: A review with focus on modified carbon black from pyrolysis. *Sci. Total Environ.* 742, 140235. doi:10.1016/j.scitotenv.2020.140235

Yu, H. Y., Deng, G. S., Wang, D. Y., Zhang, Z. Y., and Oeser, M. (2020). Warm asphalt rubber: A sustainable way for waste tire rubber recycling. *J. Central South Univ.* 27 (11), 3477–3498. doi:10.1007/s11771-020-4467-y

Yu, H., Deng, G., Zhang, Z., Zhu, M., Gong, M., and Oeser, M. (2021). Workability of rubberized asphalt from a perspective of particle effect. *Transp. Res. Part D Transp. Environ.* 91, 102712. doi:10.1016/j.trd.2021.102712

Zhang, W., Luan, Y., Ma, T., Wang, S., Chen, J., Li, J., et al. (2021). Multilevel analysis of the aging mechanisms and performance evolution of rubber-modified asphalt. *J. Mater. Civ. Eng.* 33 (12), 4. doi:10.1061/(asce)mt.1943-5533.0004000

Zheng, L., Han, Y., Li, S., and Liu, Y. (2018). Morphology effect on properties and microstructure of terminal blend crumb rubber modified asphalt. *J. Mater. Sci. Eng.* 36 (5), 720–725.

Zhong, K., Yang, X., and Luo, S. (2017). Performance evaluation of petroleum bitumen binders and mixtures modified by natural rock asphalt from Xinjiang China. *Constr. Build. Mater.* 154, 623–631. doi:10.1016/j.conbuildmat.2017.07.182

frontiers | Frontiers in Materials

TYPE Original Research
PUBLISHED 05 June 2023
DOI 10.3389/fmats.2023.1208363

OPEN ACCESS

EDITED BY
Hui Yao,
Beijing University of Technology, China

REVIEWED BY
Jue Li,
Chongqing Jiaotong University, China
Xuhui Zhang,
Xiangtan University, China
Cong Zhou,
Hunan University of Science and Technology, China
Xin Jiang,
Wuhan Institute of Technology, China

*CORRESPONDENCE
Ju Yi,
yiju094679@163.com
Ming Deng,
dengming_979@126.com

RECEIVED 19 April 2023
ACCEPTED 24 May 2023
PUBLISHED 05 June 2023

CITATION
Deng M and Yi J (2023), Fatigue life prediction of orthotropic steel deck strengthened with UHPC under stochastic traffic load.
Front. Mater. 10:1208363.
doi: 10.3389/fmats.2023.1208363

Fatigue life prediction of orthotropic steel deck strengthened with UHPC under stochastic traffic load

Ming Deng[1,2]* and Ju Yi[1,2]*

[1]School of Civil Engineering, Changsha University, Changsha, China, [2]National-Local Joint Laboratory of Engineering Technology for Long-term Performance Enhancement of Bridges in Southern District, Changsha University of Science and Technology, Changsha, China

In recent years, the ultra-high performance concrete (UHPC) has been increasingly used to strengthen orthotropic steel decks (OSD) to solve the cracking problems at fatigue-prone details and pavement damage. In this paper, the fatigue life of a cable-stayed orthotropic steel decks bridge under stochastic traffic loads is calculated before and after the orthotropic steel decks strengthened with the ultra-high performance concrete layer. The traffic data of the real bridge for 1 week is first obtained based on the weigh-in-motion system. Then, a stochastic traffic load on the bridge is simulated for its service life by the Monte Carlo method. A fatigue life analysis framework, which includes the traffic load simulation, a refined finite element model, the S-N curve and Miner linear cumulative damage criterion, is proposed for fatigue life prediction of orthotropic steel decks. For the bridge before reinforcement, the predicting results for the fatigue life of three fatigue-prone details, including the scallop cutout, rib-to-diagram and rib-to-deck joint are basically consistent with that of the actual bridge inspection results. After strengthening by ultra-high performance concrete, the fatigue life of the three structural details are increased from 15.87, 13.89, and 32.26 years to more than 100 years, respectively, as compared with the original orthotropic steel decks structure.

KEYWORDS

bridge engineering, stochastic traffic load, fatigue life, orthotropic steel deck, ultra-high performance concrete (UHPC)

1 Introduction

The orthotropic steel deck (OSD) has been widely used in bridge engineering due to its good integrity, light weight, high strength, and good applicability when comparing with the traditional concrete bridge deck, especially in the long-span cable-stayed bridges (Hu et al., 2014). Generally, the OSD consists of bridge deck, longitudinal and transverse stiffening ribs that jointly bear vehicle loads. With the fast-growing in traffic loads, some fatigue problems, however, are becoming increasingly prominent in the OSD (Walter et al., 2007; Chen et al., 2015; Fisher and Barsom, 2016). These problems may be attributed to large local deformation and serious stress concentration under the heavy load. Other factors, such as welding residual stress, poor construction quality, can also be the reasons to induce fatigue problems. In addition, the pavement of the bridge may be subjected to an easier cracking, debonding and other diseases under the wheel load. Consequently, the serviceability and safety of the bridge may be significantly deteriorated.

Several measures have been conducted by researchers to reinforce the OSD, including drilling holes to change the stress field intensity distribution at the crack tip (Choi and Kim, 2008), local structural reinforcement (May et al., 2015; Wang et al., 2015), and SPS combination reinforcement (Jong, 2007). These measures, however, may have limited positive effect on solving the fatigue cracking because the reinforcement effect on the local stiffness of OSD is still low in these cases. The bridges crack may crack again shortly after strengthening. Therefore, other measures need to be proposed to effectively increase the stiffness of the OSD. For this purpose, a kind of ultra-high performance concrete (UHPC) pavement was put forward by pouring it on the bridge deck (Jong, 2007; Zhang et al., 2023). It is widely known that, as a new type of fiber reinforced cement-based composite material, the UHPC owns outstanding characteristics such as ultra-high strength, ultra-high toughness and excellent durability, *etc.* As a result, a composite structure composed by the original OSD and UHPC is compactly formed through densely distributed shear nails. The steel-UHPC composite structure is not only used in new construction projects (Zhang et al., 2016), but also has been widely used in reinforcement projects, such as Yangtze River Bridge in China (Qin et al., 2022), Tianjin Haihe Bridge in China (Wang et al., 2020). After the strengthening of UHPC, an improvement of the fatigue resistance of the OSD can be expected.

A number of studies about the fatigue resistance of steel-UHPC composite structures have been conducted by several researchers. Deng (Deng et al., 2021) calculated the fatigue reliability of OSD-UHPC composite bridge based on reliability and fatigue cumulative damage model, and the results showed that the fatigue life of OSD-UHPC composite structure is prolonged at least 60%. Yuan (Yuan et al., 2019) studied the repair process of UHPC to the fatigue crack of the OSD specimen through full-size model test, the effectiveness of UHPC to improve the fatigue life of the OSD is also verified through the linear accumulative damage rule. Dieng et al. (2013) found that the UHPC pavement, as compared with the traditional asphalt mixture, can reduce the stress amplitude of the details. The above studies show that the fatigue life of composite structures is greater than that of the OSD, and most of these researches are conducted based on finite element simulation or laboratory experiments. The stress of these cases, however, may differs from that of the real bridge. Besides, other experimental researches are conducted on predicting the fatigue life of real steel-UHPC composite bridge (Zhu et al., 2019; Qin et al., 2022). Among them, the stress under random traffic flow is continuously monitored by arranging strain gauges in typical structural details. For this case, the number of measuring points monitored in the real bridge is limited, and errors on stress monitoring may be unable to avoid due to the influence of the environment, thus affecting the accuracy of fatigue life calculation. More effective methods are needed to calculate the fatigue life of the real bridge. This paper aims to study the fatigue life of a steel bridge strengthened by UHPC under the stochastic traffic loads, which is simulated based on the traffic flow data measured by the weigh-in-motion (WIM) system.

The fatigue performance of OSD strengthened with UHPC under stochastic traffic load is evaluated in this paper. The paper is organized as follows. First, some basic information of the bridge, the main diseases and the reinforcement scheme based on UHPC are introduced. Then, a fatigue life assessment process of typical fatigue-prone details of the OSD under stochastic traffic loads is proposed. Following that, the fatigue life of three structural details is calculated. The strengthening effect is validated by comparing the fatigue life before and after strengthening, and some conclusions are summarized.

2 Engineering background

2.1 Bridge description

Haihe Bridge is a bridge closed to the Tianjin port, China. It is a hybrid beam single tower cable-stayed bridge with a total length of 500 m and a main span of 310 m. The main span is composed of 290 m steel box girder and 20 m steel-concrete joint section, and the side spans are prestressed concrete box girder. The bridge deck is supported by 36 pairs of stay cables, and the cable spacing on the beam is 16 m. The layout of the bridge is shown in Figure 1A. The total width of the steel girder is 23 m, and the distance between each pair of stay cables on the bridge deck is 22.3 m. The thickness of the deck, webs, diaphragm are 14, 14, 10 mm, respectively. In transverse bridge direction, the steel box girder is formed by a double cell box and an opening section, each part has 12 U-ribs. The width of the U-rib is 300 mm, and the spacing between adjacent U-ribs is 300 mm too. The girder is provided with a diaphragm every 3.2 m. The deck pavement of steel box girder is modified asphalt concrete with 70 mm thick. Figure 1B shows the schematic diagram of the cross section.

The Haihe Bridge was completed and opened to traffic in 2002. It was originally designed as a four-lane bidirectional traffic. The traffic is heavy on this bridge, especially the number of trucks, as it is located in a busy port area. In order to alleviate the traffic pressure, a new bridge was built next to the bridge in 2011, and the traffic of the old bridge was changed to one-way four-lane traffic. The research object of this paper is the old bridge opened to traffic in 2002.

2.2 Description of fatigue problems

There are two types of typical fatigue diseases in bridge under long-term heavy loads. The first disease is the pavement damage, such as longitudinal cracking and steel–concrete interface debonding. The disease of asphalt pavement may be related to the compaction and stress state (Chang et al., 2023). For example, in the transverse direction of the bridge, the web of the U rib can be regarded as the fulcrum of the steel deck. Therefore, the negative bending moment is easily generated at the intersection point between the U rib and the bridge deck under vehicle loads. As a result, longitudinal cracks are occurred in bridge pavement under cyclic load. Through detailed inspection, it was found that there were nearly twenty longitudinal cracks in the asphalt pavement of Haihe bridge, which was consistent with the width and spacing of U-ribs, as shown in Figure 2. In addition, the rainwater will reach the bottom of the pavement along the cracks, which is prone to cause the bond failure in steel–concrete interface under the vehicle braking force.

The second type is the cracking of the OSD. The cracking generally appeared under the coupled effects of low stiffness of

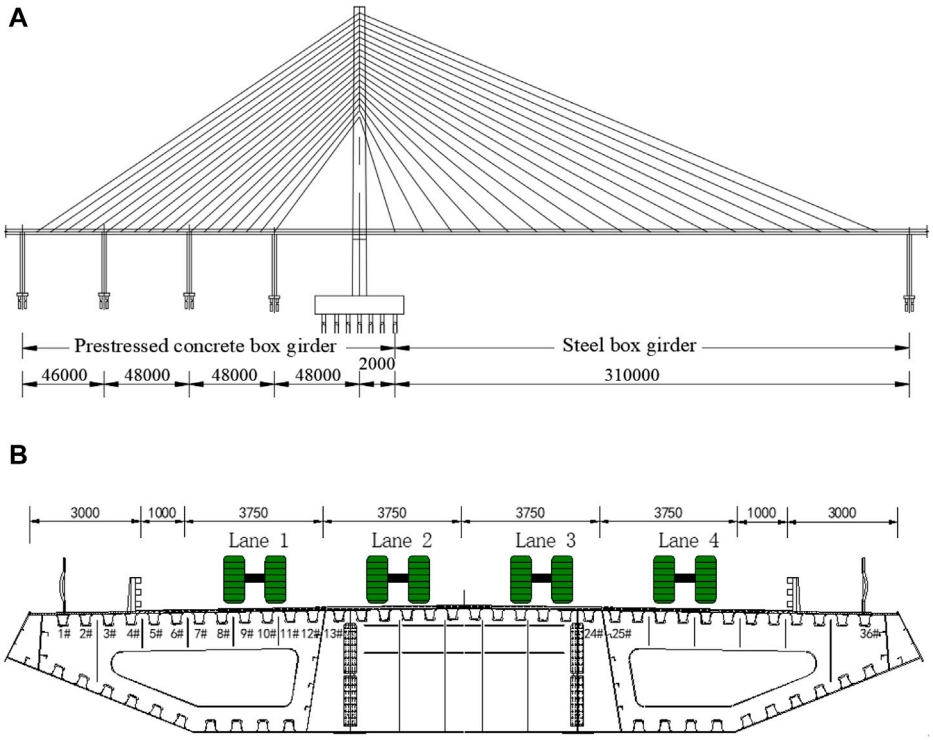

FIGURE 1
Basic information of the Haihe Bridge: **(A)** layout of the bridge (unit: mm), **(B)** cross-section (unit: mm).

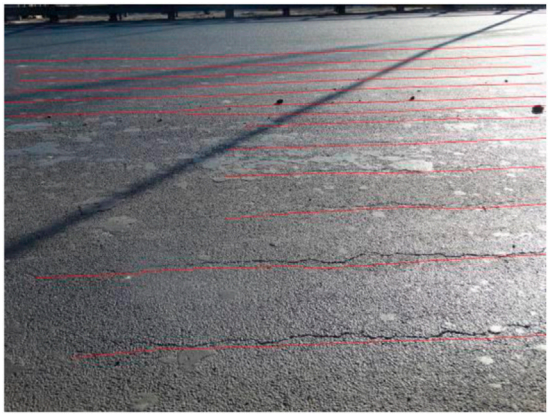

FIGURE 2
Longitudinal cracking on the asphalt pavement.

OSD and numerous heavy trucks, leading to large stress amplitudes in some typical locations of the bridge. Consequently, some fatigue cracks, as shown in Figure 3, generated inevitably. By the end of 2014, the total number of cracks in Haihe Bridge had exceeded 1,400 and the total length had exceeded 6,700 cm. Figure 4 shows the typical cracks in Haihe bridge. In the transverse direction, these cracks are mainly concentrated between 6 # U ribs and 30 # U ribs, which are under lane 2 and lane 3.

2.3 Steel-UHPC composite reinforcement

Since 2005, the Haihe Bridge had been strengthened for more than ten times, including drilling holes, bonding steel plates, replacing bridge deck pavement, *etc.*, but the disease was still developing. The above phenomenon showed that the direct repair method of steel box girder cracks and the replacement of flexible pavement system cannot change the problem of inadequate stiffness of OSDs. The stress state of the typical structural details and bridge pavement had not changed after strengthening, which was bound to cause the damage continue propagating under the load of heavy vehicles.

A layer of UHPC was added to the steel deck to improve the rigidity of the OSD. UHPC is a new type of cement-based composite material, mainly composed of quartz fine sand, silica fume, cement, quartz powder, and a certain amount of steel fibers. The most typical characteristic of UHPC is its ultra-high strength, with a compressive strength of up to 150–250 MPa and a tensile strength of around 10 MPa.

The main reinforcement scheme of the bridge includes the following: 1) UHPC pavement was adopted within 17.5 m in the transverse direction of the traffic lane. After applying 80 thick epoxy zinc rich paint to the bridge deck, a shear nail with a diameter of 13 mm and a height of 40 mm is welded to the bridge deck. The spacing between shear nails in both transverse and longitudinal directions is 150 mm. The thickness of UHPC layer was 45 mm, with a waterproof adhesive layer and an asphalt pavement layer with the thickness of 30 mm on it. 2) Considering

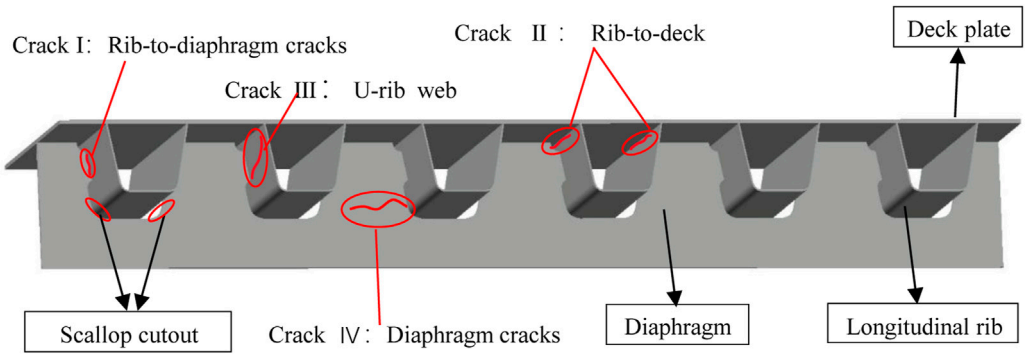

FIGURE 3
Welded details and cracking position.

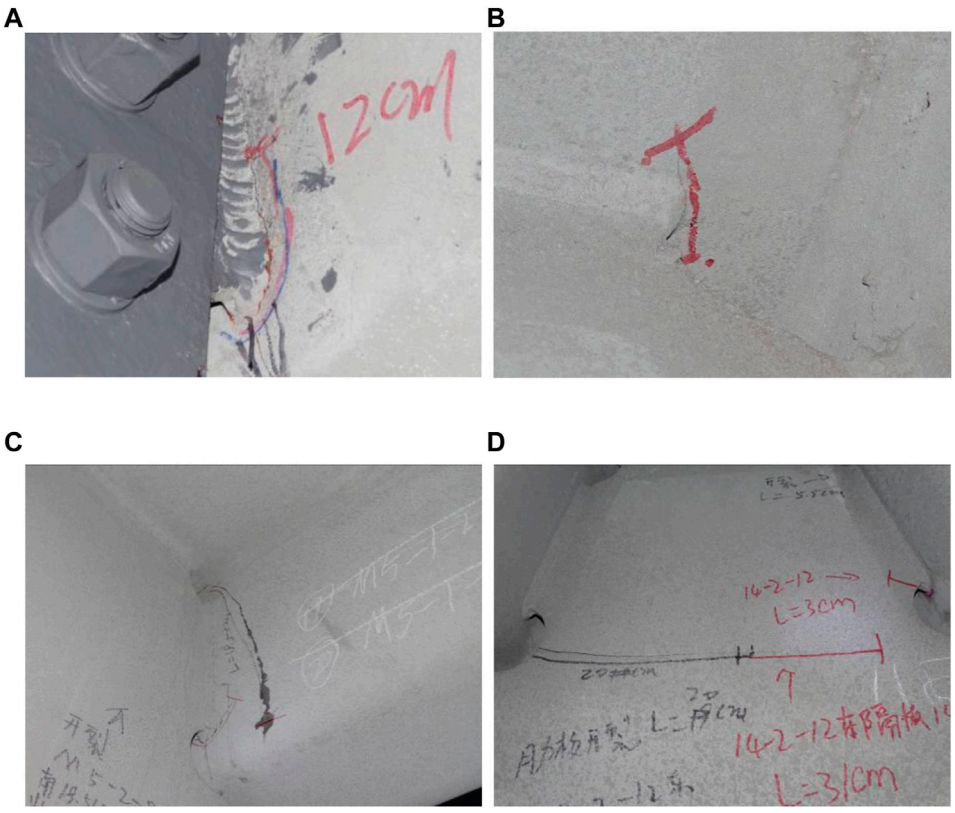

FIGURE 4
Typical cracks: **(A)** rib-to-diaphragm cracks, **(B)** rib-to-deck cracks, **(C)** U-rib cracks and **(D)** diaphragm cracks.

that the weight of UHPC-asphalt pavement on the traffic lane is greater than that of the original asphalt pavement, the area out of the traffic lane is paved with a synthetic rubber layer with 13 mm in thickness. As a result, the dead load of bridge is basically unchanged after reinforcement. A schematic diagram of the pavement configuration is shown in Figure 5.

3 Fatigue life prediction of OSD under stochastic traffic flows

A systematic procedure for fatigue life prediction of the fatigue-prone details in OSD is proposed, as schematically in Figure 6. First, the axle load, speed, lane and other information of the vehicle are extracted from

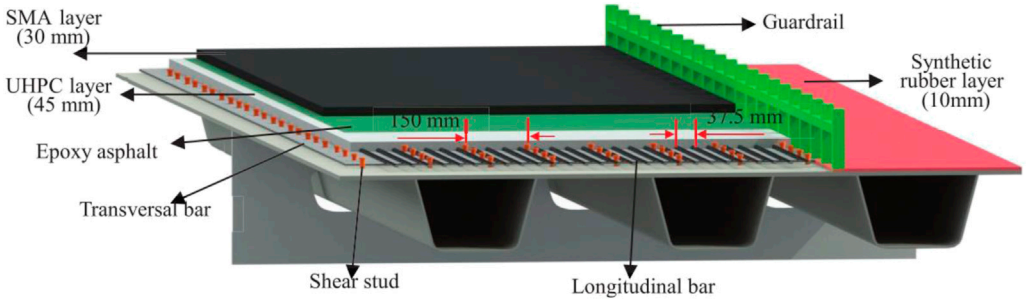

FIGURE 5
Schematic diagram of the pavement configuration.

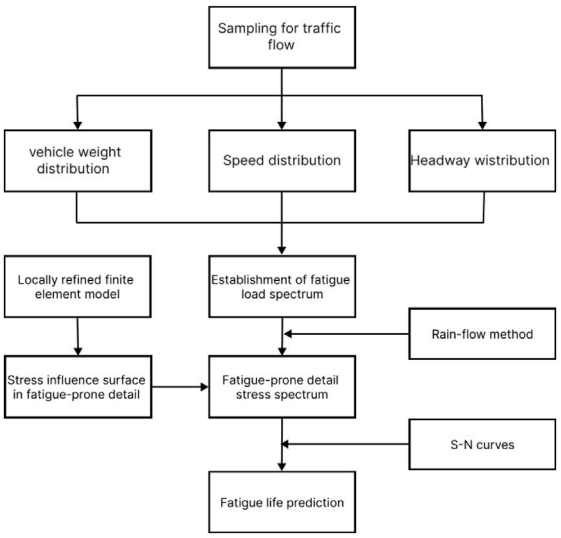

FIGURE 6
Flow chart of fatigue life assessment.

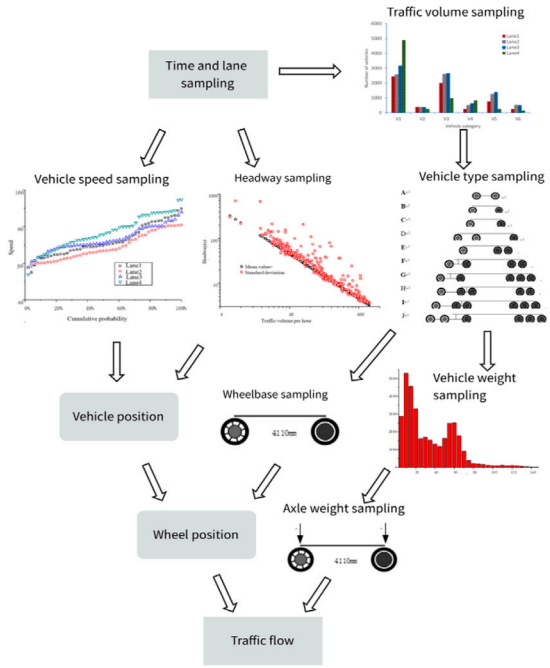

FIGURE 7
Monte-Carlo simulation for traffic flow.

the measured traffic load data, and the long-term traffic load is simulated using Monte Carlo method. Second, a local refined three-dimensional finite element model is established, which is loaded by a unit load to generate the stress influence surface of fatigue-prone details, then the stress history is obtained by means of influence surface loading. Next, according to the rain-flow counting method, the stress spectrum of the fatigue-prone detail under the stochastic traffic loads is obtained. Finally, according to the Miner linear cumulative damage criterion and the classifications of detailed categories in S-N curves, the fatigue life of the fatigue-prone details is calculated.

3.1 Traffic load simulation based on Monte Carlo method

3.1.1 Principle of Monte Carlo simulation

Monte-Carlo simulation is one way for solving mathematical or physical problems based on random sampling method (Chang et al., 2023). It is an uncertain numerical method, and is often used in the simulation of stochastic traffic loads. The following is the basic idea of the method.

Let U be a uniform random variable between [0–1], that is $U \sim R(0,1)$. Then the random variable X generated by $X = F_X^{-1}(U)$ follows the distribution of probability distribution function $F_X(x)$. So $F_X^{-1}(u) > x$ is equivalent to $U > F(x)$, where $F_X^{-1}(u)$ is the inverse function of $F(x)$. Then

$$P(X \le x) = 1 - P\left(F^{-1}(U) > x\right) = F(x) \tag{1}$$

Therefore, the random variable X generated by $X = F_X^{-1}(U)$ follows the distribution of probability distribution function $F_X(x)$.

When the statistics of the traffic vehicle loads are known, the corresponding vehicles can be generated by Monte-Carlo

simulation. In computer simulation, a group of random numbers is first generated. When the seed of the sequence is determined, all the numbers in the sequence are determined. Therefore, such random numbers are usually called pseudorandom numbers. For normal distribution, the generation of pseudorandom number can use the Box Muller method (Giray and Ahmet, 2011). As long as there are two random variables U_1 and U_2 that obey uniform distribution, a random variable X that obey normal distribution can be obtained through Formula 3:

$$X = R\cos\theta = \sqrt{-2\ln U_1}\cos(2\pi U_2) \quad (2)$$

3.1.2 Process of traffic load simulation

Two aspects are mainly considered in traffic load simulation: the loading position and the weight of wheels. The loading position of the wheel is mainly determined by the vehicle speed, headway, wheelbase; while the weight of the wheel is mainly determined by the vehicle loads and axle weight ratio.

Monte Carlo simulation is performed for each lane in every half an hour, as shown in Figure 7. After counting the traffic flow of each lane within half an hour, the first vehicle is simulated. Firstly, the mean μ_s and variance σ_s of headway are obtained from traffic flow data statistics, and the headway of vehicles is sampled from these two parameters by inverse function method. Then the vehicle speed is simulated by using the mean μ_V and variance σ_V of the vehicle speed in the lane. Next, according to the proportion of each type of vehicle in the half hour, select the model of the simulated vehicle, and get the corresponding axle weight ratio and wheelbase. Finally, the total vehicle weight is sampled according to its vehicle weight distribution, and then the axle weight of each axle is determined from the previous step. Repeat the above steps, continuously simulate the vehicle information of each lane at each time, and the traffic flow within half an hour is simulated. It is assumed that the traffic data in the life cycle is unchanged, then repeat the simulation steps to get the stochastic traffic flow for a day, a week or even a life cycle.

3.2 Stress time history

It is necessary to use the finite element software to establish the structural analysis model to calculate the stresses of the fatigue-prone details of OSD. Previous studies (Li et al., 2009; Yan et al., 2016) have shown that the fatigue-prone details have large stress when the load is applied to a small area near the details, and are not sensitive to the load outside the area. In the longitudinal direction, this area is approximately within 2 m around the fatigue-prone details. Along the transverse direction, the affected areas are roughly within the adjacent trapezoidal ribs. Therefore, a local refined finite element model can be established, which can reduce the calculation time and have high calculation accuracy. Then, the stress influence surface of fatigue-prone details can be generated based on the local refined finite element.

The stress change history of each fatigue-prone detail can be obtained by simulating the movement process of the vehicle on the influence surface. According to the simulation of vehicle speed and headway, record the vehicle position at an interval of 0.02 s. For those falling within the effective range of the influence surface, calculate the stress effect of the vehicle according to the corresponding influence surface value and vehicle axle loads. The superposition of the load effect of all vehicles falling into the effective range of the stress influence surface is the traffic load effect of the concerned fatigue-prone details at that moment. The stress history of each detail can be obtained by recording the load effect in chronological order.

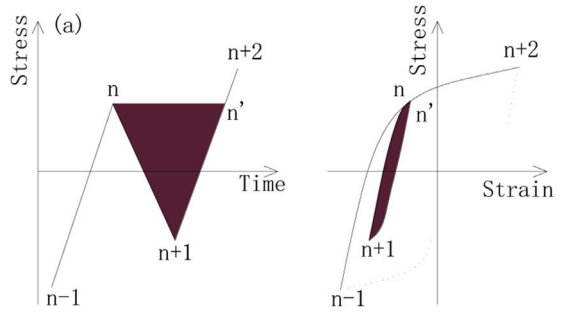

FIGURE 8
Identification of stress cycles.

3.3 Rain-flow counting method

Before the fatigue analysis, it is necessary to convert the time-varying random stress history curve into multiple constant amplitude stress cyclic loads, whose combination is called stress spectrum. Then count the damage of each constant amplitude cyclic loading in the stress spectrum to obtain the total fatigue damage.

The rain-flow counting method is widely used to obtain the stress spectrum by counting the stress history curve. After studying the stress-strain process of fatigue loading, scholars Matsuishi and Endo (Socie, 1982) proposed that each stress closed-loop formed during the loading process constitutes a stress cycle, and the shaded part as shown in Figure 8 constitutes a stress cycle. The method of identifying the stress cycle can be visually seen as the process of rain falling down the roof, so it is called rain flow method.

In this paper, the four peak-to-valley rain-flow counting method is adopted. This method is to judge whether there is a complete cycle in the four adjacent peaks and valleys, and the mathematical model is as follows:

$$|x_{n-1} - x_n| \geq |x_n - x_{n+1}| \leq |x_{n+1} - x_{n+2}| \; n = 2, 3, 4, \ldots, N-2 \quad (3)$$

where N is the length of the peak-valley value sequence.

If the points x_n and x_{n+1} meet the above criteria, the two points can be recorded as a complete fatigue cycle and then deleted from the peak-valley value sequence, so that the adjacent two points x_{n-1} and x_{n+2} can be further re-selected in the remaining sequence to form a new four-point range. Repeat the above process until all ranges meeting the four peak-to-valley criteria are recorded and deleted from the sequence.

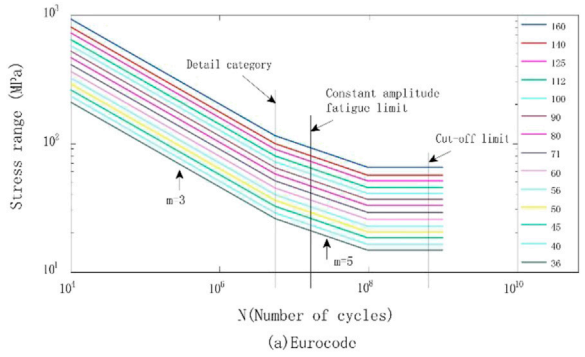

FIGURE 9
S-N curves in Eurocode.

FIGURE 10
Weigh-in-moton system.

3.4 Fatigue analysis method

The fatigue of steel bridges belongs to the category of variable amplitude, low stress and high cycle. The analysis method based on S-N curve and Miner linear cumulative damage criterion is usually adopted. The current design codes such as AASHTO, BS5400 and Eurocode 3 have adopted the method of modifying the S-N curve obtained from the constant amplitude fatigue test data, and formulated the S-N curve applicable to the fatigue-prone details of steel bridges.

The Eurocode (Eurocode, 1993) provides a series of S-N curves for fatigue life assessment, these curves show the relationship between the stress range and cycle life for different details, as shown in Figure 9. These curves are divided into 3 segments, and the formulas are as follows:

$$\Delta\sigma_R^m N_R = 2\times10^6\Delta\sigma_C^m \quad (\mathrm{m}=3\ N\le 5\times10^6) \tag{4}$$

$$\Delta\sigma_R^m N_R = 5\times10^6\Delta\sigma_C^m \quad (\mathrm{m}=5\ 5\times10^6 < N\le 1\times10^8) \tag{5}$$

$$\Delta\sigma_L = \left[\frac{5}{100}\right]^{\frac{1}{5}}\cdot\Delta\sigma_D = 0.549\Delta\sigma_D \tag{6}$$

where $\triangle\sigma_R$ is the structural detail stress amplitude; N_R is the corresponding number of cycles; $\triangle\sigma_C$ is the detail category, i.e., the constant amplitude fatigue strength when $N=2\times10^6$; $\triangle\sigma_D$ is the constant amplitude fatigue limit fatigue strength when $N=5\times10^6$; $\triangle\sigma_L$ is the corresponding cut-off stress limit when $N\ge10^8$. When $\Delta\sigma_R<\Delta\sigma_L$, it is considered that fatigue cracking will not occur in the structural details.

The Miner linear cumulative damage criterion considers that fatigue is the linear accumulation of fatigue damage caused by different stress levels $\Delta\sigma_i$ and their number of actions n_i, and its total damage degree D can be expressed as follows:

$$D=\sum_{i=1}^{n}\frac{n_i}{N_i}=\frac{n_1}{N_1}+\frac{n_2}{N_2}+\cdots\cdots+\frac{n_n}{N_n} \tag{7}$$

where n_i is the number of actions of stress amplitude $\Delta\sigma_i$; N is the fatigue life corresponding to stress amplitude $\Delta\sigma_i$ in S-N curves. When the linear cumulative damage D reaches 1, the structure will undergo fatigue failure. Therefore, the fatigue life is as follows:

$$L=1/D \tag{8}$$

where L is the fatigue life.

4 Fatigue life of structural details of Haihe Bridge

4.1 Traffic load simulation based on WIM

In May 2015, the WIM system was installed for Tianjin Haihe Bridge. The system was installed on the approach road of Haihe Bridge. Each lane was grooved and buried with a piezoelectric sensor, as shown in Figure 10. The traffic loads were monitored for 7 consecutive days from June 17 to 23, 2015. The monitoring contents included traffic time, vehicle speed, vehicle length, vehicle weight, axle number, axle load, *etc.* The statistical parameters of vehicle load are shown in Table 1. As the design load is 55 tons, the actual traffic load far exceeds the design limit value.

4.1.1 Vehicle type and driving lane

According to the one-week monitoring data of Haihe Bridge (Deng et al., 2017), traffic vehicles can be divided into two categories: cars and trucks. Among them, cars accounted for 43.2% and trucks accounted for 56.8%. It can be seen that there is a large proportion of trucks as the bridge is located in the port area. There are mainly five types of trucks, including 2-axle, 3-axle, 4-axle, 5-axle and 6-axle, of which 3-axle and 5-axle trucks account for the largest proportion. The passenger cars are recorded as V1, and the 2-axle~6-axle trucks are recorded as V2~V6 respectively. The ratio of various types of vehicles is shown in Figure 11. Figure 12 shows the traffic flow data of different lanes. It can be found that different types of vehicles have preferences for lanes. Among them, cars tend to use the inner lane because of their fast speed, while trucks tend to drive in the middle two lanes. This also led to more cracks in the steel structure under the middle lanes.

The transverse position of the vehicle has an important influence on the stress response of the structural details.

TABLE 1 Statistical parameters of vehicle load.

Date	Number of samples	Average value(t)	Median(t)	Maximum(t)	Coefficient of variation
2015/6/17	30,342	8.50	3.69	148.92	1.53
2015/6/18	27,869	17.19	8.07	149.17	1.26
2015/6/19	27,640	14.98	4.24	149.10	1.38
2015/6/20	27,585	17.12	4.20	149.57	1.38
2015/6/21	31,606	10.52	2.14	147.69	1.79
2015/6/22	28,450	14.74	3.35	147.63	1.49
2015/6/23	28,264	10.90	2.10	148.92	1.79

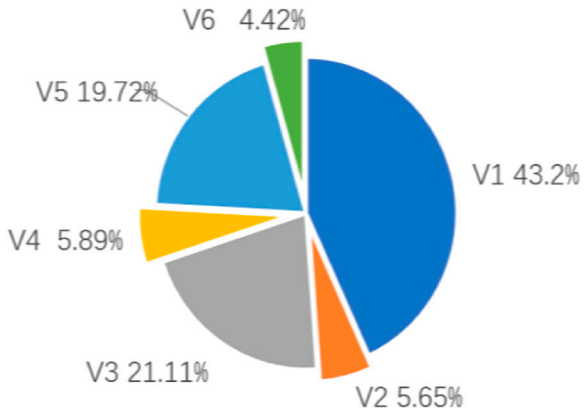

FIGURE 11
Probability densities of vehicle type.

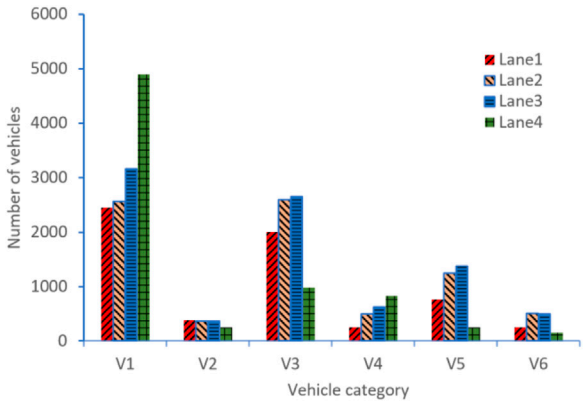

FIGURE 12
Traffic flow of different vehicle types in each lane.

However, it is difficult to monitor the accurate transverse position by the WIM system. Therefore, the probability model of the lateral position of the wheel in China's Code for Design of Steel Structures of Highway Bridges (Ding, 2015) is selected in this paper, as shown in Figure 13.

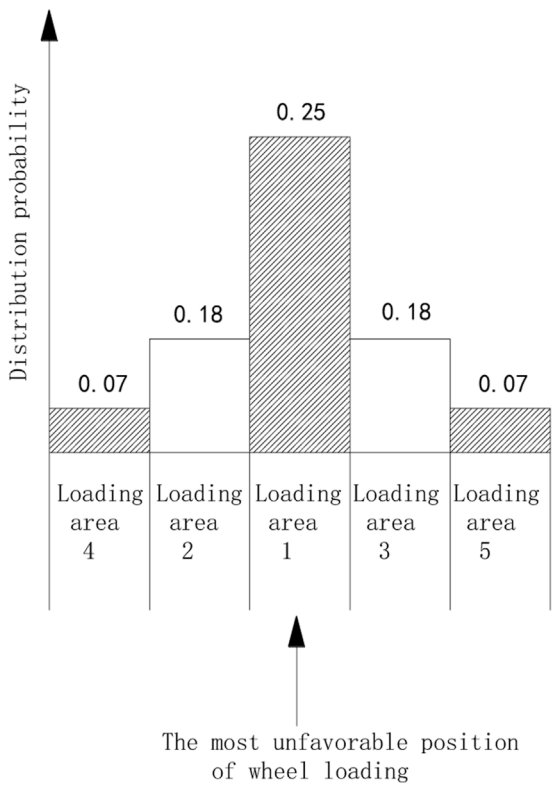

FIGURE 13
Transversal positions probability of wheel.

4.1.2 Vehicle speed characteristics

It is generally believed that the vehicle speed follows the normal distribution $N(\mu_V, \sigma_V^2)$, where μ_V and σ_V are also random variables (Donnell et al., 2001). According to the observed data, the vehicle speed will change with time. It is proposed to use the curve of the total average speed of four lanes with time as the empirical curve to simulate the impact of speed in traffic loads. That is to say, when simulating the speed, the time period will be determined first, and the corresponding average speed will be determined according to the empirical curve.

Figure 14A shows the probability distribution law of the average speed. It can be seen that the speed on each lane is

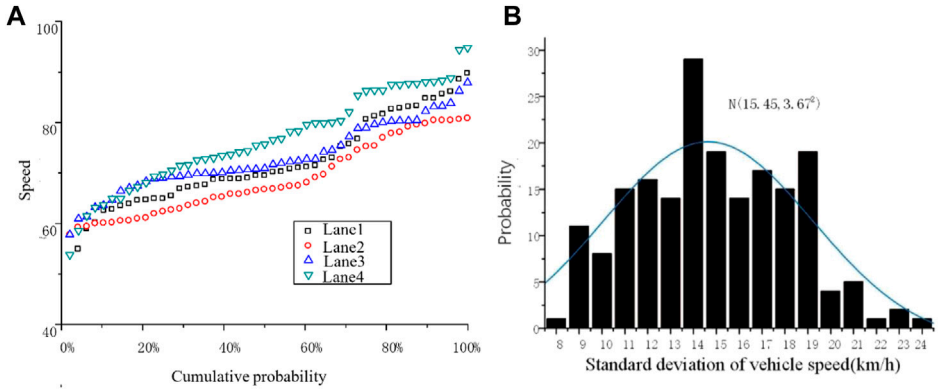

FIGURE 14
Probability distribution of mean and standard deviation of vehicle speed: **(A)** Mean and **(B)** Standard deviation.

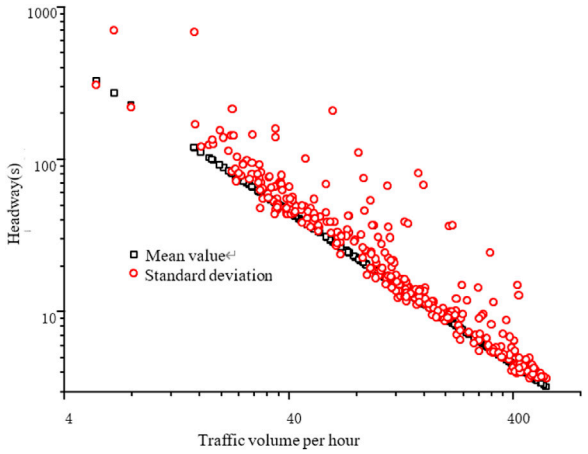

FIGURE 15
μ_S and σ_S of headway.

TABLE 2 Coefficients in the probability density function of vehicle weight.

Parameter	V2	V3	V4	V5	V6
p_1	0.662	0.454	0.412	0.313	0.168
μ_1	2.301	3.073	15.2	17.844	17.506
σ_1	0.398	0.739	3.435	3.852	1.358
P_2	0.234	0.094	0.008	0.271	0.206
μ_2	3.568	4.63	15.411	32.98	21.321
σ_1	0.845	1.172	3.352	9.303	2.571
P_3	0.07	0.452	0.395	0.349	0.41
μ_3	6.243	6.677	25.194	60.963	61.553
σ_3	2.452	4.998	9.872	7.626	9.57
P_4	0.034		0.185	0.067	0.216
μ_4	15.162		58.482	92.117	32.908
σ_4	7.708		8.71	26.655	7.76

approximately uniformly distributed, so the uniform distribution can be used to simulate the average speed μ_V The standard deviation of vehicle speed is less affected by other factors, so lanes and time periods are not considered. According to the statistical results in Figure 14B, the standard deviation of vehicle speed σ_V follows the normal distribution N (15.45, 3.672).

4.1.3 Headway

The headway and vehicle speed jointly determine the loading position of the vehicle, which are important parameters to be considered in the simulation. The distribution of headway is relatively complex, which is related to many factors such as traffic operation status, road type and traffic flow time density. Existing studies believe that the headway follows exponential distribution (Panichpapiboon, 2015), and the average μ_s and standard deviation σ_s are also random variables.

Figure 15 shows the relationship between the statistical parameters of headway and the hourly traffic volume in the double logarithmic coordinate system. It can be seen that in the double logarithmic coordinates, the mean value and standard deviation of headway are approximately linear, in which the data of the mean value are very regular, while the data of the standard deviation are relatively discrete.

The fitting formulas for the mean and standard deviation of headway are as follows:

$$\mu_S = 1800V^{-1}$$
$$\sigma_S = 3413.7232V^{-1.1055} \quad (9)$$

4.1.4 Vehicle weight

Vehicle weight is an important parameter, which plays a major role in determining the effect of traffic loads. According to

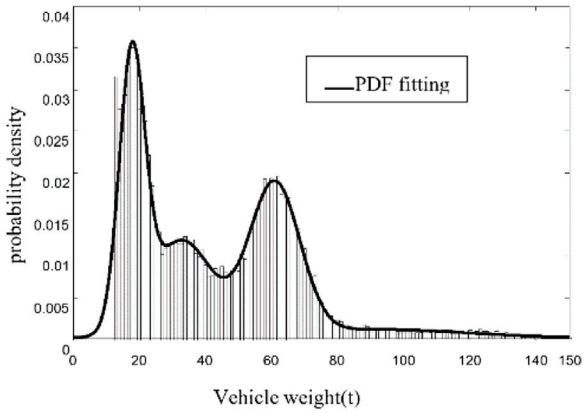

FIGURE 16
Histograms and PDFs of the 5-axle truck.

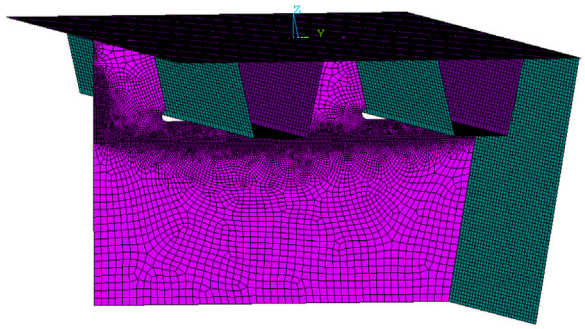

FIGURE 17
Locally refined finite element model.

the monitoring data, the vehicle weight of different axle numbers of the Haihe Bridge presents obvious multi-peak distribution. Therefore, the Gaussian mixture model (Lu et al., 2018) can be used to simulate the vehicle weight, its probability distribution function is as follows:

$$F_X(x) = \sum p_i \Phi\left(\frac{x-\mu_i}{\sigma_i}\right) \sum p_i = 1 \tag{10}$$

After analyzing the measured data, the statistical parameters of various types of trucks are shown in Table 2. Taking the five-axle truck as an example, the histogram and probability density functions (PDFs) are shown in Figure 16.

The wheelbase and wheel-load ratio of different vehicles types are also different. In this paper, the wheelbase and axle load of each vehicle type are regarded as constants, and the data in literature (Yan et al., 2021) is used.

4.2 Finite element model

The finite element model of Haihe Bridge is established using ANSYS software. Two calculation models are established to compare and analyze the fatigue life of structural details before and after reinforcement. One is orthotropic rigid bridge deck, the other is UHPC-orthotropic rigid deck composite structure. According to the detection results of the bridge, the cracks in steel box girder mostly appear near the middle web in the transverse direction. This is due to the lack of diaphragm restraint and the additional effect caused by torsion. Therefore, the established local refined finite element model includes two U ribs near the middle web in the transverse direction of the bridge. The longitudinal direction includes a diaphragm with a length of 4 m. The top of the model is the bridge deck, and the right side is the middle web. The height of the diaphragm and the middle web is 900 mm, as shown in Figure 17. The horizontal displacement on the left side of the model is constrained. SHELL63 element is used to simulate steel structural plates in the model, and SOLID45 element is used to simulate UHPC bridge deck.

Based on the refined local model above, three types of stress influence surfaces that may become the origin point of fatigue cracks are calculated to carry out the fatigue life calculation for the structural details, including the scallop cutout, the rib-to deck joint and the rib-to-diaphragm joint. Limited by space, this paper lists the *Z*-direction stress influence surface of the scallop cutout at the U rib opening position on the diaphragm, as shown in Figure 18. It can be seen from the figure that the effect of load is limited to a small range near the fatigue details, and the influence line value of

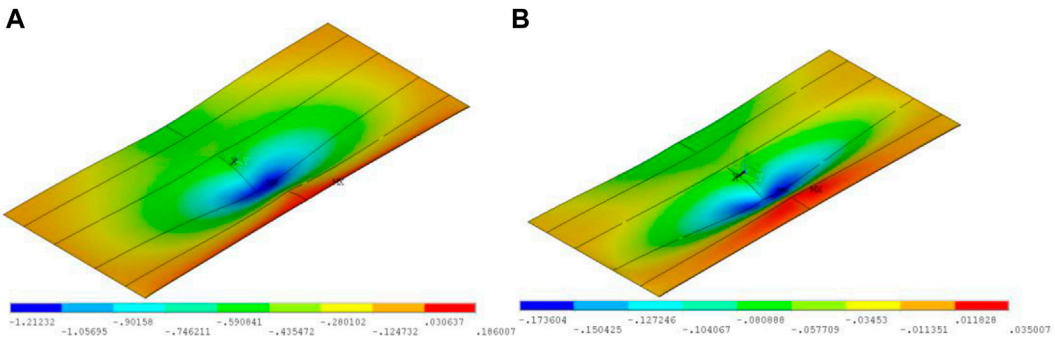

FIGURE 18
Z-direction stress influence surface of the scallop cutout at the U rib opening position on the diaphragm: **(A)** before reinforcement, **(B)** after reinforcement.

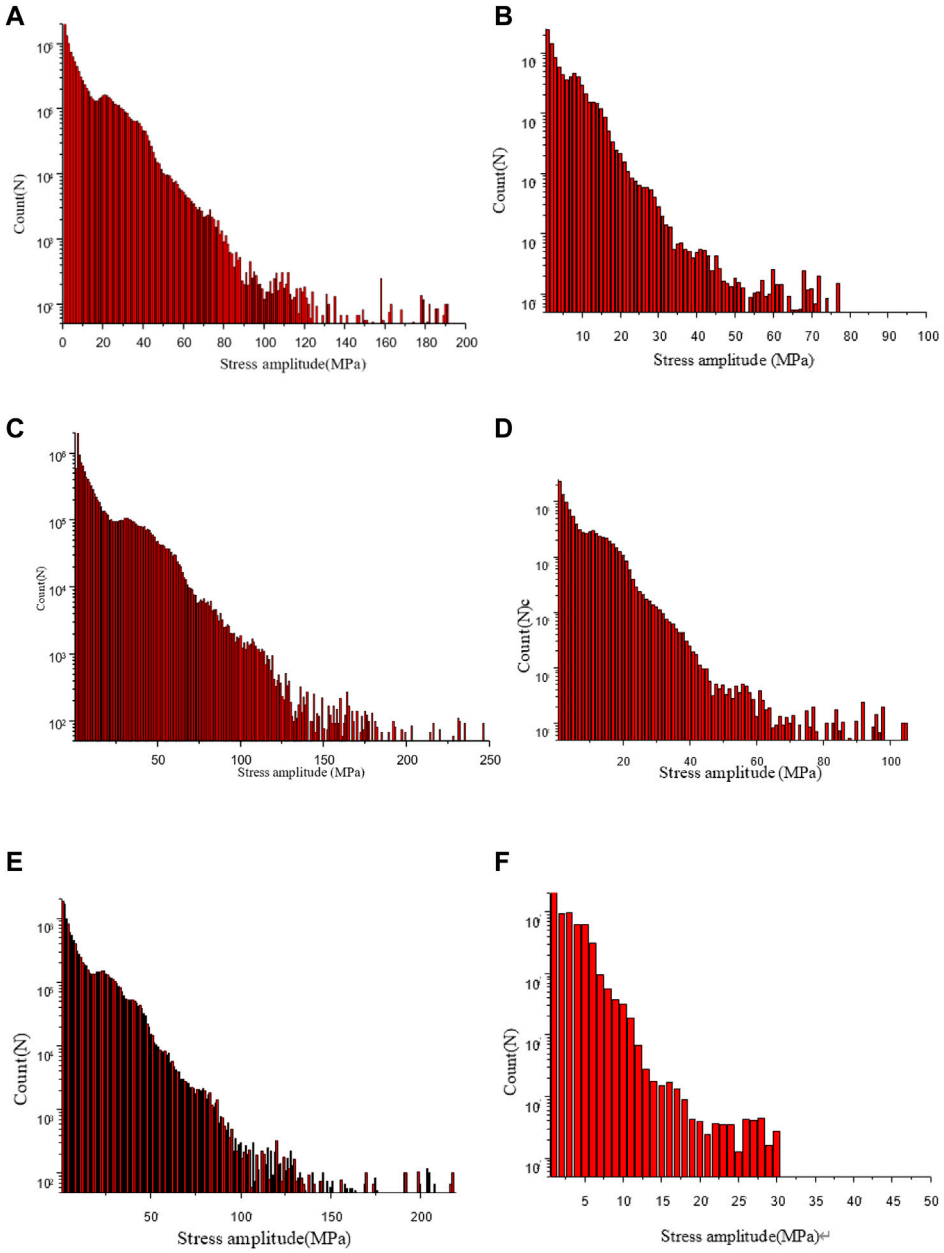

FIGURE 19
Stress spectrum of fatigue-prone details in Lane 2: **(A)** scallop cutout before reinforcement; **(B)** scallop cutout after reinforcement; **(C)** rib-to-diaphragm joints before reinforcement; **(D)** rib-to-diaphragm joints after reinforcement; **(E)** rib-to-deck joints before reinforcement and **(F)** rib-to-deck joints after reinforcement.

each point after reinforcement is significantly smaller than that before reinforcement, which indicates that the reinforcement effect is obvious.

4.3 Fatigue life assessment

4.3.1 Fatigue stress spectrum

As we can know from the previous traffic flow data that the heavy vehicles mainly drive in lane 2 and lane 3 in Haihe Bridge. It can also be seen from the distribution of fatigue cracks that the fatigue damage of the structure under the middle two lanes is more serious than the other. Therefore, lane 2 is selected for fatigue analysis in this paper.

The stress history is obtained by loading the traffic loads on the stress influence surface, then the fatigue stress spectrum of structural details can be obtained by using the rain flow counting method. Figure 19 shows the fatigue stress spectrum of the fatigue-prone details in lane 2 before and after strengthened. It can be seen from the figure that the stress amplitude of each fatigue-prone detail decreased significantly after steel-UHPC reinforcement. Among them, the maximum stress amplitude at the scallop cutout, the

TABLE 3 Fatigue life calculation.

Fatigue-prone details	Annual fatigue damage degree		Fatigue life (years)	
	Before reinforcement	After reinforcement	Before reinforcement	After reinforcement
Scallop cutout	0.063	0.0008	15.87	100
Rib-to-diaphragm joints	0.072	0.0007	13.89	100
Rib-to-deck joints	0.031	0.0001	32.26	100

rib-to-diaphragm joints and the rib-to-deck joints decreased by 60%, 58%, and 86% respectively.

4.3.2 Fatigue life

According to the S-N curve of the Eurocode and the Miner linear cumulative damage criterion theory, the fatigue life of the fatigue-prone details of the steel box girder under lane 2 before and after reinforcement are calculated, as shown in Table 3. The calculation results show that due to the difference in fatigue strength and stress amplitude of each fatigue-prone detail, their probability of fatigue risk is also different. Before reinforcement, the fatigue failure generally appears at the rib-to-diaphragm joints and the scallop cutout, while the fatigue resistance of rib-to-deck is relatively higher. This is also consistent with the bridge detection results. The data in the table also shows that the fatigue life of fatigue-prone details is greatly increased after strengthening, which indicates that this method is indeed effective for improving the fatigue life of bridges.

In addition, the fatigue life calculation results are slightly larger compared with the inspection results, as the actual bridge started to appear fatigue cracks after about 6 years of operation. This is because, on the one hand, during the first 8 years of operation of the bridge it was two-way four-lane traffic as the bridge next to it had not been built, so the traffic flow would be greater. On the other hand, defects cannot be considered in finite element analysis, especially cannot reflect the impact of additional stress concentration caused by penetration welding, which resulting in some errors in the calculation.

5 Conclusion

The fatigue life of OSD strengthened with UHPC under stochastic traffic load is calculated in this paper. A framework for fatigue life assessment of steel bridges based on stochastic traffic flow is proposed. Based on the random traffic data obtained by WIM, the traffic loads are simulated by Monte Carlo method. A refined finite element model was established to obtain the stress influence surface of fatigue-prone details. In summary, the following conclusions are drawn:

(1) Using the statistical parameters such as vehicle weight, vehicle speed and headway obtained from the measured random traffic flow data, the Monte Carlo method can effectively predict the traffic loads during the bridge life cycle.
(2) The evaluation procedures proposed in this paper can effectively predict the fatigue life of the fatigue-prone details on OSD. For the bridge before reinforcement, the fatigue life calculation results of the scallop cutout, rib-to-diagram and rib-to-deck joint are basically consistent with the actual bridge inspection results.
(3) After the steel-UHPC combination reinforcement, the stress amplitude of the bridge structural details is significantly reduced, thus the fatigue life is greatly increased. Under the traffic loads, the original structure appeared fatigue cracks in a relatively short time. After strengthening, the fatigue life of these fatigue-prone details has been extended to more than 100 years (Shao et al., 2022; Li et al., 2023).

Data availability statement

The raw data supporting the conclusion of this article will be made available by the authors, without undue reservation.

Author contributions

JY: conceptualization, methodology, writing—review and editing; MD: writing—original draft, data curation, and calculation. All authors contributed to the article and approved the submitted version.

Funding

This work was conducted with financial support from the Reuter Foundation of Education Bureau of Hunan Province, China (Grant Numbers. 19C0155 and 21B0773); The Natural Science Foundation of Hunan Province, China (Grant Numbers. 2023JJ30080); The Open Fund of National-Local Joint Laboratory of Engineering Technology for Long-term Performance Enhancement of Bridges in Southern District (Changsha University of Science and Technology) (Grant Numbers. 19KF02); the Science and Technology Development Project of Tianjin Municipal Transportation Commission, China (Grant Numbers. 202003); The Science Popularization Special Project on the Construction of Innovation-Oriented Provinces (Grant Numbers. 2021ZK4148).

Conflict of interest

The authors declare that the research was conducted in the absence of any commercial or financial relationships that could be construed as a potential conflict of interest.

Publisher's note

References

Chang, J., Li, J., Hu, H., Qian, J., and Yu, M. (2023). Numerical investigation of aggregate segregation of superpave gyratory compaction and its influence on mechanical properties of asphalt mixtures. *J. Mater Civ. Eng.* 35 (3), 04022453. doi:10.1061/(asce)mt.1943-5533.0004604

Chen, L., Qian, Z., and Wang, J. (2015). Multiscale numerical modeling of steel bridge deck pavements considering vehicle–pavement interaction. *Int. J. Geomech.* 16, B4015002.

Choi, J. H., and Kim, D. H. (2008). Stress characteristics and fatigue crack behaviour of the longitudinal rib-to-cross beam joints in an orthotropic steel deck. *Adv. Struct. Eng.* 11 (2), 189–198. doi:10.1260/136943308784466224

Deng, L., Zou, S., Wang, W., and Kong, X. (2021). Fatigue performance evaluation for composite OSD using UHPC under dynamic vehicle loading. *Eng. Struct.* 232, 111831. doi:10.1016/j.engstruct.2020.111831

Deng, M., Wang, L., Zhang, J., Wang, R., and Yan, Y. (2017). Probabilistic model of bridge vehicle loads in port area based on *in-situ* load testing. *IOP Conf. Ser. Earth Environ. Sci.* 94 (1), 012205. doi:10.1088/1755-1315/94/1/012205

Dieng, L., Marchand, P., Gomes, F., Tessier, C., and Toutlemonde, F. (2013). Use of UHPFRC overlay to reduce stresses in orthotropic steel decks. *J. Constr. Steel Res.* 89, 30–41. doi:10.1016/j.jcsr.2013.06.006

Ding, Y. (2015). *JTG D64-2015. Specifications for design of Highway steel bridge*. Delhi: S.K. Kataria and Sons.

Donnell, E., Ni, Y., Adolini, M., and Elefteriadou, L. (2001). Speed prediction models for trucks on two-lane rural highways. *Transp. Res. Rec.* 1751, 44–55. doi:10.3141/1751-06

Eurocode, C. (1993). *3: Design of steel structures DRAFT prEN*. Brussels, Belgium: European Committee for Standardization.

Fisher, J. W., and Barsom, J. M. (2016). Evaluation of cracking in the rib-to-deck welds of the bronx–whitestone bridge. *J. Bridge Eng.* 21 (3), 04015065. doi:10.1061/(asce)be.1943-5592.0000823

Giray, O., and Ahmet, G. (2011). Generating low-discrepancy sequences from the normal distribution: Box–muller or inverse transform. *Math. Comput. Model* 53 (5-6), 1268–1281. doi:10.1016/j.mcm.2010.12.011

Hu, N., Dai, G. L., Yan, B., and Liu, K. (2014). Recent development of design and construction of medium and long span high-speed railway bridges in China. *Eng. Struct.* 74, 233–241. doi:10.1016/j.engstruct.2014.05.052

Jong, F. B. P. (2007). *Renovation techniques for fatigue crack orthotropic steel bridge decks*. Delft, Netherlands: Delft University of Technology.

Li, J., Zhang, J., Yang, X., Zhang, A., and Yu, M. (2023). Monte Carlo simulations of deformation behaviour of unbound granular materials based on A real aggregate library. *Int. J. Pavement Eng.* 24 (1), 2165650. doi:10.1080/10298436.2023.2165650

Li, Y., Cui, C., and Wang, Y. "Stress distribution of orthotropic steel bridge decks under vehicle wheel loading," in Proceedings of the 19th International Offshore and Polar Engineering Conference. ISOPE, Osaka, Japan, July, 2009.

Lu, N., Yang, L., and Beer, M. (2018). Extrapolation of extreme traffic load effects on A cable-stayed bridge based on weigh-in-motion measurements. *Int. J. Reliab. Saf.* 12 (1/2), 69–85. doi:10.1504/ijrs.2018.092504

May, I. M., Roy, M., and Lang, C. (2015). CFRP for the repair of fatigue cracks in steel structures. *P I Civ. Eng.* 169 (2), 1–15.

Panichpapiboon, S. (2015). The humelock hemiarthoplasty device for both primary and failed management of proximal humerus fractures: A case series. *J. Transp. Eng.* 141, 1–6. doi:10.2174/1874325001509010001

Qin, S., Zhang, J., Huang, C., Gao, L., and Bao, Y. (2022). Fatigue performance evaluation of steel-UHPC composite orthotropic deck in a long-span cable-stayed bridge under in-service traffic. *Eng. Struct.* 254, 113875. doi:10.1016/j.engstruct.2022.113875

Shao, X., Zhao, X., Liu, Q., Deng, S., and Wang, Y. (2022). Design and experimental study of hot rolled shape steel-ultrahigh performance concrete composite beam. *Eng. Struct.* 252, 113612. doi:10.1016/j.engstruct.2021.113612

Socie, S. (1982). Simple rain-flow counting algorithms. *Int. J. Fatigue* 1 (1), 31–40.

Walter, R., Olesen, J. F., Stang, H., and Vejrum, T. (2007). Analysis of an orthotropic deck stiffened with a cement-based overlay. *J. Bridge Eng.* 12 (3), 350–363. doi:10.1061/(asce)1084-0702(2007)12:3(350)

Wang, C., Ou, C., and Zhai, M. "Cold retrofit method study for fatigue cracking of steel bridge," in Proceedings of the IABSE Conference: Structural Engineering: Providing Solutions to Global Challenges, Geneva, Switzerland, September 2015, 1227–1234.

Wang, L., Su, X., Ma, Y., Deng, M., Zhang, J., and Cai, C. (2020). Strengthening of steel decks for cable-stayed bridge using ultra-high performance concrete: A case study. *Adv. Struct. Eng.* 23 (16), 3373–3384. doi:10.1177/1369433220939210

Yan, F., Chen, W., and Lin, Z. (2016). Prediction of fatigue life of welded details in cable-stayed orthotropic steel deck bridges. *Eng. Struct.* 127, 344–358. doi:10.1016/j.engstruct.2016.08.055

Yan, Q., Zhuo, W., and Wang, Z. (2021). Vehicle load model for heavy load and heavy traffic Highway in fujian Province based on weigh-in-motion data. *J. Fuzhou Univ.* 49 (03), 421–427.

Yuan, Y., Wu, C., and Jiang, X. (2019). Experimental study on the fatigue behavior of the orthotropic steel deck rehabilitated by UHPC overlay. *J. Constr. Steel Res.* 157, 1–9. doi:10.1016/j.jcsr.2019.02.010

Zhang, S. H., Shao, X., Cao, J., Cui, J., Hu, J., and Deng, L. (2016). Fatigue performance of a lightweight composite bridge deck with open ribs. *J. Bridge Eng.* 21 (7), 1–16. doi:10.1061/(asce)be.1943-5592.0000905

Zhang, X., Wang, H., Zhang, Y., and Wang, L. (2023). Corrosion of steel rebars across UHPC joint interface under chloride attack. *Constr. Build. Mater* 387, 131591. doi:10.1016/j.conbuildmat.2023.131591

Zhu, Z., Xiang, Z., Li, J., Huang, Y., and Ruan, S. (2019). Fatigue behavior of orthotropic bridge decks with two types of cutout geometry based on field monitoring and FEM analysis. *Eng. Struct.* 209, 109926. doi:10.1016/j.engstruct.2019.109926

frontiers | Frontiers in Materials

TYPE Original Research
PUBLISHED 06 June 2023
DOI 10.3389/fmats.2023.1164693

OPEN ACCESS

EDITED BY
Hui Yao,
Beijing University of Technology, China

REVIEWED BY
Jue Li,
Chongqing Jiaotong University, China
M. N. M. Azlin,
MARA University of Technology, Malaysia

*CORRESPONDENCE
Xu Liu,
sikui2003@outlook.com

RECEIVED 13 February 2023
ACCEPTED 24 May 2023
PUBLISHED 06 June 2023

CITATION
Lan T, Wang B, Zhang J, Wei H and Liu X (2023), Utilization of waste wind turbine blades in performance improvement of asphalt mixture.
Front. Mater. 10:1164693.
doi: 10.3389/fmats.2023.1164693

Utilization of waste wind turbine blades in performance improvement of asphalt mixture

Tianhui Lan[1], Bingze Wang[1,2], Junchao Zhang[1,2], Hao Wei[1,2] and Xu Liu[3]*

[1]School of Civil and Transportation Engineering, Hebei University of Technology, Tianjin, China, [2]Jingxiong Highway Preparatory Office, Department of Transportation of Hebei, Baoding, China, [3]Fundamental Research Innovation Center, Research Institute of Highway, Ministry of Transport, Beijing, China

Redundant wind turbine blades (WTBs) retired from wind power facilities produce substantial waste annually and induce challenging environmental problems. As the most widely used materials for high-grade pavement construction, asphalt mixtures must have excellent high- and low-temperature performance, as well as water damage resistance, since pavement is subjected to complex loading, temperature, and humidity changes. This study proposed an asphalt mixture with the addition of two types of recycled WTB (rWTB): rWTB powders of granular sizes below 0.075 mm and rWTB fibers in the size range of 0.075–9.5 mm. First, the thermogravimetric analysis results indicated the accepted thermal stability of rWTB material for the requirement of compaction, paving, and service condition of asphalt mixtures. Second, the properties of the asphalt mixtures modified by using (i) rWTB powder (5 wt%, 10 wt%, and 15 wt% in fine filler), (ii) rWTB fiber (0.1 wt%, 0.2 wt% and 0.3 wt% in fine aggregate), and (iii) both rWTB powder and fiber were investigated by wheel tracking tests at 60°C, three-point bending tests at −10°C, and Marshall immersion tests. The experimental results showed that the rWTB asphalt mixtures could improve the overall road performance of asphalt mixtures, and that an optimal pavement performance could be obtained by the synergistic addition of rWTB powder and fiber. In addition, it was indicated that the improving mechanism of the rWTB material on the asphalt mixture was mainly attributed to its good compatibility with the asphalt binder, allowing the rWTB to strengthen asphalt mortar and improve the high- and low-temperature performance of the asphalt mixture.

KEYWORDS

asphalt mixture, highway performance, dynamic stability, Marshall stability, redundant wind turbine blade

1 Introduction

Wind power is the most important clean energy. The installed capacity of wind energy is dramatically increased with the rising demand of clean energy, with which the number and length of wind turbine blades (WTBs) are both substantially raised. However, the designed service life of a wind turbine is 20–25 years, leading to a vast number of decommissioned products each year (Jensen and Skelton, 2018). The WTB waste is estimated to reach more than 2 million tons by 2050 (Liu and Barlow, 2017). The majority of raw materials for wind turbine blades are made of glass fiber reinforced plastics (GFRPs) that consisted of 60%–70% of fiber and 30%–40% of cross-linked thermoset polymer formed in an irreversible process,

increasing the reclaiming difficulty (Morales et al., 2020). Currently, the most mature recycle technique is mechanical crushing, through which the size of end-of-life WTB articles is decreased progressively, and the recyclates in the various shapes are obtained, mostly in the form of fiber and powder (Majewski et al., 2022). With the mechanical crushing, the practical reuse of recycled WTB (rWTB) or the recycled GFRP (rGFRP) portion of rWTB has become another major focus of research. The mechanically recycled GFRP has been used as fiber reinforcement or fillers in the production of artificial wood (Demura et al., 1995), block/sheet molded materials BMC/SMC (Pickering, 2006; Palmer et al., 2009), wood–plastic board (Conroy et al., 2006), and rubber pavement blocks (Itoh and Kaneko, 2002). To improve the value and consumption of reuse, scholars further explored the application of rGFRP in composites (Mamanpush et al., 2018), concrete (Asokan et al., 2010), and asphalt mixture (Qiaoet al., 2020).

The reuse of rWTB is more complex, due to the highly composited properties of WTB containing various materials, including polymer foams, balsa wood, and metals (Jensen and Skelton, 2018). Beauson et al. (2016) applied the shredded composite (SC) from WTBs in new thermoset composites and found that chemical treatments of SC were necessary for improving its adhesion with the resin matrix (Beauson et al., 2016). The glass fiber below 0.4 mm length was reclaimed from the waste wind turbine blades and pelletized with polylactic acid (PLA) to produce recycled glass fiber reinforced filament (RGFRF) for 3D printing. The Young's modulus of the 3D-printed RGFRF was 8% higher than that of pure PLA (Rahimizadeh et al., 2019). The application of rWTB or rGFRP in concrete is the mostly studied topic, which focused on the influences of the size, contents, and shapes on the workability and mechanical properties of concrete (Asokan et al., 2009; García et al., 2014; Mastali et al., 2016; Zhou et al., 2021). The rGFRP fiber and powder are separately used in concrete as fiber reinforcement and filler, respectively. In most research, the mechanical strength of concrete can be improved by the addition of recycled fiber, especially when the fibers are properly classified and appropriate additives are added to modify the workability (Rodin et al., 2018; Zhou et al., 2021). However, chemical treatment is necessary to improve the alkaline resistance of the recycled GFRF fiber for longer durability of the reinforced concrete (Kimm et al., 2020). On the other hand, the addition of rGFRP powder with proper treatment at appropriate content could slightly increase the compressive and flexural strengths of concrete, while the problem of excessive fresh-state expansion or drying shrinkage is still concerned due to the ultrafine particle size, lightweight nature, and high content of metallic oxide residues (Asokan et al., 2010; Tittarelli and Shah, 2013; Farinha et al., 2019).

Asphalt mixture is the most important engineering material for high-grade pavement, which faces the challenge of various and frequently occurring early diseases, e.g., rutting, cracks, and water damage, seriously limiting the service life of the pavement structure (Gu et al., 2015; Wang et al., 2016). To solve these problems, the high- and low-temperature performance of asphalt mixture is improved by adding polymer modifiers to the binder, such as SBS, SBR, and EVA (Lu et al., 2003; Yildirim, 2007; Sengoz and Isikyakar, 2008) and adding various reinforcements to asphalt mixture, including basalt fiber, glass fiber, waste tires, and waste glass powder materials (Cao, 2007; Abtahi et al., 2010). It was found that adding fiber with appropriate size can effectively improve the rheological properties of asphalt mixture at different temperatures and the flexural strength under medium- and low-temperature conditions (Wu et al., 2007; Wu et al., 2008; Morea and Zerbino, 2018). In addition, the mesoscopic composition of the aggregate skeleton and the geometric shape of the particles will affect the damage development and deformation behavior of asphalt material (Wang et al., 2019; Li et al., 2023). The mining and production costs of gravel aggregates and mineral fillers, with huge consumption in road engineering, are continuously increasing due to the impact of environmental protection factors. These years, many scholars have begun to focus on the use of recycled materials to improve the performance of mixtures from multiple scales. Yang et al. recycled WTB chips from the components of airplane cabins and investigated the effects of crushed chips on the performance of bitumen. Since the bridging function and specific pull-out behavior of the WTB chips, the stiffness, rutting resistance, low-temperature cracking resistance, and water resistances of bitumen were all increased, with the optimum diameter of 0.5–0.71 mm, length of 10–12 mm, and mass content of 5% (Qiaoet al., 2020). Followed by this study, Jin et al. processed the recycled WTB into powders to partially replace limestone filler in asphalt mortars. The recycled WTB powder improved the medium-to high-temperature performance and anti-aging property of the asphalt mortars, while decreased the resistance to low-temperature cracking (Lin et al., 2022). However, the synergistic utilization of recycled fiber and powder for asphalt mixture to against rutting and cracking has never been explored.

In this study, the recycled WTB (rWTB) powder and fiber were added to partially replace the fine filler (<0.075 mm) in asphalt mortar and fine aggregates (0.075–9.5 mm) in the asphalt mixture. The effect of the content of the rWTB powder (5 wt%, 10 wt%, and 15 wt%) and that of rWTB fiber (0.1 wt%, 0.2 wt%, and 0.3 wt%) on the high-temperature rutting, low-temperature cracking resistance, and water stability was evaluated with wheel tracking tests (WTTs) at 60°C, three-point bending tests at −10°C, and Marshall immersion tests, respectively. In addition, the rWTB powder and fiber were added to synergistically modify the viscoelastic properties of asphalt mortar and the macro-performances of the asphalt mixture. Furthermore, the microstructure of the asphalt mixture was characterized to investigate the reinforcing mechanism of the rWTB fiber. The findings in this study were beneficial for developing new techniques to reuse the WTB wastes and sustainable reinforcing materials for extending the service life of the asphalt pavement.

2 Materials and methods

2.1 Materials and sample preparation

2.1.1 rWTB fiber and powder

The rWTB materials were obtained by cutting, crushing, and grinding the waste WTB, as shown in Figures 1A, B. Based on sieve analysis (Figure 1E), the rWTB materials were classified into powder (remained on 0.075-mm mesh) and fiber (passed 0.075-mm mesh). The rWTB powder mainly consisted of small resin particles and short glass fiber, and the rWTB fiber consisted of rod-like glass fiber bundle partially wrapped with epoxy resin and a small amount of

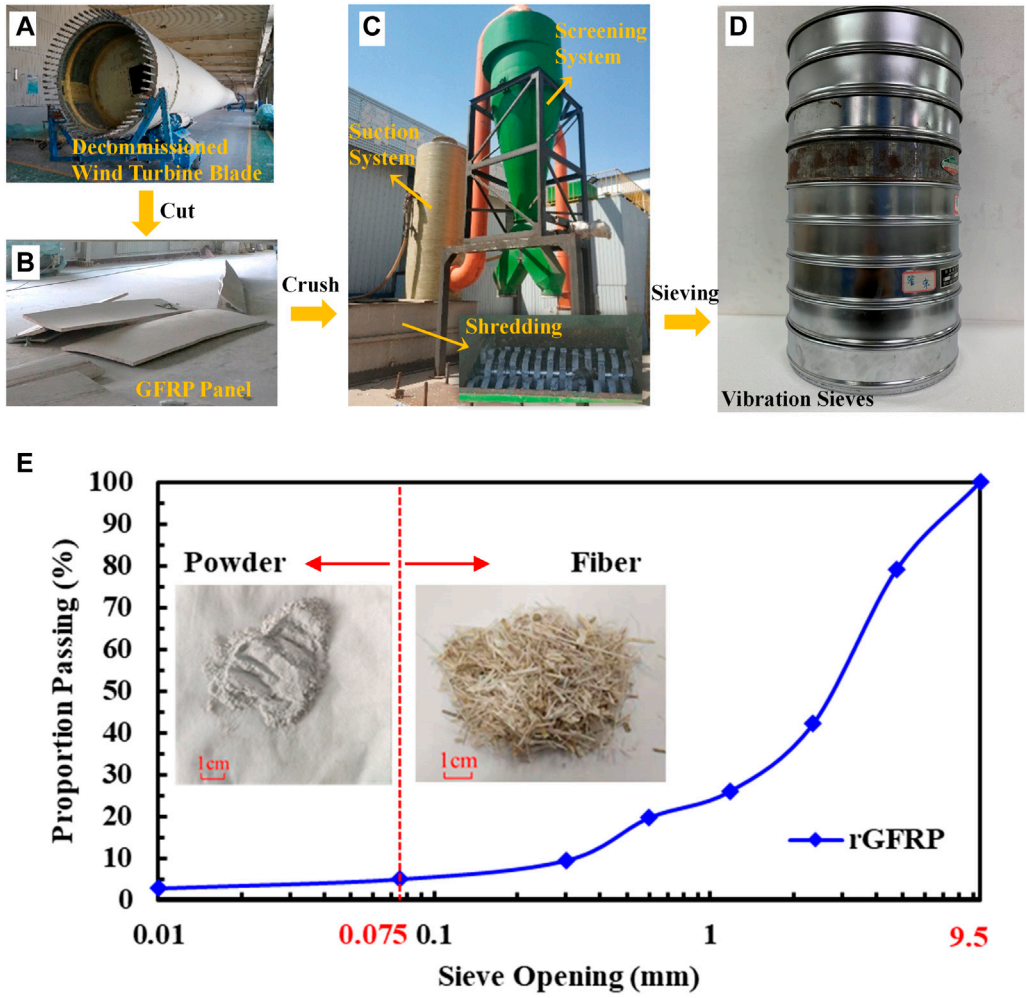

FIGURE 1
Images of **(A)** decommissioned turbine blade, **(B)** cut WTB panel, **(C)** crushing equipment, **(D)** vibration sieves, and **(E)** particle size distribution of rWTB.

TABLE 1 Chemical Composition of rWTB powder.

Chemical composition	Na_2O	MgO	Al_2O_3	SiO_2	ZnO	CaO	Fe_2O_3	Loi
wt%	0.38	2.00	11.10	48.40	0.03	29.80	5.53	2.52

wood fiber, as shown in Figure 1E. The inorganic oxide composition of the rWTB was determined via X-ray florescence (XRF), as tabulated in Table 1, which mainly consisted of SiO_2 and CaO, since the GFRP portion of WTB was made of glass fiber, resin (i.e., epoxy resin and butyral resin), and auxiliary materials (i.e., calcium carbonate and talcum powder (Seydibeyoglu et al., 2017)).

2.1.2 Asphalt binder

SBS-modified asphalt with a penetration grade of 70 was adopted in this study. Its basic performance indices, including penetration, ductility, and softening point, obtained through the ASTM standards are listed in Table2.

TABLE 2 Performance indices of the asphalt binder.

Index	SBS-modified asphalt	Specification
Penetration (25°C)	67.0	ASTM D5
Ductility (5°C, 5 cm/min)	32.0	ASTM D113
Ductility (15°C, 5 cm/min)	>100	ASTM D113
Softening point	75.0	ASTM D36

2.1.3 Asphalt mixtures

In this study, the rWTB fiber and powder were engaged in the design of asphalt mixture. Table 3 shows the aggregate gradation of all

TABLE 3 Aggregate gradation of asphalt mixtures.

Sieve size (mm)	Percentage passing (wt%)
26.5	100
19	92.8
16	86.5
13.2	76
9.5	61
4.75	41.3
2.36	28.6
1.18	20
0.6	14.6
0.3	9.6
0.15	7.1
0.075	4.7
0	0

the mixtures. The mass proportion of the asphalt binder to the mixture was 5.3%, obtained according to the Marshall method (ASTM D6927).

Three asphalt mixture experimental groups (GXP, GXF, and GXFP) were prepared in this study to verify the feasibility of incorporating rWTB materials in asphalt mixtures and investigate their impact on pavement performance under different content ratios. In the mixture design, the mineral filler (<0.075 mm) was partially replaced by the rWTB powder with the mass ratios of 5%, 10%, and 15%, and the aggregate under 9.5 mm was replaced with the rWTB fiber in three levels of 0.1%, 0.2%, and 0.3%. As illustrated in Table 4, the group labels of GXP and GXF represent the asphalt mixture containing rWTB powder and rWTB fiber, respectively, and the third group of GXFP indicates that both powder and fiber were used.

Three types of samples with different dimensions were prepared with the asphalt mixtures, as listed in Table 4, for WTT (300 mm × 300 mm × 50 mm panel), three-point bending tests (250 mm × 30 mm × 35 mm beam), and Marshall immersion tests (Φ101.6 × 63.5 mm cylinders). The asphalt binder was placed in the temperature-controlled chamber at 165°C for at least 2 h, and the fine powder, fine aggregates, and coarse aggregates were heated in an oven at 180°C for at least 4 h before sample preparation. The asphalt binder, fine filler, and aggregates were mixed at 170°C according to the mix design shown in Tables 3, 4. The 300 mm × 300 mm × 50 mm panels were prepared by the rolling method using an asphalt mixture rut sample-forming machine. The 250 mm × 30 mm × 35 mm beams were cut from the rut panels, and the Φ101.6 × 63.5 mm cylinders were prepared by using the compacting method.

2.2 Experiments

Laboratory tests were conducted to characterize the physicochemical properties of rWTB and determine the resistance of the rWTB-modified asphalt mixture to high-temperature rutting, low-temperature cracking, and water stability.

2.2.1 SEM analysis

The micromorphology of rWTB powder, fibers, and the corresponding asphalt mortar was imaged using an environmental scanning electron microscope, Quanta 450 FEG, to explore the reinforcing mechanism of the rWTB fiber and powder.

2.2.2 Thermogravimetric analysis

Since the compaction, paving, and service conditions of asphalt mixtures require high-temperature conditions, a thermogravimetric (TG) analysis was performed using a simultaneous thermal analyzer, TA SDT650 DSC/TGA system, to further investigate the thermal stability of rWTB materials and the feasibility of incorporating

TABLE 4 Asphalt mixture group information.

Material	Group	Mineral powder (<0.075 mm)	WTB powder (<0.075 mm) (%)	WTB fiber (0.075–9.5 mm) (%)
		Mass percentage of corresponding size range		
GX	Mineral powder	100%		
GXP-5%	WTB powder	95%	5	
GXP-10%		90%	10	
GXP-15%		85%	15	
GXF-0.1%	WTB fiber	100%		0.1
GXF-0.2%		100%		0.2
GXF-0.3%		100%		0.3
GXFP-0.1%	WTB powder and fiber	95%	10	0.1
GXFP-0.2%		90%	10	0.2
GXFP-0.3%		85%	10	0.3

GX, 100% mineral powder; GXP-5%, GXP-10%, and GXP-15% representing the rWTB powder replacement ratios of 5%, 10%, and 15% in fine filler; GXF-0.1%, GXF-0.2%, and GXF-0.3% representing the rWTB fiber replacement ratios of 0.1%, 0.2%, and 0.3% in aggregate (0.075–9.5 mm); GXFP-0.1%, GXFP-0.2%, and GXFP-0.3% representing the rWTB powder replacement ratios of 10% in fine filler and the rWTB fiber replacement ratios of 0.1%, 0.2%, and 0.3% in aggregate.

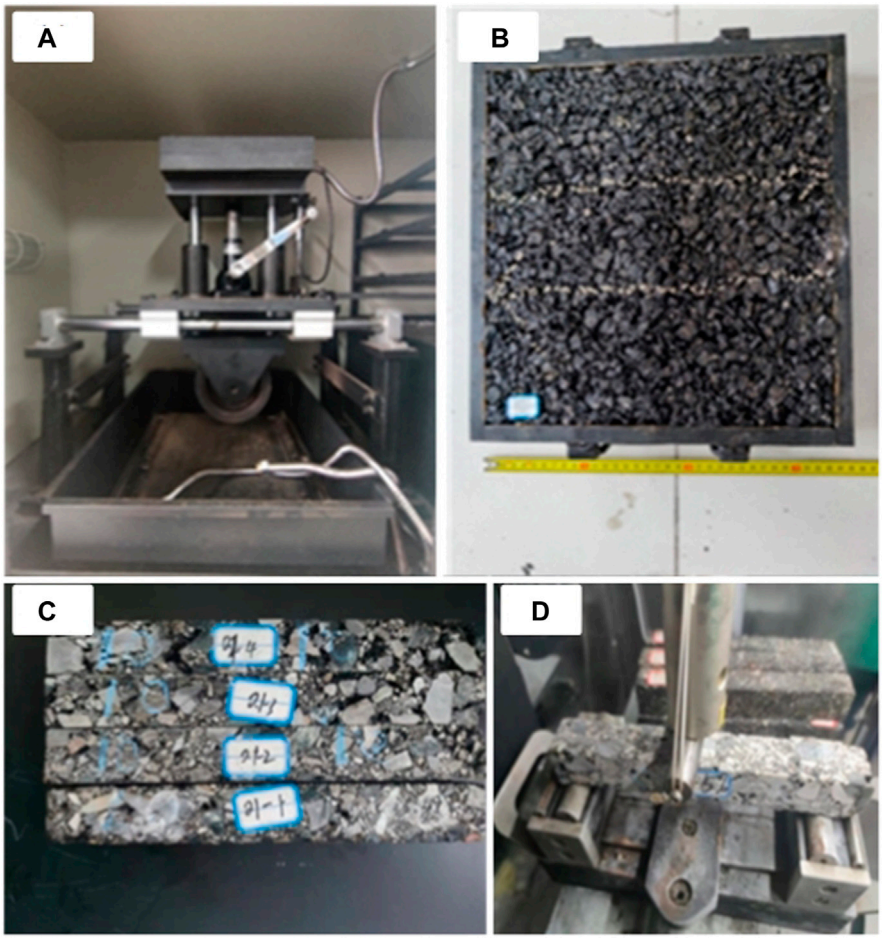

FIGURE 2
Images of **(A)** the WTT sample preparation process, **(B)** WTT sample panel, **(C)** beam sample, and **(D)** three-point bending tests of asphalt mixtures.

rWTB materials in asphalt mixtures, through the obtained TG curve, differential thermogravimetric (DTG) curve, and differential scanning calorimetry (DSC) curve. The rWTB particle sample was exposed to N_2, with the testing temperature range of 0–1,000°C and at the heating rate of 20°C/min.

2.2.3 Wheel tracking test

The resistance to high-temperature rutting of rWTB asphalt mixtures was investigated by the WTT with the dynamic stability (*DS*) value under 60°C as an indicator of mixture properties. A SYD-0719A Wheel Rutting Tester was used in this test, and more than three specimens for each mixture group were prepared before testing. The WTT specimens were subjected to repeated axle loads of 0.7 MPa at a rate of 42 passes/min, as shown in Figures 2A, B, while the *DS* was calculated according to Eq. 1 (JTG E20-2011):

$$DS = \frac{V \times (t_2 - t_1)}{d_2 - d_1}, \quad (1)$$

where V is the repeated loading rate of 42 passes/min; t_1 and t_2 are the two time nodes during loading, which are 45 min and 60 min, respectively; and d_1 and d_2 are the vertical rutting deformation values corresponding to t_1 and t_2, respectively, in mm.

The mean value was obtained through three parallel tests conducted for each asphalt mixture group to evaluate their resistance to high-temperature rutting.

2.2.4 Three-point bending test

The resistance of asphalt mixtures to low-temperature cracking was investigated by three-point bending tests.

Five beam specimens for each mixture group were prepared in this test. The beam specimens were loaded using a universal testing machine (IPC UTM-100) at a temperature of −10°C. The loading process is illustrated in Figures 2C, D. The load P_B (N) and the corresponding displacements d were recorded during the loading process at a speed of 50 mm/min until the beam cracked. The bending tensile strength R_B (MPa) and the failure strain ε_B (10^{-6} mm/mm) of the samples were calculated according to Eqs 2, 3:

$$R_B = \frac{3LP_B}{2bh}, \quad (2)$$

$$\varepsilon_B = \frac{6hd}{L^2}, \quad (3)$$

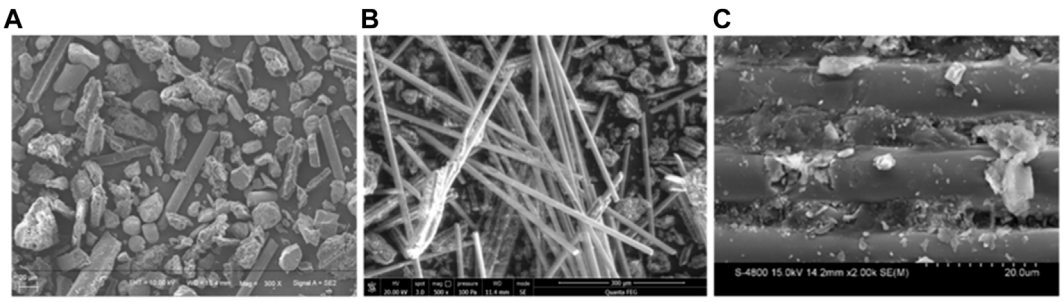

FIGURE 3
SEM images of **(A)** rWTB powder, **(B)** rWTB fiber, and **(C)** ×2000 magnification of the surface morphology of rWTB fibers.

where b and h are, respectively, the width and height of the mid-span sections of the beams, in mm; and L is the span of the beam specimens, in mm.

All the beam specimens were placed in the environmental chamber of the UTM at a temperature of −10°C for over 5 h prior to testing. The mean value was obtained based on the results of five parallel tests conducted for each asphalt mixture group to determine their resistance to low-temperature cracking.

2.2.5 Marshall immersion test

The Marshall immersion test was conducted to measure the resistance of asphalt mixtures to moisture damage. A WSY-101 Marshall Stability Tester was used in this test, and more than three specimens for each mixture group were prepared before testing. The Marshall stability results obtained after 48 h of immersion of the samples in water, which was conducted according to the standard Marshall test (ASTM D6927). The residual stability (*RS*) for each specimen was calculated according to Eq. 4:

$$RS = \frac{MS_1}{MS} \times 100\%, \quad (4)$$

where MS_1 is the Marshall stability value after 48 h of immersion in water; and MS is the Marshall stability value obtained using the standard Marshall test. Three sets of parallel tests were conducted for each mixture group, and the mean value was calculated for analysis.

3 Results and discussion

3.1 Characterization of rWTB

3.1.1 Microstructure

The microstructure images of rWTB powder are shown in Figure 3. The rWTB powder mainly consisted of ground resin particles and short glass fibers, with the particles presenting an angular and irregular surface and relatively uniform size and morphology. The rWTB fiber mixture consisted of a high proportion of glass fibers and a smaller proportion of resin particles. It contained lots of rod-like glass fibers with different sizes and directions in a spatial arrangement and fiber clusters wrapped or bonded together by resin.

3.1.2 Thermal stability

The heat stability of the rWTB particles was assessed with thermogravimetric analysis using TG, DTG, and DSC curves to ensure that rWTB would not be decomposed under the high-temperature condition during compaction and paving.

The TG curve can characterize the mass loss of the rWTB specimen with the increase of temperature, and the DTG curve represents the corresponding speed rate of mass loss. As shown in Figure 4, according to the TG and DTG curves of the rWTB powder, a significant weight loss of the sample occurred in the temperature range from 300°C to 450°C, peaking at approximately 350°C, which was due to the pyrolysis of epoxy resin. In addition, there was also an obvious mass loss at approximately 500–600°C, which was due to the oxidation of pyrolysis residual carbon in the air. Moreover, combined with the DSC curve, it can be found that the two peaks in the DTG curve presented an exothermic process, and the more severe one appeared at approximately 600°C, indicating the large energy absorbed by the rWTB for the decomposition of epoxy resin.

On the other hand, the weight loss of rWTB below 200°C was small and basically reflected in the TG curve with a level or near-plateau trend, illustrating the accepted stability for the construction of an asphalt pavement. Consistently, the energy change in the temperature range of 0–200°C was negligible, as shown in the DSC curve, illustrating almost no matter was decomposed below 200°C.

3.2 Performance analysis of rWTB mixtures

3.2.1 High-temperature performance

The dynamic stability values of the 10 rWTB asphalt mixtures are shown in Figure 5 to comprehensively compare the impact of adding rWTB powder, fiber, and a mixture of both on the resistance to high-temperature rutting.

As shown in Figure 5A, the GXP samples with the sole addition of the rWTB powder (GXP-5%, GXP-10%, and GXP-15%) attained higher dynamic stability values than those of the GX specimens. The *DS* value rose remarkably in the GXP-5% and GXP-10% samples by 13.8% and 22.4%, respectively, while the *DS* value in the GXP-15% sample rose only slightly by 6.9%. This indicated that the partial replacement of mineral powder

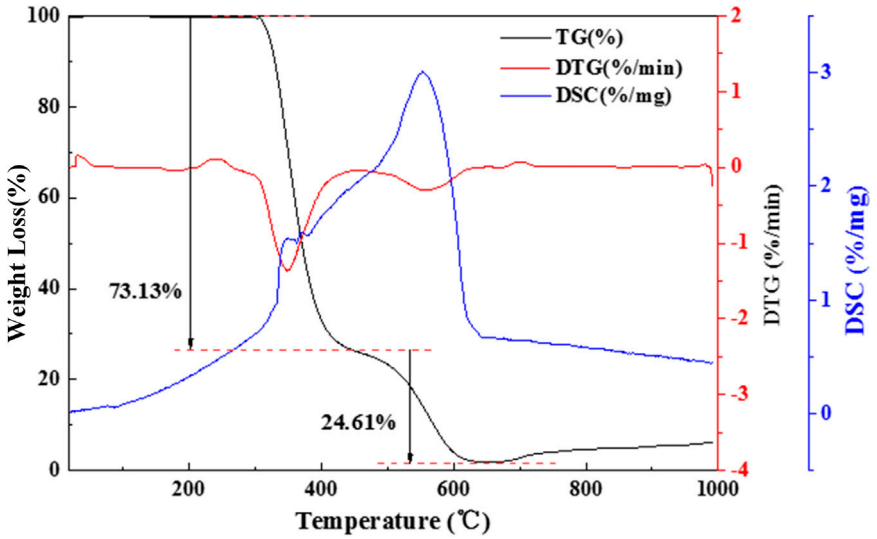

FIGURE 4
TG, DTG, and DSC curves of rWTB.

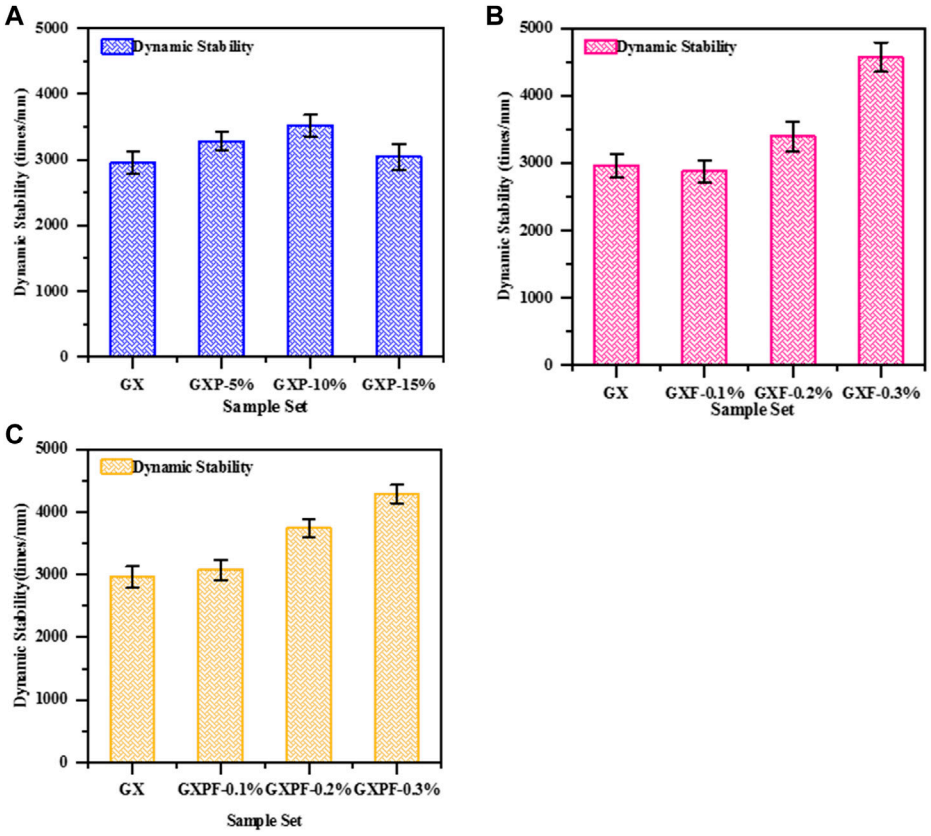

FIGURE 5
Dynamic stability of mixtures with **(A)** rWTB powder, **(B)** rWTB fiber, and **(C)** the combination of both rWTB powder and fiber.

with rWTB powder improved the resistance to high-temperature rutting of asphalt mixtures, with the optimal ratio near 10%.

The dynamic stability values of the GXF samples with the sole addition of rWTB fiber also significantly increased compared to those of the GX samples. Unlike the findings of the GXP samples, the

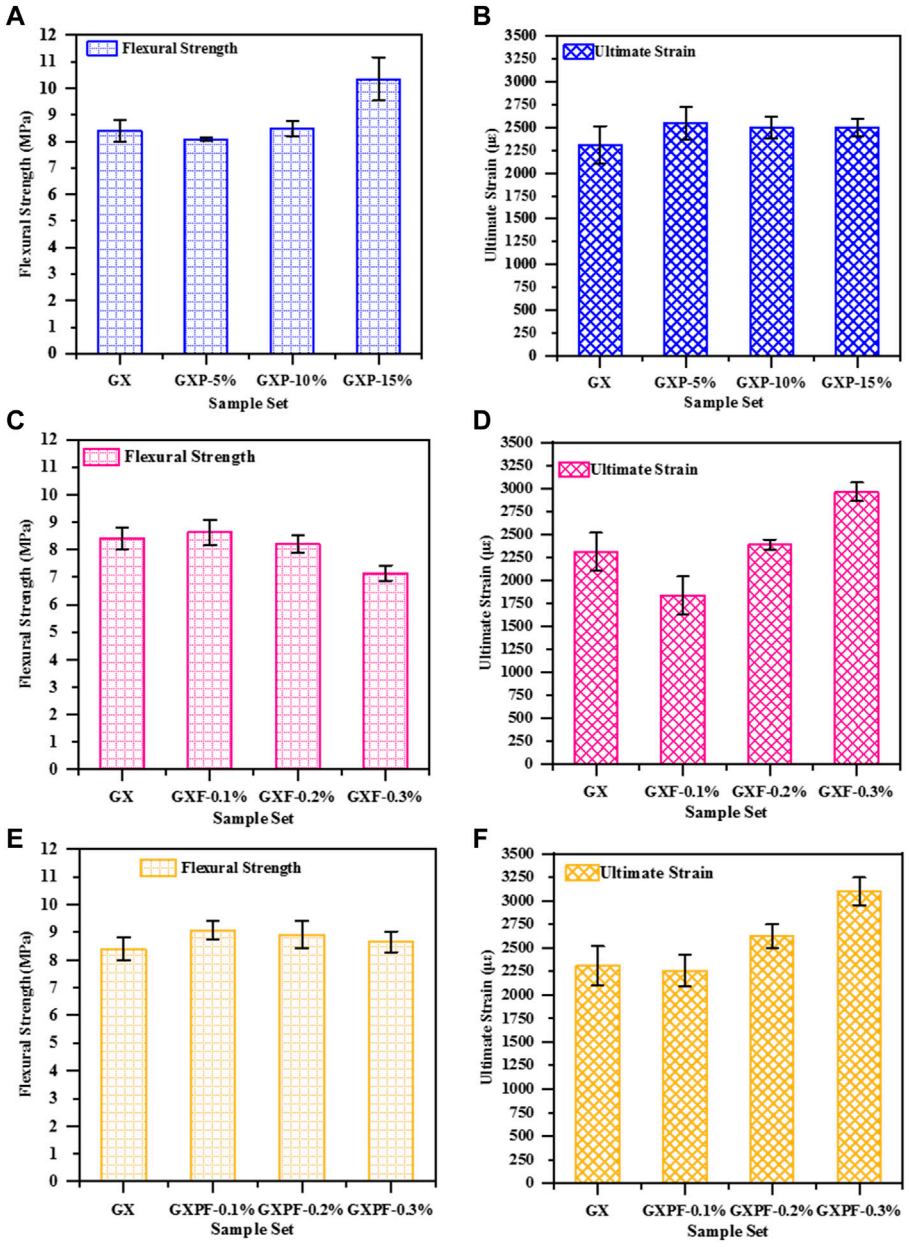

FIGURE 6
Flexural strength and ultimate strain of the asphalt mixture with the addition of **(A)** and **(B)** rWTB powder, **(C)** and **(D)** rWTB fiber, and **(E)** and **(F)** the combination of both rWTB powder and fiber.

high-temperature rutting resistance of the GXF samples was found to rise progressively as fiber was added. In particular, the *DS* value of GXF-0.1% was close to that of the GX sample, while the *DS* values of the GXF-0.2% and GXF-0.3% mixtures increased by 17.2% and 54.4%, respectively, compared to those of the GX sample. This indicated that the addition of rWTB fiber to aggregates ranging from 0.075 mm to 9.5 mm can enhance the resistance of asphalt mixtures to high-temperature rutting.

The *DS* value of the GXFP samples gradually rose as rWTB powder and fiber were synergistically added, with the GXFP-0.3% mixture achieving the highest increasing rate of 44.5%. Compared to the results of the GXF samples with the sole addition of fiber, it was indicated that the *DS* values of the asphalt mixtures with the addition of 0.1% and 0.2% fiber of a size range of 0.075–9.5 mm were further improved with the addition of rWTB powder. This elucidated that the asphalt mixtures with the synergistic addition of rWTB powder and fiber, which modified and improved the materials in multiple scales, had the most significant enhancement of performance under high-temperature conditions.

3.2.2 Low-temperature performance

The flexural strength and ultimate strain of the asphalt mixtures with different contents of rWTB fiber and powder under low-temperature conditions were compared as shown in Figures

6A–C. Compared to that of the GX sample, as shown in Figure 6A, the flexural strength of the GXP-5% and GXP-10% samples did not increase significantly. In contrast, the flexural strength of the GXP-15% specimen rose by 20% compared to that of the GX sample as more rWTB powder was added. On the other hand, the flexural strength of the asphalt mixtures did not improve with the addition of rWTB fiber in the size range of 0.075–9.5 mm, and the flexural strength of GXF-0.3% diminished as more fiber was added compared to that of the GX sample. In addition, a slight increase in the flexural strength was observed in the GXFP samples with the synergistic addition of rWTB powder and fiber, which were approximately 9.5%, 7.1%, and 4.8% for GXFP-0.1%, GXFP-0.2%, and GXFP-0.3%, respectively. In summary, the test results indicated that adding rWTB powder with particles below 0.075 mm in size could increase the flexural strength of the asphalt mixture, while the excessive addition of rWTB fiber in the size range of 0.075–9.5 mm had adverse influence on the flexural strength.

The ultimate strain of asphalt mixtures had also been selected as an important indicator in this study to measure the resistance of the materials to low-temperature cracking. As shown in Figures 6B, D, F, the ultimate strain of GXP-5%, GXP-10%, and GXP-15% rose by approximately 10% compared to that of the GX sample, with no significant fluctuation when more powder was added. For the rWTB fiber mixtures GXF-0.1%, GXF-0.2%, and GXF-0.3%, the ultimate strain increased with the addition of rWTB fiber in the size range of 0.075–9.5 mm. In particular, the ultimate strain of GXF-0.3% mixture increased by 28.2% compared to that of GX, indicating that adding a certain amount of rWTB fiber to the asphalt mixture can enhance the resistance to cracking by a higher strain tolerance. Meanwhile, the ultimate strain of the asphalt mixtures with synergistic addition of powder and fiber, i.e., GXFP-0.1%, GXFP-0.2%, and GXFP-0.3%, was further improved, and the ultimate strain was increased with the increase in fiber content, presenting the result that GXFP-0.3% showed the highest increase of 34.2% compared to GX.

In conclusion, the addition of rWTB powder and fiber in corresponding increments was found to improve the performance of asphalt mixtures under low-temperature conditions, according to the results of the flexural strength and ultimate strain results. Specifically, the addition of rWTB powder could impact the asphalt mortar and the binding between the mortar and aggregates and could further improve the flexural strength of asphalt mixtures, which depended on the added proportion. In addition, adding rWTB fiber of a larger grade range could improve the capacity of asphalt mixtures to withstand a larger deformation by its strengthening effect of the rod-like structure, which enhanced the stability of the materials. Moreover, the synergistic addition of rWTB powder and fiber to the mixtures had the most significant improvement of the performance of the asphalt mixture.

Combined with the results of the high-temperature rutting test, it can be found that the influence of the adding amount of rWTB powder or fiber on the road performance at different temperatures was consistent. This result indicated that both rWTB powder and fiber effectively strengthened the overall structure of the asphalt mixture on the mesoscopic scale, and this reinforcement can improve the high-temperature and low-temperature performance of the asphalt mixture at the same time, which was the critical precondition to having a longer service life of pavement structures.

3.2.3 Moisture damage

The water stability of asphalt mixtures is one of the key indexes for measuring pavement performance. Figures 7A–C present the test results of the Marshall stability (*MS*), Marshall immersion stability (MS_1), and the residual stability (*RS*) of the GXP, GXF, and GXFP sample groups.

The Marshall stability MS of the three rWTB powder mixtures (GXP-5%, GXP-10%, and GXP-15%) was decreased compared with that of the GX sample based on the standard Marshall test. Among the mixtures of the GXP group, the MS value of GXP-10% was the highest and attained a similar value to that of the GX sample. In addition, the *RS* values of the GXP samples after immersion in water for 48 h were all approximately 90% of the GX sample, and the *RS* value of GXP-10% was the highest (94.1%). To summarize, adding rWTB powder did not significantly reduce the water stability of the asphalt mixture.

In contrast, the test results of rWTB fiber mixtures GXF-0.1%, GXF-0.2%, and GXF-0.3% differed greatly from those of the GXP group, as shown in Figure 7B. The MS value of GXF-0.2% and GXF-0.3% mixtures increased by nearly 10% compared to that of the GX sample, while the *RS* values of the two mixtures decreased significantly as more rWTB fiber was added after the immersion in water for 48 h. Although the GXF-0.3% mixture maintained the highest *MS* value, its *RS* value became the lowest (70.3%) after water immersion. In addition, the *MS* value of the GXFP sample group GXFP-0.1%, GXFP-0.2%, and GXFP-0.3% presented in Figure 7C was similar to that of the GX sample and rose with the increase in the addition of fiber. On the other hand, the MS_1 values of the three GXFP samples were also close but slightly lower than those of the GX sample and the GXFP group with the highest fiber content (0.3%) obtained the lowest *RS* value (80.2%), which presented a lower reduction to the results of the GXF sample group.

The experimental results comprehensively showed that no distinctive loss of the *RS* value or rise of the *MS* value was identified in asphalt mixtures with the addition of rWTB powder. In contrast, the addition of rWTB fiber effectively increased the *MS* value, while significantly reduced the *RS* value after water immersion. This indicated that the addition of rWTB fiber in the size range of 0.075–9.5 mm could reduce the water stability of the mixture, and that the synergistic addition of fiber and powder could decrease the loss of water stability.

3.3 Microscopic analysis of asphalt mortar

In order to further investigate the modification mechanism of the rWTB asphalt mixtures from the test results of high-temperature rutting, low-temperature cracking, and water stability, the microscopic combination mode of rWTB and asphalt binder on the microscopic scale was characterized by SEM. The micromorphology of the cross sections of asphalt mixtures with 0.3% rWTB was imaged by SEM at 500 μm, 100 μm, and 30 μm, as shown in Figure 8A–C, respectively. It was revealed that the rWTB fiber is fully wrapped in a cluster by the asphalt mortar. No obvious breaks in the fiber were found at the cracks of the mixture, indicating that damage to fiber was mainly resulted from peeling under stress, which affected the strain behavior of fiber in the asphalt mixtures.

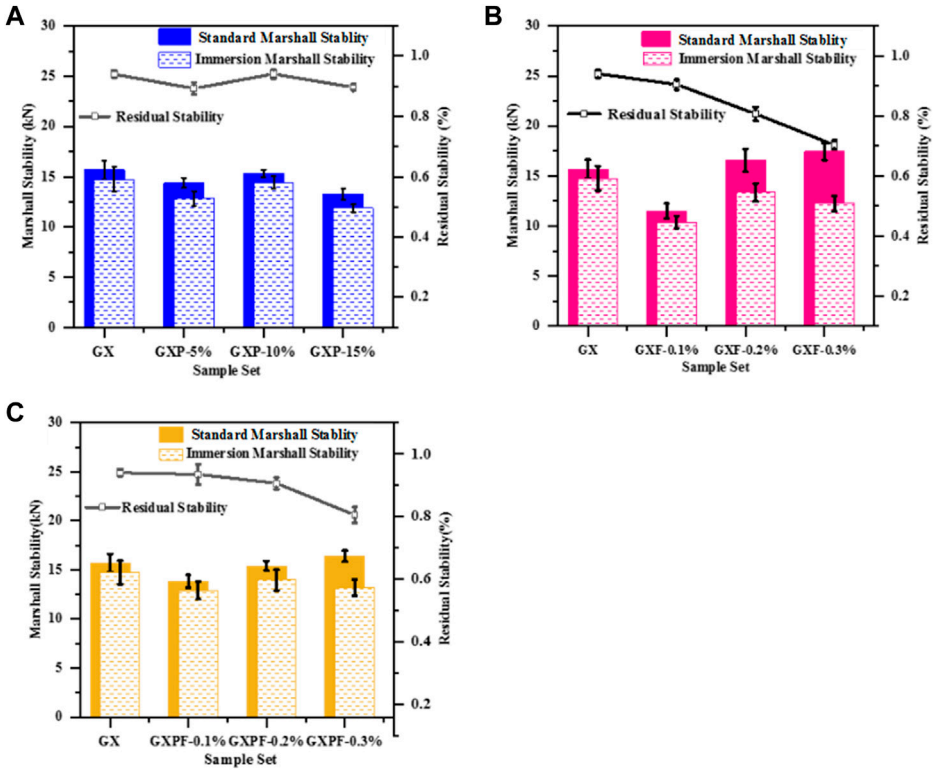

FIGURE 7
Marshall stability and residual stability of the asphalt mixtures with the addition of **(A)** rWTB powder, **(B)** rWTB fiber, and **(C)** the combination of both rWTB powder and fiber.

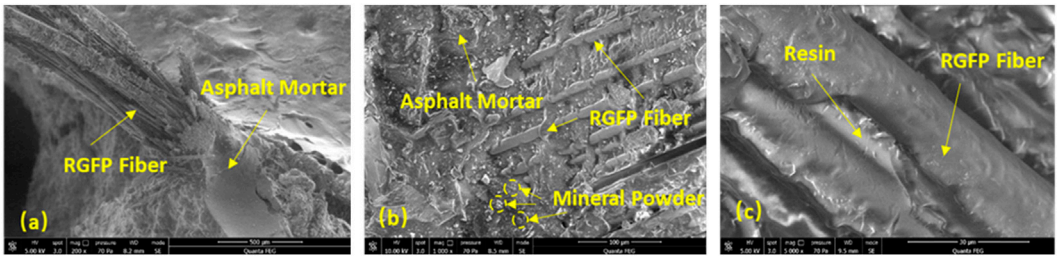

FIGURE 8
Microstructure of the asphalt mortar with rWTB fiber at magnifications of **(A)** 500 μm, **(B)** 100 μm, and **(C)** 30 μm.

As illustrated in Figure 8B, a complete interface and tight bond between the fiber and mortar was found, illustrating that the fiber could transfer the load and disperse the stress over the asphalt mixture by bridging the asphalt mixture, as well as improve its strength and resistance to deformation under low-temperature conditions. In Figure 8C, the asphalt binder has good compatibility with the resin, which can improve the dispersity of the rWTB fiber in the asphalt mortar and the formation of a uniform system between asphalt mortar and rWTB fiber. This improved the viscoelasticity of the modified asphalt mortar, thus enhancing the resistance to high-temperature rutting of asphalt mixtures.

To summarize, the performance test results of asphalt mixtures and microscopic characterization of rWTB powder and fiber elucidated that the good compatibility existed between rWTB materials and asphalt binder and that utilizing this advantage could effectively enlarge the specific surface area of fine fillers and small size aggregates within the mixture. As a result, the high stiffness of rWTB fiber can effectively improve the high-temperature rutting performance and ultimate flexural strain of asphalt mixtures through the bridging effect. However, the utilization of fiber was also found to potentially decrease the flexural strength and water stability of asphalt mixtures because the fibers with different particle sizes were

distributed unevenly and displayed a spatial rod stacking tendency. It indicated that the amount and particle size range of the rWTB fiber should be considered when designing asphalt mixtures and that optimal material properties could be obtained by the synergistic incorporation of powder and fiber.

4 Conclusion

This study explored the feasibility of introducing rWTB material into the design of the asphalt mixture and investigated the performance of high-temperature rutting, low-temperature cracking, and water stability of the mixtures with different proportions of rWTB powder and fiber based on laboratorial experiments. The following conclusions were obtained:

a. The significant mass loss of rWTB particles occurred at approximately 350°C and 600°C in the thermogravimetric test and presented a high thermal stability below 200°C, including that it could be used in the process of asphalt mixture compaction, paving, and service condition.
b. The partial replacement of mineral powder with rWTB powder improved the resistance of asphalt mixtures to rutting deformation with the optimal ratio of approximately 10%, and the addition of rWTB fiber can also improve the high-temperature performance as more fiber was added.
c. rWTB powder could enhance the flexural strength of the asphalt mixture under low temperature conditions, while rWTB fiber could increase the ultimate strain of asphalt mixtures based on three-point bending tests.
d. The water stability of the asphalt mixture was not significantly affected by the addition of the rWTB powder, while the MS of rWTB fiber mixtures was increased obviously and had a lower RS after water immersion.
e. The synergistic addition of rWTB powder and fiber can further improve the performance of asphalt mixtures. The presence of rWTB particles in different scales modified the microstructure of the asphalt mortar and improved the strength and deforming properties of the mixture (ASTM, 2006a, ASTM, 2006b, ASTM, 2006c, ASTM, 2007, Ministry of Transport, 2011).

Data availability statement

The original contributions presented in the study are included in the article/Supplementary Material; further inquiries can be directed to the corresponding author.

Author contributions

Conceptualization, XL and HW; methodology, TL and BW; formal analysis, JZ; investigation, BW and JZ; resources, HW; data curation, TL; writing—original draft preparation, BW and TL; writing—review and editing, TL and XL. All authors contributed to the article and approved the submitted version.

Funding

This research was funded by the Central Public-interest Scientific Institution Basal Research Fund (2020-9074) and the Scientific and Technological Innovation Special Fund of Research Institute of Highway Ministry of Transport (2019-I111 and 2020-C101).

Conflict of interest

The authors declare that the research was conducted in the absence of any commercial or financial relationships that could be construed as a potential conflict of interest.

Publisher's note

All claims expressed in this article are solely those of the authors and do not necessarily represent those of their affiliated organizations, or those of the publisher, the editors, and the reviewers. Any product that may be evaluated in this article, or claim that may be made by its manufacturer, is not guaranteed or endorsed by the publisher.

References

Abtahi, S. M., Sheikhzadeh, M., and Hejazi, S. M. (2010). Fiber-reinforced asphalt-concrete–a review. *Constr. Build. Mater.* 24 (6), 871–877. doi:10.1016/j.conbuildmat.2009.11.009

Asokan, P., Osmani, M., and Price, A. D. (2009). Assessing the recycling potential of glass fibre reinforced plastic waste in concrete and cement composites. *J. Clean. Prod.* 17 (9), 821–829. doi:10.1016/j.jclepro.2008.12.004

Asokan, P., Osmani, M., and Price, A. D. (2010). Improvement of the mechanical properties of glass fibre reinforced plastic waste powder filled concrete. *Constr. Build. Mater.* 24 (4), 448–460. doi:10.1016/j.conbuildmat.2009.10.017

Astm (2007). ASTM D113-07, Standard test method for ductility of bituminous materials. https://www.astm.org/.doi:10.1520/D0113-07

Astm (2006c). ASTM D36-06, Standard test method for softening point of bitumen (ring-and-ball apparatus).https://www.astm.org/. .doi:10.1520/D0036-06

Astm (2006b). ASTM D5-06, Standard test method for penetration of bituminous materials. https://www.astm.org/.doi:10.1520/D0005-06

Astm (2006a). ASTM D6927-06, Standard test method for Marshall stability and flow of bituminous mixtures. https://www.astm.org/.doi:10.1520/D6927-06

Beauson, J., Madsen, B., Toncelli, C., Brøndsted, P., and Bech, J. I. (2016). Recycling of shredded composites from wind turbine blades in new thermoset polymer composites. *Compos. Part A Appl. Sci. Manuf.* 90, 390–399. doi:10.1016/j.compositesa.2016.07.009

Cao, W. (2007). Study on properties of recycled tire rubber modified asphalt mixtures using dry process. *Constr. Build. Mater.* 21 (5), 1011–1015. doi:10.1016/j.conbuildmat.2006.02.004

Conroy, A., Halliwell, S., and Reynolds, T. (2006). Composite recycling in the construction industry. *Compos. Part A Appl. Sci. Manuf.* 37 (8), 1216–1222. doi:10.1016/j.compositesa.2005.05.031

Demura, K., Ohama, Y., and Satoh, T. (1995). "Properties of artificial woods using FRP powder," in *Disposal and recycling of organic and polymeric construction materials* (Boca Raton, Florida, United States: CRC Press), 135–143. doi:10.1201/9781482294897

Farinha, C. B., de Brito, J., and Veiga, R. (2019). Assessment of glass fibre reinforced polymer waste reuse as filler in mortars. *J. Clean. Prod.* 210, 1579–1594. doi:10.1016/j.jclepro.2018.11.080

García, D., Vegas, I., and Cacho, I. (2014). Mechanical recycling of GFRP waste as short-fiber reinforcements in microconcrete. *Constr. Build. Mater.* 64, 293–300. doi:10.1016/j.conbuildmat.2014.02.068

Gu, X., Dong, Q., and Yuan, Q. (2015). Development of an innovative uniaxial compression test to evaluate permanent deformation of asphalt mixtures. *J. Mater. Civ. Eng.* 27 (1), 04014104. doi:10.1061/(ASCE)MT.1943-5533.0001038

Itoh, T., and Kaneko, M. (2002). Pavement blocks from recycled GRP material. *Proc. Compos.* 2 (2).

Jensen, J. P., and Skelton, K. (2018). Wind turbine blade recycling: Experiences, challenges and possibilities in a circular economy. *Renew. Sustain. Energy Rev.* 97, 165–176. doi:10.1016/j.rser.2018.08.041

Kimm, M., Pico, D., and Gries, T. (2020). Investigation of surface modification and volume content of glass and carbon fibres from fibre reinforced polymer waste for reinforcing concrete. *J. Hazard. Mater.* 390, 121797. doi:10.1016/j.jhazmat.2019.121797

Li, J., Zhang, J., Yang, X., Zhang, A., and Yu, M. (2023). Monte Carlo simulations of deformation behaviour of unbound granular materials based on a real aggregate library. *Int. J. Pavement Eng.* 24 (1), 2165650. doi:10.1080/10298436.2023.2165650

Lin, J., Guo, Z., Hong, B., Xu, J., Fan, Z., Lu, G., et al. (2022). Using recycled waste glass fiber reinforced polymer (GFRP) as filler to improve the performance of asphalt mastics. *J. Clean. Prod.* 336, 130357. doi:10.1016/j.jclepro.2022.130357

Liu, P., and Barlow, C. Y. (2017). Wind turbine blade waste in 2050. *Waste Manag.* 62, 229–240. doi:10.1016/j.wasman.2017.02.007

Lu, X., Isacsson, U., and Ekblad, J. (2003). Influence of polymer modification on low temperature behaviour of bituminous binders and mixtures. *Mater. Struct.* 36 (10), 652–656. doi:10.1007/BF02479497

Majewski, P., Florin, N., Jit, J., and Stewart, R. A. (2022). End-of-life policy considerations for wind turbine blades. *Renew. Sustain. Energy Rev.* 164, 112538. doi:10.1016/j.rser.2022.112538

Mamanpush, S. H., Li, H., Englund, K., and Tabatabaei, A. T. (2018). Recycled wind turbine blades as a feedstock for second generation composites. *Waste Manag.* 76, 708–714. doi:10.1016/j.wasman.2018.02.050

Mastali, M., Dalvand, A., and Sattarifard, A. R. (2016). The impact resistance and mechanical properties of reinforced self-compacting concrete with recycled glass fibre reinforced polymers. *J. Clean. Prod.* 124, 312–324. doi:10.1016/j.jclepro.2016.02.148

Ministry of Transport (2011). *JTG E20-2011, Standard test methods of bitumen and bituminous mixture for highway engineering*. Beijing, China: Ministry of Transport.

Morales, C. N., Claure, G., Álvarez, J., and Nanni, A. (2020). Evaluation of fiber content in GFRP bars using digital image processing. *Compos. Part B Eng.* 200, 108307. doi:10.1016/j.compositesb.2020.108307

Morea, F., and Zerbino, R. (2018). Improvement of asphalt mixture performance with glass macro-fibers. *Constr. Build. Mater.* 164, 113–120. doi:10.1016/j.conbuildmat.2017.12.198

Palmer, J., Ghita, O. R., Savage, L., and Evans, K. E. (2009). Successful closed-loop recycling of thermoset composites. *Compos. Part A Appl. Sci. Manuf.* 40 (4), 490–498. doi:10.1016/j.compositesa.2009.02.002

Pickering, S. J. (2006). Recycling technologies for thermoset composite materials—Current status. *Compos. Part A Appl. Sci. Manuf.* 37 (8), 1206–1215. doi:10.1016/j.compositesa.2005.05.030

Qiao, Y., Zhang, Y., Zhu, Y., Lemkus, T., Stoner, A. M., Zhang, J., et al. (2020). Assessing impacts of climate change on flexible pavement service life based on Falling Weight Deflectometer measurements. *Phys. Chem. Earth* 120, 102908. doi:10.1016/j.pce.2020.102908

Rahimizadeh, A., Kalman, J., Fayazbakhsh, K., and Lessard, L. (2019). Recycling of fiberglass wind turbine blades into reinforced filaments for use in Additive Manufacturing. *Compos. Part B Eng.* 175, 107101. doi:10.1016/j.compositesb.2019.107101

Rodin, H., Nassiri, S., Englund, K., Fakron, O., and Li, H. (2018). Recycled glass fiber reinforced polymer composites incorporated in mortar for improved mechanical performance. *Constr. Build. Mater.* 187, 738–751. doi:10.1016/j.conbuildmat.2018.07.169

Sengoz, B., and Isikyakar, G. (2008). Evaluation of the properties and microstructure of SBS and EVA polymer modified bitumen. *Constr. Build. Mater.* 22 (9), 1897–1905. doi:10.1016/j.conbuildmat.2007.07.013

Seydibeyoglu, M. O., Mohanty, A. K., and Misra, M. (2017). *Fiber technology for fiber-reinforced composites*. Sawston, United Kingdom: Woodhead Publishing. doi:10.1016/C2015-0-05497-1

Tittarelli, F., and Shah, S. P. (2013). Effect of low dosages of waste GRP dust on fresh and hardened properties of mortars: Part 1. *Constr. Build. Mater.* 47, 1532–1538. doi:10.1016/j.conbuildmat.2013.06.043

Wang, H., Fan, Z., and Zhang, J. (2016). Development of a full-depth wheel tracking test for asphalt pavement structure: Methods and performance evaluation. *Adv. Mater. Sci. Eng.* 2016. doi:10.1155/2016/1737013

Wang, Y., Peng, Y., Kamel, M. M., and Ying, L. (2019). Mesomechanical properties of concrete with different shapes and replacement ratios of recycled aggregate based on base force element method. *Struct. Concr.* 20 (4), 1425–1437. doi:10.1002/suco.201800261

Wu, S., Ye, Q., Li, N., and Yue, H. (2007). Effects of fibers on the dynamic properties of asphalt mixtures. *J. Wuhan Univ. Technology-Mater. Sci. Ed.* 22 (4), 733–736. doi:10.1007/s11595-006-4733-3

Wu, S., Ye, Q., and Li, N. (2008). Investigation of rheological and fatigue properties of asphalt mixtures containing polyester fibers. *Constr. Build. Mater.* 22 (10), 2111–2115. doi:10.1016/j.conbuildmat.2007.07.018

Yildirim, Y. (2007). Polymer modified asphalt binders. *Constr. Build. Mater.* 21 (1), 66–72. doi:10.1016/j.conbuildmat.2005.07.007

Zhou, B., Zhang, M., Wang, L., and Ma, G. (2021). Experimental study on mechanical property and microstructure of cement mortar reinforced with elaborately recycled GFRP fiber. *Cem. Concr. Compos.* 117, 103908. doi:10.1016/j.cemconcomp.2020.103908

frontiers | Frontiers in Materials

TYPE Review
PUBLISHED 03 July 2023
DOI 10.3389/fmats.2023.1225830

OPEN ACCESS

EDITED BY
Hui Yao,
Beijing University of Technology, China

REVIEWED BY
Xinxing Zhou,
Shanxi Transportation Technology Research & Development Co., Ltd., China
Peiwen Hao,
Chang'an University, China

*CORRESPONDENCE
Adham Mohammed Alnadish,
adhmalnadish@gmail.com
Yaser Gamil,
yaser.gamil@ltu.se

RECEIVED 19 May 2023
ACCEPTED 20 June 2023
PUBLISHED 03 July 2023

CITATION
Alnadish AM, Katman HYB, Ibrahim MR, Gamil Y and Mashaan NS (2023), A bibliometric analysis and review on the performance of polymer-modified bitumen.
Front. Mater. 10:1225830.
doi: 10.3389/fmats.2023.1225830

A bibliometric analysis and review on the performance of polymer-modified bitumen

Adham Mohammed Alnadish[1]*, Herda Yati Binti Katman[2], Mohd Rasdan Ibrahim[3], Yaser Gamil[4,5]* and Nuha S. Mashaan[6]

[1]Department of Transportation and Geotechnical Engineering, Balochistan Campus, National University of Sciences and Technology (NUST), Quetta, Pakistan, [2]Department of Civil Engineering, Universiti Tenaga Nasional, Kajang, Malaysia, [3]Department of Civil Engineering, Universiti Malaya, Kuala Lumpur, Malaysia, [4]Departement of Civil and Natural Resources Engineering, Lulea University of Technology, Lulea, Sweden, [5]Department of Civil Engineering, School of Engineering, Monash University Malaysia, Selangor, Malaysia, [6]School of Engineering, Edith Cowan University, Perth, WA, Australia

The addition of polymer to a base binder has been documented as a successful approach in terms of improving physical and rheological properties of the base bitumen. However, the main drawbacks of polymer-modified bitumen are incompatibility and degradation of polymer due to aging. This article aims to introduce a bibliometric analysis and review on modifying bitumen with polymers. Additionally, this article intent to highlight the significant gaps and recommendations for future work. Furthermore, another objective of this article is to provide a worth attempt regrading reducing the negative impact of polymer's drawbacks on the performance of polymer-modified base binder. The findings of this article demonstrated that the test of storage stability for polymer-amended bitumen should be modified, in which the softening point of aluminum tube centerpiece should be measured to introduce a better evaluation for the storage stability of polymer-amended bitumen. In addition, the effects of kinetic factors (mixing sequence, viscosity of blend, shear rate, and time of mixing) on the compatibility of polymer-amended bitumen should be investigated. Moreover, the addition of compatibilizers and stabilizers to polymer-modified binder is recommended to improve compatibility and reduce the effect of aging on degradation of polymer.

KEYWORDS

polymer-modified bitumen, compatibility, degradation, aging, compatibility improvement methods

1 Introduction

Bitumen is a by-product of crude oil, which is obtained from crude oil distillation. The distillation procedures are started by removing the lighter fractions through heating crude oil at temperature of 300°C–350°C in the distillation column. Subsequently, residue is further distilled in a vacuum distillation column (Waheed and Oni, 2015; Boczkaj et al., 2017). However, bitumen is widely used in the applications of pavement due to its adhesion property. In other words, bitumen works as an adhesive material that binds coarse aggregates, fine aggregates, and filler to form the layer of asphalt on the roads (Pyshyev et al., 2016; Oliviero Rossi et al., 2017; Nizamuddin et al., 2021; Alnadish et al., 2020b). On the other hand, bitumen is a viscoelastic material that behaves as an elastic material at high temperature and viscous at low temperature. The elastic property indicates the ability of

bitumen to recover after deformation, while the viscous property implies the inability of bitumen to recover after deformation (Behzadfar and Hatzikiriakos, 2013; Alnadish et al., 2020a; Alnadish et al., 2021). Moreover, the physical and rheological properties of bitumen play a major role in terms of identifying the lifespan of the asphalt layer. The better the physical and rheological properties of bitumen, the longer the lifespan of the asphalt layer. Otherwise, the main distresses that significantly affect the performance of bitumen are rutting, fatigue, low-temperature cracking, and aging. The damage of rutting occurs at high temperature, in which the bitumen becomes soft and susceptible to the vertical deformation due to the traffic loads. While at low/intermediate temperatures the distresses of thermal cracking and fatigue cracking (horizontal cracks) occur due the stiff behaviour of bitumen at low/intermediate temperatures due to aging. However, these cracks rapidly decrease the life span of the asphalt layer due to the water seepage to the pavement layers. Therefore, the bitumen should be hard enough at high temperatures to resist the vertical deformation and elastic at low/intermediate temperatures to resist the occurrence of horizontal cracks (Subhy, 2017; Teltayev and Radovskiy, 2018; Alnadish et al., 2022; Ishaq et al., 2022).

Accordingly, vigorous efforts by researchers have been made to improve performance of bitumen in terms of hardness and elasticity. Modifying bitumen with polymers is one of the well-known approaches in enhancing performance of bitumen (Brasileiro et al., 2019; Nizamuddin et al., 2021; Martinho et al., 2022). It is documented that introducing polymer to a base binder significantly improves the hardness of bitumen at high temperatures and low-temperature performance through enhancing elasticity of the base binder. Thus, the service life of the asphalt layer incorporated modified bitumen with polymer is notably improved (Pérez-Lepe et al., 2005; Sengoz and Isikyakar, 2008; Bulatović et al., 2012; Zhu et al., 2014; Nizamuddin et al., 2020). Moreover, the main drawbacks of utilizing polymers as bitumen modifiers are incompatibility and degradation. Incompatibility occurs due to the differences in polarity, densities, and high interfacial tension, while the degradation of polymer-amended bitumen is attributed to subjecting bitumen to short-term and long-term aging (Kalantar et al., 2012; Munera and Ossa, 2014; Behnood and Gharehveran, 2019; Porto et al., 2019; Zhou et al., 2020).

The objective of this article is to introduce a bibliometric analysis in order to discover the trend of modifying bitumen with polymers. Another aim of this article is to conduct a review on the performance of polymer-modified bitumen. However, the drawbacks of polymer blend/polymer-amended binder in terms of immiscibility/separation phase and degradation were highlighted in this article. In addition, the common methods regarding evaluating and enhancing the phase separation of polymer blend have been introduced. Lastly, the research gaps and recommendations on the polymer-modified bitumen were highlighted. Additionally, strategies for reducing the influence of polymers' drawbacks were proposed.

2 Chemical composition of bitumen

Bitumen can be separated into the chemical groups of asphaltenes and maltenes. However, maltenes can be sub-divided into aromatics, resins, and saturates. Asphaltenes are insoluble solids characterized by the color of black/brown and the molecular weight of 800–3,500 g/mol. Asphaltenes represents 5%–20% by bitumen weight. However, asphaltenes components have direct effect on the physical properties of bitumen. The higher the content of asphaltenes, the higher the viscosity, softening point and the lower the penetration of bitumen. Resins are soluble solids with drack brown color. The range of resins molecular weight is 780–1400 g/mol. Bitumen weight consisting of resins by about 30%–45%. Resins are responsible for ductility and adhesion properties of bitumen. Aromatics are non-polar carbon viscous liquids characterized by dark brown color and the molecular weight of 570–980 g/mol. However, 30%–45% of bitumen weight composed of aromatics. The molecular weight range of saturates is 470–880 g/mol, which are white in color, and non-polar viscous oils. Saturates represents 5%–15% by bitumen weight. Aromatics and saturates are responsible for viscosity of bitumen (Read et al., 2003; Lesueur, 2009; Redelius and Soenen, 2015). Table 1 summarizes the chemical components of asphaltenes, resins, aromatics, and saturates.

2.1 Methods of bitumen separation into four fractions

Methods of bitumen separation play a vital role in identifying asphaltenes, resins, aromatics, and saturates components in bitumen. Thus, the method of separation has a significant impact on the chemical evaluation of bitumen. There are different methods have been utilized in separating the components of bitumen. However, the most utilized methods in separating bitumen are Rostler and Sternberg (ASTM D2006), the clay-gel method (ASTM D2007), and Corbett-Swarbrick (ASTM D4124). According to the method developed by Rostler and Sternberg, the separation process starts by removing asphaltenes components from bitumen using n-pentane. Thereafter, the other fractions are separated in sequence using the solution of sulfuric acid. Figure 1A shows the procedures of separation (Goodrich et al., 1986). However, this method has been discounted in 1976 due to the hazardous work environment and the exotic acidic conditions that prevent the recovery of frictions for additional analysis. Therefore, the method of clay-gel has been developed. Figure 1C summarizes the separation processes of bitumen frictions. In this method, the asphaltenes components are removed firstly using n-pentane. Thereafter, the other frictions are introduced into two columns, the upper and lower column are filled with clay and activated silica gel. Then, the sample is filtered using n-pentane. This method is characterized by its simplicity, lower cost, and safe work environment. On the other hand, Corbett-Swarbrick method is an adsorption chromatography technique used to separate bitumen into frictions. The procedures of this method is illustrated in Figure 1B. In this method, the processes starts by removing asphaltenes using n-pentane, followed by adsorbing the remaining fractions on a chromatographic column with solvents of increasing polarity. This method is characterized by separating bitumen into frictions with homogeneity and less complex. In addition, the remaining frictions in this method can be used for further separations and analysis (Claine, 1984; Thenoux, 1987).

TABLE 1 Chemical composition of bitumen (Read et al., 2003; Lesueur, 2009; Redelius and Soenen, 2015).

Composition	Carbon (%)	Hydrogen (%)	Oxygen (%)	Nitrogen (%)	Sulphur (%)
Asphaltenes	78–88	7–9	0.3–5	0.6–4	0.3–11
Saturates	78–84	12–14	<0.1	<0.1	<0.1
Aromatics	80–86	9–13	0.2	0.4	0–4
Resins	67–88	9–12	0.3–2	0.2–1	0.4–5

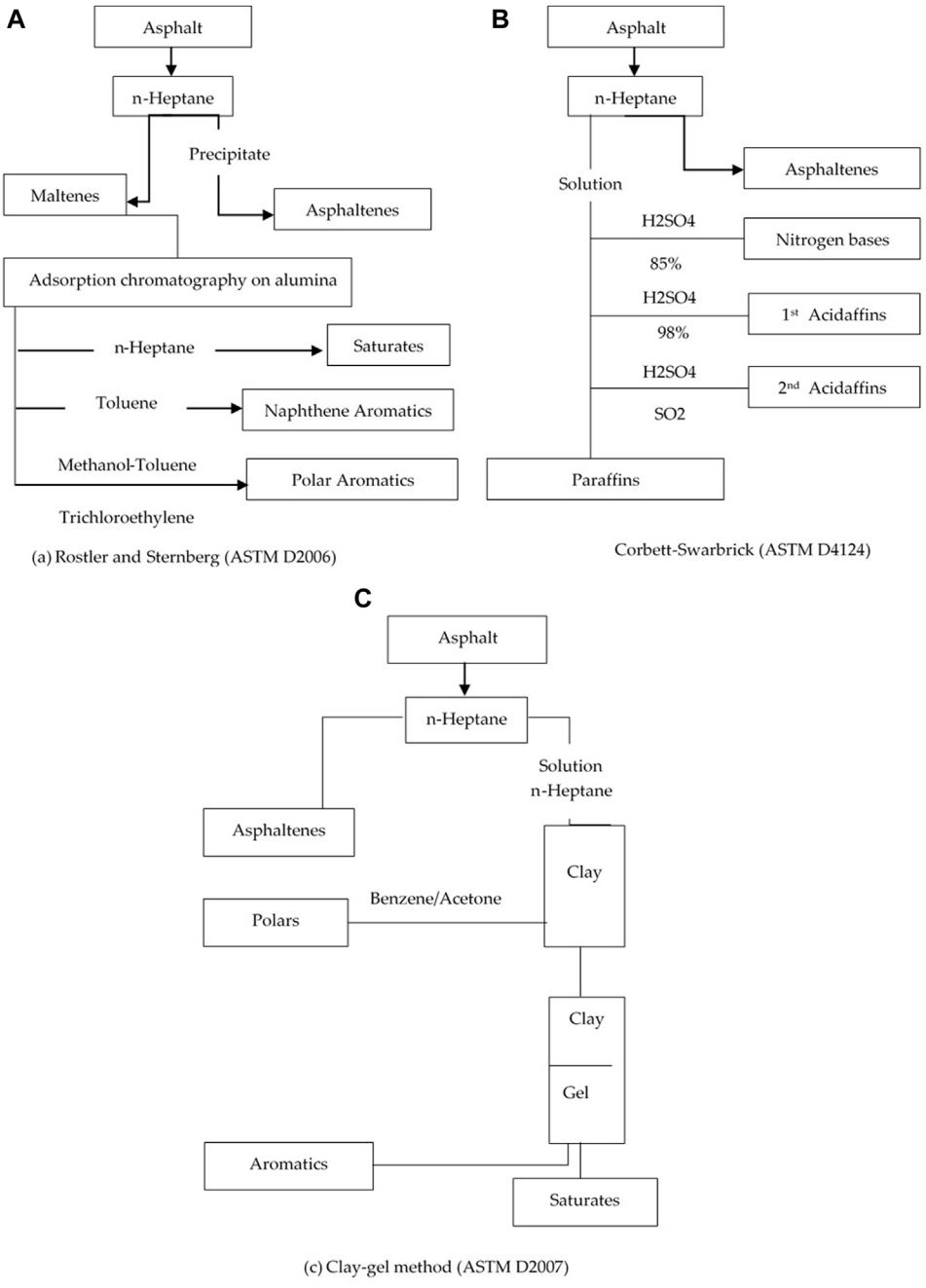

FIGURE 1
Methods of bitumen separation (Claine, 1984; Goodrich et al., 1986; Thenoux, 1987).

2.1.1 Physical properties of bitumen

2.1.1.1 Hardness

Harness refers to the ability of bitumen to resist deformation. The hardness of bitumen is assessed using the test of penetration (Tarefder et al., 2010). Penetration test aims to determine the penetrated depth by a needle with a load of 100 g at a temperature of 25°C. The lower the depth of a needle, the better the hardness of bitumen (Jia et al., 2005).

2.1.1.2 Ductility

Ductility of bitumen indicates the capability of bitumen to elongate without failure under traffic loads (Pereira et al., 2018). The empirical experiment of ductility is used to measure bitumen ductility through stretching a bitumen sample at a temperature of 25°C until breaking point. The longer the stretching, the higher ductile and elastic behavior of bitumen (Jia et al., 2005).

2.1.1.3 Viscosity

The ability of bitumen to be mixed with aggregates and desirable coating refers to viscosity. The viscosity of bitumen is determined using the device of rotational viscometer (Redelius and Soenen, 2015). This test aims to measure the required torque to maintain a constant speed of 20 RPM at testing temperature of 135°C (Jia et al., 2005).

2.1.1.4 Durability

Durability refers to the ability of bitumen to resist environment condition. In other words, durability indicates the resistance of bitumen to aging. The high bitumen resistance to aging implies the longer life of bitumen *in situ*. Aging of bitumen result in a significant change of the physical and chemical properties. However, bitumen aging occurs due to the reaction between bitumen and oxygen, evaporation of bitumen lightweight components during mixing and placing, and strict hardening. Aging of bitumen can be divided into short-term aging and long-term aging. Short-term aging occurs during mixing and placing of asphalt mix, while long-term aging is occurred during the service life of asphalt layer by the reactions between environment conditions and bitumen (Sirin et al., 2018; Prosperi and Bocci, 2021). However, the test of rolling thin film oven (RTFO) is used to simulate the short-term aging of binder. In this test, an eight glass bottles are filled with 35 g of bitumen. Thereafter, the bottles are placed in a heated oven at a temperature of 163°C and rotated for 85 min at 85 RPM. The test of pressure aging vessel is used to simulate the long-term aging of bitumen. In this test, the subjected samples of bitumen to short-term aging are placed in steel pans. Subsequently, subjecting the samples of binder to aging for 20 h in a heated vessel pressurized at temperature 90°C–110°C to 2.10 MPa. Then, the physical, rheological, and chemical properties of binder are determined to study the effect of aging on the properties (Jia et al., 2005).

2.1.2 Rheological properties of bitumen

The viscoelastic property of bitumen is measured using dynamic shear rheometer (DSR). However, elastic property refers to the bitumen ability to recover after deformation, while the viscous property indicates the inability of binder to recover after removing load (Pszczola et al., 2018). DSR aims to determine the performance of bitumen at high, intermediate, and low temperatures through identifying the complex shear modulus (G*) and phase angle (δ). In other words, DSR test measures the resistance of binder to rutting and fatigue. However, G* refers to the rutting resistance of binder, while δ indicates the elastic behavior of bitumen. The increase in G* implies the better resistance to rutting, while the decrease in the δvalue implies the better elastic behavior of binder. In other words, higher G* and lower δ refers to the desirable performance of bitumen. However, the rutting factor of G*/sinδ is used to assess the rutting resistance of bitumen sample (Zeng et al., 2022; Gu et al., 2019; Liu et al., 2022). According to Superpave specifications, the value of rutting factor must be at least 1 kPa for unaged binder, while the rutting factor of short-term aged (RTFO) bitumen should be higher than 2.20 kPa.On the other hand, the factor of G*sinδ refers to the resistance of bitumen to fatigue cracking. The lower the factor of G*sinδ, the better the resistance to fatigue. According to Superpave specifications, the value of G*sinδ for long-term (PAV) aged binder should be less than 5,000 kPa. Additionally, the value of G*sin for long-term (PAV) aged binder at low temperature must be less than 5,000 kPa (Jia et al., 2005).

2.1.3 Low-temperature properties of bitumen

The decrease in the surrounding temperature leads to shrinkage of bitumen, which, in turn, generates stresses leading to thermal cracks due to inability of bitumen to relax stresses. However, the tests of bending beam rheometer (BBR) and direct tension tester (DTT) are used to measure the stiffness and relaxation properties at low temperatures. In the test of BBR, the bitumen specimen is submerged in a cold liquid bath, followed by subjecting the center of the sample to a specific load. Thereafter, the generated deflection by the load is identified. However, the stiffness and relaxation of bitumen is measured by the test of DTT through subjecting the sample to a constant rate of elongation, followed by the determination of sample stress and strain at failure (Jia et al., 2005).

3 Polymers

3.1 Types of polymers

Modifying bitumen with polymers is the most used approach to enhance the physical and rheological properties of bitumen. However, bitumen modifiers can be divided into thermoplastic elastomers, thermoplastic polymers, and thermosetting resins. Thermoplastic elastomers is also called rubber, while thermoplastic polymers called plastics. However, thermoplastic elastomers/rubbers can be classified into Styrene-butadiene-styrene (SBS), Styrene-butadiene- rubber (SBR), Styrene-isoprene-Styrene (SIS), Styrene-ethylene-butylene -Styrene (SEBS), natural rubber, while thermoplastic polymers/plastics can be categorized into Ethylene-vinyl-acetate (EVA), Polyethylene (PE), ethylene butyl acrylate (EBA), polyvinyl chloride (PVC), polypropylene (PP), polystyrene (PS) (Fakirov, 2006; Shanks, 2012). Thermoplastic elastomers are produced naturally from trees such as latex rubber or industrially from petroleum oil, while thermoplastic polymers are obtained from crude oil. However, thermoplastic elastomers and thermoplastics are widely used in modifying bitumen due to their abilities to enhance physical and

TABLE 2 Glass transition temperature (Tg), melting temperature (Tm), and density of polymers (Beyler and Hirschler, 2002; Fred-Ahmadu et al., 2020).

Polymer	Tg (°C)	Tm (°C)	Density (g/cm^3)
High density polyethylene (HDPE)	−125	130–135	0.94–0.97
Low-density polyethylene (LDPE)	−130	109–125	0.91–0.93
Polypropylene (atactic)	−20 to −5	170	0.85–0.94
Polypropylene (isotactic)	100	170	0.92
Polytetrafluoroethylene (PTEF)	120 to 130	220	2.2
Polyethylene terephthalate (PET)	70 to 80	265	1.34–1.39
Polyvinyl chloride (PVC)	65 to 85	90–105	1.16–1.20
Polyvinyl alcohol	80 to 90	200	1.19
Polyacrylamide	160 to 170	84	1.11
Polystyrene (PS)	90 to 110	230	1.04–1.09
Poly (methyl methacrylate)	85 to 105	90–105	1.18
Polyamide (Nylon 6–6)	50 to 60	250–260	1.13–1.15
Polyurethane (PU)	120 to 160	-	1.20

rheological properties of bitumen. Furthermore, the main drawbacks of using polymers in binder are incompatibility and degradation of polymers due to aging (Nizamuddin et al., 2021; Xu et al., 2022). However, asphalt layer is subjected to low and high temperature during its service life. Therefore, the glass transition (Tg) of polymer play a vital role in changing the properties of polymers. Glass transition refers to the temperature at which polymer becomes stiff (glassy state) when subjected to a temperature below glass transition temperature, while the polymer becomes elastic (rubbery state) when exposed to a temperature higher than the glass transition temperature (Beyler and Hirschler, 2002; Fred-Ahmadu et al., 2020). Table 2 summarizes the glass transition temperature (Tg), melting temperature (Tm), and density for some polymers.

3.2 Polymer blend

Polymer blend refers to the blending of one or more polymer to produce a new type of polymer characterized by its desired performance and low cost. However, different methods are used to blend polymers, which are solution mixing, melt blending, latex blending, partial block/graft copolymerization, and interpenetrating polymer networks (IPN) (Mao et al., 2020).

3.3 Drawbacks of polymer blend

3.3.1 Immiscibility/separation phase

The blend of polymers maybe miscible (homogeneous) or immiscible (heterogeneous). The main factors that affect miscibility of polymer blend are temperature, polarity, molecular weight, pressure, interfacial tension, and composition of polymer. The higher the temperature of blend, the better the miscibility of polymer blend, while the difference in polarity of polymers refers to the immiscibility of blend. This is because polar materials are attractive to polar materials and polar solvent, while the non-polar materials are attractive to the non-polar materials and non-polar solvent. In other words, there is no attraction between the polar materials and non-polar materials. Additionally, the increase in the weight of molecular significantly decrease the miscibility of blend. The high interfacial tension between the components of polymers leads to immiscibility/separation phase in the blend of polymer. Furthermore, the blend of polymer can be classified into miscible polymer blend, partially miscible blend (compatible blend), and immiscible polymer blend (Robeson, 2014; Ajitha and Thomas, 2020a; Shanks, 2020). However, the thermodynamic parameter of Gibbs free energy is used to evaluate the separation phase of polymer blend. Gibbs free energy (ΔGm) is calculated through the difference between enthalpy (ΔHm) and entropy (TΔSm) of mixing (ΔGm = ΔHm- TΔSm). Polymer blend is considered miscible if the Gibbs free energy is negative, while the positive value of Gibbs free energy implies the immiscibility of polymer blend. In other words, the negative Gibbs free energy indicates the superior interaction between the components of polymers in the blend.

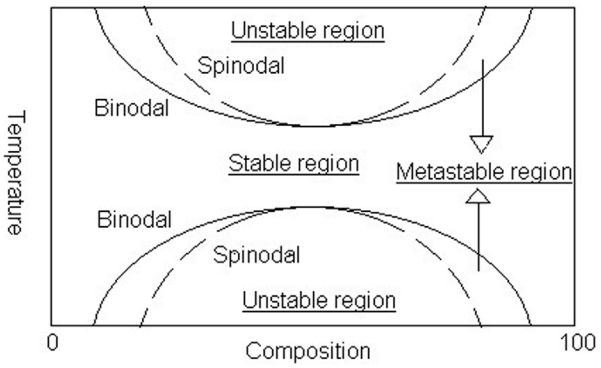

FIGURE 2
Phase diagram of polymer blend of polymer blend (Robeson, 2014).

Moreover, the miscible blend shows negative Gibbs free energy, single-phase morphology, and single glass transition, while the compatible blend shows negative Gibbs free energy, single/two-phase morphology, and single/two glass transition. Otherwise, the immiscible blend displays positive Gibbs free energy, two-phase morphology, and two-glass transition. Furthermore, the degree of miscibility of polymer blend can be identified through the diagram of phase. Figure 2 shows the phase diagram of polymer blend. It can be seen in the figure that there are three regions, which are stable/miscible region, unstable/immiscible region, and metastable region. The miscible region is located between the two binodal, while the immiscible region is surrounded by the curve of spinodal. Otherwise, the region area between the curve of binodal and spinodal refers to the metastable region. However, the binodal separation phase occurs when the temperature of miscible polymer blend brought to the temperature

of immiscible/unstable region. The phase of binodal separation produces a fine two-phase. The separation phase of spinodal occurs when the miscible blend at the stable region is forced to the immiscible/unstable region. This separation phase generates an interconnected structures in both minor and major phases (Utracki and Wilkie, 2002; Sarath et al., 2014; Shanks, 2020). However, incompatibility/separation of polymer-modified bitumen is occurred by the same mechanism of separation phase/immiscibility of polymer blend, in which the occurrence of incompatibility and uneven poorly structure/spherical droplets between polymer and bitumen is attributed to the difference in polarity, high interfacial tension, and different in density between the components of blend. Therefore, the addition of compatibilizer to polymer-modified bitumen is required to improve homogeneity between polymer and bitumen. However, the occurrence of separation due to difference in densities of blend components is slightly different from the separation phase that occurs at the interface of the blend due to the differences in polarity, high interfacial tension, and temperature. However, the change in densities results in a significant change in the physical properties and rheological properties of polymer-modified bitumen. This is because the addition of polymer/nanomaterials with low density as compared to that of bitumen will float, while the introduction of polymer/nanomaterials with a density higher than the density of bitumen will sink. The sinking/floating of bitumen modifiers depends on the diameter and viscosity of polymer-modified blend. According to the principles of the Stokes' law, the higher the viscosity of blend, the lower the sinking/floating (velocity of separation) of bitumen modifiers, while the lower the diameter of nanomaterials/droplet of blend, the lower the velocity of separation. The velocity of separation is identified through the equation below (Munera and Ossa, 2014; Porto et al., 2019; Behnood and Gharehveran, 2019; Brûlé, 1996).

$$V = \frac{2^{*}g^{*}r^{2*}(d1 - d2)}{9^{*}\mu} \quad (1)$$

Where V is velocity of separation, g is the acceleration of gravity, r is the radius of droplet, d1is the density of minor phase (nanomaterials/polymer), d2is the density of major phase (bitumen), and μ is the viscosity of the major phase (bitumen). The negative value of velocity indicates that the minor phase will float, while the positive value implies that the minor phase will sink. Furthermore, it should be indicated that this formula is used to describe the sepration due to difference in density and not the separation at the interface of blend. The separation at the interface of blend is evaluated using of morphology and glass transition temperature.

Understandably, the separation between water and oil is occurred by the difference in density, in which oil floats due to its low density as compared to density of water. In addition, separation phase/immiscibility at interface is attributed to the difference in polarity, in which water is polar and oil is non-polar, thus there are no attraction between molecules. Furthermore, the difference in polarity leads to the increase of interfacial tension, which, in turn, leads to the immiscibility between water and oil (separation phase at interface). The sepration phase at interface leads to uneven poorly structure/spherical droplets. Thus, the addition of emulsifier/surfactant is required to stabilize the blend of water and oil through coating droplets and eliminate forming of coalescing. In other words, the blend of water and oil becomes miscible by the addition of emulsifier/surfactant, this is because the molecules of emulsifier has one end attracted to water (polar) and one end attracted to oil (non-polar). Therefore, the addition of emulsifier reduces the interfacial tension and links between molecules of water and oil, which, in turn, improve morphology at interface and separation due to the difference in densities (Lu et al., 1999; Pérez-Lepe et al., 2006; Pérez-Lepe et al., 2006; Xue et al., 2014; Padaki et al., 2015; Gupta et al., 2017; Pérez-Lepe et al., 2007).

3.3.1.1 Methods to evaluate the separation phase/immiscibility of polymer blend

3.3.1.1.1 Morphology (microscopy). The immiscibility/separation phase of polymer blend at interface can be evaluated by means of morphology. Morphology is used to describe the minor dispersion phase (domain/droplet) on major continuous phase, fibers phase on the major phase, degree of miscibility through identifying the domain size, shape, distribution of polymer blend. Figure 3 shows the minor phase (domain/dispersed phase) of polymer (B) and the major phase of polymer (A) for polymer blend (A/B) (Utracki and Wilkie, 2002).

However, the formation of morphology depends on viscosity, interfacial tension, interfacial adhesion, and blending protocol. The domain size (dispersed phase) distribution depends on the concentration of polymer (B) composition in the blend. The increase in the concentration of polymer (B) in the blend leads to the increase in the number of domain particles and size of domain due to coalescence. The high rate of coalescence between domain particles occurs at the high interfacial tension, low shear rate, and long mixing time. Otherwise, the viscosity of polymer blend (A/B) play a major role in terms of the coalescence rate. If the viscosity of minor phase is lower than that of major phase the rate of coalescence is dramatically reduced due to the restricted diffusion of minor phase on the high viscous of major phase. Moreover, the size of domain has a significant effect on the mechanical properties of blend. The higher the size of domain, the poorer the performance of polymer blend. On the other hand, the common techniques in analyzing the morphology of polymer blend are transmission electron microscopy (TEM), scanning electronic microscopy (SEM), atomic force microscopy (AFM), optical microscopy, fluorescence microscopy, confocal microscopy. These techniques aim to identify the phase separation, domain size, distribution of separated phase, and surface roughness of polymer blend (Utracki and Wilkie, 2002; Sarath et al., 2014; Ajitha and Thomas, 2020b; Shanks, 2020).

3.3.1.1.2 Glass transition temperature. The most accepted approach in evaluating the immiscibility/phase separation is by identifying the glass transition temperature of polymer blend. The single glass transition of polymer blend indicates the miscibility of blend, while the multiple glass transition glass implies the partially miscible/immiscibility of blend. However, the crosslinking degree, average mass of molar, flexibility of chain, and crystallinity are the main factors that affect the glass transition temperature. Otherwise, the most common technique in determining the glass transition temperature of polymer blend is differential scanning calorimetry (DSC). Furthermore, the techniques of dynamic mechanical analysis (DMA), dielectric relaxation spectroscopy (DRS), thermogravimetric Analysis

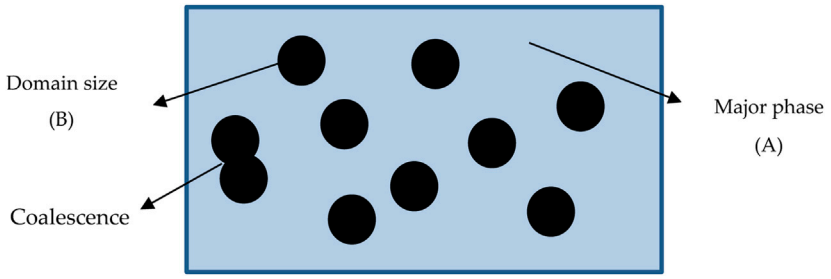

FIGURE 3
Minor phase and major phase of polymer blend **(A, B)**.

(TGA), and Solid-state nuclear magnetic resonance (NMR) are utilized to determine the glass transition temperature of polymer blend (Utracki and Wilkie, 2002; Sarath et al., 2014; Ajitha and Thomas, 2020a; Shanks, 2020).

3.3.2 Degradation of polymers

Most polymers are susceptible to degradation over time when exposed to heat, light, and oxygen. These conditions make a significant change in the physical and mechanical properties of polymers. However, the mechanism of polymers degradation can be divided into initiation, propagation, and termination. In the initiation mechanism, when the polymer is exposed to heat and light, the oxidative degradation is started by forming radical chains/free radical (R) through the hydrogen abstraction (He et al., 2021; Visan et al., 2021). The reactions of initiation are shown below.

$$RH \rightarrow R^{*} + H^{*}$$

The propagation mechanism refers to the form of peroxy radical (ROO*) by the reaction between free radical (R) and Oxygen (O_2), which then produce new radical to react with more chains and obtain more base radicals. The reactions are described as follow:

$$R^{*} + O2 \rightarrow ROO^{*}$$
$$ROOH \rightarrow RO^{*} + OH^{*}$$
$$RO^{*} + RH \rightarrow R^{*} + ROH$$
$$OH^{*} + RH \rightarrow R^{*} + H2O$$

In the termination, the coupling termination is occurred by the reactions between radicals with each other. The reactions of termination are demonstrated below.

$$ROO^{*} + ROO^{*} \rightarrow ROOR + O2$$
$$ROO^{*} + R^{*} \rightarrow ROOR$$
$$R^{*} + R^{*} \rightarrow R - R$$

3.3.3 Methods of enhancing miscibility/compatibility, stabilization, and performance of polymer blend

3.3.3.1 Approaches of polymer blend compatibilization

Compatibilization refers to the addition of compatibilizers into polymer blend to improve the behavior of polymer blend through reducing the interfacial tension, morphology stabilization, and improve the adhesion between phases in the solid state. This in turn results in the fine distribution of polymer composition and decreases the conglomeration. However, the common approaches in improving the compatibility of polymer blend can be classified into.

3.3.3.1.1 Non-reactive copolymers. Block/graft copolymers are used as non-reactive copolymers (compatibilizers) to improve compatibility of polymer blend. However, the addition of block/graft copolymers to polymer blend is able to create a stable morphology of blend through reducing the interfacial tension and this leads to the reduction in domain size and better distribution of dispersed phase. This is because the addition of compatibilizers to the blend of polymer (A/B) works as emulsifiers/surfactants, which means one end of block/graft copolymers is attractive/miscible to one part of the blend (A), while the another end is attractive to the second part of the blend (B). In other words, the interaction between compatibilizers and polymer blend (A/B) produces the fine distribution of polymer blend composition through breaking up the domain size into small sizes. However, the efficiency of compatibilizers is highly affected by the molecular weight, which means that if the molecular weight of homopolymer is much higher than that of arm copolymer, the compatibilizers cannot behave as surfactant. Therefore, the increase in the molecular weight and concentration of copolymer reduces the interfacial tension. The common used compatibilizers for the blend of polymer are block copolymers, this is attributed to the greater interfacial adhesion as compared to graft copolymers. Moreover, the main difference between graft copolymers and block copolymers is that the repeating units of graft copolymers are chain, while repeating units of the block copolymers are linear (Koning et al., 1998; Ajitha and Thomas, 2020b). Table 3 demonstrates some of compatibilizers for polymer blend.

3.3.3.1.2 Reactive copolymers. The use of graft/block copolymers as compatibilizers depends on the miscibility between compatibilizers and components of blend. In some cases, it is difficult to obtain a miscible compatibilizer with components of blend. Therefore, the use of reactive copolymers is worthwhile. The compatibilization of polymer blend by reactive copolymers is done by adding a copolymer with at least one component incorporating functional groups. However, the copolymer component that

TABLE 3 Compatibilizers of polymer blend (Chen and White, 1993; Oliphant et al., 1993; Jarukumjorn, 2007).

Polymer blends	Compatibilizers
Polyethylene (PE) and polycarbonate	SEBS
Polystyrene (PS) and terephthalic acid	Polystyrene ethylene and butylene terephthalate
Polyethylene (PS) and polystyrene (PE)	Styrene and ethylene or SEBS
Polyethylene (PE) and polypropylene (PP)	Ethylene propylene (EP) or very low density polyethylene (VLDPE)
Polyethylene (PE) and Polyvinyl chloride (PVC)	EVA or chlorinated PE
Polyethylene (PE) and Polyethylene terephthalate (PET)	SEBS
Polyethylene (PE) and polyamides	PP lonomer or MAH-grafted PE
High density polyethylene (HDPE) and Polyethylene terephthalate (PET)	Maleic anhydride grafted polyethylene (PE-g-MA)

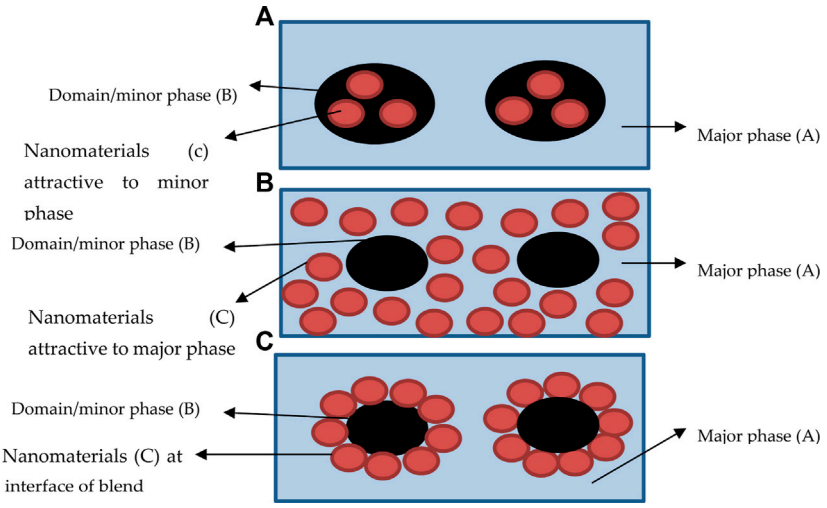

FIGURE 4
Localizations of nanomaterials in the blend of polymer.

consisted of functional groups is attractive/miscible with one component of polymer blend, i.e., (A) through the addition of copolymer to the polymer blend (A/B) during preparation of blend (melt mixing). Thereafter, the melt preparation is followed by the in situ-formed graft/block copolymer, in which the component of added copolymer is attractive/miscible with the another component of polymer blend, i.e., (B) (Utracki and Wilkie, 2002; Sarath et al., 2014; Shanks, 2020).

3.3.3.1.3 Nanomaterials. Nanomaterials with size in the range of 1–100 nm are considered nanofiller. Nanofillers/nanomaterials can be categorized based on the nanoscale into zero-dimensional (0D), one-dimensional (1D), two-dimensional (2D), and three-dimensional (3D). Zero-dimensional indicates that all dimensions of particles are less than 100 nm such as carbon nanocapsules, and quantum dots, while one-dimensional nanomaterials implies that one dimension of the particle is higher than 100 nm and the another dimension is lower than 100 nm such as nanotubes, nanorods, and nanowires. Additionally, the two-dimensional nanomaterials refers to the materials that all their dimensions are higher than 100 nm such as silicates, clays, graphene, while the materials that are not confined to the nanoscale such as silica and nanoparticles metal are considered 3D nanomaterials. However, the addition of nanomaterials to an immiscible polymer blend significantly improves compatibility/miscibility and performance of polymer blend. This is because introducing nanomaterials to the polymer blend reduces the size of dispersed phase and suppress the coalescence between dispersed phases through reducing the interfacial tension. Furthermore, the compatibilization mechanism of polymer blend by means of nanomaterials depends on the selective localization of nanomaterials (Mochane et al., 2020; Munera and Ossa, 2014; Porto et al., 2019; Behnood and Gharehveran, 2019; Brûlé, 1996). Localization of nanomaterials in polymer blend can be at major/minor phase or at the interface of polymer blend. The uniform distribution of nanomaterials in the major/minor phase of polymer blend improves compatibility through increasing the viscosity of blend and this in turn prevent the coarsening of dispersed phase. In other words, the addition of nanomaterials into a polymer blend significantly improves the consistency between the viscosity of minor phase and viscosity of

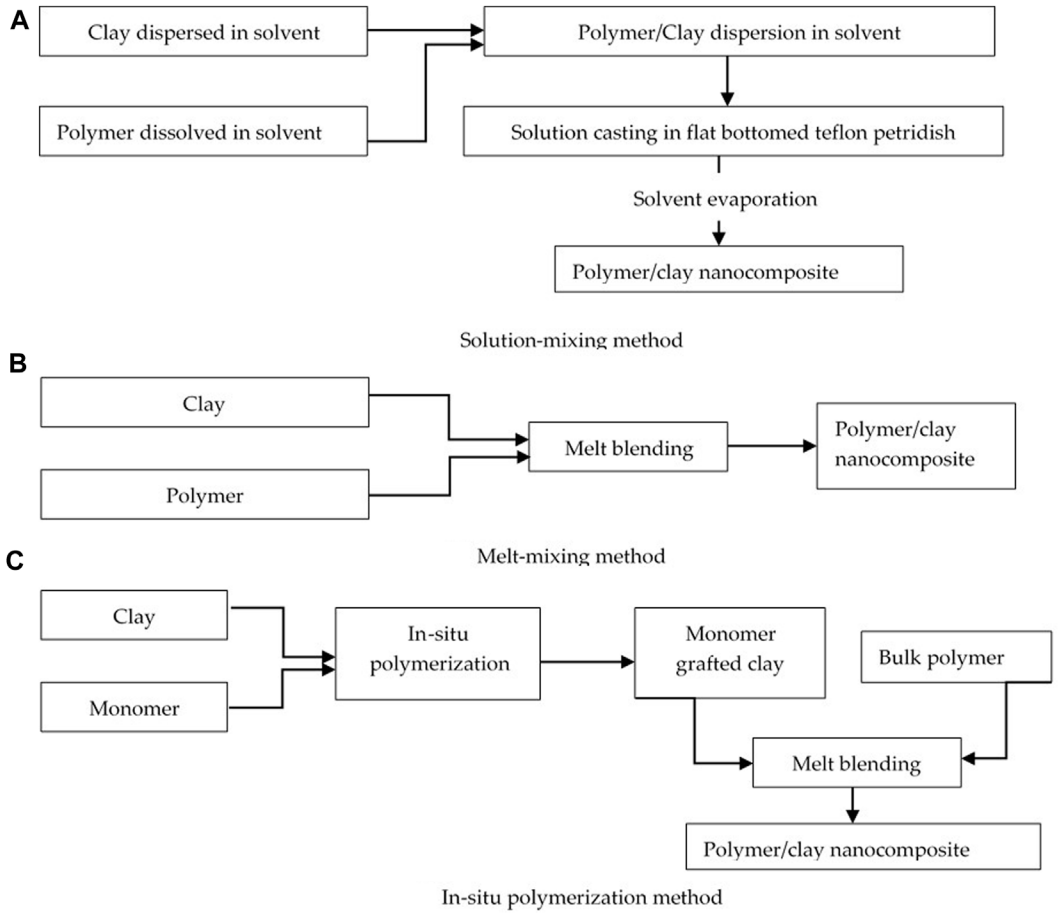

FIGURE 5
Processing Methods of modifying polymer with nanoclay (Guo et al., 2018).

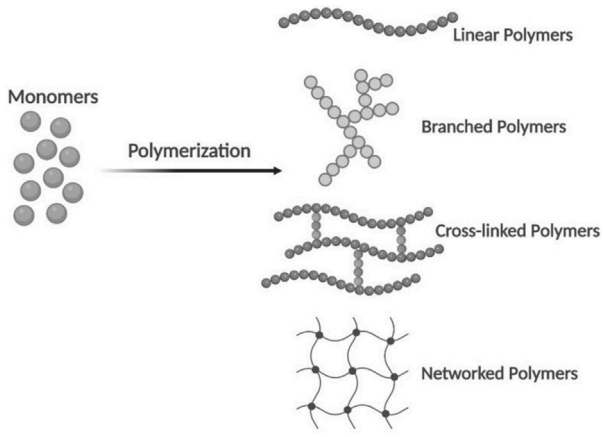

FIGURE 6
Types of polymerization (Damiati et al., 2022).

major phase. However, at the interface localization of nanomaterials the domains (dispersed phases) are surrounded by the nanomaterials. The localization of nanomaterials at the interface of blend enhances compatibility through reducing coalescence of domains. This is because the localization of nanomaterials at interface prevents coalescence between domains. Figures 4A–C display the localization of nanomaterials at the minor phase, major phase, and at the interface of blend, respectively. However, the main factors that affect the selective localization are thermodynamic (polarity and interaction between component of blend) and kinetic (mixing sequence, viscosity of blend, shear rate, and time of mixing). Regarding the thermodynamic factors, if the nanomaterials are attractive to the component of minor phase, the localization of nanomaterials will be at the minor phase. While if the nanomaterials are attractive to the major phase, the localization of nanomaterials will be at the major phase. The localization of nanomaterials can be predicted based on the wetting coefficient expressed in Eq. 2.

$$\omega = \frac{\gamma_{A/C} - \gamma_{B/C}}{\gamma_{A/B}} \quad (2)$$

Where ω is the wetting coefficient, $\gamma_{A/C}$ is the interfacial between the polymer components of (A) and nanomaterials (C), $\gamma_{B/C}$ is the interfacial between the polymer components of (B) and nanomaterials (C), and $\gamma_{A/B}$ is the interfacial between the polymer components of (A) and nanomaterials (B).

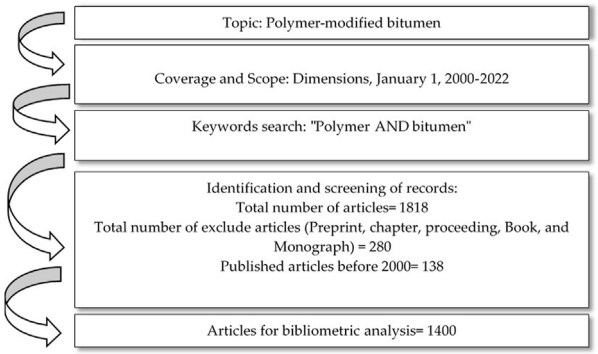

FIGURE 7
Approach of selecting the published documents.

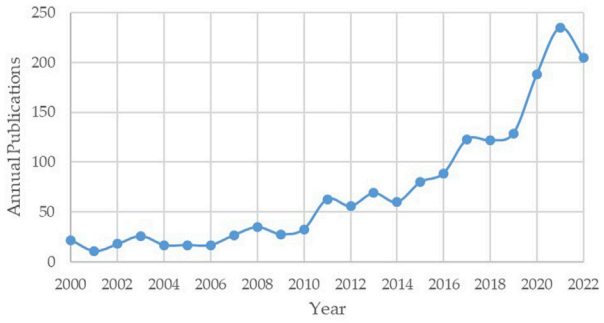

FIGURE 8
Annual publishing.

The localization of nanomaterials will be in the phase of A (major phase), if the value of wetting coefficient is higher than 1, while if the value of wetting coefficient lower than—1, the localization of nanomaterials will be in the phase of B (minor phase). However, the localization of nanomaterials will be at the interface, if $-1 < \omega < 1$. Furthermore, the kinetic factors such as mixing sequence, viscosity of blend, shear rate, and time of mixing play a major role on the localization of nanomaterials and compatibility of polymer blend. Mixing sequence refers to the premixing of nanomaterials with first component of blend, which is less attractive to nanomaterials than the second component of blend, followed by adding the second component of blend. This strategy aims to migrate nanomaterials from non-attractive phase to attractive phase. In addition, the viscosity of blend, shear rate and mixing time play a vital role in terms of identify the degree of compatibility. The lower the viscosity of blend, the better the diffusion of nanomaterials in the major phase. While, the longer the time and higher share rate of mixing, the better the migration of nanomaterials from phase to another phase (Ajitha et al., 2020; Mochane et al., 2020).

Moreover, the addition of nanoparticles (nanosilica, nanoclay, carbon nanotubes, and nanofibers) has been documented as a successful approach in terms of enhancing compatibility, thermal stability and mechanical properties of polymers such as naylon 6, polypropylene (PP), polyethylene terephthalate (PET), epoxy, polyethylene (PE) (Loste et al., 2019). Regarding improving mechanical and physical properties of polymers by modifying polymer with nanoclay/nanoparticles, Soleimani et al. (2012), stated that introducing nanoclay of 1%–5% by weigh to polypropylene matrix improved the Young's modulus by about 36.4% and 17.6% at the temperatures of 25°C and 196°C, respectively. Chan et al. (2011), confirmed that the incorporation of 5% nanoclay to polymer composite enhanced Young's modulus and tensile strength by about 28% and 25%, respectively. Furthermore, it is reported that the size and density of nanoparticles play a vital role in enhancing properties of polymers. The smaller the diameter of nanoparticles, the higher the surface area, and the better the performance and interface properties of polymer (Ashraf et al., 2018).

On the other hand, processing (mixing) method play an essential role on influencing the mechanical properties of polymers. This is attributed to the heterogeneity between nanocaly and polymers. The common processing of nanoclay/polymer can be classified into solution method, melt mixing, and *in situ* polymerization. In the solution method, polymer is dissolved using a solvent, then nanoclay are added and mixed with dissolved polymer. Thereafter, the solvent is evaporated. However, in the method of *in situ* polymerization the nanoclay are mixed within a liquid monomer subjected to heating, followed by the polymerization. In the melt method, polymer is melted, followed by mixing nanoclay with the melted polymer without the use of solvents. The method of melt mixing became interesting due to the high production (Albdiry et al., 2013; Guo et al., 2018; Rafiee and Shahzadi, 2019). Figures 5A–C show the procedures of solution-mixing, melt-mixing, and *In-situ* polymerization, respectively.

On the other hand, it is reported that the use of nanoclay/nanoparticles in polymer-modified bitumen significantly improves compatibility and homogeneity between polymers and binder (Munera and Ossa, 2014; Porto et al., 2019; Behnood and Gharehveran, 2019; Brûlé, 1996). This is because nanoparticles decreases the interfacial tension between polymer and bitumen, in which the addition of nanoparticles leads to break up the size of separated particles into small sizes, this in turn decrease the interfacial tension (Ashraf et al., 2018).

3.3.3.2 Cross-linking agents

A unit of polymer containing hundreds/thousands of monomers. However, through the process of polymerization the structure of polymer can be classified into linear polymers, cross-linked polymers, branched polymers, and networked polymers (Damiati et al., 2022). Figure 6 displays the types of polymerization. Linear polymers such as thermoplastic are characterized by their long chains, these long chains are held together by hydrogen bonding. However, bonding of linear polymers is susceptible to break by heat. Branched polymers such as thermoplastic are created by the addition of short chains through replacing monomers by covalently-bonded. However, branched polymers chains distinguished by the low density as compared to linear polymers and the susceptibility to break by heating. Otherwise, cross-linked polymers such as thermosetting are

10.3389/fmats.2023.1225830

TABLE 4 The outputs of bibliometric analysis.

Top contributing countries			
Author	Documents	Citations	Total link strength
Gallegos, C	18	1172	3063
García-Morales, M	16	721	3100
Giustozzi, Filippo	17	218	1088
Lu, Xiaohu	16	633	707
Partal, P	21	1105	3489
Sengoz, Burak	15	906	597
Top contributing sources			
Construction and Building Materials	162	6109	15952
Energy and Fuels	24	940	1421
Fuel	29	2107	2436
International Journal of Pavement Engineering	33	518	4309
International Journal of Pavement Research and Technology	18	104	2455
Iop Conference Series Earth and Environmental Science	17	21	434
Iop Conference Series Materials Science and Engineering	65	195	2590
Journal of Applied Polymer Science	20	771	3468
Journal of Cleaner Production	16	386	2220
Journal of Materials in Civil Engineering	39	620	3910
Materials	33	234	3859
Materials and Structures	33	720	2834
Petroleum Science and Technology	26	373	2291
Road Materials and Pavement Design	71	1489	5617
Sustainability	18	196	2410
Top contributing organization			
Belgorod State Technological University	15	26	429
Delft University of Technology	29	490	1888
Fırat University	15	233	1220
Iran University Of Science And Technology	31	501	1417
Kielce University of Technology	15	109	656
Marche Polytechnic University	21	433	1005
Rmit University	22	369	2568
Royal Institute of Technology	21	1244	2331
University of Alberta	43	1336	12
University of Huelva	48	2174	3207
University of Nottingham	37	2189	2509
Top contributing countries			
Australia	34	603	11533
Canada	79	2707	3215

(Continued on following page)

TABLE 4 (*Continued*) The outputs of bibliometric analysis.

Top contributing countries			
China	101	1795	20327
Egypt	15	32	1068
France	35	1001	7119
India	70	1027	11723
Indonesia	22	61	1997
Iran	90	2300	15398
Italy	83	1614	17714
Malaysia	44	991	13110
Netherlands	33	724	7386
Poland	50	732	6325
Portugal	19	570	5493
Russia	103	209	5925
Spain	81	2942	20356
Sweden	32	1353	10390
Switzerland	16	264	3010
Turkey	52	2078	13659
Ukraine	18	120	3447
United kingdom	76	3107	12797
United states	76	1776	11356

characterized by the strong bond in comparison with linear and branched polymers. This is because the monomers of polymers are held together by covalent bond through the addition of cross-linking agent. Networked polymers are represented by the complex form of network, in which monomers are heavily linked to each other. Networked polymers are characterized by the high resistance to heat (Biesenberger and Sebastian, 1983; Daniels, 1989; Hirao et al., 2005).

However, the addition of crosslinking agents to create cross-linked/bonding monomers of polymers are the most common type of polymerization in the applications of polymers. Chemical bond between monomers occurs by the covalent bond, in which the electron pairs between atoms are formed by sharing electrons. Furthermore, the most use of cross-linking agent approach is in the applications of rubber vulcanization, in which the addition of cross-linking agent to rubber leads to improve rigidity (glassy state) of rubber (Bacskay et al., 1997; Huang et al., 2020). In addition, it is proven that adding cross-linking agent to polymers improves thermal stability, physical properties, and mechanical properties. This is because adding cross-linking agent aims to create chemical bonds between monomers/molecules of polymers by covalent bond. Additionally, the content of cross-linking agent play a vital role in the physical, mechanical, thermal properties of polymers (Mane et al., 2015; Guo et al., 2019). The higher the content of cross-linking agent, the higher the density of crosslinking, weight of molecular, viscosity, and glassy state (less flexibility) of polymer (Mane et al., 2015; Hoti et al., 2021). Therefore, the addition of cross-linking agent to a miscible blend leads to the separation due to the increase in the molecular weight of blend (Sarath et al., 2014). However, sulfur is the most common type of cross-linking agents. Sulfur is characterized by its density of 2.07 g/$\mathbf{cm^3}$ and a melting point of 115°C (Zhao et al., 2021).

Otherwise, it is documented that the addition of sulfur to polymer-modified bitumen significantly enhances compatibility. This enhancement may attributed to the increase in density of the polymer component, in which the addition of sulfur creates a chemical bonds/links between molecules of polymer and bitumen. However, the increase in the density of polymer leads to the decrease of separation phase that occurs by the difference in densities between bitumen and polymer.

3.3.3.3 Polymer stabilizers

Thermal and mechanical properties of polymers can be enhanced using chemical additive. Stabilizers are utilized to prevent degradation of polymers during manufacturing or service life of polymers. However, antioxidants are well-known additives that have been utilized in enhancing thermal stability of polymers. Antioxidants can be classified into primary antioxidants and secondary antioxidants (Atta et al., 2017; Zafar et al., 2019; Brito et al., 2021). Primary antioxidants is aimed to remove propagation radicals, free radicals, and peroxy

radical (ROO*). This can be done by means of chain breaking donor antioxidant (CB-D) such as BHT, Topanol O, Topanol C, Irganox 1076, Irganox 1010, and Cyanox 2246. However, CB-D is used to react with AH and ROO* in order to produce ROOH and A* (non-radicals products) (Al-Malaika, 1998). The reaction is described below.

$$AH + ROO^{*} \rightarrow^{CB-D} ROOH + A^{*}$$

Secondary antioxidants are used to prohibit the generation of free radicals (R). This can be done by using decompose hydroperoxides stoichiometrically (PD-S) or decompose hydroperoxides catalytically (PD-C). The reaction below describes how PD-S prevent the generation of free radicals.

$$P(OR)3 + ROOH \rightarrow^{PD-S} O = P(OR)3 + ROH$$

Furthermore, sulfur/nanoparticles can be used to enhance thermal stability of polymers because reinforcing polymers with nanoparticles significantly improves the properties of polymers (Chrissafis and Bikiaris, 2011; Senthil Kumar et al., 2018; Terada et al., 2020).

4 Materials and methods

4.1 Approach of study

In this article, the bibliometric analysis was conducted to identify the most contributing authors, organizations, sources, and countries on the polymer-modified bitumen. Furthermore, the trend of published articles of polymer-amended binder was also determined. However, bibliometric analysis was carried out by means of VOSviewer tool (version 1.6.18). The data of bibliometric

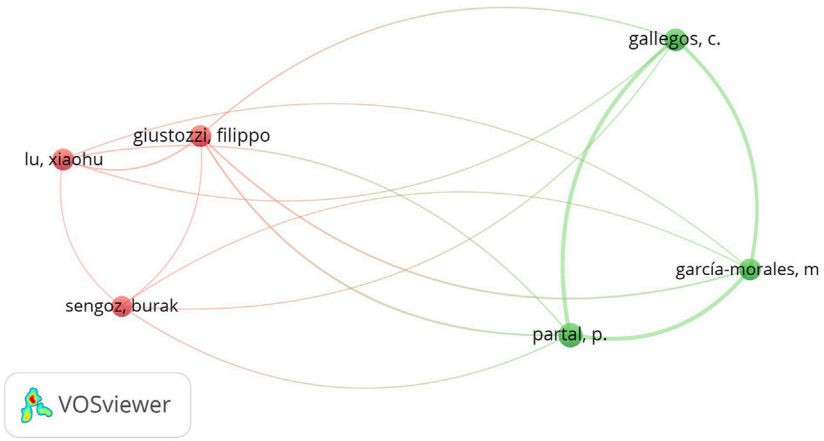

FIGURE 9
Network visualization of top contributing authors.

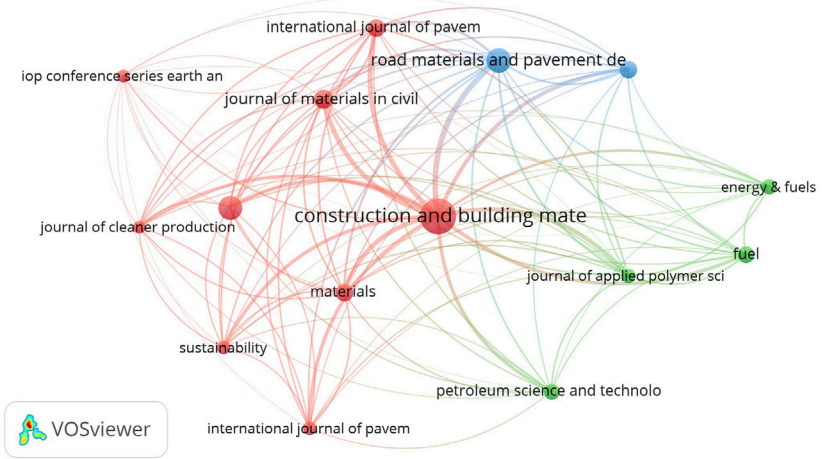

FIGURE 10
Network visualization of top contributing sources.

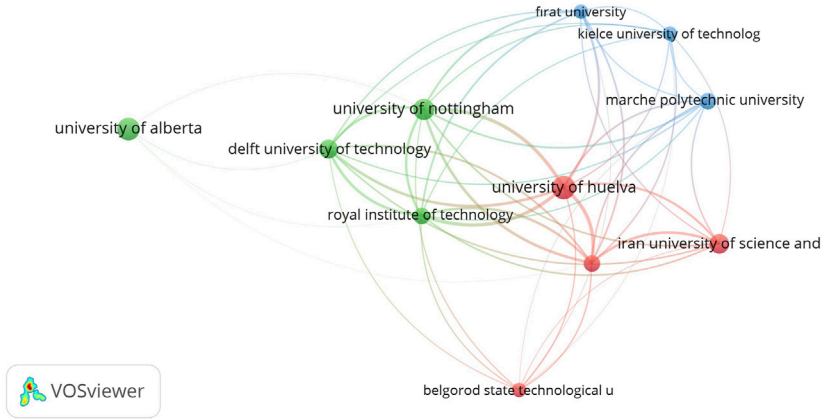

FIGURE 11
Network visualization of top contributing organizations.

analysis can be obtained from different sources such as Scopus, Web of Science, PubMed, google scholar, and Dimensions. However, obtaining the data from Scopus and Web of Science requires subscription, while the data from Dimensions, google scholar, and PubMed are obtained free (Alnadish et al., 2023).

4.2 Source of data

In this article, the data of bibliometric analysis were obtained in the form of CSV from Dimensions by searching in the title and abstract for the keywords of "Polymer And bitumen". The keywords were researched from 1 January 2000 to 31 December 2022.

4.3 Eligibility criteria

In this study, articles such as original articles, review, and letters were considered for bibliometric analysis, while chapters, proceeding, book, monograph and preprint were excluded. Figure 7 displays the approach of selecting documents for bibliometric analysis.

4.4 Data analysis

In this study, the analysis between bibliometric coupling, authors, sources, organizations, and countries was carried out. However, the minimum number of published articles was set to 1, while the resolution parameter and size of cluster was set to 1.

5 Results and discussions

5.1 Bibliometric analysis

5.1.1 Annual publishing

Figure 8 shows the trend of annual publications of utilizing polymers as bitumen modifier. It can be seen in the figure that the published articles on polymer-modified bitumen has been notably increased from 2011 onwards. The highest number of publications was in the year of 2021 with 235 articles, followed by the year of 2022 with 205 articles. However, the number of published articles slightly decreased in the year of 2022 as compared to the published articles in the year of 2011. It can be said that the interest in the use of polymer as binder modifier is increasing exponentially. This is attributed to the benefits of polymer-modified binder in terms of enhancing the physical and rheological properties that enhances the lifespan of modified binder.

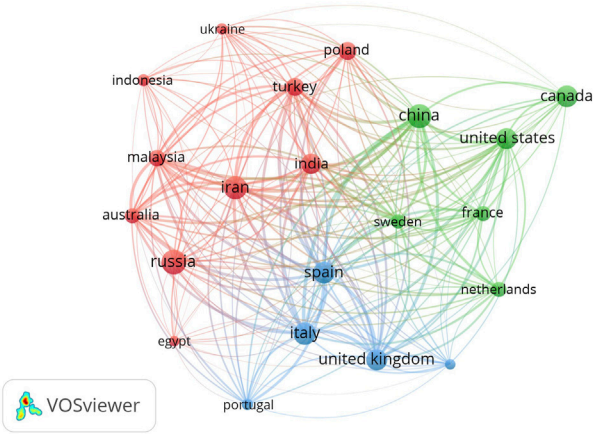

FIGURE 12
Network visualization of top contributing countries.

5.1.2 Top contributing authors

The outputs of authors, number of documents, citations, and total link strength for the bibliometric analysis of bibliographic coupling *versus* authors are summarized in Table 4. In addition, the outputs of network visualization is used to highlight the top authors through size of node and link. The larger the size of node and the thicker the links indicate the significant contributing of an author.

As highlighted in Table 4; Figure 9, the most contributing authors are Gallegos, C, Giustozzi, Filippo, and Partal, P. In addition, the highest link strength is between Gallegos, C and Partal, P, followed by the link strength between García-Morales, M and Partal, P. However, the link strength indicates the co-occurrence/co-authorship between studies. The higher the strength of link, the more the connections between the content/keywords of studies.

5.1.3 Top contributing sources

The bibliometric analysis for bibliographic coupling *versus* sources is used to identify the most contributing sources in a specific field. However, the name of sources, number of documents, citations, and total link strength are listed in Table 4, while the network visualization is shown in Figure 10. As can be seen in the table, the sources of Construction and Building Materials, Road Materials and Pavement Design, and Iop Conference Series Materials Science and Engineering are the top three in terms of number of published documents. While the sources of Construction and Building Materials, Fuel, and Road Materials and Pavement Design are the most contributing in terms of number of citations. In addition, the most contributing sources in terms of total link strength are Construction and Building Materials, Road Materials and Pavement Design, and International Journal of Pavement Engineering. However, the large size of node in the network visualization shown in Figure 10 indicates the most contributing sources in terms of number of published articles. The thicker link strength presented in the figure implies the strong connection between the documents of sources.

5.1.4 Top contributing organizations

The most contributing organizations in modifying base binder with polymers is identified by the bibliometric analysis between bibliographic couplings *versus* organizations. Table 4 and Figure 11 shows the outputs of the bibliometric analysis. As observed in Table 4 and network visualization shown in Figure 11 the most contributing organizations in terms of number of documents are University of Alberta, University of Huelva, and University of Nottingham, while the top organizations in terms of citations are Royal Institute of Technology, University of Alberta, and University of Huelva. However, the top contributing organizations in terms of total link strength are University of Huelva, Rmit University, and Royal Institute of Technology. In addition, the link strength between organizations shown in Figure 11 implies the co-occurrence/co-authorship between published documents from organizations. The thicker the strength of link, the more the relatedness between published documents in terms of content/keywords. Otherwise, it is observed that the most contributing organizations are from the developed countries. Therefore, there should be a salient support for the organizations in developing countries in terms of publishing articles and case studies related to the modification of base bitumen with polymer.

5.1.5 Top contributing countries

The most contributing countries in modifying bitumen with polymer is determined through the bibliometric analysis between bibliographic couplings *versus* countries. The findings of bibliometric analysis are displayed in Table 4; Figure 12. It can be concluded from Table 4; Figure 12 that the top contributing countries in terms of published documents are Russia, China, and Iran, while the most contributing countries in terms of citations are United Kingdom, Spain, and Canada. The higher the number of citations, the more the impact of documents. However, China, Italy, and Iran are the top contributing countries in terms of total link strength. It can be concluded that the published articles from developing countries still limited as compared to the published documents from developed countries.

5.2 Performance of polymer-modified bitumen

5.2.1 Physical properties of polymer-modified bitumen

The incorporation of polymers with bitumen significantly increases the physical properties of binder in terms of softening point and viscosity. On the contrary, the addition of polymers notably decreases penetration and ductility. It is documented that the addition of SBS to a base binder increased viscosity and softening point, while the penetration and ductility are reduced (Bai, 2017; Hao et al., 2017; Shah and Mir, 2020; Tang et al., 2021; Kong et al., 2021). Similarly, various studied (Zhang et al., 2012; Liang et al., 2017; Li et al., 2021), concluded that modifying a base bitumen with SBR significantly improved the physical properties of aged and unaged binder. However, introducing SIS to a bitumen notably enhanced penetration, softening point, viscosity, and ductility (Kim et al., 2019; Ji et al., 2020; Mazumder et al., 2020). According to the findings of studies (Bachir et al., 2016; Zapién-Castillo et al., 2016; Zhang et al., 2018), SEBS amended-bitumen improved physical properties of unaged and aged modified binder. It is confirmed that the physical properties of bitumen subjected to short-term aging and long-term aging could be enhanced by the addition of EVA (Al-Mansob et al., 2014; Jiang et al., 2017; Keymanesh et al., 2017). Furthermore, adding PE to a base binder produces a modified bitumen with superior physical properties (Yan et al., 2020; Liang et al., 2021; Yan et al., 2021).

5.2.2 Morphological properties of polymer-modified bitumen

Morphology properties are used to identify the size, shape, and structure of polymer-modified bitumen. In addition, the compatibility between polymer and binder is evaluated through morphology properties. Fluorescence microscopy is the common test utilized in the evaluation of morphology properties. It is reported that the addition of polymers to a binder negatively affects the homogeneity between bitumen and polymer due to the difference in the densities. Tang et al. (2021) noticed the incompatibility of 9% SBS-amended binder, in which the structure of polymers was like honeycomb. Furthermore, the concertation of polymers remarkably decreased after subjecting modified binder to short-term aging (RTFO) and long-term aging (PAV). However, authors observed the enhancement in the compatibility and aging resistance of 9% SBS-modified bitumen by introducing 0.15% sulfur. Similarly, Hao et al. (2017) concluded that adding 0.15% sulfur to 4.5% SBS-modified binder significantly enhanced compatibility and decreased degradation of polymer. On the contrary; Zhang et al. (2012) pointed out that modifying base binder with 4% SBR caused incompatibility and subjecting SBR-amended binder to aging significantly decreased the existence of polymers due to degradation. In addition, researchers stated that

the addition of 0.03% sulfur improved compatibility, but sulfur is more susceptible to degradation due to aging; Li et al. (2021) confirmed that the incorporation of 4% Sasobit and 4% epoxidized soybean pol (ESO) to 4% SBS-modified binder significantly enhanced homogeneity and resistance to aging. Authors claimed that the addition of Sasobit and ESO maintained structure and concertation of polymers after aging. Liang et al. (2017) confirmed that the addition of 1.5% polyphosphoric acid (PPA) to 3% SBR-modified bitumen notably improved the compatibility. Mazumder et al. (2020) noticed that the addition of 15% SIS to a base binder significantly reduced the honeycomb structure of binder. Researchers stated that the reduction in bee structure is attributed to the dissolution of waxy particles by the addition of SIS. Zapién-Castillo et al. (2016) assured that modifying bitumen with 6% SEBS displayed poor compatibility. However, researchers observed the remarkable enhancement in compatibility after adding 6% nanoclay to SEBS-amended bitumen. Authors stated that the addition of nanoclay balanced the difference in the densities of polymer and bitumen. Al-Mansob et al. (2014) demonstrated that the addition of 6% natural rubber to a base binder showed satisfactory compatibility. Jiang et al. (2017) evaluated the compatibility of bitumen-modified with 5% EVA, 2% SBS, and 0.05% sulfur. The morphological evaluation results exhibited that before aging the modified binder with EVA showed incompatibility between bitumen and polymers, in which the interface of polymer was like honeycomb. However, the addition of SBS to EVA-modified binder improved the compatibility through the appearance of the polymer particles in the form of a continuous filament network. Furthermore, the addition of sulfur to modified bitumen with EVA and SBS displayed the best compatibility. After aging, researchers noticed that the concentration of polymer particles significantly decreased for all modified bitumen. Authors stated that the crosslinked of polymers were destroyed due to aging processes. Yan et al. (2021) indicated that the addition of 4% PE to a base binder displayed poor compatibility. However, authors declared that introducing 4% EVA to PE-modified binder enhanced the compatibility.

5.2.3 Chemicals properties of polymer-modified bitumen

In a study conducted by Hao et al. (2017), the chemical composition of 4.5% SBS-modified bitumen was investigated by means of gel permeation chromatography (GPC). The findings of study demonstrated that subjecting modified binder to short-term aging (RTFTO) and long-term aging (PAV) decreased the molecular weight of polymer. Additionally, the asphaltenes components notably increased, while the maltenes composition decreased after subjecting modified bitumen to RTFTO and PAV. Authors indicated that the decrease in molecular weight is attributed to the degrading of polymer. However, researchers concluded that the addition of 0.15% sulfur to 4.5% SBS-modified binder further reduced the molecular weight of polymers. In similar content, Hu et al. (2020) noticed that subjecting 4.5% SBS-modified binder to PAV decreased percentage molecular weight of polymers from 3.5% to 0.8%, while asphaltenes content increased by about 30%; Tang et al. (2021) observed that subjecting 9% SBS-modified bitumen to PAV significantly decreased the average molecular weight of polymers and increased the average molecular weight of asphaltenes. However, researchers found that the addition of 0.15% sulfur to 9% SBS-modified binder further decreased molecular weight of polymers and increased the average molecular weight of asphaltenes. Authors attributed this change in the average molecular weight to filtration of gel permeation chromatography (GPC) specimens. Bachir et al. (2016) obtained similar findings, in which the addition of 5% SEBS to base bitumen increased the content of asphaltenes before aging and after aging.

5.2.4 Rheological properties of polymer-modified bitumen

The aim of adding polymers to a base binder is to improve the rheological properties. The rheological properties are evaluated through complex shear modulus (G*) and phase angle (δ). Complex shear modulus refers to the resistance of binder to rutting, while phase angle implies the elastic behavior of binder. The higher the complex shear modulus, the better the resistance to rutting. On the contrary, the low phase angle indicates the better elastic behavior. Furthermore, rutting factor (G*/sinδ) and fatigue factor (G*sinδ) are used to assess the resistance of bitumen to rutting and fatigue cracking. The higher the rutting factor the better the resistance to rutting, while the low value of fatigue factor indicates the better resistance of binder to fatigue cracking. However, numerous studies have investigated of modifying a base binder with polymers. In a comparative study conducted by Hu et al. (2020), a base binder was modified with 4.5% SBS, 12% high viscosity modified asphalt (HVMA), and 16% HVMA. However, the rheological properties of modified bitumen subjected to RTFO and PAV were investigated. The findings of study demonstrated that the unaged and aged of 12% and 16% HVMA-modified bitumen showed better complex shear modulus and phase angle than the modified bitumen with 4.5% SBS. Hao et al. (2017) concluded that subjecting 4.5% SBS-modified bitumen to RTFTO and PVA significantly increased complex modulus and reduced phase angle. Authors noticed that the addition of 0.15% sulfur improved complex shear modulus and phase angle. According to Shah and Mir. (2020), the addition of 2% montmorillonite clay (OMMT) to 4% SBS-amended binder notably enhanced rutting factor and fatigue factor. However, the authors noticed that subjecting 4% SBS modified-bitumen decreased rutting and fatigue factor. Researchers confirmed that the addition of OMMT improved rutting and fatigue factor of aged bitumen. Similarly, Zhang et al. (2012) indicated that the phase angle of 4% SBR modified-binder significantly decreased after modified bitumen exposed to PAV; Li et al. (2021) observed that the addition of 4% Sasobit and 6% epoxidized soybean pol (ESO) to 4% SBR amended-bitumen notably enhanced complex shear modulus and phase angle of subjected modified binder to short and long-term aging. Mazumder et al. (2020) confirmed that modifying base binder with 15% SIS significantly improved rutting and fatigue factor as compared to unmodified binder. Bachir et al. (2016) concluded that adding 5% SEBS to a base binder improved complex shear modulus and phase angle before and after aging. In a research conducted by Al-Mansob et al. (2014), natural rubber was introduced to a base binder at different contents 0%–12% in 3% increment by bitumen weight. The study findings displayed that adding natural

TABLE 5 Summary of findings.

Polymer	Dosage (wt%)	Unaged modified binder					Aged modified binder				
		P	C	G*/sinδ	G*sinδ	m-value	P	G*/sinδ	G*sinδ	m-value	D
SBS Tang et al. (2021)	9	↑	↓	↑			↑	↑			√
SBS + Sulfur Tang et al. (2021)	9 + 0.15	↑	↑	↑			↑	↑			√
SBS Hao et al. (2017)	4.5	↑	↓	↑			↑	↑			√
SBS + Sulfur Hao et al. (2017)	4.5 + 0.15	↑	↑	↑			↑	↑			√
SBS Shah and.Mir (2020)	5	↑			↑	↑					
SBS Bai. (2017)	5						↑	↑		↓	
SBS + Rejuvenator Bai. (2017)	5 + 9						↑	↑		↑	
SBR Zhang et al. (2012)	4	↑	↓	↑			↑	↑			√
SBR + Sulfur Zhang et al. (2012)	4 + 0.03	↑	↑	↑			↑	↑			√
SBS + Sasobit + EOS Li et al. (2021)	4 + 4+6	↑	↑	↑							
SBR + PPA Liang et al. (2017)	3 + 1.5	↑	↑	↑		↑					
SIS Mazumder et al. (2020)	15	↑	↑	↑	↑	↑					
SIS Ji et al. (2020)	15	↑	↑	↑							
SIS + GTR Kim et al. (2019)	5 + 10	↑	↑	↑	↑	↑					
SEBS Zapién-Castillo et al. (2016)	6	↑	↓	↑							
SEBS + Nanoclay Zapién-Castillo et al. (2016)	6 + 6	↑	↑	↑							
SEBS Bachir et al. (2016)	5	↑	↓	↑			↑	↑			
SEBS + PPA Zhang et al. (2018)	4 + 0.8	↑	↑	↑		↑	↑	↑		↑	√
Natural rubber Al-Mansob et al. (2014)	6	↑	↓	↑	↑						
EVA Jiang et al. (2017)	5	↑	↓	↑		↑	↑	↑		-	√
EVA + SBS Jiang et al. (2017)	5 + 2	↑	↑	↑		↑	↑	↑		↑	√
EVA + SBS + Sulfur Jiang et al. (2017)	5 + 2+0.05	↑	↑	↑		↑	↑	↑		↑	√
EVA + CR Keymanesh et al. (2017)	3 + 4	↑				↑					
EVA + CR Yan et al. (2020)	4 + 15	↑	↑	↑		↑					
PE Yan et al. (2021)	4	↑	↓	↑		↑	↑	↑		↓	
PE + EVA Yan et al. (2021)	4 + 4	↑	↑	↑		↑	↑	↑		↑	
PE Liang et al. (2021)	5	↑	↓	↑		↑					
SBS + Waste bio-oil Nie et al. (2020)	8 + 4		↑	↓			↑	↑			
SBS + Aromatic oil Nie et al. (2020)	8 + 4		↑	↓			↑	↑			
SBR + Waste cocking oil Ren et al. (2021)	3 + 10		↑	↓	↑	↑	↑	↑	↑	↑	
SBR + Waste engine oil Ren et al. (2021)	3 + 10		↓	↓	↑	↑	↑	↑	↑	↑	
SBS + Polyethylene + Waste oil Luo et al. (2017)	5.5 + 5+5		↑	↓			↑	↑			
Waste Polyethylene + Waste engine oil Peng et al. (2020)	4 + 6		↑		↑	↑					
SBS + Nano-ZnO Xie et al. (2020)	4 + 3.2	↑	↑			↑	↑			↑	
SBS + Nano-ZnO + nano-TiO2 Xie et al. (2020)	3.2 + 4+1.5	↑	↑			↑	↑			↑	
SBS + Nano-ZnO + Nano-TiO2 Zhang et al. (2016)	3.7 + 3+0.5	↑	↑	↑		↑	↑	↑		↑	
SBR + Nano-CaCO3 Zhang et al. (2016)	4 + 5	↑	↑	↑		↑	↑	↑		↑	

(Continued on following page)

TABLE 5 (*Continued*) Summary of findings.

Polymer	Dosage (wt%)	Unaged modified binder					Aged modified binder				
SBS + Nano-ZnO Zhang et al. (2016)	4.2 + 5	↑	↑	↑		↑	↑	↑		↑	

P= physical properties, C= compatibility, D = degradation.
↑ = Increase of the parameter, ↓ = Decrease of the parameter, √ = Occurrence of degradation.

rubber at content of 6% improved unaged bitumen performance to rutting and fatigue cracking in comparison with unmodified binder. In a comparative study conducted by Jiang et al. (2017) a base binder was modified with EVA, SBS, and sulfur to investigate the impact of utilizing these polymers on the rheological, properties of modified binder. Three types of modified binder were prepared, the first type was prepared by modifying a base bitumen with 5% EVA, the second type was fabricated by amending base binder with 5% EVA and 2% SBS, the third type was equipped by introducing 0.05% sulfur to a bitumen incorporated 5% EVA and 2% SBS. According to dynamic shear rheometer evaluation, the short-term aged modified bitumen with EVA exhibited the highest complex shear modulus and phase angle, followed by the modified bitumen with EVA and SBS, while the modified bitumen with EVA, SBS, and sulfur showed the lowest complex shear modulus and phase angle. However, the higher complex shear modulus indicates the better resistance to rutting, while the lowest phase angle implies the better elastic behavior. Thus, the addition of sulfurificantly improved aging resistance of bitumen. Yan et al. (2021) assessed the performance of modified bitumen with EVA and low-density polyethylene (LDPE). In the study, EVA was introduced to a base binder at different proportions 0, 4, 6, 8% by binder weight. Furthermore, EVA modified-binder was also amended with 4% of LDPE. Researches noticed that the unaged modified bitumen with 4% LDPE showed the best complex shear modulus, phase angle, followed by the modified bitumen with 4% LDPE and 8% EVA. Senise et al. (2017) evaluated the performance of different polymers modified-bitumen (3% SBS/0.05% sulfur, 3% EVA/0.05% sulfur, and 3% EBA/0.05% sulfur). The findings of study demonstrated that SBS/sulfur showed the best complex shear modulus and phase angle, followed by EBA/sulfur, and EVA/sulfur modified bitumen.

5.2.5 Low-temperature performance of polymer-modified bitumen

The low-temperature performance of bitumen are evaluated by means of bending beam rheometer (BBR) and direct tension tester (DTT). The parameters of relaxation ratio (m-value) and elongation are used to identify the performance of bitumen at low temperature. The higher the m-value and elongation, the better the resistance of binder to cracking at low temperature. However, several studies investigated the performance of polymer-modified bitumen at low temperature. Liang et al. (2021) investigated low-temperature performance of bitumen modified with 3% SBR and different proportions of polyphosphoric acid (PPA) i.e. 0%–2% in 0.5% increment. The findings of bending beam rheometer test showed that the base binder at low temperature exhibited higher stiffens and lower relaxation rate (m-value) than the modified binder, while the addition of 3% improved the performance of binder at low-temperature, in which relaxation rate (m-value) was increased. Researchers stated that the optimum content of PPA is 1.5% by binder weight. Mazumder et al. (2020) indicated that modifying a base binder with 15% SIS displayed superior performance at low-temperature, in which the relaxation ratio (m-value) of 15% SIS modified-bitumen remarkably increased. Zhang et al. (2018) noticed that adding 0.8% PPA to 4% SEBES significantly enhanced m-value of aged and unaged bitumen. In a comparative study conducted by Jiang et al. (2017), a base binder was modified with EVA, SBS, and sulfur to investigate the impact of utilizing these polymers on the low-temperature performance of binder. Three types of modified binder were prepared. The first type was prepared by modifying base bitumen with 5% EVA, the second type was fabricated by amending base binder with 5% EVA and 2% SBS, the third type was equipped with introducing 0.05% sulfur to bitumen incorporated 5% EVA and 2% SBS. The low-temperature assessment findings demonstrated that the unaged and aged modified binder with EVA and SBS displayed the highest m-value, followed by the modified bitumen with EVA, SBS, and sulfur. Yan et al. (2021) assessed the low-temperature performance of modified bitumen with EVA and low-density polyethylene (LDPE). In the study, EVA was introduced to a base binder at different proportions, i.e. 0, 4, 6, 8% by binder weight. Thereafter, EVA modified binder was also amended with 4% of LDPE. Authors observed that unaged modified bitumen with 4% LDPE showed the best m-value, followed by the modified bitumen with 4% LDPE and 8% EVA. Table 5 summarizes the findings of the literature review.

5.2.6 Compatibilization of polymer-modified bitumen

Incompatibility is considered as the main drawback of polymer-amended bitumen However; different strategies have been used to decrease the incompatibility of polymer-modified bitumen such as adding waste oil, nanomaterials/nanoclay, sulfur, wax, polymers, and compatibilizers (reactive elastomeric terpolymer, PE-g-MA). It is documented that the addition of waste oil into polymer-amended bitumen significantly improves compatibility, aging resistance, and low-temperature performance. This is because adding oil reduces the viscosity of the major phase (bitumen) in the blend, which, in turn, decreases the phase separation. In addition, introducing oil to a modified binder with polymers reduces viscosity, softening point, rutting factor, and increases penetration, elastic recovery, and ductility. This is attributed to the improvement of elastic behavior of blend, which, in turn, increases the resistance of polymer blend to aging and improves low-temperature performance (Nie et al., 2020; Ren et al., 2021). Otherwise, the decrease in the performance of polymer-amended bitumen incorporating oil is attributed to the fact that the introduction of oil softens the blend. Furthermore, it is proven that adding nanomaterials such as (nanoclay, nanosilica, nano-ZnO, nano-TiO_2, and nano-$CaCO_3$) to a polymer-modified binder

improves compatibility, aging resistance, physical properties, and rheological properties. The improvement in the compatibility of polymer-amended binder is attributed to the reduction in dispersed phase by decreasing the interfacial tension (Luo et al., 2017; Peng et al. 202; Zhang et al., 2016). Moreover, introducing EVA to SBS/GTR/PE-amended base binder significantly enhances compatibility, physical properties, and rheological properties of the modified binder.

5.3 Discussions

This study aimed to conduct a bibliometric analysis and review on the applications of polymers as bitumen modifiers. However, the purpose of bibliometric analysis is to discover the trend and evolutionary of scientific research in a specific field. According to the trend of published documents, there is a notable increase in the number of published articles since the year of 2010 and forward. The remarkable increase in the published articles in terms of polymer-modified bitumen indicates the growing interest in modifying bitumen with polymer. This is because the addition of polymer into a base binder significantly improves the performance of the asphalt layer, and this in turn leads to protect environment and minimize the cost of repairing. Furthermore, according to the outputs of the bibliometric analysis, the top three contributing sources in terms of number of published documents are Construction and Building Material, Road Materials and Pavement Design, and Iop Conference Series Materials Science and Engineering, with the number of 162, 71, and 65, respectively. However, there should be an inspirational encouragement in terms of publishing documents related to the performance of polymer-amended bitumen through launching special issues. On the other hand, the outputs of the bibliometric analysis showed that the top contributing organizations and countries based on the number of published documents are University of Huelva, University of Alberta, University of Nottingham, China, Russia, and Iran, respectively. This indicates that the developed countries are the most contributing in terms of the published articles. The low number of published researches from developing countries as compared to developed countries may be due to a lack of interest in publishing findings or modifying bitumen with polymer. Thus, there should be a constant stimulation for universities in developing to impose the culture of modifying bitumen with polymers through clarification the benefits of polymer-amended bitumen with regard to saving natural sources and minimizing costs of repairing/rehabilitation of the asphalt layer. Furthermore, there should be a premium support for the universities that suffer from a lack of equipment in developing countries. In addition, strenuous efforts should be made in promoting universities in developing countries to publish articles and case studies with regard to performance of polymer-modified bitumen such as organizing scientific conferences and launch special issues with premium offers.

On the other hand, another objective of this study is to introduce a review on the applications of polymers in bitumen. According to the review studies, the addition of polymer into a base binder notably enhances physical properties, rutting resistance, and fatigue resistance of modified binder. This is because the addition of polymer stiffs the bitumen, which, in turn, improve the performance of modified bitumen at high temperatures. Otherwise, the main drawbacks of amending bitumen with polymers are incompatibility, degradation, and low-temperature performance. The incompatibility of polymer-amended bitumen is occurred by the difference in polarity and densities, in which the component of polymer is not attractive to bitumen, while the difference in densities may make polymer compositions floats or sinks in the liquid of bitumen. However, the degradation of polymer-modified bitumen is attributed to the phenomenon of aging. The increase in temperature of mixing/storing and the exposure of polymer-modified bitumen to oxygen, light of Sun, and environmental factors lead to aging/degradation of polymer-amended bitumen. Furthermore, the addition of polymer to a base binder may negatively affects the low-temperature performance of modified bitumen; this is because modifying bitumen with polymer stiffs the bitumen, which, in turn, decreases the elastic behavior of amended bitumen (Zhang et al., 2012; Bai, 2017; Hao et al., 2017; Liang et al., 2017; Kim et al., 2019; Ji et al., 2020; Mazumder et al., 2020; Shah and Mir. 2020; Li et al., 2021; Tang et al., 2021). Otherwise, it is proven that the addition of waste oil to polymer-modified binder significantly enhances compatibility and resistance to aging. This is because the introduction of oil to polymer-amended bitumen decreases the viscosity of the blend and improves elasticity of blend. This in turn notably reduces the phase separation of the blend. In addition, the addition of nanomaterials to polymer-modified improves compatibility, resistance to aging, and resistance to degradation. This is because the addition of nanomaterials reduces the domain/dispersed phase through decreasing interfacial tension between components of blend. Additionally, nanomaterials work as reinforced materials, which, in turn, improve the performance of polymer in terms of resistance to degradation (Luo et al., 2017; Peng et al. 202; Zhang et al., 2016; Nie et al., 2020; Ren et al., 2021). However, Table 5 summarizes the findings of the review studies.

6 Research gaps and recommendations

The factors of processing/mixing protocol (mixing sequence, viscosity of blend, shear rate, and time of mixing) play a major role on quality of compatibility and performance of nanoparticles-modified polymer/bitumen. The proper the sequence of blending, longer time of mixing, lower viscosity of blend, and higher shear rate, the better the compatibility of blend. However, in accordance with the review studies, the addition of nanomaterials/sulfur to polymer-modified bitumen contributes toward the improvement of compatibility. In most studies, modifying bitumen with polymers and nanomaterials is started by blending bitumen with polymer, and then nanomaterials are introduced to the blend of polymer-amended bitumen. However, the preparation of polymer-modified bitumen is done by mixing bitumen with polymer at high mixing temperature 170°C–180°C by means of high shear mixer at a shear rate of 500–5000 RPM for 30–90 min. Thereafter, nanomaterials are added to the blend of polymer and bitumen, followed by blending with the same conditions of mixing polymer with bitumen in terms of mixing temperature, shear rate, and

blending time. Therefore, there is a lack of information in terms of studying the effect of preparation protocol of the addition of nanomaterials into polymer-amended bitumen. This is because homogeneity/compatibility is highly affected by mixing sequence, viscosity of blend, shear rate, and time of mixing.

On the other hand, incompatibility/separation between polymer and bitumen occurs by the differences in the densities, in which the lighter additive floats to the top of stored bitumen at elevated temperature and denser modifier sinks to the bottom of stored bitumen. However, according to ASTM D7173, the compatibility/separation in polymer-modified bitumen is assessed through placing a filled aluminum tube (25 mm in diameter and 125–140 mm in length) with 50 g of bitumen vertically in an oven at a temperature of 163°C ± 5°C for 48 h, followed by placing the aluminum tube in a freezer at a temperature of 10°C ± 10°C for 4 h. Subsequently, the aluminum tube is then cut into three equal pieces. Thereafter, the difference between softening point of the top piece and the bottom piece is measured, while the centerpiece is discarded. It is recommended that the difference in softening point should be less than 2.2°C, in which polymer-modified binder is considered compatible. However, it is reported that the addition of polymer to a base binder shows poor compatibility because polymer floats to the top of aluminum tube. Therefore, the softening point of the top aluminum tube piece is much higher than the softening point of the bottom piece. Otherwise, it is reported that introducing nanoclay to polymer-modified bitumen significantly increase the softening point of the aluminum tube bottom as compared to the softening aluminum tube top (Zou et al., 2017). This is because the sinks of nanocaly enhances the compatibility. This enhancement may attributed to the dives of nanoclay to bottom of aluminum tube because nanoclay are denser than binder, while polymer floats to the top of aluminum tube because of its low density. Thus, the softening point at the bottom of aluminum tube is enhanced due to nanoclay, and the difference between softening point between the top and bottom of aluminum is minimized. Therefore, it can be said that the softening point of aluminum tube centerpiece should be evaluated and compared with softening point of top and bottom of aluminum tube.

Additionally, density of modifier play a vital role in terms of compatibility. In other words, the modifier will float if its density less than that of bitumen, while the modifier will sink if the modifier density is higher than that of bitumen, and this will make significant changes in the performance of polymer-modified bitumen. Therefore, the density of polymer should be equal to that of bitumen to avoid the separation by the change in densities. However, it is difficult to obtain a polymer with a density similar to that of binder. Therefore, the density of polymer can be obtained by means of blending polymer with another polymer or nanomaterials. The density of polymer blend can be predicted using the equation expressed below. This equation aims to identify the density of composite materials.

$$\mathrm{Gsb} = \frac{\mathbf{P_{A+}P_{B+\ldots}}}{\frac{\mathbf{P_A}}{\mathbf{G_A}}+\frac{\mathbf{P_B}}{\mathbf{G_B}}+\ldots} \tag{3}$$

Where Gsb is specific gravity of composite material, $\boldsymbol{P_A}$ $\boldsymbol{P_B}$. are weight by percent of each material, while $\boldsymbol{G_A}$,$\boldsymbol{G_B}$. refers to the specific gravity of each material.

Clearly, if bitumen needs to be amended with the polymer of LDPE and nanomaterials, in which the density of LDPE is 0.92 g/$\boldsymbol{cm^3}$ and density of nanomaterials is 1.40 g/$\boldsymbol{cm^3}$. Eq. 3 is used by means of trial and error method to identify the proportion of LDPE and nanomaterials to produce a composite modifier with a density similar to that of bitumen (1.03 g/$\boldsymbol{cm^3}$). As can be seen, about 31% of LDPE components should be replaced with nanomaterials to produce a composite material with a density similar to that of bitumen. In other words, if bitumen will be modified with 5% of LDPE, this percentage should be replaced with 31% of nanomaterials. Therefore, the proportion of LDPE will be 3.45%, while the proportion of nanomaterials will be 1.55%.

$$\mathrm{Gsb} = \frac{\mathbf{69+31}}{\frac{\mathbf{69}}{\mathbf{092}}+\frac{\mathbf{31}}{\mathbf{1.40}}} \cong \mathbf{1.03}\,\mathrm{g}\Big/\boldsymbol{cm^3}$$

Similarly, the density of a polymer can be amended by adding another type of polymer, i.e., density of LDPE (0.92 g/$\boldsymbol{cm^3}$) need to be amended by the addition of PVC (1.20 g/$\boldsymbol{cm^3}$), and EVA (0.95 g/$\boldsymbol{cm^3}$) as compatibilizer. According to the equation of composite materials density, the proportions of LDPE, PVC, and EVA to produce a composite modifier with a density similar to that of bitumen should be 50, 45, and 5%, respectively. However, it should be indicated that the addition of EVA is to enhance compatibility of polymer blend. Therefore, another additive such as nanomaterials/waste oil should be added to the blend of bitumen and polymer composite to improve compatibility.

Furthermore, it should be noted that mixing protocols (mixing sequence, temperature of blending, time of mixing, and share rate) play a vital role in the quality of compatibility of blend. Regarding the sequence of mixing, the less attractive components of blend should be blended together first, followed by blending the premixed components with the attractive components.

Based on the gaps mentioned above, the following recommendations are proposed.

- Effects of mixing sequence on the compatibility of blend should be investigated. In other words, the first blend should be started by modifying bitumen with nanomaterials, followed by the addition of polymer to the blend. Similarly, the second blend should be started by the mixing polymer with nanomaterials, followed by introducing bitumen to the blend. The third blend should be started by mixing bitumen with polymer, followed by the addition of nanomaterials. Thereafter, a comparative analysis should be done for the three blends to identify the suitable mixing sequence that achieve the best compatibility.
- Different mixing temperature for the blend should be studied to identify the appropriate mixing temperature that produce a compatible blend. In addition, the effects of the share rate and mixing time on the compatibility of polymer-amended bitumen should be investigated.
- Density of additive should be taking into account to avoid separation by the difference in densities. However, the density of modifier should be amended to be similar to that of bitumen by adding polymers/nanomaterials. Moreover, the softening point of aluminum tube centerpiece should be measured to introduce a better evaluation for compatibility between polymer-modified binder and nanomaterials/nanoclay.
- The use of antioxidants in polymer-modified binder should be studied. Furthermore, the performance of modified

bitumen with high thermal stable property of plastics such as polyetherimide (PEI), polyether ether ketone (PEEK), polybenzimidazole (PBI), and polytetrafluoroethylene (PTFE) should be evaluated.

7 Conclusion

This study aimed to introduce a bibliometric analysis and review on the polymer-modified bitumen. However, the conclusions of the article can be stated as follows.

- The trend of annual publishing in a steady increase, in particular for the last 7 years. Additionally, the most contributing organizations and countries are from the developed countries.
- The addition of polymer to a base binder notably enhance physical and rheological properties of binder. Otherwise, introducing polymer to the base binder negatively affects compatibility.
- Subjecting polymer-modified bitumen to aging leads to the degradation of polymer. In addition, elastic behavior of amended bitumen with polymers decreases by aging.
- The addition of waste oil into polymer-amended binder significantly improves compatibility and aging resistance of modified binder. Additionally, introducing nanoparticles/sulfur to polymer-amended binder significantly enhances compatibility.

Author contributions

AA: conceptualizing, analysis, investigation, and writing—original draft. HK: editing and reviewing. MI and NM, editing, and reviewing. YG: editing, reviewing, and funding. All authors contributed to the article and approved the submitted version.

Acknowledgments

The authors extend their appreciation to Lulea University of Technology for the financial and technical support.

Conflict of interest

The authors declare that the research was conducted in the absence of any commercial or financial relationships that could be construed as a potential conflict of interest.

Publisher's note

All claims expressed in this article are solely those of the authors and do not necessarily represent those of their affiliated organizations, or those of the publisher, the editors and the reviewers. Any product that may be evaluated in this article, or claim that may be made by its manufacturer, is not guaranteed or endorsed by the publisher.

References

Ajitha, A. R., Mathew, L. P., and Thomas, S. (2020). "Compatibilization of polymer blends by micro and nanofillers," in *Compatibilization of polymer blends* (Amsterdam, Netherlands: Elsevier), 179–203.

Ajitha, A. R., and Thomas, S. (2020a). *Compatibilization of polymer blends*. Amsterdam, Netherlands: Elsevier, 640.

Ajitha, A. R., and Thomas, S. (2020b). "Introduction: Polymer blends, thermodynamics, miscibility, phase separation, and compatibilization," in *Compatibilization of polymer blends* (Amsterdam, Netherlands: Elsevier), 1–29.

Albdiry, M. T., Yousif, B. F., Ku, H., and Lau, K. T. (2013). A critical review on the manufacturing processes in relation to the properties of nanoclay/polymer composites. *J. Compos. Mater.* 47 (9), 1093–115.

Al-Malaika, S. (1998). "Antioxidants: An overview," in *Plastics additives: An AZ reference*. United Kingdom: Springer, 55–72.

Al-Mansob, R. A., Ismail, A., Alduri, A. N., Azhari, C. H., Karim, M. R., and Yusoff, N. I. M. (2014). Physical and rheological properties of epoxidized natural rubber modified bitumens. *Constr. Build. Mater.* 63, 242–248. doi:10.1016/j.conbuildmat.2014.04.026

Alnadish, A. M., Aman, M. Y., Katman, H. Y. B., and Ibrahim, M. R. (2020b). Laboratory assessment of the performance and elastic behavior of asphalt mixtures containing steel slag aggregate and synthetic fibers. *Int. J. Pavement Res. Technol.* 14, 473–481. doi:10.1007/s42947-020-1149-y

Alnadish, A. M., Aman, M. Y., Katman, H. Y. B., and Ibrahim, M. R. (2021). Characteristics of warm mix asphalt incorporating coarse steel slag aggregates. *Appl. Sci.* 11 (8), 3708. doi:10.3390/app11083708

Alnadish, A. M., Aman, M. Y., Katman, H. Y. B., and Ibrahim, M. R. (2020a). Influence of the long-term oven aging on the performance of the reinforced asphalt mixtures. *Coatings* 10 (10), 953. doi:10.3390/coatings10100953

Alnadish, A. M., Aman, M. Y., Katman, H. Y. B., and Ibrahim, M. R. (2022). Laboratory evaluation of fiber-modified asphalt mixtures incorporating steel slag aggregates. *CMC-Computers Mater. Continua* 70 (3), 5967–5990. doi:10.32604/cmc.2022.017387

Alnadish, A. M., Singh, N. S. S., and Alawag, A. M. (2023). Applications of synthetic, natural, and waste fibers in asphalt mixtures: A citation-based review. *Polymers* 15 (4), 1004. doi:10.3390/polym15041004

Ashraf, M. A., Peng, W., Zare, Y., and Rhee, K. Y. (2018). Effects of size and aggregation/agglomeration of nanoparticles on the interfacial/interphase properties and tensile strength of polymer nanocomposites. *Nanoscale Res. Lett.* 13 (1), 214–217. doi:10.1186/s11671-018-2624-0

Atta, E. M., Mohamed, N. H., and Silaev, A. A. A. (2017). Antioxidants: An overview on the natural and synthetic types. *Eur. Chem. Bull.* 6 (8), 365–375. doi:10.17628/ecb.2017.6.365-375

Bachir, D. S., Dekhli, S., and Mokhtar, K. A. (2016). Rheological evaluation of ageing properties of SEBS polymer modified bitumens. *Period. Polytech. Civ. Eng.* 60 (3), 397–404. doi:10.3311/ppci.7853

Bacskay, G. B., Reimers, J. R., and Nordholm, S. (1997). The mechanism of covalent bonding. *J. Chem. Educ.* 74 (12), 1494. doi:10.1021/ed074p1494

Bai, M. (2017). Investigation of low-temperature properties of recycling of aged SBS modified asphalt binder. *Constr. Build. Mater.* 150, 766–773. doi:10.1016/j.conbuildmat.2017.05.206

Behnood, A., and Gharehveran, M. M. (2019). Morphology, rheology, and physical properties of polymer-modified asphalt binders. *Eur. Polym. J.* 112, 766–791. doi:10.1016/j.eurpolymj.2018.10.049

Behzadfar, E., and Hatzikiriakos, S. G. (2013). Viscoelastic properties and constitutive modelling of bitumen. *Fuel* 108, 391–399. doi:10.1016/j.fuel.2012.12.035

Beyler, C. L., and Hirschler, M. M. (2002). Thermal decomposition of polymers. *SFPE Handb. fire Prot. Eng.* 2 (7), 111–131.

Biesenberger, J. A., and Sebastian, D. H. (1983). "Principles of polymerization engineering," in *Princ of polym eng* (Hoboken, NJ: John Wiley and Sons).

Boczkaj, G., Fernandes, A., and Gągol, M. (2017). "Studies on treatment of bitumen effluents by means of advanced oxidation processes (AOPs) in basic pH conditions," in *Frontiers in wastewater treatment and modelling: Ficwtm 2017* (Cham: Springer International Publishing), 1, 331–336.

Brasileiro, L., Moreno-Navarro, F., Tauste-Martínez, R., Matos, J., and Rubio-Gámez, M. D. C. (2019). Reclaimed polymers as asphalt binder modifiers for more sustainable roads: A review. *Sustainability* 11 (3), 646. doi:10.3390/su11030646

Brito, J., Hlushko, H., Abbott, A., Aliakseyeu, A., Hlushko, R., and Sukhishvili, S. A. (2021). Integrating antioxidant functionality into polymer materials: Fundamentals, strategies, and applications. *ACS Appl. Mater. Interfaces* 13 (35), 41372–41395. doi:10.1021/acsami.1c08061

Brûlé, B. (1996). Polymer-modified asphalt cements used in the road construction industry: basic principles. *Transp. Res. Rec.* 1535 (1), 48–53.

Bulatović, V. O., Rek, V., and Marković, K. J. (2012). Polymer modified bitumen. *Mater. Res. innovations* 16 (1), 1–6. doi:10.1179/1433075x11y.0000000021

Chan, M. L., Lau, K. T., Wong, T. T., Ho, M. P., and Hui, D. (2011). Mechanism of reinforcement in a nanoclay/polymer composite. *Compos. Part B Eng.* 42 (6), 1708–1712. doi:10.1016/j.compositesb.2011.03.011

Chen, C. C., and White, J. L. (1993). Compatibilizing agents in polymer blends: Interfacial tension, phase morphology, and mechanical properties. *Polym. Eng. Sci.* 33 (14), 923–930. doi:10.1002/pen.760331409

Chrissafis, K., and Bikiaris, D. (2011). Can nanoparticles really enhance thermal stability of polymers? Part I: An overview on thermal decomposition of addition polymers. *Thermochim. Acta* 523 (1-2), 1–24. doi:10.1016/j.tca.2011.06.010

Claine, P. J. (1984). Chemical composition of asphalt as related to asphalt durability: State of the Art. *Transp. Res. Rec.* 999, 13–30.

Damiati, L. A., El-Yaagoubi, M., Damiati, S. A., Kodzius, R., Sefat, F., and Damiati, S. (2022). Role of polymers in microfluidic devices. *Polymers* 14 (23), 5132. doi:10.3390/polym14235132

Daniels, C. A. (1989). *Polymers: Structure and properties*. Boca Raton, FL: CRC Press.

Fakirov, S. (2006). *Handbook of condensation thermoplastic elastomers*. Hoboken, NJ: John Wiley and Sons.

Fred-Ahmadu, O. H., Bhagwat, G., Oluyoye, I., Benson, N. U., Ayejuyo, O. O., and Palanisami, T. (2020). Interaction of chemical contaminants with microplastics: Principles and perspectives. *Sci. Total Environ.* 706, 135978. doi:10.1016/j.scitotenv.2019.135978

Goodrich, J. L., Goodrich, J. E., and Kari, W. J. (1986). "Asphalt composition tests: Their application and relation to field performance," in 65th Annual Meeting of the Transportation Research Board, Washington, January 13-16, 1986.

Gu, L., Chen, L., Zhang, W., Ma, H., and Ma, T. (2019). Mesostructural modeling of dynamic modulus and phase angle master curves of rubber modified asphalt mixture. *Materials* 12 (10), 1667. doi:10.3390/ma12101667

Guo, F., Aryana, S., Han, Y., and Jiao, Y. (2018). A review of the synthesis and applications of polymer–nanoclay composites. *Appl. Sci.* 8 (9), 1696. doi:10.3390/app8091696

Guo, H., Yue, L., Rui, G., and Manas-Zloczower, I. (2019). Recycling poly (ethylene-vinyl acetate) with improved properties through dynamic cross-linking. *Macromolecules* 53 (1), 458–464. doi:10.1021/acs.macromol.9b02281

Gupta, R. K., Dunderdale, G. J., England, M. W., and Hozumi, A. (2017). Oil/water separation techniques: A review of recent progresses and future directions. *J. Mater. Chem. A* 5 (31), 16025–16058. doi:10.1039/c7ta02070h

Hao, G., Huang, W., Yuan, J., Tang, N., and Xiao, F. (2017). Effect of aging on chemical and rheological properties of SBS modified asphalt with different compositions. *Constr. Build. Mater.* 156, 902–910. doi:10.1016/j.conbuildmat.2017.06.146

He, Y., Li, H., Xiao, X., and Zhao, X. (2021). Polymer degradation: Category, mechanism and development prospect. *E3S Web Conf.* 290, 01012. doi:10.1051/e3sconf/202129001012

Hirao, A., Hayashi, M., Loykulnant, S., Sugiyama, K., Ryu, S. W., Haraguchi, N., et al. (2005). Precise syntheses of chain-multi-functionalized polymers, star-branched polymers, star-linear block polymers, densely branched polymers, and dendritic branched polymers based on iterative approach using functionalized 1, 1-diphenylethylene derivatives. *Prog. Polym. Sci.* 30 (2), 111–182. doi:10.1016/j.progpolymsci.2004.12.002

Hoti, G., Caldera, F., Cecone, C., Rubin Pedrazzo, A., Anceschi, A., Appleton, S. L., et al. (2021). Effect of the cross-linking density on the swelling and rheological behavior of ester-bridged β-cyclodextrin nanosponges. *Materials* 14 (3), 478. doi:10.3390/ma14030478

Hu, M., Sun, G., Sun, D., Zhang, Y., Ma, J., and Lu, T. (2020). Effect of thermal aging on high viscosity modified asphalt binder: Rheological property, chemical composition and phase morphology. *Constr. Build. Mater.* 241, 118023. doi:10.1016/j.conbuildmat.2020.118023

Huang, S., Kong, X., Xiong, Y., Zhang, X., Chen, H., Jiang, W., et al. (2020). An overview of dynamic covalent bonds in polymer material and their applications. *Eur. Polym. J.* 141, 110094. doi:10.1016/j.eurpolymj.2020.110094

Ishaq, M. A., Venturini, L., and Giustozzi, F. (2022). Correlation between rheological rutting tests on bitumen and asphalt mix flow number. *Int. J. Pavement Res. Technol.* 15 (6), 1297–1316. doi:10.1007/s42947-021-00089-z

Jarukumjorn, K. (2007). *Compatibilization of recycled high density polyethylene (HDPE)/polyethylene terephthalate (PET) blends*. Suranari, Thailand: Suranaree University of Technology.

Ji, B., Lee, S. J., Mazumder, M., Lee, M. S., and Kim, H. H. (2020). Deep regression prediction of rheological properties of SIS-modified asphalt binders. *Materials* 13 (24), 5738. doi:10.3390/ma13245738

Jia, Y., Cao, R. J., and Li, B. (2005). "Superpave fundamentals reference manual," in *NHI course*. United States: Federal Highway Administration.

Jiang, Z., Hu, C., Easa, S. M., Zheng, X., and Zhang, Y. (2017). Evaluation of physical, rheological, and structural properties of vulcanized EVA/SBS modified bitumen. *J. Appl. Polym. Sci.* 134 (21), 44850. doi:10.1002/app.44850

Kalantar, Z. N., Karim, M. R., and Mahrez, A. (2012). A review of using waste and virgin polymer in pavement. *Constr. Build. Mater.* 33, 55–62. doi:10.1016/j.conbuildmat.2012.01.009

Keymanesh, M. R., Ziari, H., Damyar, B., and Shahriari, N. (2017). Effect of waste EVA (ethylene vinyl acetate) and waste CR (crumb rubber) on characteristics of bitumen. *Petroleum Sci. Technol.* 35 (22), 2121–2126. doi:10.1080/10916466.2017.1384840

Kim, H. H., Mazumder, M., Lee, M. S., and Lee, S. J. (2019). Evaluation of high-performance asphalt binders modified with SBS, SIS, and GTR. *Adv. Civ. Eng.* 2019, 1–11. doi:10.1155/2019/2035954

Kong, P., Xu, G., Chen, X., Shi, X., and Zhou, J. (2021). Effect of different high viscosity modifiers on rheological properties of high viscosity asphalt. *Front. Struct. Civ. Eng.* 15 (6), 1390–1399. doi:10.1007/s11709-021-0775-z

Koning, C., Van Duin, M., Pagnoulle, C., and Jerome, R. (1998). Strategies for compatibilization of polymer blends. *Prog. Polym. Sci.* 23 (4), 707–757. doi:10.1016/s0079-6700(97)00054-3

Lesueur, D. (2009). The colloidal structure of bitumen: Consequences on the rheology and on the mechanisms of bitumen modification. *Adv. colloid interface Sci.* 145 (1-2), 42–82. doi:10.1016/j.cis.2008.08.011

Li, Q., Zhang, H., and Chen, Z. (2021). Improvement of short-term aging resistance of styrene-butadiene rubber modified asphalt by Sasobit and epoxidized soybean oil. *Constr. Build. Mater.* 271, 121870. doi:10.1016/j.conbuildmat.2020.121870

Liang, M., Xin, X., Fan, W., Zhang, J., Jiang, H., and Yao, Z. (2021). Comparison of rheological properties and compatibility of asphalt modified with various polyethylene. *Int. J. Pavement Eng.* 22 (1), 11–20. doi:10.1080/10298436.2019.1575968

Liang, P., Liang, M., Fan, W., Zhang, Y., Qian, C., and Ren, S. (2017). Improving thermo-rheological behavior and compatibility of SBR modified asphalt by addition of polyphosphoric acid (PPA). *Constr. Build. Mater.* 139, 183–192. doi:10.1016/j.conbuildmat.2017.02.065

Liu, F., Zhou, Z., and Zhang, X. (2022). Construction of complex shear modulus and phase angle master curves for aging asphalt binders. *Int. J. Pavement Eng.* 23 (3), 536–544. doi:10.1080/10298436.2020.1758934

Loste, J., Lopez-Cuesta, J. M., Billon, L., Garay, H., and Save, M. (2019). Transparent polymer nanocomposites: An overview on their synthesis and advanced properties. *Prog. Polym. Sci.* 89, 133–158. doi:10.1016/j.progpolymsci.2018.10.003

Lu, X., Isacsson, U., and Ekblad, J. (1999). Phase separation of SBS polymer modified bitumens. *J. Mater. Civ. Eng.* 11 (1), 51–57. doi:10.1061/(asce)0899-1561(1999)11:1(51)

Luo, W., Zhang, Y., and Cong, P. (2017). Investigation on physical and high temperature rheology properties of asphalt binder adding waste oil and polymers. *Constr. Build. Mater.* 144, 13–24. doi:10.1016/j.conbuildmat.2017.03.105

Mane, S., Ponrathnam, S., and Chavan, N. (2015). Effect of chemical cross-linking on properties of polymer microbeads: A review. *Can. Chem. Trans.* 3 (4), 473–485. doi:10.13179/canchemtrans.2015.03.04.0245

Mao, H., Yang, Y., Zhang, H., Zhang, J., and Huang, Y. (2020). A critical review of the possible effects of physical and chemical properties of subcritical water on the performance of water-based drilling fluids designed for ultra-high temperature and ultra-high pressure drilling applications. *J. Petroleum Sci. Eng.* 187, 106795. doi:10.1016/j.petrol.2019.106795

Martinho, F. C., Picado-Santos, L. G., Lemos, F. M., Lemos, M. A. N., and Santos, E. R. (2022). Using plastic waste in a circular economy approach to improve the properties of bituminous binders. *Appl. Sci.* 12 (5), 2526. doi:10.3390/app12052526

Mazumder, M., Siddique, A., Ahmed, R., Lee, S. J., and Lee, M. S. (2020). Rheological and morphological characterization of Styrene-Isoprene-Styrene (SIS) modified asphalt binder. *Adv. Civ. Eng.* 2020, 1–13. doi:10.1155/2020/8877371

Mochane, M. J., Sefadi, J. S., Motsoeneng, T. S., Mokoena, T. E., Mofokeng, T. G., and Mokhena, T. C. (2020). The effect of filler localization on the properties of biopolymer blends, recent advances: A review. *Polym. Compos.* 41 (7), 2958–2979. doi:10.1002/pc.25590

Munera, J. C., and Ossa, E. A. (2014). Polymer modified bitumen: Optimization and selection. *Mater. Des.* 62, 91–97. doi:10.1016/j.matdes.2014.05.009

Nie, X., Li, Z., Yao, H., Hou, T., Zhou, X., and Li, C. (2020). Waste bio-oil as a compatibilizer for high content SBS modified asphalt. *Petroleum Sci. Technol.* 38 (4), 316–322. doi:10.1080/10916466.2019.1703741

Nizamuddin, S., Boom, Y. J., and Giustozzi, F. (2021). Sustainable polymers from recycled waste plastics and their virgin counterparts as bitumen modifiers: A comprehensive review. *Polymers* 13 (19), 3242. doi:10.3390/polym13193242

Nizamuddin, S., Jamal, M., Gravina, R., and Giustozzi, F. (2020). Recycled plastic as bitumen modifier: The role of recycled linear low-density polyethylene in the modification of physical, chemical and rheological properties of bitumen. *J. Clean. Prod.* 266, 121988. doi:10.1016/j.jclepro.2020.121988

Oliphant, K., Rajalingam, P., Baker, W. E., and La Mantia, F. P. (1993). "Chapter 11—ground rubber tire-polymer composites," in *Recycling of plastic materials*. Editor F. P. La Mantia (Toronto, ON, Canada: ChemTec Publishing), 153–170.

Oliviero Rossi, C., Teltayev, B., and Angelico, R. (2017). Adhesion promoters in bituminous road materials: A review. *Appl. Sci.* 7 (5), 524. doi:10.3390/app7050524

Padaki, M., Murali, R. S., Abdullah, M. S., Misdan, N., Moslehyani, A., Kassim, M. A., et al. (2015). Membrane technology enhancement in oil–water separation. A review. *Desalination* 357, 197–207. doi:10.1016/j.desal.2014.11.023

Peng, C., Guo, C., You, Z., Xu, F., Ma, W., You, L., et al. (2020). The effect of waste engine oil and waste polyethylene on UV aging resistance of asphalt. *Polymers* 12 (3), 602. doi:10.3390/polym12030602

Pereira, L., Freire, A. C., da Costa, M. S., Antunes, V., Quaresma, L., and Micaelo, R. (2018). Experimental study of the effect of filler on the ductility of filler-bitumen mastics. *Constr. Build. Mater.* 189, 1045–1053. doi:10.1016/j.conbuildmat.2018.09.063

Pérez-Lepe, A., Martínez-Boza, F. J., and Gallegos, C. (2005). Influence of polymer concentration on the microstructure and rheological properties of high-density polyethylene (HDPE)-modified bitumen. *Energy and fuels* 19 (3), 1148–1152. doi:10.1021/ef0497513

Pérez-Lepe, A., Martínez-Boza, F. J., Attané, P., and Gallegos, C. (2006). Destabilization mechanism of polyethylene-modified bitumen. *J. Appl. Polym. Sci.* 100 (1), 260–267. doi:10.1002/app.23091

Pérez-Lepe, A., Martínez-Boza, F. J., and Gallegos, C. (2007). High temperature stability of different polymer-modified bitumens: A rheological evaluation. *J. Appl. Polym. Sci.* 103 (2), 1166–1174. doi:10.1002/app.25336

Porto, M., Caputo, P., Loise, V., Eskandarsefat, S., Teltayev, B., and Oliviero Rossi, C. (2019). Bitumen and bitumen modification: A review on latest advances. *Appl. Sci.* 9 (4), 742. doi:10.3390/app9040742

Prosperi, E., and Bocci, E. (2021). A review on bitumen aging and rejuvenation chemistry: Processes, materials and analyses. *Sustainability* 13 (12), 6523. doi:10.3390/su13126523

Pszczola, M., Jaczewski, M., Rys, D., Jaskula, P., and Szydlowski, C. (2018). Evaluation of asphalt mixture low-temperature performance in bending beam creep test. *Materials* 11 (1), 100. doi:10.3390/ma11010100

Pyshyev, S., Gunka, V., Grytsenko, Y., and Bratychak, M. (2016). *Polymer modified bitumen*. Ukraine: National Aviation University.

Read, J., Whiteoak, D., and Hunter, R. N. (2003). *The shell bitumen handbook*. Westerkirk, UK: Thomas Telford.

Rafiee, R., and Shahzadi, R. (2019). Mechanical properties of nanoclay and nanoclay reinforced polymers: a review. *Polym. Compos.* 40 (2), 431–445.

Redelius, P., and Soenen, H. (2015). Relation between bitumen chemistry and performance. *Fuel* 140, 34–43. doi:10.1016/j.fuel.2014.09.044

Ren, S., Liu, X., Fan, W., Qian, C., Nan, G., and Erkens, S. (2021). Investigating the effects of waste oil and styrene-butadiene rubber on restoring and improving the viscoelastic, compatibility, and aging properties of aged asphalt. *Constr. Build. Mater.* 269, 121338. doi:10.1016/j.conbuildmat.2020.121338

Robeson, L. (2014). Historical perspective of advances in the science and technology of polymer blends. *Polymers* 6 (5), 1251–1265. doi:10.3390/polym6051251

Sarath, C. C., Shanks, R. A., and Thomas, S. (2014). "Polymer blends," in *Nanostructured polymer blends* (Norwich, NY: William Andrew Publishing), 1–14.

Sengoz, B., and Isikyakar, G. (2008). Evaluation of the properties and microstructure of SBS and EVA polymer modified bitumen. *Constr. Build. Mater.* 22 (9), 1897–1905. doi:10.1016/j.conbuildmat.2007.07.013

Senise, S., Carrera, V., Navarro, F. J., and Partal, P. (2017). Thermomechanical and microstructural evaluation of hybrid rubberised bitumen containing a thermoplastic polymer. *Constr. Build. Mater.* 157, 873–884. doi:10.1016/j.conbuildmat.2017.09.126

Senthil Kumar, M. S., Mohana Sundara Raju, N., Sampath, P. S., and Chithirai Pon Selvan, M. (2018). Influence of nanoclay on mechanical and thermal properties of glass fiber reinforced polymer nanocomposites. *Polym. Compos.* 39 (6), 1861–1868. doi:10.1002/pc.24139

Shah, P. M., and Mir, M. S. (2020). Performance of OMMT/SBS on the rheological properties of asphalt binder. *Korea-Australia Rheology J.* 32, 235–242. doi:10.1007/s13367-020-0022-5

Shanks, R. A. (2020). "Concepts and classification of compatibilization processes," in *Compatibilization of polymer blends* (Amsterdam, Netherlands: Elsevier), 31–56.

Shanks, R. (2012). "Thermoplastic elastomers," in *Thermoplastic elastomers* (London, UK: InTech), 137–154.

Sirin, O., Paul, D. K., and Kassem, E. (2018). State of the art study on aging of asphalt mixtures and use of antioxidant additives. *Adv. Civ. Eng.* 2018, 1–18. doi:10.1155/2018/3428961

Soleimani, N., Khalili, S. M., Farsani, R. E., and Hedayatnasab, Z. (2012). Mechanical properties of nanoclay reinforced polypropylene composites at cryogenic temperature. *J. Reinf. Plastics Compos.* 31 (14), 967–976. doi:10.1177/0731684412450349

Subhy, A. (2017). Advanced analytical techniques in fatigue and rutting related characterisations of modified bitumen: Literature review. *Constr. Build. Mater.* 156, 28–45. doi:10.1016/j.conbuildmat.2017.08.147

Tang, N., Huang, W., and Hao, G. (2021). Effect of aging on morphology, rheology, and chemical properties of highly polymer modified asphalt binders. *Constr. Build. Mater.* 281, 122595. doi:10.1016/j.conbuildmat.2021.122595

Tarefder, R. A., Zaman, A. M., and Uddin, W. (2010). Determining hardness and elastic modulus of asphalt by nanoindentation. *Int. J. Geomechanics* 10 (3), 106–116. doi:10.1061/(asce)gm.1943-5622.0000048

Teltayev, B., and Radovskiy, B. (2018). Predicting thermal cracking of asphalt pavements from bitumen and mix properties. *Road Mater. Pavement Des.* 19 (8), 1832–1847. doi:10.1080/14680629.2017.1350598

Terada, N., Kouge, K., Komaguchi, K., Hayakawa, S., and Tsutsumi, H. (2020). Thermal stability change of insoluble sulfur by a heat treatment and its mechanism study. *Anal. Sci.* 36 (1), 75–79. doi:10.2116/analsci.19sap05

Thenoux, G. (1987). Chemical characterization of asphalt cements using chromatographic techniques: Relation to rheological properties and field performance. Available at: https://ir.library.oregonstate.edu/downloads/sf268776w (Accessed April 30, 1987).

Utracki, L. A., and Wilkie, C. A. (2002). *Polymer blends handbook*, 1. Dordrecht: Kluwer academic publishers, 2.

Visan, A. I., Popescu-Pelin, G., and Socol, G. (2021). Degradation behavior of polymers used as coating materials for drug delivery—A basic review. *Polymers* 13 (8), 1272. doi:10.3390/polym13081272

Waheed, M. A., and Oni, A. O. (2015). Performance improvement of a crude oil distillation unit. *Appl. Therm. Eng.* 75, 315–324. doi:10.1016/j.applthermaleng.2014.10.078

Xie, X., Hui, T., Luo, Y., Li, H., Li, G., and Wang, Z. (2020). Research on the properties of low temperature and anti-UV of asphalt with nano-ZnO/nano-TiO2/copolymer SBS composite modified in high-altitude areas. *Adv. Mater. Sci. Eng.* 2020, 1–15. doi:10.1155/2020/9078731

Xu, P., Zhu, Z., Wang, Y., Cong, P., Li, D., Hui, J., et al. (2022). Phase structure characterization and compatibilization mechanism of epoxy asphalt modified by thermoplastic elastomer (SBS). *Constr. Build. Mater.* 320, 126262. doi:10.1016/j.conbuildmat.2021.126262

Xue, Z., Cao, Y., Liu, N., Feng, L., and Jiang, L. (2014). Special wettable materials for oil/water separation. *J. Mater. Chem. A* 2 (8), 2445–2460. doi:10.1039/c3ta13397d

Yan, K., Chen, J., You, L., and Tian, S. (2020). Characteristics of compound asphalt modified by waste tire rubber (WTR) and ethylene vinyl acetate (EVA): Conventional, rheological, and microstructural properties. *J. Clean. Prod.* 258, 120732. doi:10.1016/j.jclepro.2020.120732

Yan, K., Hong, Z., You, L., Ou, J., and Miljković, M. (2021). Influence of ethylene-vinyl acetate on the performance improvements of low-density polyethylene-modified bitumen. *J. Clean. Prod.* 278, 123865. doi:10.1016/j.jclepro.2020.123865

Zafar, M. S., Quarta, A., Marradi, M., and Ragusa, A. (2019). Recent developments in the reduction of oxidative stress through antioxidant polymeric formulations. *Pharmaceutics* 11 (10), 505. doi:10.3390/pharmaceutics11100505

Zapién-Castillo, S., Rivera-Armenta, J. L., Chávez-Cinco, M. Y., Salazar-Cruz, B. A., and Mendoza-Martínez, A. M. (2016). Physical and rheological properties of asphalt modified with SEBS/montmorillonite nanocomposite. *Constr. Build. Mater.* 106, 349–356. doi:10.1016/j.conbuildmat.2015.12.099

Zeng, Z. A., Underwood, B. S., and Castorena, C. (2022). Low-temperature performance grade characterisation of asphalt binder using the dynamic shear rheometer. *Int. J. Pavement Eng.* 23 (3), 811–823. doi:10.1080/10298436.2020.1774766

Zhang, F., Hu, C., and Zhang, Y. (2018). Research for SEBS/PPA compound-modified asphalt. *J. Appl. Polym. Sci.* 135 (14), 46085. doi:10.1002/app.46085

Zhang, F., Yu, J., and Wu, S. (2012). Influence of ageing on rheology of SBR/sulfur-modified asphalts. *Polym. Eng. Sci.* 52 (1), 71–79. doi:10.1002/pen.22047

Zhang, H. L., Su, M. M., Zhao, S. F., Zhang, Y. P., and Zhang, Z. P. (2016). High and low temperature properties of nano-particles/polymer modified asphalt. *Constr. Build. Mater.* 114, 323–332. doi:10.1016/j.conbuildmat.2016.03.118

Zhao, H., Zhang, Q., Wen, X., Wang, G., Gong, X., and Shi, X. (2021). Dual covalent cross-linking networks in polynorbornene: Comparison of shape memory performance. *Materials* 14 (12), 3249. doi:10.3390/ma14123249

Zhou, T., Zhou, J., Li, Q., and Li, B. (2020). Aging properties and mechanism of microwave-activated crumb rubber modified asphalt binder. *Front. Mater.* 7, 603938. doi:10.3389/fmats.2020.603938

Zhu, J., Birgisson, B., and Kringos, N. (2014). Polymer modification of bitumen: Advances and challenges. *Eur. Polym. J.* 54, 18–38. doi:10.1016/j.eurpolymj.2014.02.005

Zou, X., Sha, A., Ding, B., Tan, Y., and Huang, X. (2017). Evaluation and analysis of variance of storage stability of asphalt binder modified by nanotitanium dioxide. *Adv. Mater. Sci. Eng.* 2017, 1–12. doi:10.1155/2017/6319697

frontiers | Frontiers in Materials

TYPE Original Research
PUBLISHED 10 July 2023
DOI 10.3389/fmats.2023.1190031

OPEN ACCESS

EDITED BY
Hui Yao,
Beijing University of Technology, China

REVIEWED BY
Haibo Ding,
Southwest Jiaotong University, China
Ali Raza,
University of Engineering and Technology, Taxila, Pakistan

*CORRESPONDENCE
Wenrui Yang,
wryang99@163.com

RECEIVED 20 March 2023
ACCEPTED 09 June 2023
PUBLISHED 10 July 2023

CITATION
Zhang K, Yang W, Tang Z, Wu W, Quan W and Wang S (2023), The effect of pore characteristics on the bonding properties of steam-cured concrete and GFRP bars. *Front. Mater.* 10:1190031.
doi: 10.3389/fmats.2023.1190031

The effect of pore characteristics on the bonding properties of steam-cured concrete and GFRP bars

Kai Zhang[1], Wenrui Yang[2]*, Zhiyi Tang[2], Weiwei Wu[3,4], Weijie Quan[2] and Shiyu Wang[2]

[1]Department of Road and Materials, Jiangxi Transportation Institute, Nanchang, China, [2]School of Civil and Architectural Engineering, East China University of Technology, Nanchang, China, [3]School of Transportation and Logistics Engineering, Wuhan University of Technology, Wuhan, China, [4]Hubei Province Highway Engineering Research Center, Wuhan, China

Steam cured concrete prefabricated components has the advantages of short construction period, less environmental pollution, convenient construction and low cost, and is widely used in high-speed railway projects. However, the changes of later strength, capillary water absorption and pore distribution led to the reduction of durability of steam-curing concrete and accelerated the damage speed of GFRP bars and bond performance between concrete and GFRP bars. In this study, the method of steam curing is adopted to simulate the damage of components caused by actual steam curing environment. The influence of pore characteristics on the bonding properties of steam cured concrete and GFRP steel bar is analyzed from both micro and macro perspectives. Analysis method combining pore characteristics with bonding strength. The test results showed that the hydration products of concrete were unaffected, but the density of the hydration products changed due to the steam curing. The porosity of the steam-cured concrete was much higher than that of the standard-cured concrete. The number of gel pores smaller than 20 nm accounted for 12.27% of the total number of pores on average, which was about twice the proportion of the gel pores of this size in the standard-cured concrete. The proportion of harmful voids with pore size of 50–200 nm and greater than 200 nm is higher than that of standard curing concrete. The bond strength of the steam-cured concrete and GFRP bars was 30% lower than that of the standard-cured concrete. With the change of the thickness of the concrete cover and the diameter of GFRP bars, the bond strength changed significantly. Based on the analysis of the test data, a predictive model of the bond strength deterioration for the steam-cured concrete and GFRP bars was established. The model fully accounted for influence factors such as the porosity, diameter, anchor length, and concrete strength.

KEYWORDS

steam-cured concrete, GFRP bars, bonding performance, pore characterization, damage prediction model

1 Introduction

In the process of general high-speed railway construction, the main load-bearing components such as track slab and prestressed simply-supported beams are mostly prefabricated components of steam-cured concrete. The steam curing method in high-speed railway essentially refers to adding water vapor during the curing process, which

accelerates the hydration rate of cement and the formation rate of concrete internal structure during the curing process, thus improving the early strength and hardening rate of concrete. Therefore, the use of steam curing concrete improves the production efficiency of concrete, to a certain extent, and reduces the construction time, and then produces greater economic benefits. At present, the application of autoclaved concrete prefabricated components has been put into use in many practical projects such as bridges and pavements and is gradually becoming mature.

According to statistics, it is a key issue that the service life of steam-curing precast concrete component greatly differs with the design life, which not only causes serious economic losses, but also cannot meet the requirements of high-speed railway construction for the safe development in China. The use of glass fiber reinforced plastic (GFRP) with strong corrosion resistance and high-cost performance ratio to replace or partially replace the steel bars in the steam curing concrete prefabricated components can effectively improve the corrosion of steel bars and increase the service life of concrete (Yang et al., 2017; Zhang et al., 2021). During the steam-curing process, a high-temperature and high-humidity environment accelerates the hydration reaction rate of concrete and has a certain impact on the concrete structure (Shi et al., 2021; Zhou et al., 2022). Jiang et al. (Jiang et al., 2017) and Shi et al. (Shi et al., 2020a) have proposed that the degree of hydration of the surface of steam-cured concrete is greater than that of the interior. The thermal gravimetric damage can reach 0.65%, which is twice as high as the value for standard-cured concrete, and the porosity and number of micro-cracks increase. Eventually, steam-cured concrete facilities deteriorate more quickly, which is one of the most significant challenges facing the international construction industry (Chen et al., 2019; Liu et al., 2019; Zou et al., 2019; Liu et al., 2020a; Yang et al., 2022).

Other researchers have improved the damage resistance and durability of precast concrete by changing the concrete composition, using additives and optimizing the steam curing system (Maruyama et al., 2017; Wang et al., 2022). Shi et al. (Shi et al., 2020b)showed that the thermal damage of steam-cured concrete will accelerate the corrosion of internal bars and reduce the bonding performance, leading to serious economic issues and safety hazards. However, there are few studies on the damage of bars in steam-cured concrete. Yang (Yang, 2016) proposed that the performance degradation of glass fiber reinforced plastic (GFRP) bars in steam cured concrete is far lower than that of ordinary steel bars, which effectively improves the durability and service life of steam cured components. Zeyad (Zeyad et al., 2021) found that adding fine palm oil waste ash to replace part of cement can reduce the damage to concrete caused by steam curing. Isleem (Isleem et al., 2021) conducted numerical and empirical research on the axial compression performance of GFRP reinforced concrete hollow columns using ABAQUS finite element software, and proposed a concrete damage plasticity model (CDPM) for complex column response. Furthermore, he proposed different empirical formulas and artificial neural network models for predicting the softening and hardening behavior of GFRP-RC concrete.

The bond performance between GFRP bars and concrete is one of the most important factors to evaluate the performance of GFRP reinforced concrete structures, and the sufficient bond performance is the basic requirement to ensure the cooperative work of reinforcement and concrete (Maranan et al., 2015; Yoo et al., 2015). Therefore, researchers have carried out most of the research on the bond performance between reinforcement and concrete, such as the type of reinforcement, the form of rib on the surface of reinforcement, the diameter of FRP reinforcement, and the thickness of concrete cover, which will affect the bond strength (Ellis et al., 2018; Wang et al., 2018; Wu et al., 2022). However, there are still insufficient researches on the influence of diameter of FRP bars, anchorage length and thickness of concrete protective layer on the bond performance of GFRP bars under steam curing environment, thus increasing the investment of steam-cured concrete in Engineering practice. However, in the steaming environment, the concrete will have the different degree of hydration reaction, also produce a large number of micro-pore and cause thermal damage to various materials in the concrete, which will affect the bonding performance between GFRP bars and concrete (Han et al., 2019; Bi et al., 2021; Zou et al., 2021). The porosity of concrete directly affects the bond area between GFRP bars and steam cured concrete, which leads to the decrease of bond performance. However, there have been few studies on the effect of the pore characteristics on the bonding properties of steam-cured concrete.

The existing research only discusses the mechanical properties, time cost, early strength, convenience and practicality of steam cured concrete, but ignores the influence of structural stability and structural distribution on the performance of steam cured concrete in the middle term. Due to the influence of steam curing on the internal pore characteristics of concrete, a brief introduction will be given to the related properties of concrete. So, in this paper, the influence of pore characteristics of steam cured concrete on the bond performance is studied from the micro and macro perspectives, and the bond mechanism between steam cured concrete and GFRP reinforcement is revealed from the perspective of pore size distribution. Furthermore, the influence was quantified, and a model was established to predict the relationship between the porosity and the bonding performance. This provides a theoretical

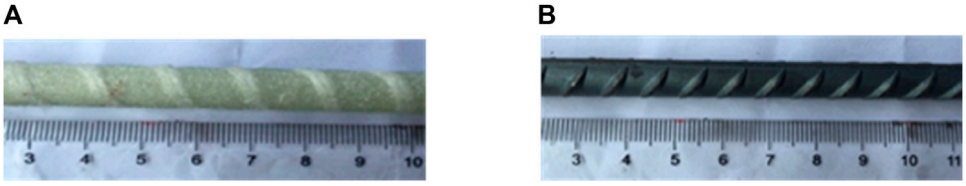

FIGURE 1
GFRP bar **(A)** and steel bar **(B)**.

TABLE 1 Tensile test results of GFRP bars.

Temperature	Relative humidity	Extensometer gauge length	Diameter	Ultimate tension	Tensile strength	Elasticity modulus
˚C	%	mm	*d*/mm	F/kN	R/MPa	E/MPa
20	40	100	10	88	1,023	51,900
				95	1,107	51,800
				93	1,089	51,000
				97	1,131	51,700
Mean value				92	1,087	51,600
20	40	100	16	85	932	47,000
				92	921	47,300
				86	917	47,200
				89	910	47,300
Mean value				88	920	47,200
20	40	100	19	85	871	46,500
				81	875	47,200
				82	885	46,800
				84	897	47,500
Mean value				83	882	47,000
20	40	100	22	78	724	46,600
				79	735	46,000
				82	732	46,200
				77	729	46,800
Mean value				79	730	46,400

10.3389/fmats.2023.1190031

TABLE 2 GFRP bars/reinforced steam-cured concrete beams.

Maintenance method	Reinforcement type	Diameter: *d*	Concrete beam: *b*×*h*×*L*	Concrete cover thickness	Beam number	Working condition abbreviation
		(mm)	(mm)	*c* (mm)		
Steam curing	GFRP bars	10	80 × 110×1,100	15	1–4#	G-Ste1-1
		10	80 × 110×1,100	20	5–8#	G-Ste1-2
		10	80 × 110×1,100	25	9–12#	G-Ste1-3
		10	80 × 110×1,100	35	13–16#	G-Ste1-4
		16	150 × 150×1,100	25	17–20#	G-Ste2
		19	178 × 178×1,100	25	21–24#	G-Ste3
		22	206 × 206×1,100	25	25–28#	G-Ste4
	Steel bars	10	80 × 110×110	25	29–32#	S-Ste
Standard Conservation	GFRP bars	10	80 × 110×110	25	33–36#	G-Sta

basis for the modification of the concrete performance parameters for the design of steam-cured GFRP-reinforced concrete precast members.

2 Test

2.1 Experiment material

(1) GFRP and steel bars A comparison test was carried out using steel bars with diameters of 10 mm.

The GFRP bars have a helical indent formed by wrapping a resin-impregnated E-glass tow along the length of the bar with a pitch, L, of 14 mm and a depth, h, of 0.325 mm (Figure 1). The designated diameters are 10, 16, 19, and 22 mm, respectively. The equivalent diameters of the bars, d, measured by the writers using the immersion method, are 10.2, 16.3, 19.1, and 22.2 mm (immersed cross-sectional areas = 82, 209, 286 and 387 mm^2). The relevant mechanical parameters provided by the tensile test are shown in Table 1. The tensile tests of GFRP bars were performed by an SHT4106-G type microcomputer control electro-hydraulic servo universal testing machine (ACI American Concrete Institute, 2005). Loading force was recorded by the automatic sensor. To prevent shear failure on both ends of the GFRP bars, a 250-mm-long steel pipe anchorage was fixed on the GFRP bar ends.

(2) Concrete

The concrete was provided by a local ready-mix plant and had a water-to-cement ratio of 0.59. The coarse aggregate shall be 5–20 mm continuously graded natural aggregate with crushing index of 12% and bulk density of 1,400–1700 kg/m^3. The sand had medium coarseness with a fineness modulus of 2.8. The cementitious material consisted of 75% by weight of Type I Portland cement with pH 12.65% and 25% Class F fly ash. The tensile strengths of the standard-cured and steam-cured concrete were measured to be 3.14 and 2.93 MPa, respectively.

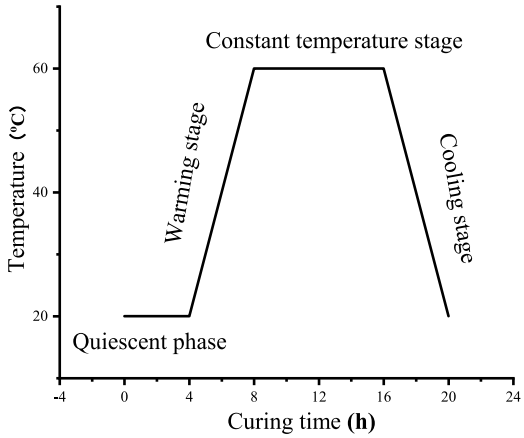

FIGURE 2
Steam curing method.

2.2 Sample fabrication

(1) GFRP bars/reinforced concrete prisms

There was some variability in the porosity due to the different amounts of damage to the surfaces and interiors of the concrete caused by the steam curing. Therefore, in this test, the concrete-prism with 10 mm GFRP reinforcement and 15mm, 20mm, 25mm and 35 mm thickness of concrete cover was used for microstructure observation and pore structure test. After 28 days of curing, cut the concrete with German automatic cutting-machine, and then dry the bonding section for microstructure observation and pore structure test.

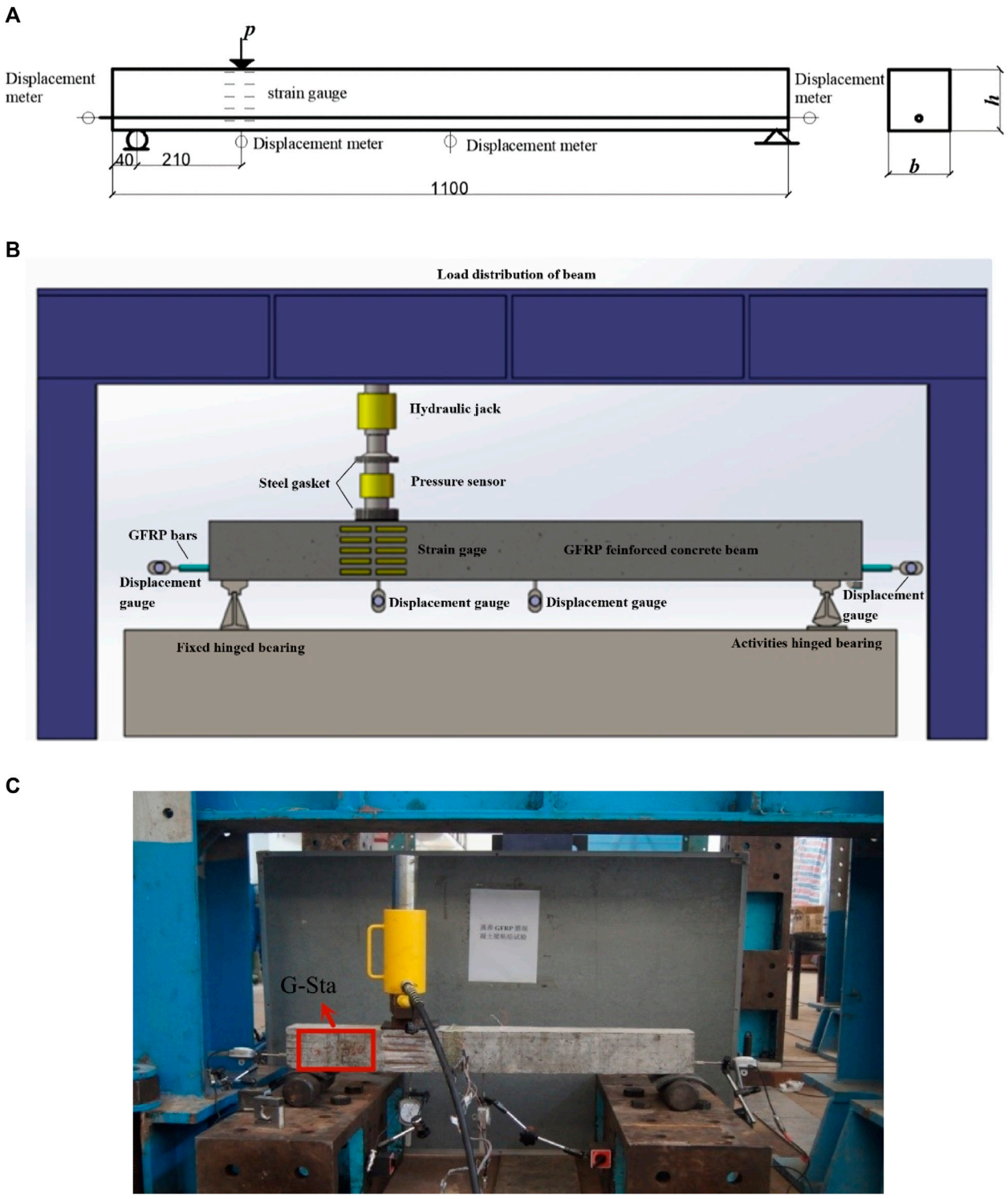

FIGURE 3
Three-point beam bonding test: **(A)** Test schematic (unit: mm); **(B)** Test model diagram; and **(C)** Field test pictures.

(2) GFRP bars/reinforced concrete beams

Esfahani et al. (Esfahani et al., 2013) compared the test data and calculation results of GFRP reinforced concrete beams (ACI American Concrete Institute, 2006). The comparison showed that the evaluation of the bond performances of the GFRP bars and concrete without lateral reinforcement was not conservative enough and even overestimated. Therefore, it is important to study the bonding between GFRP bars and concrete without lateral reinforcement. In order to avoid the influence of transverse

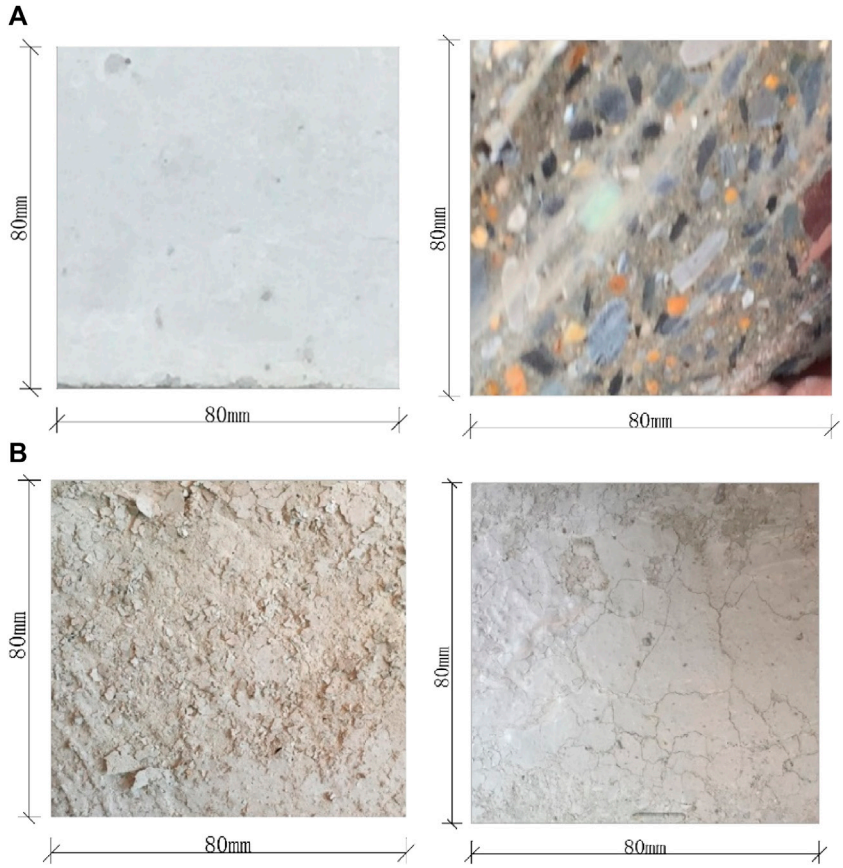

FIGURE 4
Concrete surface morphology diagram: **(A)** Standard curing concrete specimens and Steam cured concrete cutting surface; **(B)** Steam cured concrete surface.

reinforcement and other factors on the bond performance, this paper only installs a tensile GFRP bar at the bottom of the beam.

In this study, steam-cured reinforced concrete beams were used as comparison specimens. The variables set in the test are: curing method, reinforcement diameter and cover thickness. Three-point beam bond tests were conducted on the corresponding GFRP reinforced concrete beams. The thermal damage behaviors of the steam-cured GFRP-reinforced concrete beams were studied. Four test beams were prepared for each group. All the abbreviations for the beam conditions are shown in Table 2.

2.3 Curing condition

Two curing methods, standard curing and steam curing, were used to compare and analyze the influence of different maintenance processes on bonding performance.

(1) Standard curing method:

After pouring the standard-cured specimens, specimens were kept at 20°C ± 5°C for 1–2 days, then they were kept in a standard curing room at 20°C ± 2°C and 95% relative humidity for curing 28 days after the molds were removed.

(2) Steam curing method:

The purpose of steam curing concrete is to accelerate the hydration rate of cement under the action of a moist heat medium (water vapor), which accelerates the rapid formation of the internal structure of the concrete and promotes early strength and fast hardening. However, different steam curing methods will cause different physical, chemical, and mechanical changes in the concrete, which lead to different types of thermal damage during the steam curing process (Liu et al., 2020b; Wang et al., 2020). At present, the curing regime refer to *TZ 210–2005* (Wikidata, 2005). In this research, the quiescent phase was determined to be 4 h at normal temperature, 4 h for heating, 8 h at 60°C ± 5°C, and 4 h for cooling according to the construction quality acceptance standards for high-speed railway bridges and culverts (Figure 2). According to the humidity and temperature conditions in Wuhan, China, the number of steaming days is set at 14 days.

2.4 Test method

(1) Microscopic observations

Microscopic observations of the microstructure of steam-cured concrete were performed via scanning electron microscopy. The cut

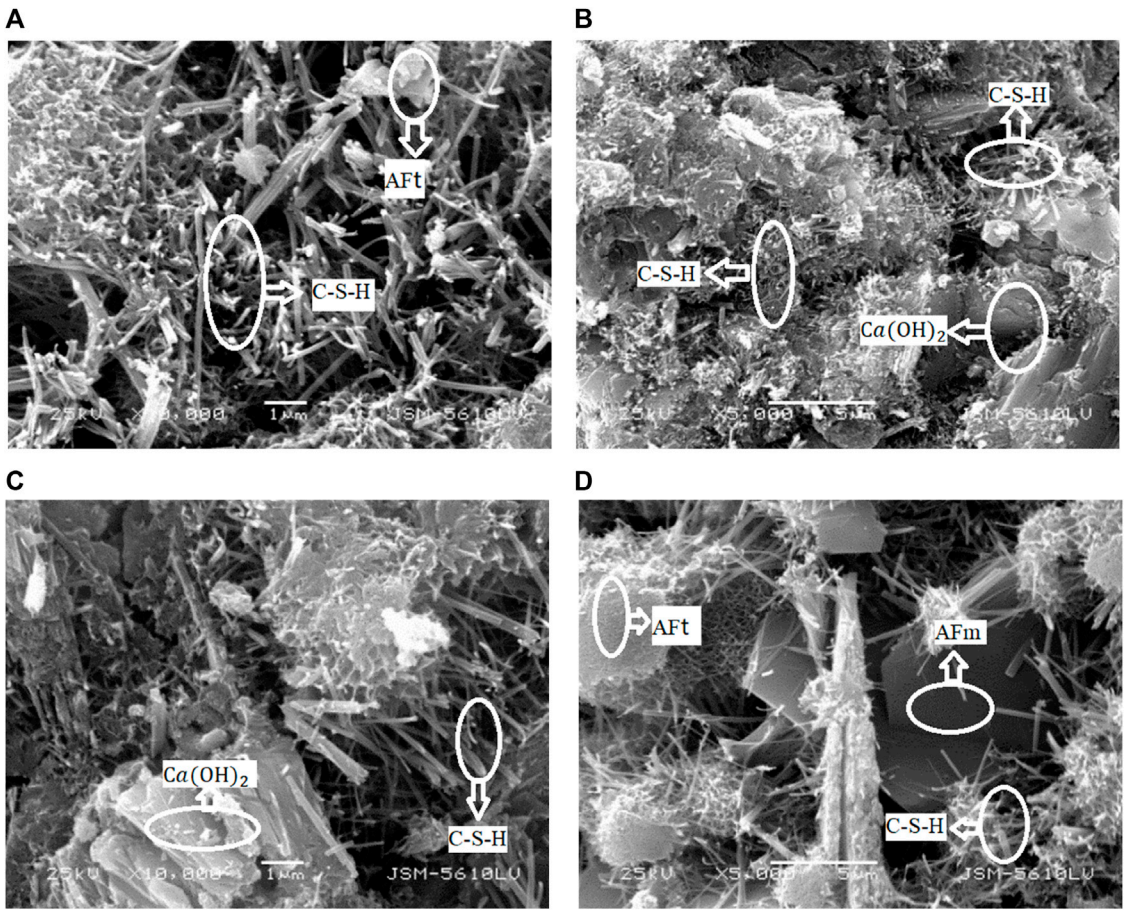

FIGURE 5
SEM figures of hydration products and their distribution of concrete with different curing methods: **(A)** Standard curing concrete surface (× 10,000); **(B)** Standard curing concrete surface (× 5,000); **(C)** Steam curing concrete (× 10,000); and **(D)** Steam curing concrete (× 5,000).

section of steam cured concrete is observed, and the microstructure characteristics of steam cured concrete under different conditions are analyzed. According to the theory of composite materials, the micro mechanism of thermal damage of steam cured concrete is analyzed.

(2) Pore structure distribution

The research emphasis on the internal structure of concrete materials has shifted to the testing and evaluation of pore gradation, pore morphology and porosity. In this paper, the pore structure distribution in the bonding surface of steam cured, and standard cured concrete was studied by mercury intrusion test. The mercury intrusion test is based on the functional relationship between the pressure applied to cement-based or other porous material systems, and the amount of mercury injected (Cieszko et al., 2019; Sidiq et al., 2020). The pore volume and the pore size were calculated. In this study, the pore size distribution of concrete samples after 28 days of steam curing and standard curing was quantitatively analyzed. First, dry the sample, then cut it into 5–7 mm concrete particles and immerse it in anhydrous ethanol for 3–4 days to stop hydration. Finally, the sample is dried in a drying oven until the sample has a constant weight, and the pore structure is determined by applying pressure in the mercury test.

(3) Three-point beam test method

The test method for assessing the bonding performances of the GFRP bars with concrete included an articulated beam bending test and a pulling test based on pulling in a well-anchored concrete block or column (Al-Sibahy and Sabhan, 2020; Esmaeili et al., 2020; Rossi et al., 2020). Zheng et al. (Zheng et al., 2016) conducted a comparative study based on beam and pull-out tests. They found that the bond strengths determined via the hinged beam test were significantly less than those of the pull-out test due to fewer bond constraints and more longitudinal cracks. Bakis et al. (Bakis et al., 2007) also suggested that the bond strengths measured by the three-point eccentric load beam test were different from those obtained by the pull-out test. This difference is mainly because the beam bond performance test considers the existing shear or bending moment of the actual member.

The three-point eccentric-load bonding performance tests of the GFRP-reinforced concrete beams were carried out using a reaction frame and a hydraulic jacking device. Based on the results of the three-point bending optimal anchorage length test in the previous study (Sidiq et al., 2019), the test used 250 mm anchorage section and load application location 210 mm from the support. A schematic diagram of the test device layout is shown in Figure 3,

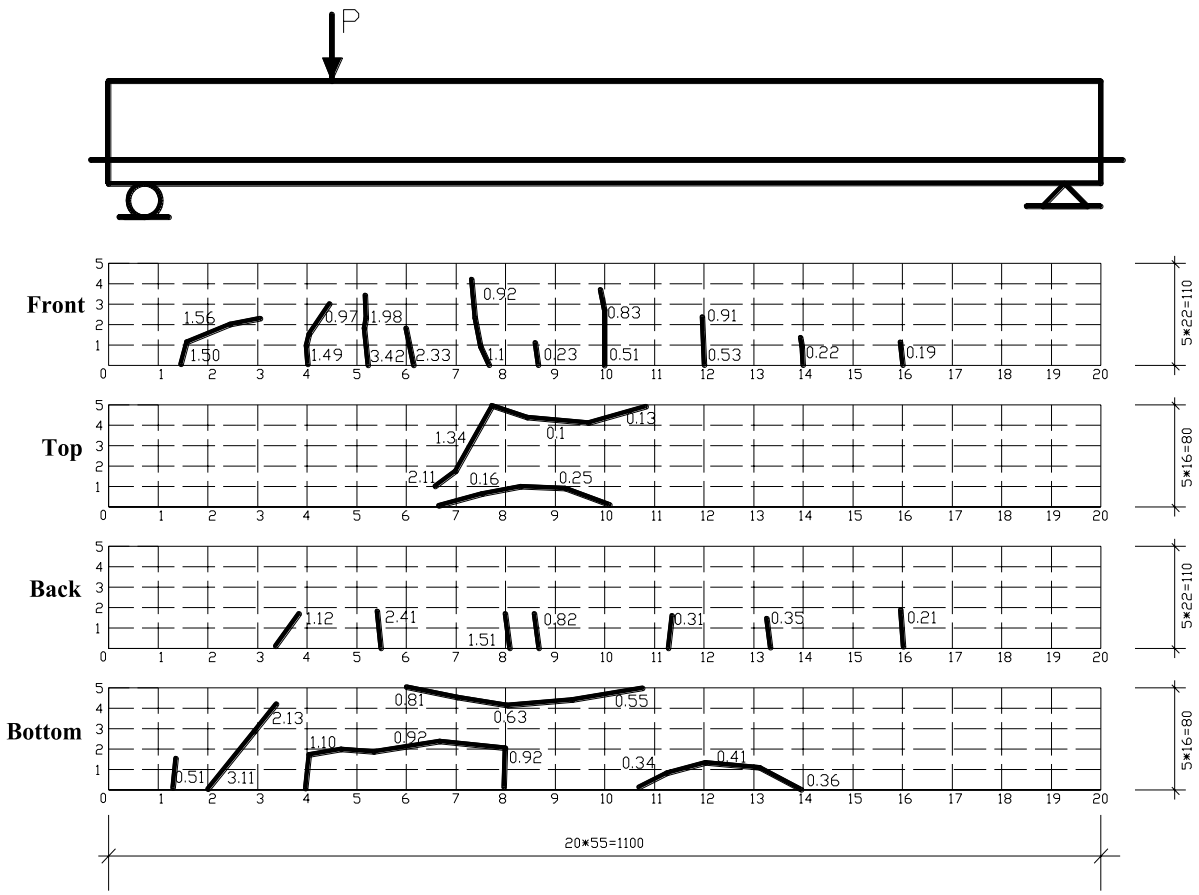

FIGURE 6
G-sta beam crack development diagram: the number next to the crack is the cracking load, kN. (unit: mm).

along with the field test images. The load slip curve and crack development shall be recorded during the test. According to the test data, sliding load and maximum bond strength theory, the bond properties of autoclaved concrete and reinforcement under different conditions are compared and analyzed. The deterioration of the bonding performances for the steam-cured concrete and GFRP bars were determined.

3 Analysis of test results

3.1 Apparent appearance of steam-cured concrete

A comparison of Figures 4A, B shows that the surface of the steam-cured concrete produced clear peeling and micro-cracks, whereas the surface of the standard-cured concrete was relatively smooth. However, after cutting and polishing, the concrete cutting surface showed aggregated particles with different sizes and shapes and discontinuous cement paste. Therefore, the apparent morphology of the steam-cured concrete showed that the steam curing caused thermal damage to the concrete surface, but the steam-cured concrete was still a two-phase material with aggregate particles dispersed throughout the cement slurry matrix, which was no different from the standard-curing concrete.

3.2 Hydration product micromorphology

The microstructure of steam cured concrete is very important to study its performance mechanism. The composition of concrete will change the hydration products of cement, and different curing environment and curing age will also have a certain impact on the degree of cement hydration. Therefore, it is necessary to consider the influence of concrete composition, curing environment, curing age and other factors on the microstructure. As the transition zone between concrete grout and interface will change with the change of ambient temperature, humidity and time, the microstructure of concrete is not inherent to the material. During steam curing, the degree of hydration of cement may be affected due to the difference in temperature and humidity between the surface and the middle of concrete in direct contact with the bottom surface. Therefore, this paper makes a comparative analysis between standard curing concrete and steam curing concrete.

TABLE 3 Pore structure distribution of concrete.

Maintenance method	Specimen number	Porosity	Solid-pore ratio	Pore size distribution			
				(%)			
				<20	20–50	50–200 nm	>200 nm
		(%)	(%)	nm	nm		
Steam curing	G-Ste1-1	13	86	13	55	17	15
	G-Ste1-2	14	86	12	54	17	17
	G-Ste1-3	13	87	12	54	16	18
	G-Ste1-4	12	88	11	54	17	18
	mean	13	86.7	12	54.3	16.8	17
	Standard deviation	0.7	0.8	0.7	0.4	0.4	1.2
	Coefficient of variation	5.3	0.9	5.8	0.7	2.3	7
Standard maintenance	G-Ste1-1	8	92	6	67	15	12
	G-Ste1-2	7	93	7	65	16	13
	G-Ste1-3	7	93	7	68	15	11
	G-Ste1-4	6	94	6	63	16	15
	mean	7	93	6.5	65.7	15.5	12.7
	Standard deviation	0.7	0.7	0.5	1.9	0.5	1.5
	Coefficient of variation	10	0.8	7.7	2.9	3.2	11.8

Figure 5 shows the microstructure of standard curing and steam curing concrete. The scanning electron microscopy images of the microstructure of the concrete at a 10,000× resolution showed needle-like crystals of calcium sulfur aluminate hydrides (ettringite), which appeared mainly due to the reaction of calcium, sulfate, aluminate, and hydroxide in the early stage of hydration. With the progress of hydration, prismatic calcium hydroxide crystals and fibrous calcium silicate flocs continue to fill between the undissolved cement particles. The "calcium alumina" may have decomposed into hexagonal flakes of mono-sulfurous sulfur aluminate hydrates. Figure 6 shows that at 10,000 × There is obvious acicular crystal hydrate at the resolution of 5,000 × A columnar calcium hydroxide crystal is observed at resolution. The comparative analysis of the microstructure and morphology of standard curing concrete and steam curing concrete shows that the surface hydration degree of the latter is significant and the hydration crystal is dense. This shows that steam curing accelerates the hydration degree of concrete and affects the overall density, making the porosity and cracks of steam curing concrete more obvious. This is also related to the formation of water loss products during the hydration reaction process.

3.3 Pore structure of steam-cured concrete

The pore structures inside the concrete had different sizes and shapes, which directly affected the material properties of the concrete. The strength and permeability of concrete have an exponential relationship with the porosity, and the porosity of concrete directly determines the bonding area with the internal bars. Therefore, the porosity was one of the decisive factors of the macroscopic mechanical properties and durability of the concrete.

3.3.1 Analysis of test results of concrete pore structure

The pore-gradation, porosity and morphology characterization of concrete have become the research focus of concrete materials. Sidiq et al. (Sidiq et al., 2020) (Sidiq et al., 2019) divided the pore-size of cement-based image materials into the gel pores (pore size is less than 10 nm); capillary pores (pore size is 5–5,000 nm), large pores (air formation) and insufficient pores. In this study, based on the appearance shown in Figure 6, the curing method of high-temperature and high-humidity has caused some damage to the concrete surface, making its surface pores and cracks more obvious. Table 3 shows that the porosity of steam curing concrete is significantly higher than that of standard-curing concrete, while the corresponding solid hole ratio is lower than that of standard curing concrete. The number of gel pores smaller than 20 nm accounted for 12.27% of the total number of pores, which was about twice the proportion of these gel-pores in the standard-cured concrete. This is mainly because the high-temperature steam environment accelerates the hydration reaction of cement clinker, promotes the formation of gel, such as

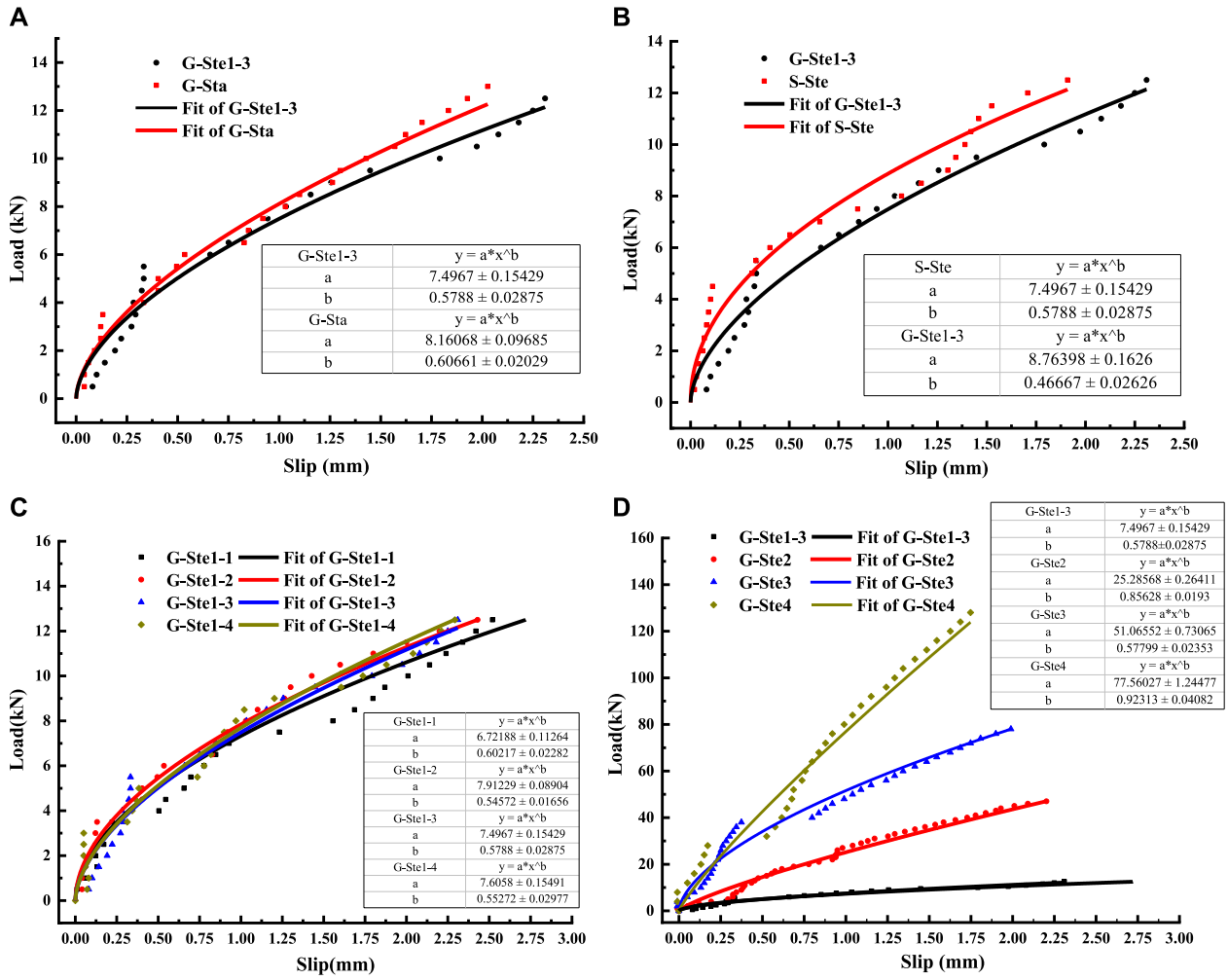

FIGURE 7
Load-slip curve: **(A)** Different maintenance methods; **(B)** Different bars; **(C)** Different concrete cover thickness; and **(D)** Different GFRP rib diameter.

hydrated calcium silicate and calcium aluminate, and ultimately leads to a large increase in the number of gel pores.

The apertures could be divided into harmless pores (apertures less than 20 nm), less harmful pores (apertures of 20–50 nm), harmful pores (apertures of 50–200 nm), and more harmful pores (apertures larger than 200 nm). Some studies have shown that pore diameters less than 50 nm have no effect on the performance of concrete and even can improve the performance (Hong et al., 2018; Qiu et al., 2019). However, pore diameters greater than 100 nm have a greater adverse effect on the performance of concrete. Table 3 shows that the lower hazard classes (pore sizes of 20–50 nm) in steam-cured concrete have a lower proportion of total pore size than standard-cured concrete, while the higher hazard classes (pore sizes greater than 50 nm) have a higher proportion of total pore size than standard-cured concrete. The detrimental porosity of concrete cured with steam was 33.8%, which was 5.9% greater than that of conventionally cured concrete. This implies that the distribution of pores over inside steam-cured concrete produces higher damage to the concrete structure, which not only affects the bonding area of the GFRP bars to the concrete but also their bonding characteristics. This is also the primary reason why chloride ion penetration is less than that of conventionally cured concrete.

3.4 Analysis of changes in bonding performance between concrete and GFRP

In the three-point beam bond test, most of the members show shear failure, and the initial cracks appear near the load application point. As the load was continuously applied, the edge cracks continued to increase until the main cracks appeared (Figure 6).

3.4.1 Load–slip curve

Figure 7A shows that, compared with the GFRP reinforced concrete beams under standard curing, the beam members under steam curing have 1.34 times of slip, and the ultimate load has decreased by 4%. The steam curing system had a certain degradation effect on the bonding performance of the GFRP bars and concrete. Figure 7B shows that the slippage of steam cured GFRP reinforced concrete beams is 1.42 times that of ordinary steam cured beam

TABLE 4 Bond slip parameters of steam-cured GFRP reinforced concrete beam.

Contrast	Specimen number	Maximum slip	Slip parameter	Slip parameter	Slip load	Maximum bond strength
		S_{max}: (mm)	a	C	N_{smax} :(kN)	τ_{max} :(MPa)
Different forms of maintenance	G-Sta	2	0.58	4.3	27	2.3
	G-Ste1-3	2.3	0.57	3.3	26	1.9
Different bars	S-Ste	1.9	0.48	1.2	27	0.6
	G-Ste1-3	2.3	0.58	3.3	26	1.9
Different concrete cover thickness	G-Ste1-1	2.5	0.67	2.3	23	1.4
	G-Ste1-2	2.4	0.52	2.7	25	1.6
	G-Ste1-3	2.3	0.58	3.3	27	1.9
	G-Ste1-4	2.3	0.58	4.5	31	2.6
Different diameters	G-Ste1-3	2.3	0.58	3.3	27	1.9
	G-Ste2	2	0.8	6.2	67	3.4
	G-Ste3	2	0.6	7.7	91	4
	G-Ste4	1.8	0.85	12	121	5.4

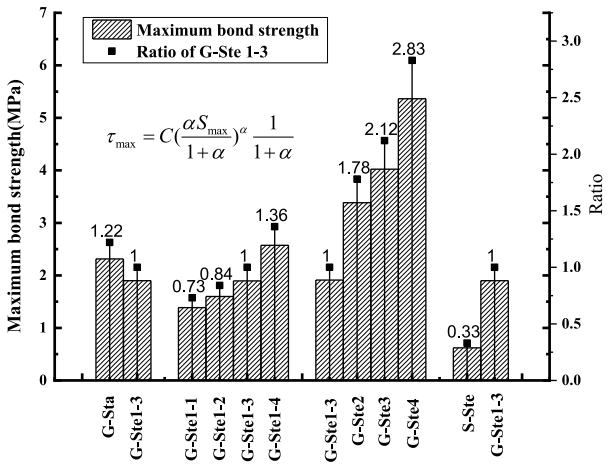

FIGURE 8
GFRP reinforced concrete beam maximum bond strength.

members. Figure 7C shows that under different concrete cover thickness conditions, the bonding properties of the GFRP bars and the steam-cured concrete did not show significant changes. Figure 7D shows that the variation rate of the bond–slip curve was the fastest when the diameter was 10 mm, and the curve variation rate was the lowest when the diameter was 19 mm.

3.4.2 Maximum bond strength

The traditional average bond strength ignores the amount of slipping or cracking change between the components during the stress process. If the sliding load and stress per unit area of the two materials are the same, the bond strength is also the same. The maximum bond strength theory used in this study is based on experiments and calculations of material mechanics. The theory relates the actual material slip relationship and the material properties, so it is better for use in analyzing the bond strengths between steam-cured concrete and different reinforcements. The variation of the bond strength between the steam-cured concrete and the GFRP bars can be explained by the degree of damage.

The bond–slip mechanism of the steam-cured concrete and the GFRP bars was similar to that of the standard-cured concrete. Therefore, the bond–slip constitutive relationship also conformed to the modified Bertero-Popov-Eligehausen (mBPE) bond–slip constitutive relationship. As the steam curing caused some damage to the bonding performance of the two, the steam-cured concrete and the GFRP bar were analyzed based on the theoretical maximum bonding strength using the typical mBPE bond–slip constitutive model and the test data of the bar bonding performance deterioration, as described in this section.

The mBPE model is mainly used to analyze the bond–slip relationship for the fiber-reinforced plastic (FRP) and concrete. This model was obtained by the modification of the Bertero-Popov-Eligehausen (BPE) bond–slip constitutive model (Zou et al., 2021) (Cosenza et al., 1995; Altalmas et al., 2015; Yan and Lin, 2017). The horizontal section with a constant bond strength is not considered in the mBPE model. The expression is as follows:

$$\frac{\tau}{\tau_{max}} = \begin{cases} \left(\frac{s}{s_{max}}\right)^{\alpha} & (0 < s < s_{max}) \\ 1 - \rho\left(\frac{s}{s_{max}} - 1\right) & (s_{max} < s < s_c) \\ \frac{\tau_c}{\tau_{max}} & (s < s_c) \end{cases} \quad (1)$$

where τ is the bond strength. τ_{max} is the maximum bond strength. τ_c is the corresponding bond strength at the beginning of linear slip.S is the slip value. s_{max} is the corresponding slip value τ_{max}. s_c is the

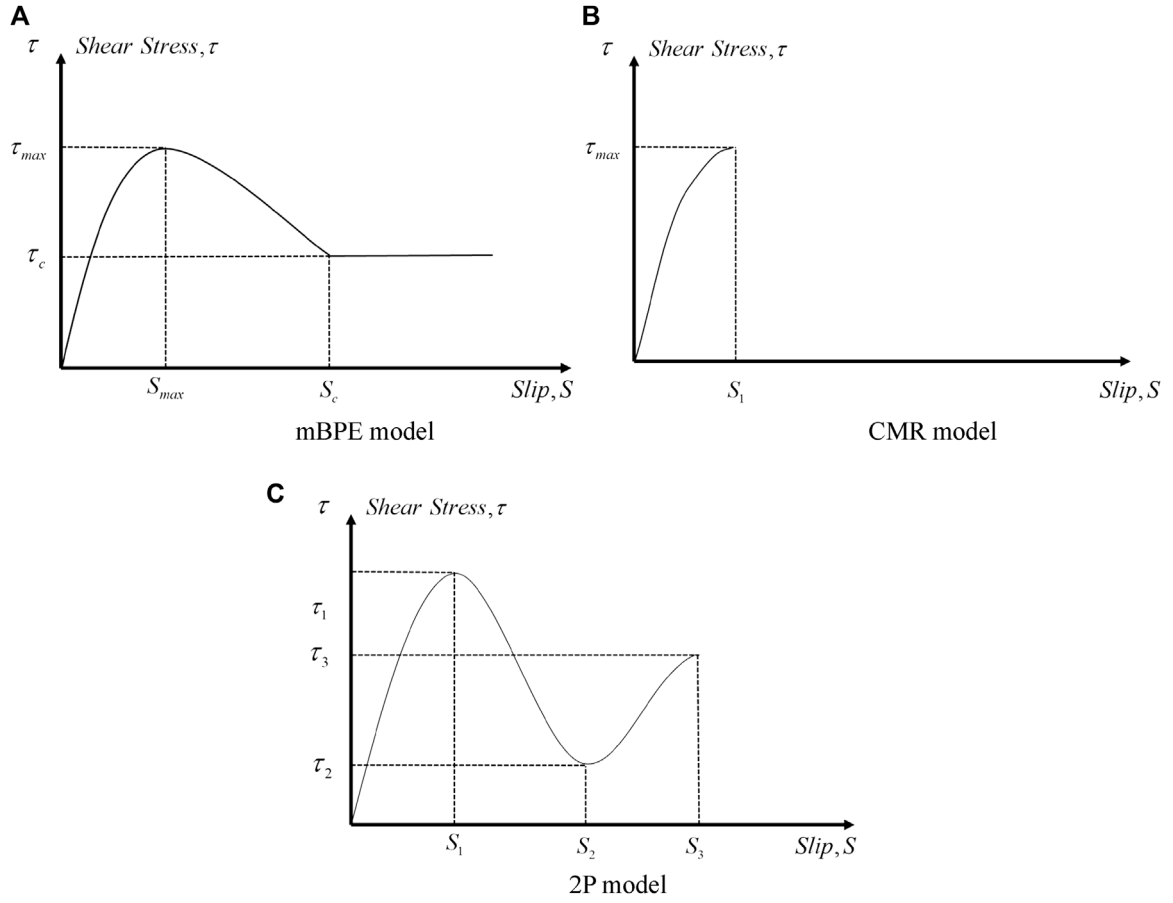

FIGURE 9
Bond slip model. **(A)** mBPE model **(B)** CMR model **(C)** 2P model.

corresponding slip value τ_c . α and ρ are the fitting parameters of the test data.

To further improve the accuracy of the mBPE model in analyzing the bond slip of FRP-reinforced concrete structures, Bakis et al. (Bakis et al., 2007) and Focacci et al. (Focacci et al., 2000) modified the mBPE model and proposed the expressions shown in Equations 2, 3. The curve produced by the modified mBPE model mainly intersects the curve in Figure 9 with the abscissa axis. The third stage with a constant slip strength can be simplified into a graph closed with the transverse coordinate axis. The expressions of the maximum bond slip load and maximum bond strength are shown in Equations 4, 5. The Levenberg Marquardt theory is used to determine the unknown parameters through the square difference between the test slip load and the theoretical slip load of GFRP bars (Bakis et al., 2007) (Press et al., 2007; Troian-Gautier et al., 2016; Xu et al., 2017).The calculation results of each specimen are shown in Table 4.

$$\tau = CS^{\alpha}\left(1 - \frac{S}{\bar{S}}\right) \tag{2}$$

$$S_{\max} = \alpha\bar{S}\Big/(1+\alpha) \tag{3}$$

$$N_f = S^{(1+\alpha)/2} \cdot \sqrt{4CE_f A_f \pi d_b \Big/ (1+\alpha)(2+\alpha)} \tag{4}$$

$$\tau_{\max} = C\left(\frac{\alpha\bar{S}}{1+\alpha}\right)^{\alpha}\frac{1}{1+\alpha} \tag{5}$$

Bakis et al. (Bakis et al., 2007)obtained the following expressions for the local maximum bond strength ($\tau_{\max}$) and the maximum slip load (N_{smax}) based on the mBPE model:

$$\tau_{\max} = C\left(\frac{aS_{\max}}{1+a}\right)^{a}\frac{1}{1+a} \tag{6}$$

$$N_{\mathrm{smax}} = \sqrt{4\pi d A_b E_b}\sqrt{c\Big/(1+a)(2+a)}s^{(1+a)/2} \tag{7}$$

As shown in Table 4 and Figure 8, the bonding strengths of the GFRP bars reached three times that of the steel bars. In addition, due to the corrosion resistance of the two reinforcement materials, the bond performance of ordinary reinforcement and GFRP reinforcement will be different. Therefore, the method of using the GFRP bars to replace or partially replace steel bars in steam-cured concrete components is worth popularizing and has certain engineering significance.

The maximum bond strength of GFRP reinforced concrete was reduced from 2.31 MPa to 1.90 MPa, and the reduction range

10.3389/fmats.2023.1190031

TABLE 5 RMSE of the mBPE, 2P and CMR models.

Specimen		RMSE		
		mBPE	CMR	2P
Different forms of maintenance	G-Sta	0.0582	0.0938	0.0395
	G-Ste1-3	0.0255	0.0343	0.0174
Different bars	S-Ste	0.0072	0.0075	0.0072
	G-Ste1-3	0.0255	0.0343	0.0174
Different concrete cover thickness	G-Ste1-1	0.0262	0.0396	0.016
	G-Ste1-2	0.0188	0.0215	0.0172
	G-Ste1-3	0.0255	0.0343	0.0174
	G-Ste1-4	0.0331	0.0469	0.0252
Different diameters	G-Ste1-3	0.0255	0.0343	0.0174
	G-Ste2	0.0246	0.0337	0.0147
	G-Ste3	0.0389	0.039	0.0386
	G-Ste4	0.0538	0.0923	0.0401

after steam curing was 22%.Wang (Wang, 2013) proposed that the reduction factor K_T of the bond strength between the GFRP bars and the concrete was 0.8 when the temperature was lower than 200°C, and K_T was taken as 0.65 when the temperature was between 200°C and 300°C. The reduction ratio of the bonding strength of the concrete and the GFRP bars was relatively large after steam curing at high temperatures, which showed that steam curing did indeed diminish the bond performance of the concrete and the GFRP bars. The decrease of bond performance is closely related to the change of structural performance of concrete during hydration and after high temperature steam curing.

The maximum bond strength of GFRP reinforced concrete after steam curing increases with the increase of concrete cover thickness. When the thickness of the concrete cover was in the range of 15–20 mm, the maximum bonding strength increased by 15%. When the thickness of the concrete cover was in the range of 20–25 mm, the maximum bonding strength increased by 19%. When the thickness of the concrete cover was in the range of 25–35 mm, the maximum bond strength increased by 35%. This is mainly related to the structural performance of steam cured concrete, and more cracks and pores on its surface layer are shown in Figure 4. These would provide more channels for external media to enter the interior of the concrete, affecting the internal reinforcement and the bonding interface. Therefore, the damage in steam cured concrete is relatively small. When the thickness of concrete cover is 35mm, the bonding performance is significantly enhanced.

Figure 8 shows that the maximum bond strength of steam cured concrete and GFRP reinforcement increases with the increase of diameter. When the diameter was in the range of 10–16 mm, the bond strength increased by 78%, which was not only related to the steam curing damage but also had a significant relationship with the ratio of C/d_b to d_b/l_e.

3.4.3 Theoretical analysis

The bond-slip constitutive model proposed by early researchers provides an effective method to study the bond-slip behavior between FRP bars and concrete. However, the single model cannot satisfy most of the studies for different test and engineering applications. Based on this, researchers modified the bond-slip model of foundation to obtain a more applicable bond-slip constitutive model. At present, the existing bond slip models mainly include the Malvar, the Bertero-Eligehausen-Popov (BPE), the modified BPE (mBPE), the Cosenza-Manfredi-Realfonzo (CMR), the Wei (2P),etc. As shown in Figure 9, the main test process in the bond-slip test is located in the ascending section on the bond-slip curve. When the test is in the pull-out stage of the FRP bar, the mBPE curve appears as a curve downtrend until it maintains a horizontal straight line in the final stage. The CMR model can only describe the ascending segment of the bond-slip curve, and lacks the curve expressing the decreasing segment and the horizontal segment of the bond strength, which is more in line with the trend of the experimental data from this paper. The 2P theoretical model is based on the establishment of the bond-slip curve, which can more accurately express the changing trend of the curve. The expression of the mBPE model is shown in Eq. 1.

3.4.3.1 CMR model

In order to solve the problem that Malvar model did not conform with the test results because of its complex formula, unclear physical meaning of parameters and small initial slope to

TABLE 6 The parameters of the mBPE, CMR and 2P models.

Specimen		mBPE		CMR			2P					
		τ_{max} (MPa)	a	τ_{max} (MPa)	β	S_r	τ_{max} (MPa)	b	η	ω	φ	c
Different forms of maintenance	G-Sta	2.3100	0.5840	2.5600	0.7881	1.2544	2.2514	−2.9576	0.7120	−0.0003	0.4069	2.8930
	G-Ste1-3	1.9000	0.5770	2.1000	0.7865	1.3707	1.8701	−2.3978	0.6143	−0.0004	0.3679	2.4116
Different bars	S-Ste	0.6200	0.4850	0.7000	0.5906	1.4297	0.5923	−1.3795	1.1199	−0.0003	1.1254	0.6624
	G-Ste1-3	1.9000	0.5770	2.1000	0.7865	1.3707	1.8701	−2.3978	0.6143	−0.0004	0.3679	2.4116
Different concrete cover thickness	G-Ste1-1	1.3800	0.6650	1.5000	1.0059	1.3028	1.3536	−2.0281	0.4569	−0.0003	0.3801	1.9493
	G-Ste1-2	1.6100	0.5250	1.8500	0.6518	1.8570	1.5545	−2.1185	0.7378	0.0002	−0.6555	1.8342
	G-Ste1-3	1.9000	0.5770	2.1000	0.7865	1.3707	1.8701	−2.3978	0.6143	−0.0004	0.3679	2.4116
	G-Ste1-4	2.5700	0.5860	2.9000	0.8022	1.4462	2.5223	−4.0255	0.6301	−0.0001	0.7057	3.2448
Different diameters	G-Ste1-3	1.9000	0.5770	2.1000	0.7865	1.3707	1.8701	−2.3978	0.6143	−0.0004	0.3679	2.4116
	G-Ste2	3.3800	0.7940	4.8000	1.0518	1.9136	3.3566	−12.4222	0.2846	0.0001	−0.9761	7.0567
	G-Ste3	4.0200	0.6000	5.2000	0.7338	1.8411	3.9012	−5.4129	0.7074	−0.0002	0.5008	5.0634
	G-Ste4	5.3600	0.8530	6.5000	1.4309	0.9725	5.3175	−17.3922	0.2424	0.0002	−0.5096	15.2591

the curve, Cosenza et al. (Cosenza et al., 1995) proposed CMR model, which can better express the development trend of bond-slip curve between FRP bars and concrete in the ascending phase. The expression of the CMR model is shown in Eq. 8:

$$\frac{\tau}{\tau_{max}} = \left(1 - \exp\left(-\frac{s}{s_r}\right)\right)^{\beta} \quad (0 \leqslant s \leqslant s_{max}) \tag{8}$$

where τ and s are bond stress and slip, respectively. τ_{max} is the maximum bond stress under the ultimate load. S_r and β are parameters that require curve fitting from the test data.

3.4.3.2 2P model

In part of the bond-slip curve obtained by the mBPE model, the descending section shows a linear trend, while the CMR model only shows the rising section on the bond-slip curve. Therefore, Wei (Wei et al., 2019) proposed the 2P model based on bonding mechanism and bonding characteristics, which can better represent the accuracy of the bond-slip constitutive model. The expression of the 2P model is shown in Eq. 9:

$$\tau = be^{-\eta s}\cos(\omega s + \varphi) + c \tag{9}$$

where τ and s are bond stress and slip, respectively. b、η、ω、φ、c are parameters that require curve fitting from the test data.

3.4.3.3 Comparisons between the mBPE, CMR models and 2P models

In this paper, mBPE model, CMR model and 2P model (the relevant parameters of the model are shown in Table 5) are used to establish bond-slip curves. Root mean squared error (RMSE) is used to compare the mBPE, CMR and 2P models, to obtain the applicability and accuracy of the models. The calculation formula of RMSE is shown in Eq. 10, and the calculation results are shown in Table 6. The results show that the fitting effect of mBPE model and 2P model is the best, and the fitting effect is more accurate in the upstream section than that of mBPE model and CMR model.

$$RMSE = \sqrt{\frac{\sum\left(\tau_{exp} - \tau_{fit}\right)^2}{n}} \tag{10}$$

where τ_{exp} is test value of bond stress. τ_{fit} is the fitting value of bond stress. n is the number of test data.

Figures 10–13 are the bond-slip curves of test beams under different models. The figure shows that the bond-slip curves between mBPE, CMR and 2P models have similar trends, but the mBPE model and 2P model have better correlation. On the other hand, the RMSE of the mBPE model and the 2P model are smaller than that of the CMR model, indicating that the mBPE model and the 2P model are more in line with the actual bond slip trend of GFRP reinforcement.

4 Correlation model analysis of pore structure and bonding performance of steam-cured concrete

There are many factors that influence the bonding performance, such as the GFRP bar diameter, anchor length, and concrete compressive strength (Yoo and Yoon, 2017; Xingyu et al., 2020). In

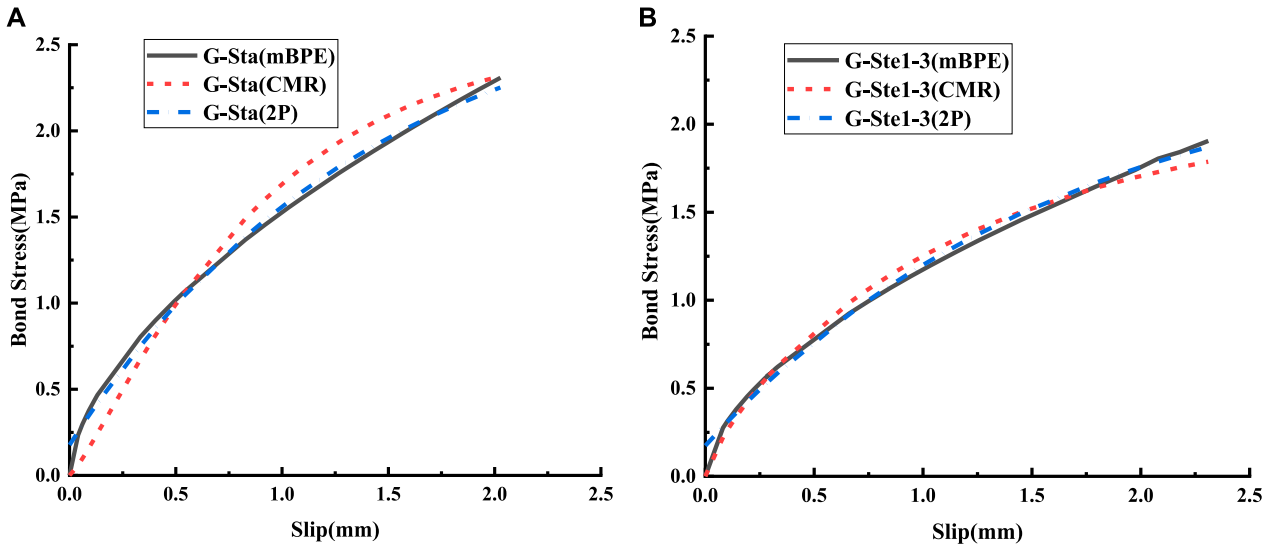

FIGURE 10
Bond-slip curves under different curing methods: **(A)** Bond slip curve under standard curing; **(B)** Bond slip curve under steam curing.

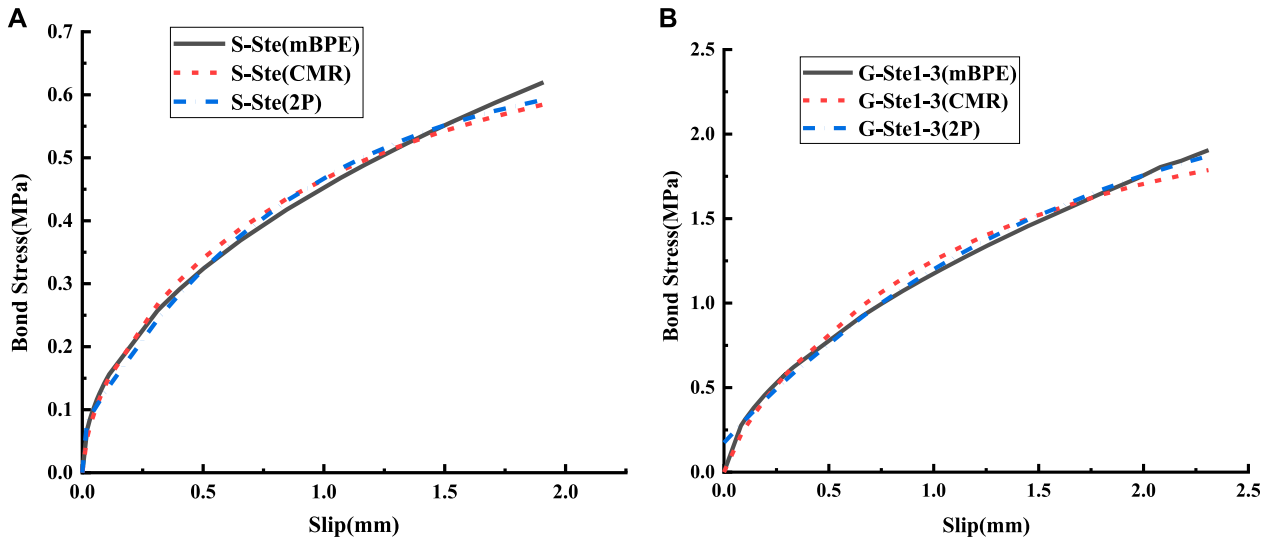

FIGURE 11
Bond-slip curves of different steels: **(A)** Bond slip curve of reinforced concrete beams; **(B)** Bond slip curve of GFRP reinforced concrete beams.

the correlation model analysis, the influence of the porosity of steam-cured concrete was considered in addition to the diameter, anchoring length, and compressive strength of concrete.

Zheng and Xue (Zheng and Xue, 2008) considered the influence of the bonding length and the diameter of the GFRP bars on the bonding strength by introducing the bonding length coefficient (ϕ), defined as follows:

$$\frac{\tau_u}{(8.00 - 0.17d_b)f_t} = k\phi\left(\frac{l_e}{d_b}\right)^{-0.4} \tag{11}$$

In this formula, k is an undetermined coefficient. When $l_e \leq 10d_b$, $\phi = 2.05$, when $l_e = 20d_b$, $\phi = 1.05$, and when $10d_b < l_e < 20d_b$, ϕ is a linear interpolation.

As shown in Table 7, the bond strength of steam-cured concrete and GFRP rods increased gradually with increasing diameter for G-Ste1-3, G-Ste2, G-Ste3 and G-Ste4. This indicates that this is not only related to the ratio of anchor length to diameter, but also to the damage caused by steam maintenance due to the increase in diameter. It can be seen from the change of bond strength in the three models that the bond strength of G-Ste2, G-Ste3 and G-Ste4 increases with the

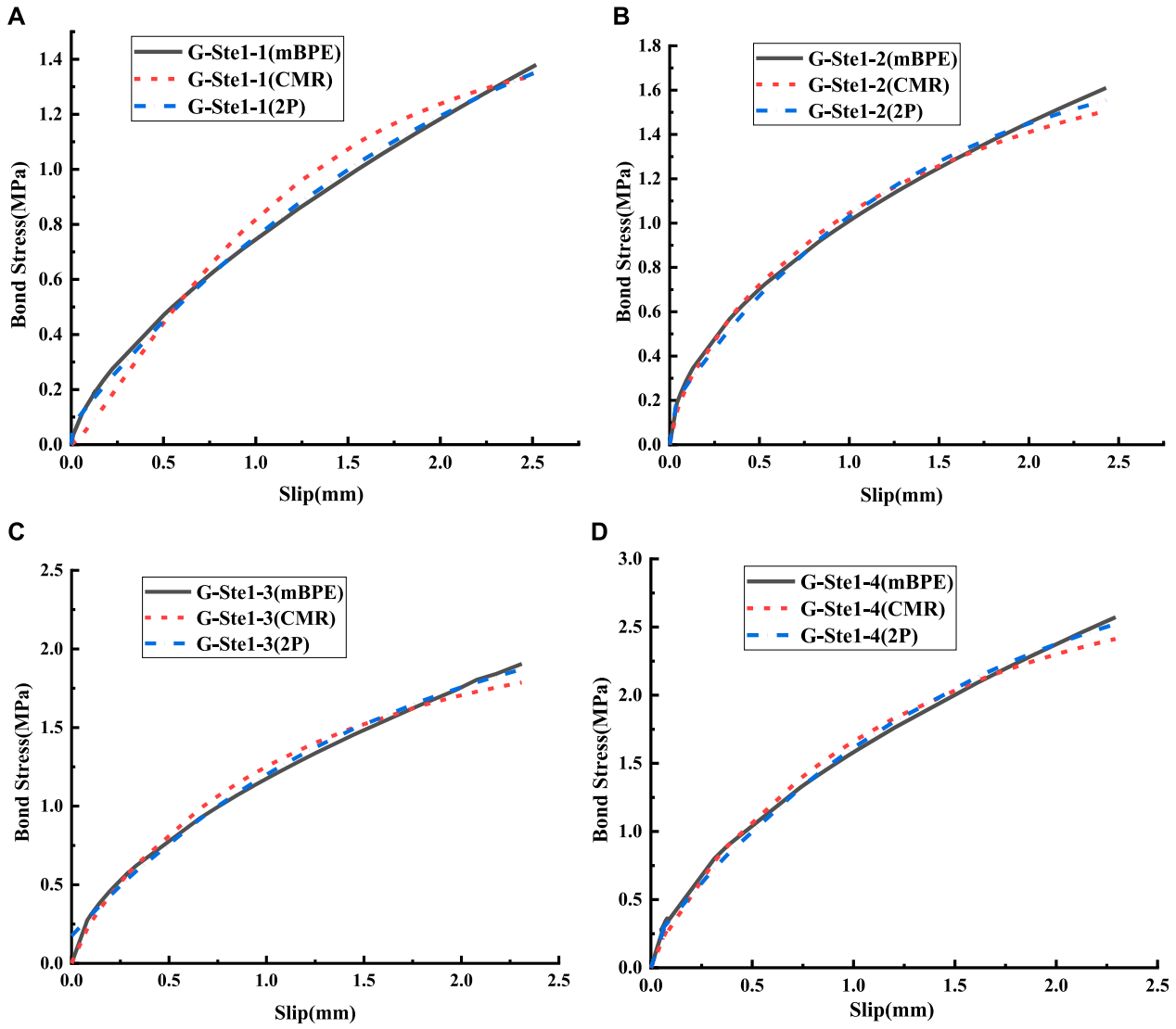

FIGURE 12
Bond-slip curves of different concrete cover thickness: **(A)** The thickness of the concrete protective layer is 15 mm; **(B)** The thickness of the concrete protective layer is 20 mm; **(C)** The thickness of the concrete protective layer is 25 mm; **(D)** The thickness of the concrete protective layer is 35 mm.

increase of bond length. The change of bonding strength is shown in Figure 14.

(1) Coefficient of bond length influence

The differences of the tensile properties between the steam-cured and standard-cured concrete affected the bonding performances of the steam-cured concrete and GFRP bars. Therefore, the following model was used to comprehensively consider the influence of the concrete tensile strength and l_e/d_b:

$$Y_d = \frac{\tau_u}{(8.00 - 0.17d_b)f_t} = K_d\left(\frac{l_e}{d_b}\right)^t \tag{12}$$

where K_d *and* t are the fitting parameters.

The fitting of the test data is shown in Figure 15, and the fitting formula is shown in Eq. 13 According to the RMSE value, the fitting effect between different models is evaluated. The RMSE value of mBPE model is 0.02 and closest to the test value. Therefore, when the variable is the bond length, the mBPE model is finally selected to establish the pore characteristic damage study.

$$\frac{\tau_u}{(8.00 - 0.17d_b)f_t} = \begin{cases} 51.86\left(\frac{l_e}{d_b}\right)^{-1.99} & mBPE \\ 43.21\left(\frac{l_e}{d_b}\right)^{-1.82} & CMR \\ 55.03\left(\frac{l_e}{d_b}\right)^{-2.02} & 2P \\ 47.71\left(\frac{l_e}{d_b}\right)^{-1.92} & exp \end{cases} \tag{13}$$

(2) Coefficient of porosity influence

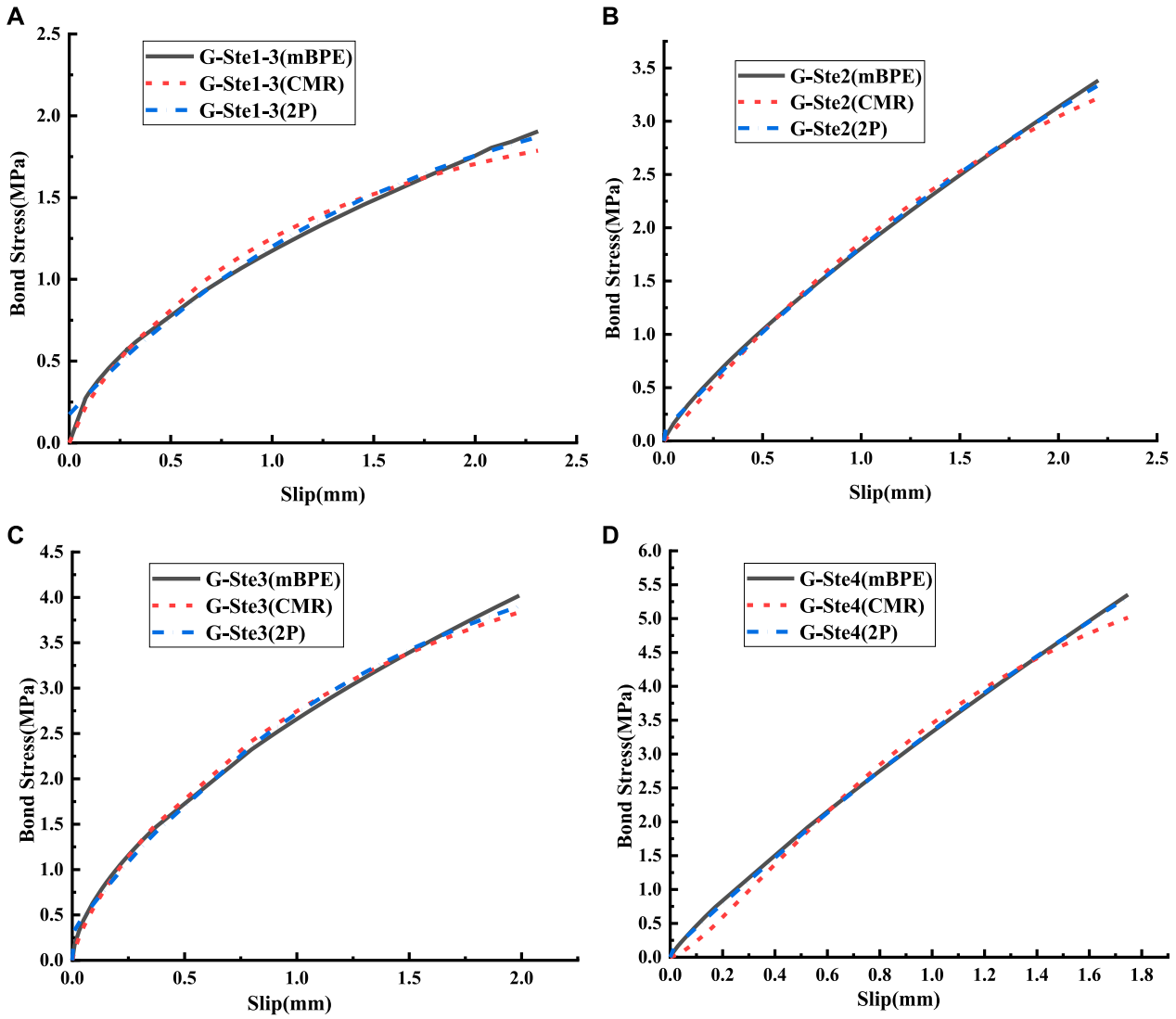

FIGURE 13
Bond-slip curves of different GFRP bar diameters: **(A)** Composite reinforcement with a diameter of 10 mm; **(B)** Composite reinforcement with a diameter of 16 mm; **(C)** Composite reinforcement with a diameter of 19 mm; **(D)** Composite reinforcement with a diameter of 22 mm.

The concrete porosity will directly affect the bonding area and reduce the bond performance. Table 4; Table 7 show that the porosity varied with the thickness of the concrete cover, resulting in different bonding strengths. There was a linear variation trend between the two, which agreed with the variation trend of the bond strength calculation method and the thickness of the concrete cover according to *ACI 440.1R-15* (ACI Committee 440, 2015). It can be seen from the change of bond strength in the three models that the bond strength of G-Ste1-1/2/3/4 increases with the increase of porosity. The change of bonding strength is shown in Figure 16. The bond strength model is shown in Eq. 14:

$$Y_p = \frac{\tau_u}{(8.00 - 0.17d_b)f_t} = K_p + wp \tag{14}$$

Where K_c and w are the test fitting parameters.

The fitting formula is shown in Eq. 15 and the RMSE value is used to evaluate the fitting effect between different models. Therefore, when the variable is porosity, the 2P model is selected to establish the pore-characteristic damage study.

The fit of the test data is shown in Figure 17. The bonding strengths of the steam-cured concrete and the GFRP bars with different porosities were determined.

$$\frac{\tau_u}{(8.00 - 0.17d_b)f_t} = \begin{cases} 0.52 - 0.03P\ mBPE \\ 0.48 - 0.03P\ CMR \\ 0.52 - 0.03P\ 2P \\ 0.51 - 0.03P\ exp \end{cases} \tag{15}$$

The above analysis model was mainly based on the test results, and it was used to perform data fitting. When considering the effects of the maintenance mode, diameter, and concrete cover thickness on

TABLE 7 Parameters related to maximum bond strength.

Contrast	Specimen number	Tensile strength of concrete axis	Diameter	Thickness of concrete cover	Anchoring section	Anchor length/diameter	Porosity	Maximum bond strength		
		f_t :(MPa)	d_b :(mm)	C: (mm)	l_e :(mm)	$\frac{l_e}{d_b}$	P: (%)	τ_{max} :(MPa)		
								mBPE	CMR	2P
Different forms of maintenance	G-Sta	3.1	10	25	250	25	6.7	2.30	2.56	2.25
	G-Ste1-3	2.9	10	25	250	25	12.9	1.90	2.10	1.87
Different concrete cover thickness	G-Ste1-1	2.9	10	15	250	25	13.9	1.40	1.50	1.35
	G-Ste1-2	2.9	10	20	250	25	13.5	1.60	1.85	1.55
	G-Ste1-3	2.9	10	25	250	25	13	1.90	2.10	1.87
	G-Ste1-4	2.9	10	35	250	25	11.9	2.60	2.90	2.52
Different diameters	G-Ste1-3	2.9	10	25	250	25	13	1.90	2.10	1.87
	G-Ste2	2.9	16	25	250	15.6	13	3.40	4.80	3.34
	G-Ste3	2.9	19	25	250	13.2	13	4.00	5.20	3.90
	G-Ste4	2.9	22	25	250	11.4	13	5.40	6.50	5.32

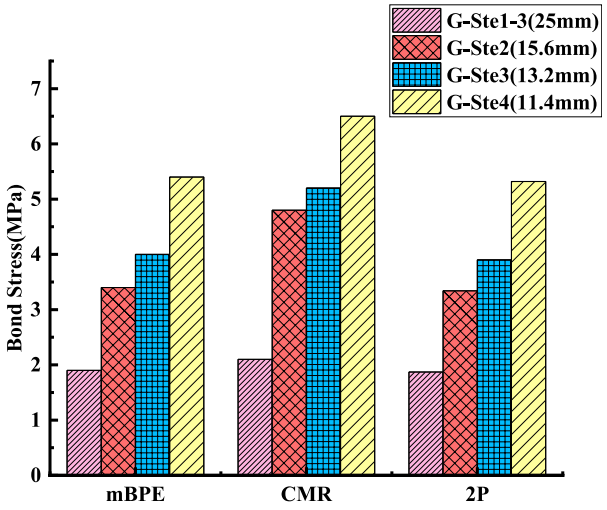

FIGURE 14
Relationship between bond strength and bond length under different models.

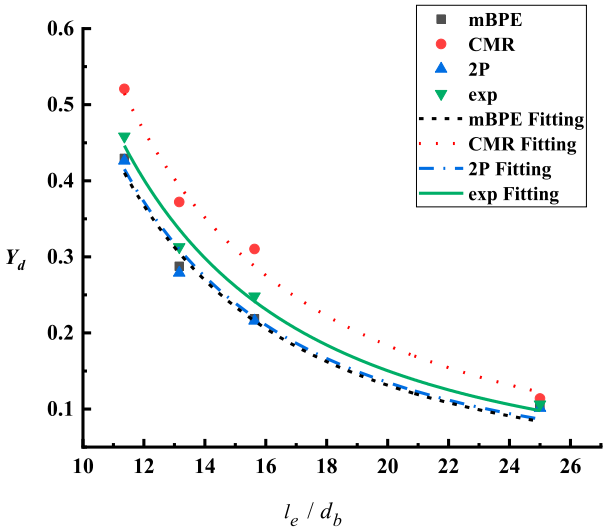

FIGURE 15
Variation of maximum bond strength with l_e/d_b ratio.

the bond strength model, the base number for each working condition needs to be integrated, and the final model for the data integration accounts for the effect of the concrete tensile strength f_t as follows:

$$\frac{\tau_u}{(8.00 - 0.17d_b)f_t} = \alpha + \beta p + \gamma\left(\frac{l_e}{d_b}\right)^x \tag{16}$$

where α, β, γ, and x were all obtained by fitting during the experiment. The bond strength model of the steam-cured concrete and the GFRP bars is expressed by Equation 14. Figure 18 shows that the fitted model was reliable based on comparative analysis of the fitted bond strength model and the test values.

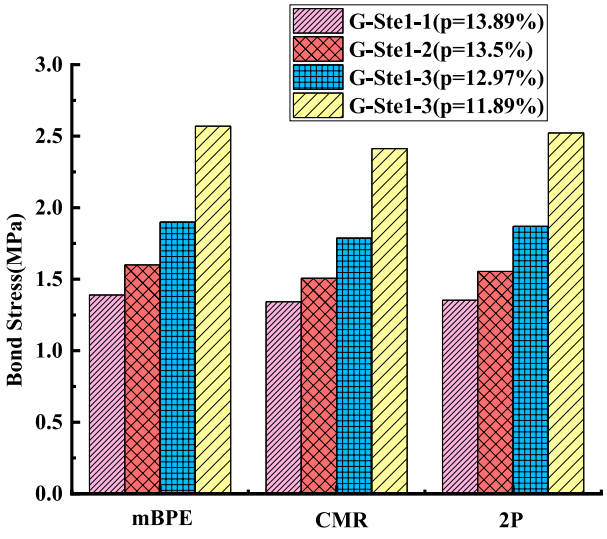

FIGURE 16
Relationship between bond strength and porosity under different models.

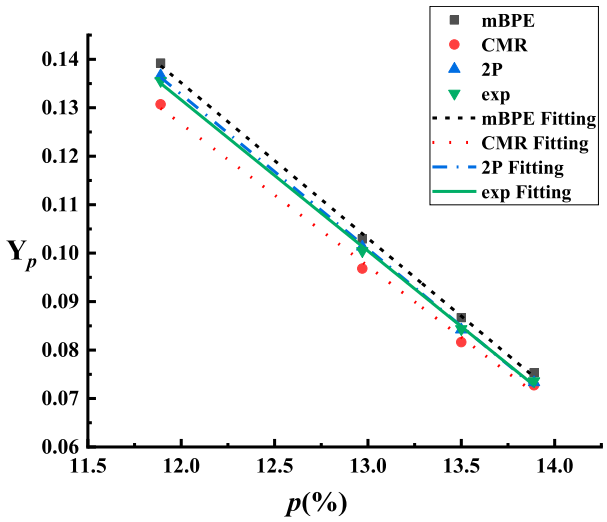

FIGURE 17
Variation of maximum bond strength with l_e/d_b ratio.

$$\frac{\tau_u}{(8.00 - 0.17d_b)f_t} = 0.44 + 0.03p + 41.5\left(\frac{l_e}{d_b}\right)^{-1.99} \quad (17)$$

5 Discussion

The tensile strength damage and bonding performance damage of GFRP bars in steam cured concrete are significantly lower than those of steel bars. Moreover, due to the increase in harmful pore structures in steam cured concrete, the difference in corrosion degree between steel bars and GFRP bars will be greater during long-term service. Steam cured

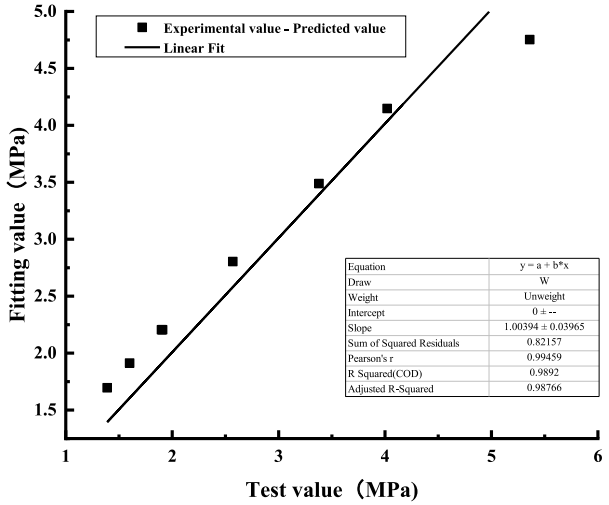

FIGURE 18
Comparative analysis of fitted value and test value.

reinforced concrete prefabricated components face greater durability issues. Therefore, replacing or partially replacing steel bars with high-strength and corrosion-resistant GFRP bars in steam cured concrete prefabricated components is indeed an effective way to solve the low service life of steam cured concrete prefabricated components. However, steam curing has caused damage to the later strength, capillary water absorption performance, and pore structure of concrete, which can have a certain impact on the bonding performance of GFRP bars in concrete. In addition to the high-temperature and high humidity environment of steam curing, the structural performance changes of steam cured concrete and the surface damage of GFRP bars are the main reasons for the bond strength damage of both. Studying any aspect of damage alone is not enough for the overall structure. Based on the classic bond slip constitutive model, using existing specifications and some researchers' research to calculate bond strength models, a bond strength damage prediction model for steam cured concrete and GFRP reinforcement was established. The model fully considers factors such as diameter, anchorage length, protective layer thickness, and concrete strength.

6 Conclusion

Analysis of the microscopic and macroscopic experimental results showed that the distribution of the concrete pore structure changed during steam curing at high temperatures and humidity, affecting the bonding of concrete and GFRP bars.

(1) Significant peeling and micro-cracking occurred on the surface of the steam-cured concrete. However, the interface comparison after cutting and polishing showed that the internal composition of the steam-cured concrete was no different from that of standard-cured concrete. Based on the analysis of the microstructure of the steam-cured concrete, the hydration products were not changed, but the density of the hydration products changed during the steam curing at high temperatures and humidity.

(2) The porosity of the steam-cured concrete was higher than that of the standard-cured concrete, and the solid-to-pore ratio was lower. The number of gel pores smaller than 20 nm accounted for 12.27% of the total number of pores on average, which was about twice the proportion of the gel pores of this size in the standard-cured concrete. The proportion of less harmful pores in the steam-cured concrete was lower than that of the standard-cured concrete. In contrast, the proportion of harmful pores and multi-harmful pores in the total pore size was significantly higher than that in standard-cured concrete. This showed that the distribution of the pore structure in the steam-cured concrete was significantly affected by the steam curing at high temperatures and humidity.

(3) The bond strength of the steam-cured concrete and GFRP bars was 30% lower than that of standard-cured concrete. The bond strength varied with the thickness of the concrete cover and the diameter. The maximum bond strength of the steam-cured concrete and the GFRP bars increased with the increase in the concrete cover thickness and diameter.

(4) Based on the classical bond-slip constitutive model, the damage prediction model of bond strength between steam cured concrete and GFRP bar is established by using existing specifications and some researchers. The model takes into account the effects of porosity, diameter, anchorage length and concrete strength on bond-slip strength. The results show that the fitting value is close to the test value, and the fitting effect is better.

(5) Based on the results of damage test research, a damage prediction model was established for the strength (compressive and tensile) of steam cured concrete, the tensile strength of GFRP bars in steam cured concrete, and the bonding strength between the two.

Data availability statement

The original contributions presented in the study are included in the article/Supplementary Material, further inquiries can be directed to the corresponding author.

Author contributions

ZT: Data curation, Writing—Original draft. WY: Methodology, Supervision, Conceptualization. KZ: Supervision. WW: Supervision, Writing—Reviewing and Editing. WQ: Experiment participation. SW: Experiment participation. All authors contributed to the article and approved the submitted version.

Funding

This study was funded by the Natural Science Foundation of Jiangxi Province (grant number 20181BAB216027), the Science and Technology Project Founded by the Education Department of Jiangxi Province (grant number GJJ170486), the Key Science and Technology Project of Jiangxi Provincial Department of Transportation (Project No. 2016C0007) and the Research Fund for the Doctoral Program of Higher Education of China (grant number DHBK2017119).

Conflict of interest

The authors declare that the research was conducted in the absence of any commercial or financial relationships that could be construed as a potential conflict of interest.

Publisher's note

All claims expressed in this article are solely those of the authors and do not necessarily represent those of their affiliated organizations, or those of the publisher, the editors and the reviewers. Any product that may be evaluated in this article, or claim that may be made by its manufacturer, is not guaranteed or endorsed by the publisher.

References

ACI (American Concrete Institute) (2005). *Guide for the design and construction of concrete reinforced with FRP bars*. Farmington Hills, MI: ACI Publishing.

ACI (American Concrete Institute) (2006). *Guide for the design and construction of structural concrete reinforced with FRP bars*. Farmington Hills, MI: ACI Publishing. ACI 440.1 R-06.

ACI Committee 440 (2015). *Guide for the design and construction of structural concrete reinforced with fiber reinforced polymer bars"*. Farmington Hills, MI: ACI Publishing. ACI 440.1R-15.

Al-Sibahy, A., and Sabhan, M. (2020). Corrosion effects on the bond behaviour of steel bars in self-compacting concrete. *Constr. Build. Mater.* 250, 118568. doi:10.1016/j.conbuildmat.2020.118568

Altalmas, A., El Refai, A., and Abed, F. (2015). Bond degradation of basalt fiber-reinforced polymer (BFRP) bars exposed to accelerated aging conditions. *Constr. Build. Mater.* 81, 162–171. doi:10.1016/j.conbuildmat.2015.02.036

Bakis, C. E., Boothby, T. E., and Jia, J. (2007). Bond durability of glass fiber-reinforced polymer bars embedded in concrete beams. *J. Compos. Constr.* 11 (3), 269–278. doi:10.1061/(asce)1090-0268(2007)11:3(269)

Bi, L., Long, G., Ma, C., and Xie, Y. (2021). Experimental investigation on the influence of phase change materials on properties and pore structure of steam-cured mortar. *Archives Civ. Mech. Eng.* 21 (1), 11–10. doi:10.1007/s43452-020-00170-7

Chen, L., Zheng, K., Xia, T., and Long, G. (2019). Mechanical property, sorptivity and microstructure of steam-cured concrete incorporated with the combination of metakaolin-limestone. *Case Stud. Constr. Mater.* 11, e00267. doi:10.1016/j.cscm.2019.e00267

Cieszko, M., Kempiński, M., and Czerwiński, T. (2019). Limit models of pore space structure of porous materials for determination of limit pore size distributions based on mercury intrusion data. *Transp. Porous Media* 127 (2), 433–458. doi:10.1007/s11242-018-1200-5

Cosenza, E., Manfredi, G., and Realfonzo, R. (1995). Analytical modelling of bond between FRP reinforcing bars and concrete, Proceedings of the non-metallic (FRP) reinforcement for concrete structures" - proceedings of the second international RILEM symposium(FRPRCS-2).Ghent, Belgium, January 1995

Ellis, D. S., Tabatabai, H., and Nabizadeh, A. (2018). Residual tensile strength and bond properties of GFRP bars after exposure to elevated temperatures. *Mater.* 11 (3), 346. doi:10.3390/ma11030346

Esfahani, M. R., Rakhshanimehr, M., and Mousavi, S. R. (2013). Bond strength of lap-spliced GFRP bars in concrete beams. *J. Compos. Constr.* 17 (3), 314–323. doi:10.1061/(ASCE)CC.1943-5614.0000359

Esmaeili, Y., Eslami, A., Newhook, J., and Benmokrane, B. (2020). Performance of GFRP-reinforced concrete beams subjected to high-sustained load and natural aging for 10 years. *J. Compos. Constr.* 24 (5), 04020054. doi:10.1061/(ASCE)CC.1943-5614.0001065

Focacci, F., Nanni, A., and Bakis, C. E. Local bond-slip relationship for FRP reinforcement in concrete. *J. Compos. Constr.*, 2000, 4(1): 24–31. doi:10.1061/(asce)1090-0268(2000)4:1(24)

Han, F., Song, S., Liu, J., and Huang, S. (2019). Properties of steam-cured precast concrete containing iron tailing powder. *Powder Technol.* 345, 292–299. doi:10.1016/j.powtec.2019.01.007

Hong, S., Kim, S., Lee, Y., and Jeong, J. (2018). Estimation of compressive strength of reinforced concrete structure using impact testing method and rebound hardness method. *Archit. Res.* 20 (4), 137–145. doi:10.5659/AIKAR.2018.20.4.137

Isleem, H. F., Tayeh, B. A., Alaloul, W. S., Musarat, M. A., and Raza, A. (2021). Artificial neural network (ANN) and finite element (FEM) models for GFRP-reinforced concrete columns under axial compression. *Mater.* 14 (23), 7172. doi:10.3390/ma14237172

Jiang, P., Jiang, L., Zha, J., and Song, Z. (2017). Influence of temperature history on chloride diffusion in high volume fly ash concrete. *Constr. Build. Mater.* 144, 677–685. doi:10.1016/j.conbuildmat.2017.03.225

Liu, B., Jiang, J., Shen, S., Zhou, F., Shi, J., and He, Z. (2020b). Effects of curing methods of concrete after steam curing on mechanical strength and permeability. *Constr. Build. Mater.* 256, 119441. doi:10.1016/j.conbuildmat.2020.119441

Liu, B., Shi, J., Zhou, F., Shen, S., Ding, Y., and Qin, J. (2020a). Effects of steam curing regimes on the capillary water absorption of concrete: Prediction using multivariable regression models. *Constr. Build. Mater.* 256, 119426. doi:10.1016/j.conbuildmat.2020.119426

Liu, M., Tan, H., and He, X. (2019). Effects of nano-SiO2 on early strength and microstructure of steam-cured high volume fly ash cement system. *Constr. Build. Mater.* 194, 350–359. doi:10.1016/j.conbuildmat.2018.10.214

Lü, Q., Qiu, Q., Zheng, J., Wang, J., and Zeng, Q. (2019). Fractal dimension of concrete incorporating silica fume and its correlations to pore structure, strength and permeability. *Constr. Build. Mater.* 228, 116986. doi:10.1016/j.conbuildmat.2019.116986

Maranan, G., Manalo, A., Karunasena, K., and Benmokrane, B. (2015). Bond stress-slip behavior: Case of GFRP bars in geopolymer concrete. *J. Mater. Civ. Eng.* 27 (1), 04014116. doi:10.1061/(ASCE)MT.1943-5533.0001046

Maruyama, T., Karasawa, H., and Date, S. (2017). Effect of type of cement and expansive agent on the hardening of steam-cured concrete. *Trans. Tech. Publ. Ltd.* 744, 105–113. doi:10.4028/www.scientific.net/KEM.744.105

Press, W. H., Teukolsky, S. A., and Vetterling, W. T. (2007). "Numerical recipes," in *The art of scientific computing*. 3rd edition (Cambridge: Cambridge University Press).

Rossi, C. R. C., C Oliveira, D. R., Picanço, M. S., Pompeu Neto, B. B., and Oliveira, A. M. (2020). Development length and bond behavior of steel bars in steel fiber–reinforced concrete in flexural test. *J. Mater. Civ. Eng.* 32 (1), 04019333. doi:10.1061/(ASCE)MT.1943-5533.0002979

Shi, J., Liu, B., Wu, X., Tan, J., Dai, J., and Ji, R. (2020a). Effect of steam curing on surface permeability of concrete: Multiple transmission media. *J. Build. Eng.* 32, 101475. doi:10.1016/j.jobe.2020.101475

Shi, J., Liu, B., Zhou, F., Shen, S., Dai, J., Ji, R., et al. (2020b). Heat damage of concrete surfaces under steam curing and improvement measures. *Constr. Build. Mater.* 252, 119104. doi:10.1016/j.conbuildmat.2020.119104

Shi, J., Liu, B., Zhou, F., Shen, S., Guo, A., and Xie, Y. (2021). Effect of steam curing regimes on temperature and humidity gradient, permeability and microstructure of concrete. *Constr. Build. Mater.* 281, 122562. doi:10.1016/j.conbuildmat.2021.122562

Sidiq, A., Gravina, R. J., Setunge, S., and Giustozzi, F. (2020). High-efficiency techniques and micro-structural parameters to evaluate concrete self-healing using X-ray tomography and mercury intrusion porosimetry: A review. *Constr. Build. Mater.* 252, 119030. doi:10.1016/j.conbuildmat.2020.119030

Sidiq, A., Gravina, R. J., Setunge, S., and Giustozzi, F. (2019). Microstructural analysis of healing efficiency in highly durable concrete. *Constr. Build. Mater.* 215, 969–983. doi:10.1016/j.conbuildmat.2019.04.233

Troian-Gautier, L., Beauvilliers, E. E., Swords, W. B., and Meyer, G. J. (2016). Redox active ion-paired excited states undergo dynamic electron transfer. *J. Am. Chem. Soc.* 138 (51), 16815–16826. doi:10.1021/jacs.6b11337

Wang, J., Long, G., Xiang, Y., Dong, R., Tang, Z., Xiao, Q., et al. (2022). Influence of rapid curing methods on concrete microstructure and properties: A review. *Case Stud. Constr. Mater.* 17, e01600. doi:10.1016/j.cscm.2022.e01600

Wang, L., Mao, Y., Lv, H., Chen, S., and Li, W. (2018). Bond properties between FRP bars and coral concrete under seawater conditions at 30, 60, and 80 °C. *Constr. Build. Mater.* 162, 442–449. doi:10.1016/j.conbuildmat.2017.12.058

Wang, M., Xie, Y., Long, G., Ma, C., Zeng, X., and Qiang, F. (2020). The impact mechanical characteristics of steam-cured concrete under different curing temperature conditions. *Constr. Build. Mater.* 241, 118042. doi:10.1016/j.conbuildmat.2020.118042

Wang, Y. L. (2013). *Experimental study on tensile properties of FRP bars and the bond properties to concrete after high temperature*. Zhengzhou, China: Zhengzhou University.

Wei, W., Liu, F., Xiong, Z., Lu, Z., and Li, L. (2019). Bond performance between fibre-reinforced polymer bars and concrete under pull-out tests. *Constr. Build. Mater.* 227, 116803. doi:10.1016/j.conbuildmat.2019.116803

Wikidata (2005). *TZ 210-2005, "technical specification for construction of railway concrete works"*. Beijing , China: China Railway Publishing House.

Wu, L., Xu, X., Wang, H., and Yang, J. Q. (2022). Experimental study on bond properties between GFRP bars and self-compacting concrete. *Constr. Build. Mater.* 320, 126186. doi:10.1016/j.conbuildmat.2021.126186

Xingyu, G., Yiqing, D., and Jiwang, J. (2020). Flexural behavior investigation of steel-GFRP hybrid-reinforced concrete beams based on experimental and numerical methods. *Eng. Struct.* 206, 110117. doi:10.1016/j.engstruct.2019.110117

Xu, J., Marsac, R., Costa, D., Cheng, W., Wu, F., Boily, J. F., et al. (2017). Co-Binding of pharmaceutical compounds at mineral surfaces: Molecular investigations of dimer formation at goethite/water interfaces. *Environ. Sci. Technol.* 51 (15), 8343–8349. doi:10.1021/acs.est.7b02835

Yan, F., and Lin, Z. (2017). Bond durability assessment and long-term degradation prediction for GFRP bars to fiber-reinforced concrete under saline solutions. *Compos. Struct.* 161, 393–406. doi:10.1016/j.compstruct.2016.11.055

Yang, W. (2016). *Damage research on steam-curing GFRP reinforced precast concrete components in high-speed railway*. Hubei, China: Wuhan University of Technology.

Yang, W., He, X., Zhang, K., Yang, Y., and Dai, L. (2017). Combined effects of curing temperatures and alkaline concrete on tensile properties of GFRP bars. *Int. J. Polym. Sci.* 2017, 1–8. doi:10.1155/2017/4262703

Yang, W., Tang, Z., Wu, W., Zhang, K., Yuan, J., and Li, H. (2022). Effect of different fibers on impermeability of steam cured recycled concrete. *Constr. Build. Mater.* 328, 127063. doi:10.1016/j.conbuildmat.2022.127063

Yoo, D. Y., Kwon, K. Y., Park, J. J., and Yoon, Y. S. (2015). Local bond-slip response of GFRP rebar in ultra-high-performance fiber-reinforced concrete. *Compos. Struct.* 120, 53–64. doi:10.1016/j.compstruct.2014.09.055

Yoo, D. Y., and Yoon, Y. S. (2017). Bond behavior of GFRP and steel bars in ultra-high-performance fiber-reinforced concrete. *Adv. Compos. Mater.* 26 (6), 493–510. doi:10.1080/09243046.2016.1197493

Zeyad, A. M., Johari, M. A. M., Abutaleb, A., and Tayeh, B. A. (2021). The effect of steam curing regimes on the chloride resistance and pore size of high–strength green concrete. *Constr. Build. Mater.* 280, 122409. doi:10.1016/j.conbuildmat.2021.122409

Zhang, K., Yang, W., Li, H., Tang, Z., Wu, W., Yuan, J., et al. (2021). Semi-reliability probability damage assessment of GFRP bars embedded in steam-curing concrete beams based on the multiple factors related moisture absorption model. *Polymers* 13 (24), 4409. doi:10.3390/polym13244409

Zheng, J. J., Dai, J. G., and Fan, X. L. (2016). Fracture analysis of frp-plated notched concrete beams subjected to three-point bending. *J. Eng. Mech.* 142 (3), 04015096. doi:10.1061/(ASCE)EM.1943-7889.0001021

Zheng, Q. W., and Xue, W. -C. (2008). Bond slip constitutive relation of GFRP bars with sand deformation. *Eng. Mech.* (09), 162–169.

Zhou, X., Zhao, H., Xie, Y., Long, G., Zeng, X., Li, J., et al. (2022). Mechanical behavior of bonded interface between steam-cured concrete and SCC under direct shear test: Experimental and numerical studies. *J. Build. Eng.* 63, 105517. doi:10.1016/j.jobe.2022.105517

Zou, C., Long, G., Xie, Y., He, J., Ma, C., and Zeng, X. (2019). Evolution of multi-scale pore structure of concrete during steam-curing process. *Microporous Mesoporous Mater.* 288, 109566. doi:10.1016/j.micromeso.2019.109566

Zou, C., Long, G., Zeng, X., Ma, K., and Xie, Y. (2021). Hydration and multiscale pore structure characterization of steam-cured cement paste investigated by X-ray CT. *Constr. Build. Mater.* 282, 122629. doi:10.1016/j.conbuildmat.2021.122629

10.3389/fmats.2023.1190031

Nomenclature

A_f	The cross-sectional area
A_b	Section area of reinforcement
b	The width of beams
C	Slip parameter
c	Concrete cover thickness
d	Diameter
d_b	Diameter of reinforcement
E	Elasticity Modulus
E_b	Elasticity modulus of reinforcement
E_f	Longitudinal modulus of elasticity
F	Ultimate tension
f_t	Tensile strength of concrete axis
h	Height
K_c	Fitting parameters
K_d	Fitting parameters
K_T	Reduction factor
k	Undetermined coefficient
l	Length
l_e	Anchoring section
N_{smax}	Maximum slip load
P	Load
p	Porosity
R	Tensile Strength
S	Slip value
S_c	Corresponding slip value τ_c
S_{max}	Corresponding slip value τ_{max}
t	Fitting parameters
w	Fitting parameters
x	Fitting parameters
α	Fitting parameters
β	Fitting parameters
γ	Fitting parameters
τ	Bond strength
τ_c	Corresponding bond strength at the beginning of linear slip
τ_{max}	Maximum bond strength
ϕ	Linear interpolation
ρ	Fitting parameters
b	Fitting parameters
η	Fitting parameters
ω	Fitting parameters
φ	Fitting parameters
Y_d	Calculated value of bond strength
Y_p	Calculated value of bond strength

frontiers | Frontiers in Materials

TYPE Original Research
PUBLISHED 03 August 2023
DOI 10.3389/fmats.2023.1231461

OPEN ACCESS

EDITED BY
Dawei Wang,
RWTH Aachen University, Germany

REVIEWED BY
Peiwen Hao,
Chang'an University, China
Xinxing Zhou,
Shanxi Transportation Technology Research and Development Co., Ltd., China

*CORRESPONDENCE
Wenju Peng,
pwj1112@foxmail.com
Jing Mao,
may_mao.nn@foxmail.com

RECEIVED 30 May 2023
ACCEPTED 14 July 2023
PUBLISHED 03 August 2023

CITATION
Li P, Peng W, Mao J, Yan X, Liu Z and Kong L (2023), Airport pavement performance evaluation of pavement fog seal based on optimized test technology. *Front. Mater.* 10:1231461. doi: 10.3389/fmats.2023.1231461

Airport pavement performance evaluation of pavement fog seal based on optimized test technology

Ping Li[1], Wenju Peng[1,2]*, Jing Mao[1]*, Xin Yan[3], Zhaohui Liu[1] and Lingyi Kong[4]

[1]School of Traffic and Transportation Engineering, Changsha University of Science and Technology, Changsha, China, [2]School of Civil Engineering, Hubei Engineering University, Xiaogan, China, [3]Hunan Hengyong Expressway Construction and Development Co., Ltd, Changsha, China, [4]China Construction Seventh Engineering Division Corp., Ltd, Zhengzhou, China

Fog seal technology is widely used in airport asphalt pavement. The research on the performance and application of fog seal material is basically at the level of modified emulsified asphalt. The fog seal test method in the existing specification has defects. Three kinds of fog seal materials with different substrates were selected in this paper. Based on the characteristics of fog seal treatment and the relevant specifications of fog seal and airport pavement. Wet Track Abrasion Test (WTAT), Cantabro test, Water seepage test, and Pendulum instrument tester pavement friction coefficient test were improved. Test the pavement performance of different types of fog seals. The results show that the mass loss of material C was less than 10% after 200 and 400 cycles of wear. The improvement effect of material C on raveling resistance and impermeability was far better than that of materials A and B. The improvement of material C on the raveling resistance of the mixture could reach 50%. The immediate improvement effect on the impermeability was nearly 100%. The skid resistance performance of the three fog seal materials decreased after treatment. The decrease in material C was more significant than in materials A and B. In constructing material C, the dose of emery should be appropriately increased. It was advisable to not be less than 0.35 kg/m^2. The fog seal layer improves pavement performance. It has reference significance for using fog seal technology to treat early airport pavement diseases.

KEYWORDS

fog seal, airport pavement, non-emulsified asphalt fog seal, pavement performance, testing technologies

1 Introduction

Airport pavement is one of the significant infrastructures in various countries that require different investments to ensure the safety of aircraft transportation (Xiao et al., 2019). However, the airport pavement is exposed to a particular service environment. These factors can cause more damage to the pavement surface materials than ordinary flexible pavement due to the frequent effects of temperature stress, dynamic stress, and tire wear (Peng et al., 2023; Zhang et al., 2023). Preventive maintenance is an effective strategy to extend the service life of airport pavements and mitigate the risk of pavement deterioration (Feng X. et al.,

2019; You et al., 2020). The fog seal technology has been applied to airport pavement maintenance and has received wide recognition (Xu et al., 2021). Fog seals can increase the adhesion of pavement asphalt, reduce the destructive rate of the pavement, extend the service life of the road, and defer the need for expensive repair and reconstruction work (Jia et al., 2021; Xu et al., 2021). The fog seal material has high fluidity and can penetrate the gaps and microcracks in the road surface structure after spraying, improving the impermeability of the pavement (Xv et al., 2022). Aggregates can be effectively stabilized by fog seal technology (Guo et al., 2017). Prevent traffic accidents caused by aggregate spatter on the road surface. Traffic can usually resume in about 3 h, which meets the high road traffic supply demand at the airport (Minaka et al., 2021). The performance of conventional emulsified asphalt fog seals is often unsatisfactory regarding mechanical strength, cohesion, water resistance, and durability (Rahman et al., 2020). The performance test method of the fog seal layer differs from the actual pavement condition (Im and Kim, 2013).

Many researchers have attempted to improve its effectiveness through modification. For example, Feng (Feng P. et al., 2019) prepared a bio-oil-modified emulsified asphalt fog seal and tested its permeability and indoor skid resistance, finding that it had a good treatment effect on the pavement. Jiang (Jiang et al., 2021) prepared an epoxy-emulsified asphalt fog seal with emery sand. The skid resistance fog seal specimen met the technical requirements of ordinary asphalt pavement, with only a 27.4% reduction in British Pendulum Number (BPN) after 100,000 times of wear. Hu et al. (Hu et al., 2020) used waterborne epoxy-modified asphalt emulsion as a fog seal. They conducted laboratory and field tests, showing that the pavement texture and skid resistance was significantly improved after sand fog sealing. Liu (Liu et al., 2021) prepared a waterborne epoxy resin SBR composite modified emulsified asphalt fog sealing layer. He tested its pavement performance and durability, concluding it had good durability and could extend its service life. Cui et al. (Cui et al., 2019) prepared a silicone resin polymer-based fog seal and tested its ability to isolate water, improving the moisture resistance of asphalt mixtures. They also determined the optimal ratio of this kind of fog seal by impermeability test, Marshall test, and rutting test. Xu (Xu et al., 2022) modified emulsified asphalt by adding two thermosetting materials. The materials were waterborne cationic acrylate (WCA) and waterborne epoxy resin, and their potential in airport pavement fog sealing technology was tested and analyzed. It can be seen from recent studies that although modified emulsified asphalt fog seal has been extensively researched, there are few studies on non-emulsified asphalt fog seal.

As the road surface is treated by fog seal technology, its skid resistance performance cannot be guaranteed (Islam et al., 2017; Zhang et al., 2019). To test its improvement effect, researchers mostly use the pendulum value method to test the skid resistance performance of the road (Qureshi et al., 2013; Ministry of Transport of the People's Republic of China, 2019). Still, the test is directly measured after the fog seal material is dried and the pendulum value method is tested. The swing direction is consistent with the driving law, and the vehicle will also have a sideslip on the road surface (Wu et al., 2021). There is a big gap between the test and the actual driving condition of the road surface. The basic principle of fog seal to improve the pavement is that the emulsion penetrates the interconnected voids and small cracks to prevent water from eroding the pavement (Cui et al., 2019). Therefore, the fog seal is significant for improving the impermeability of the pavement. Currently, researchers mostly use the test method of seepage coefficient to test. Still, because of the connected voids on the top and side of the rutting plate, the seepage coefficient is larger than the actual result. In addition, when the airport pavement is subjected to aircraft landing, the pavement aggregate is prone to scattering, and the aggregate can be protected after fog seal treatment (Praticò et al., 2015). Currently, the researchers mostly use the asphalt mixture Cantabro Test (T 0733–2011) to test its performance. The Cantabro Test measures the degree of aggregate loss on the pavement surface under traffic load. This loss is caused by the lack of asphalt content or cohesiveness, which differs from the principle of fog seal treatment of pavement dispersion. At the same time, the application of fog seal technology in airport pavement is more and more extensive. There are few studies on airport pavement, and the test methods of such studies have not changed accordingly due to airport pavement (Xu et al., 2022).

In this paper, three kinds of fog seal materials are selected. The material properties are emulsified asphalt, modified emulsified asphalt and special material properties. The Cantabro test, water seepage test and pavement friction coefficient test were improved. Verify the rationality of the test improvement. The performance of fog seal was tested by improved test and wet track abrasion test (WTAT). The improvement effect of non-emulsified asphalt fog seal on the performance of the mixture is analyzed, which provides a theoretical reference for the application of fog seal technology in airport asphalt pavement.

2 Materials and methods

2.1 Materials

Three kinds of fog seal materials were selected. Material A is a fog seal with emulsified asphalt as a matrix additive, and materials B and C were non-emulsified asphalt fog seals.

Material A consisted of emulsified asphalt as the base, blended with clay, modifier, additive, tackifier, and fine sand. The additive was a polymer-based viscosity modifier that enhanced the elasticity and oil resistance of the cover materials. It also formed a black and dry film on the asphalt pavement surface.

Material B comprised modified asphalt, fine aggregate, polymer modifier, and catalyst. The modified asphalt did not contain harmful substances such as coal tar, which was less harmful to environmental pollution and the human body.

Material C consisted of natural rock asphalt as the main ingredient and petroleum, petroleum asphalt, heavy in solvent naphtha, solvent, additives, and emery. The medium molecular-weight additive improved the solubility of each component and ensured the material's stability.

The recommended dose of various fog seal materials is shown in Table 1.

TABLE 1 Recommended dose of various materials.

Fog seal	Recommended dose range (kg/m^2)
A	0.55–0.75
B	0.65–0.85
C	0.63–0.79

2.2 Mixture design

SBS-modified asphalt is selected. The gradation of the asphalt mixture is shown in Figure 1. The optimum oil-stone ratio is 4.0%. AC-13 gradation is adopted. Marshall and rutting plate pieces are made according to JTG E20-2011 (Ministry of Transport of the People's Republic of China, 2011). The Marshall specimen was used to test the raveling resistance performance, and the rutting plate specimen was used to test the impermeability and skid resistance performance.

2.3 Test method

Fog seal is a common technique for pavement maintenance, but it may not meet the practical engineering requirements of skid resistance performance, wear resistance, and impermeability (Islam et al., 2017; Zhang et al., 2019). In addition, the current specification imposes higher standards for pavement quality after fog seal treatment (Airport Department of China Civil Aviation Administration, 2010; Civil Aviation Administration of China, 2017; Civil Aviation Administration of China, 2019). This paper tests and analyzes the performance of wear resistance, loose resistance, impermeability, and skid resistance to verify the rationality of the new test method.

Currently, only the wear resistance of the fog seal has a direct measurement method, and the other three properties need to be completed using an asphalt mixture performance test. The raveling resistance and impermeability tests are based on standard JTG E20-2011 (Ministry of Transport of the People's Republic of China, 2011) 'Cantabro test of asphalt mixture (T 0733–2011)' and 'Water seepage test of asphalt mixture (T0730-2011)'. The skid resistance test is based on standard JTG 3450–2019 (Ministry of Transport of the People's Republic of China, 2019) 'Pendulum instrument tester pavement friction coefficient test (T 0964–2008)'. However, these three methods are designed for asphalt mixture performance, so it is necessary to modify the principle of fog seal treatment to obtain optimal test results. The overall test scheme is shown in Figure 2.

2.3.1 Wet track abrasion test

WTAT method from standard JT/T 1330–2020 (Airport Department of China Civil Aviation Administration, 2020) was used to evaluate the wear resistance of the fog seal material by studying the difference in wear resistance under the dose and wear revolution conditions. A circular WTAT oil-felt substrate with a diameter of 286 mm was made and floated up and down according to the recommended dose range in Table 1. Four different test doses were determined for each fog seal material. According to the dose, the fog seal material was evenly applied to the oil felt, and the wet wheel abrasion tester was used to carry out the abrasion test in two 200 revolutions each. The mass loss after two wear times was measured, m_0 and m_1, respectively. The wear resistance of the fog seal was evaluated by comparing the residual mass fraction of the two times. The residual mass fraction of the first and second wear was calculated as T_1 and T_2, respectively.

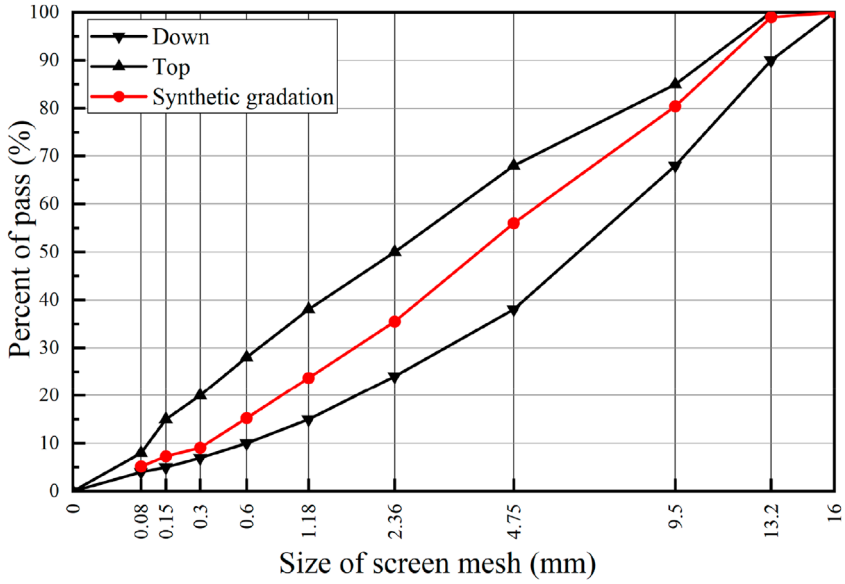

FIGURE 1
Design curve of mix proportion.

Calculation formula of residual mass fraction:

$$T = \frac{m_0 - m_1}{m_0} \quad (1)$$

Where T is wear abrasion mass fraction, m_0 is test dose, and m_1 is wear mass loss.

2.3.2 Improve cantabro test

To determine the optimal asphalt-aggregate ratio, the standard test method of JTG E20-2011 (Ministry of Transport of the People's Republic of China, 2011) Cantabro test of asphalt mixture (T 0733–2011) was adopted. The fog seal material was applied on both surfaces of the Marshall specimens, and the mass loss before and after the application was measured and compared. The test results are presented in Schedule 2.

As shown in Figure 3, the mass loss of the specimens after the fog seal material treatment was not significantly reduced, and the error due to the specimen preparation was too large. Therefore, several groups of immersion standard Cantabro tests were conducted using material A to increase the mass loss rate and make it more observable. The test results are presented in Schedule 3.

From the test data of the immersion mentioned above Cantabro test, it can be found that the improvement effect of fog seal treatment on the raveling resistance performance of Marshall specimens cannot be highlighted. The optimum oil-stone ratio of AC-13 was reduced to 3.4% and 3.6%, respectively. This increased the area of the coating material, and the outer surface of the specimen was completely coated with the material. As a result, the mass loss rate of the specimen increased. The dose value of the material was based on the recommended dose range in Table 1 to obtain the median dose. In addition, an upper limit dose and a lower limit dose outside the recommended range were selected for the test, and the specific dose is shown in Schedule 4.

Testing procedures are below. Marshall specimens with 3.4% and 3.6% oil-stone ratios were made, respectively. The identical samples were divided into groups I and II (three in each). The specimens were immersed in water at room temperature for 3 days. The 9 min Cantabro test was performed directly in group I, and the mass loss was ΔS_1. According to Schedule 5, the amount of fog seal material required on the surface of the specimen was calculated. All kinds of fog seal materials were evenly applied on the surface of group II models, then placed in an oven at 50°C for 3 h to completely dry the surface fog seal material. The group II specimens were subjected to the 9 min Kentucky Flying Test, and the mass loss was ΔS_2. Two mass losses obtained from the same oil-stone ratio were taken, and the mass loss ratio was S.

Calculation formula of mass loss ratio:

$$S = \Delta S_2 / \Delta S_1 \quad (2)$$

Where S is the mass loss ratio, ΔS_1 is the group I quality loss, and ΔS_2 is group II quality loss.

2.3.3 Improve water seepage test

The impermeability test was based on the Water seepage test of asphalt mixture (T 0730–2011) in standard JTG E20-2011 (Ministry of Transport of the People's Republic of China, 2011). The trial compared the impermeability of the mixture before and after applying the fog seal material under different doses and void content conditions to evaluate the ability of the fog seal material to fill the cracks and voids of the pavement. To enhance the testing effect, simulate various road conditions, and improve the accuracy and efficiency of the test, a new water seepage test method was developed in this paper.

1) Simulate different pavement conditions

In order to simulate the seepage rate of the pavement with different degrees of slight cracks on the pavement, the parameters

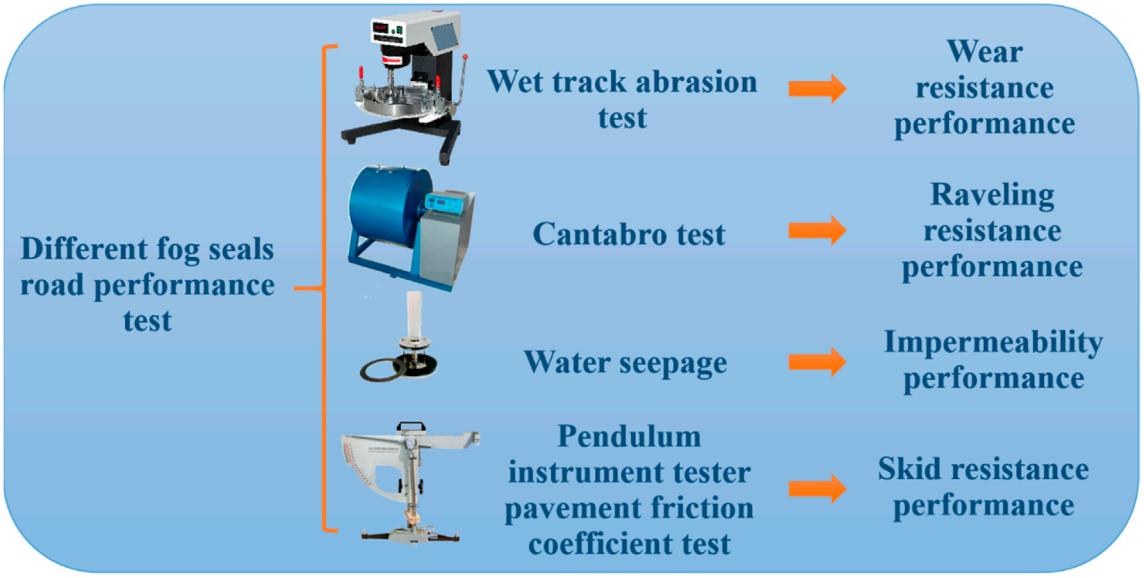

FIGURE 2
Test method.

FIGURE 3
Plate after testing.

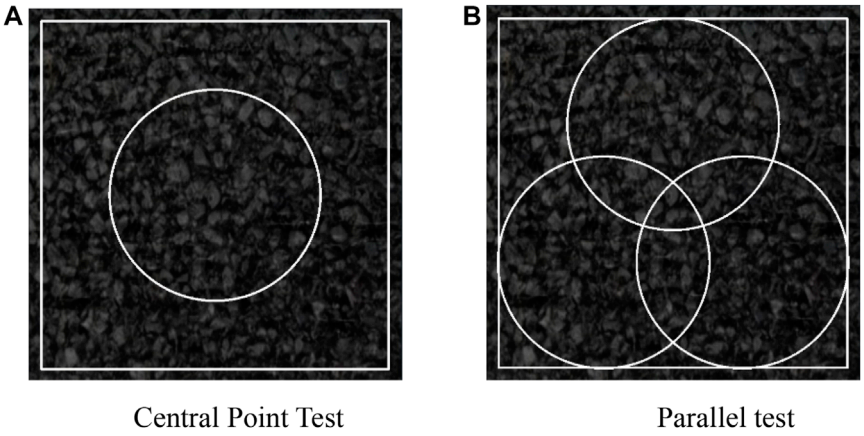

FIGURE 4
Regional of improve test. **(A)** Central Point Test. **(B)** Parallel test.

of the specimens were adjusted, and the void content of the models was controlled by the number of rolling times and the oil-stone ratio. Finally, the rutting plate specimens with 5%, 8%, and 11% void content were prepared according to the parameters in Schedule 5.

2) Improve the test method

To avoid the influence of plugging material on the subsequent application of fog sealing material, the plugging material was changed to light clay in the test, which had low cost, no residue, and could be recycled. The comparison data of the same specimen was fundamental, so considered increasing the number of single plate tests. To ensure that the surface of the model was dry, a test was first carried out in the center of the specimen. The light clay was taken down, the water in the sample was dried, and the position was adjusted upward, lower left, and lower right. Four comparative tests were carried out (see Figure 4 in the test area), and the average value of the four data was taken as the specimen's original seepage rate.

To minimize the effect of the interconnected voids on the surface of the rutting plate on the test accuracy, applying the fog seal material was divided into two steps. The fog seal material was used outside the water seepage area after measuring the water seepage rate of the original specimen. After sealing the interconnected voids outside the water seepage area (radius of 75 mm) (as shown in Figure 4A, denoted as A_1, with an area of 0.072 m^2) to eliminate interference, the water seepage rate at this stage was measured. Then, the water seepage area (as shown in Figure 4B, the shaded part is denoted as A_2, with an area of 0.018 m^2) was sealed with the fog seal material, and then the water seepage rate at this stage was measured.

The influence of connected voids was eliminated. The number of tests on the same specimen was increased as much as possible. The final test method made the data more accurate. The specific test methods were as follows.

The rutting plate was made according to the intermediate gradation of Figure 1. The models were coated with hot asphalt and wrapped with paper to avoid too high temperatures. This prevented the surrounding asphalt from flowing closed and causing pollution. The first measuring point was taken in the center of the specimen. The water permeability coefficient of the point was measured. Then, the sample was placed in a dry, ventilated place to dry. Three to four measuring points were selected near the center point, and the above steps were repeated. The water permeability coefficient was measured, and the average value was the water permeability coefficient of the original specimen. According to Schedule 4, the shadow part in Figure 5A was smeared with the corresponding

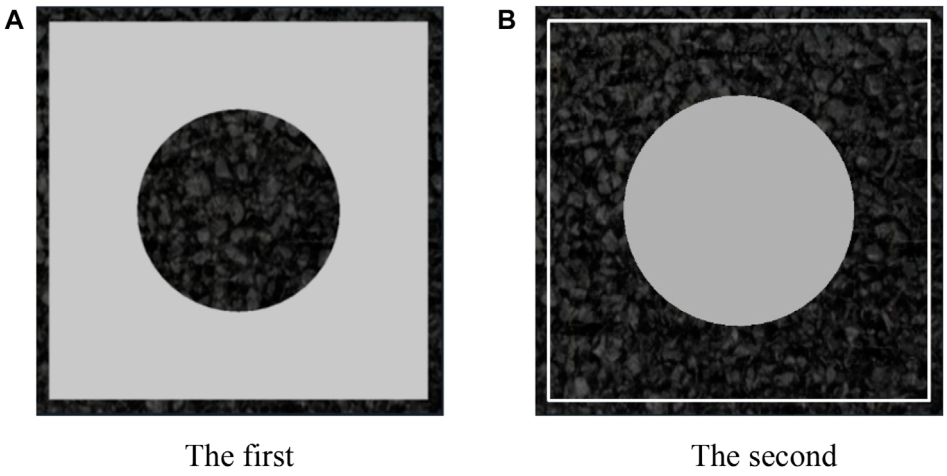

FIGURE 5
Paint area diagram. **(A)** The first. **(B)** The second.

quality of fog seal material. After it reaches complete drying, the point seepage coefficient was measured as S_1. The corresponding dose in Schedule 5 shows that the shadow part in Figure 5B was smeared with the corresponding fog seal material. After it was completely dried, the water permeability coefficient was measured, which was the water permeability coefficient of the specimen after the fog seal material was sealed, which is counted as S_2.

Calculation formula of seepage coefficient:

$$S = \frac{v_1 - v_0}{t_1 - t_0} \times 60 \tag{3}$$

Where S is the water permeability coefficient, v_0 is the first timing of the water (mL), usually 100 mL, v_1 is the second timing of the water (mL), usually 500 mL, t_0 is the time of the first time (s), and t_1 is the time of the second timing (s).

2.3.4 Improve pendulum instrument tester pavement friction coefficient test

The Method of testing pavement friction coefficient with pendulum instrument (T 0964–2008) in standard JTG 3450–2019 (Ministry of Transport of the People's Republic of China, 2019) was adopted. This method evaluated the effect of fog seal material on pavement skid resistance by comparing the changes in pavement friction coefficient under different materials and doses. The rutting plate wear test was used to simulate the condition of the asphalt pavement after a period of use, and the fog seal material (as shown in Schedule 6) with the typical dose and the increased dose (about 30% higher than the standard dose) was applied for testing.

1) Rutting plate specimens were prepared according to the method in water seepage test. The friction coefficient of the original specimen was tested, which was counted as B;
2) The surface of the specimen was treated with a wet wheel abrasion tester (the wear range is the circular area in Figure 6). The surface of the specimen was ground to a friction coefficient of about 75 BPN. The friction coefficient was calculated to be B_1;

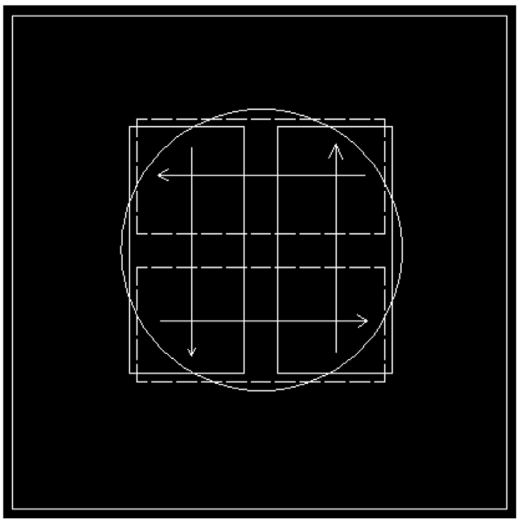

FIGURE 6
Friction coefficient test diagram.

3) The prescribed dose of fog seal material was applied on the surface of the specimen according to the rectangular range shown in Figure 6;
4) After it reached complete drying, the four friction coefficients at this time were tested according to the arrow direction in Figure 6. The average value was taken, which was the friction coefficient on the surface of the specimen after applying the fog seal, which was counted as B_2.

Friction coefficient calculation formula:

$$BPN_{20} = BPN_T + \Delta BPN \tag{4}$$

Where BPN_{20} is converted to the BPN at a standard temperature of 20 °C; BPN_T is BPN measured at road surface temperature T; ΔBPN is temperature correction.

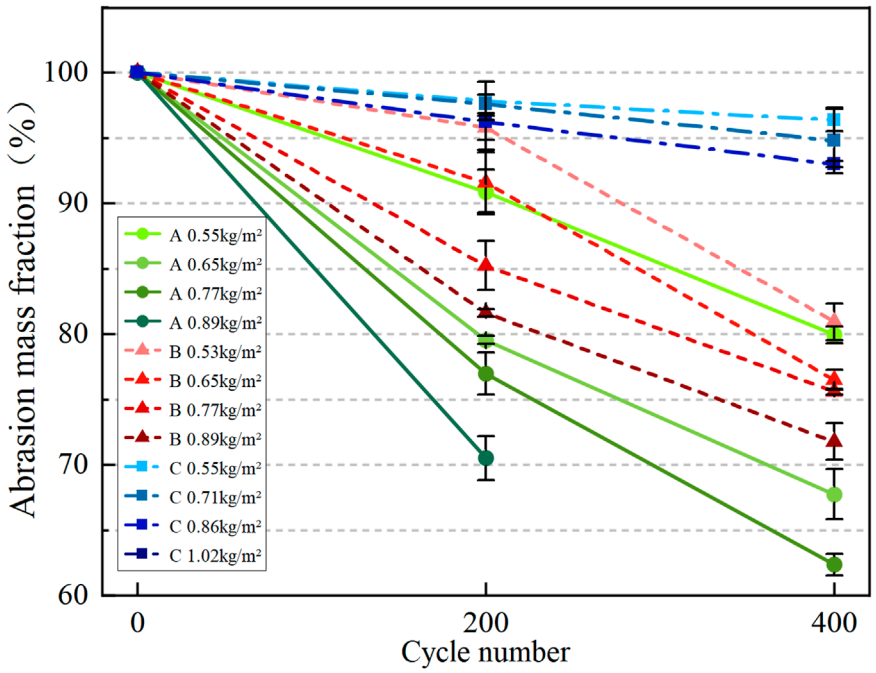

FIGURE 7
Quality change of fog seal. Note: Among them, the third group of specimens of material A ended the test process in advance because of the wear of the models without completing the specified times. The fourth concentration of material C was too large for the oil-felt specimen, and it was not easy to smear evenly.

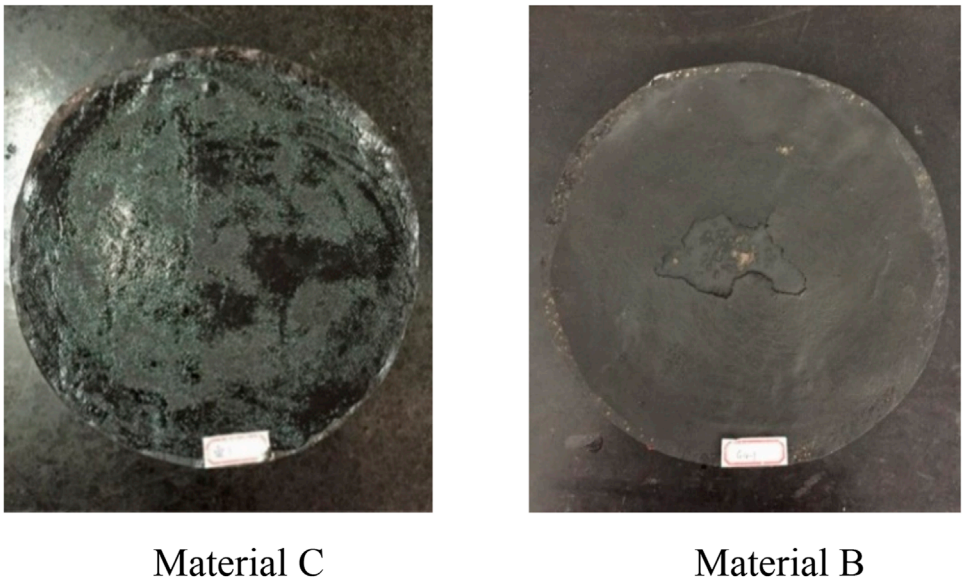

FIGURE 8
Specimen after test.

3 Results and discussion

3.1 Wear resistance performance analysis

Quality change of fog seal is shown in Figure 7, specimen after test is shown in Figure 8. The wear loss of the fog seal layer increased linearly with the increase of wear cycles. The wear loss of the three fog seal materials was significantly different, and material C had much better wear resistance than the other two materials. After 400 cycles of wear, the remaining mass of material C was consistently above 90%, while the remaining group of the other two materials was only about 70%. This was due to the different

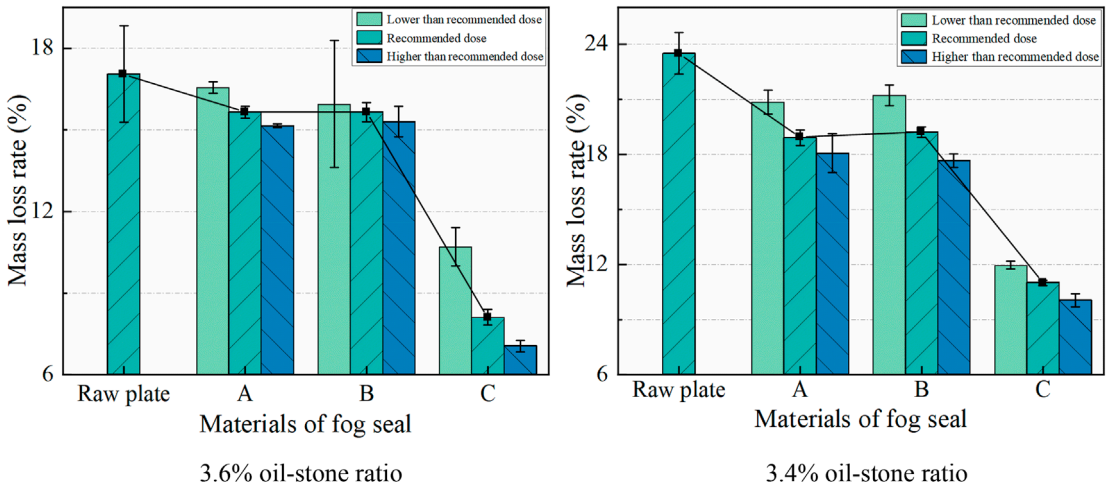

FIGURE 9
Mass loss rate under different oil-stone ratios.

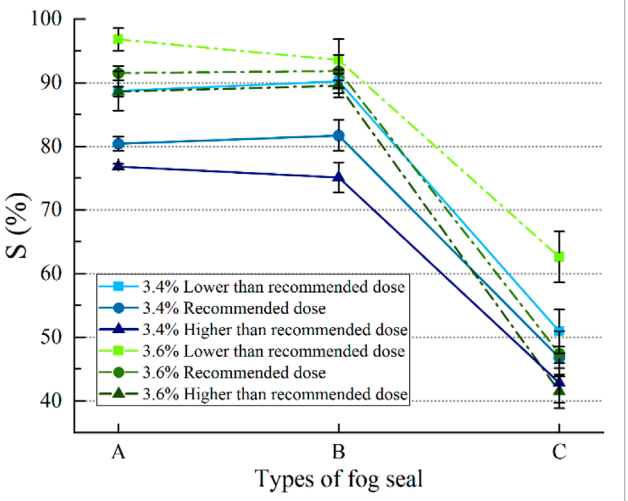

FIGURE 10
Mass loss ratio under different oil-stone ratios.

adhesion of the interface between the three materials and the mixture in the water environment. The adhesion of materials A and B decreased after soaking in water, which made them more prone to wear. On the other hand, material C was water-insoluble, and the additive was a medium molecular weight substance, which gave it excellent overall stability, showing the best durability among the three materials (Huang et al., 2020). This indicated that under the combined conditions of rainwater weather and tire wear, the performance of the fog seal would gradually deteriorate.

The mass loss of the three fog seals increased with the increase of the dose of the material, and the wear resistance of cloth C was the least sensitive to the change of the dose. The proliferation of the dose did not enhance the adhesion between the material and the mixture interface. On the contrary, the humidity sensitivity of the fog seal material continued to rise, and it was easier to fall off underwear and water. Under different doses, the residual mass of material C changed within 7%. The primary material of material C was rock asphalt. This material had higher strength and peel resistance, forming a dense, bright protective film on the free surface (Li et al., 2020). This film could effectively prevent the wet wear of wheels.

3.2 Raveling resistance performance analysis

Figure 9 showed mass loss rate under different oil-stone ratios. The fog seal treatment significantly reduced the mass loss rate of the specimens, and material C had a much better treatment effect than materials A and B. The three kinds of fog seal materials could fill the voids and microcracks on the road surface after coating and wrapping the exposed aggregates of the road surface. This reduced the possibility of raveling and improved the overall performance of the road surface (Guo et al., 2017; Sahebzamani et al., 2018). After applying material C, its raveling resistance performance was significantly improved. The mass loss of the specimens was reduced by up to 50%, and the improvement range was 2–3 times that of materials A and B. The primary raw material of material C was natural rock asphalt. This material had a molecular weight of up to 9,000, a high temperature viscosity, and excellent adhesion with alkaline aggregates. Hence, the specimens showed excellent raveling resistance properties.

The raveling resistance performance of the mixture increased with the increase of the material dose. Still, the change in the material dose had little effect on the raveling resistance performance, and the change range was within 3%. This indicated that increasing the dose did not significantly improve the adhesion of the fog seal material. The improvement effect depended more on the primary adhesion of each material. The slight performance improvement caused by the increase in dose was assumed to be due to the slight increase in viscosity. However, from the practical application

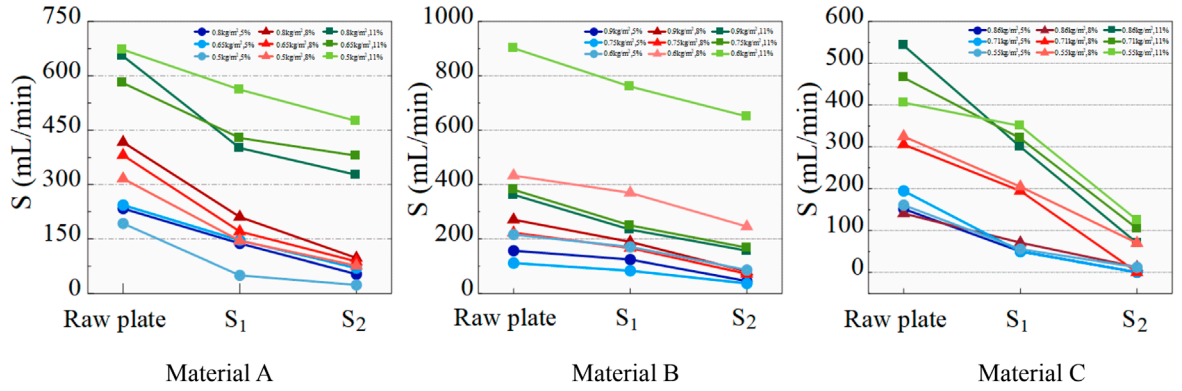

FIGURE 11
Results of the water seepage test.

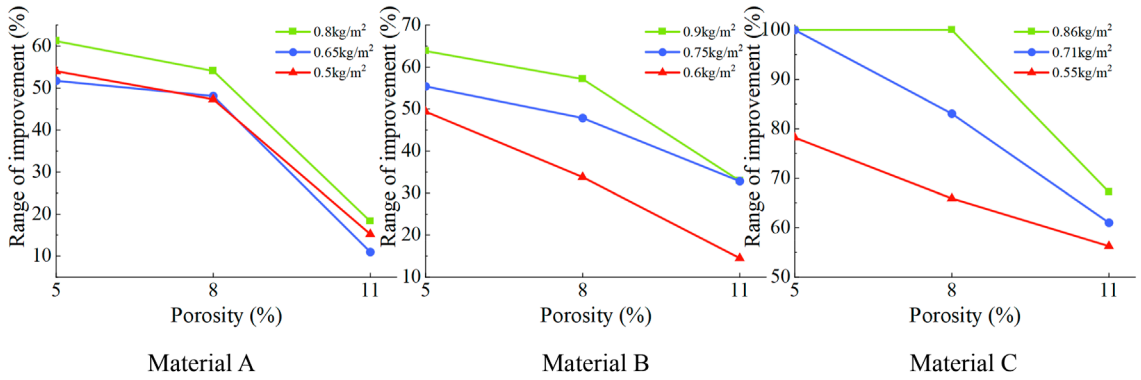

FIGURE 12
The improvement of different doses.

perspective, considering the wear resistance test results, increasing the dose of materials was not recommended to obtain better raveling resistance.

The smaller the oil-stone ratio was, the more significant the improvement effect of the fog seal material was on the raveling resistance performance. The impermeability after material C treatment was the least sensitive to the change in the oil-stone ratio. As the oil-stone ratio decreased, under the same gradation condition, the surface voids of the mixture became larger, and the fog seal material penetrated the surface voids more easily. This material acted as a binder, enhancing the cohesion from the inside, and protected the aggregate during the impact and rolling process. The sensitivity of the raveling resistance performance of the three materials to the change in oil-stone ratio was different. From high to low was A > B > C. Figure 10 showed that material C had a stable and superior performance in raveling resistance for different oil-stone ratio specimens, as long as the dose of the fog seal met or exceeded the recommended level. Materials A and B were inferior to material C in this aspect. It could be seen that material C was a better choice under different degrees of pavement damage.

3.3 Impermeability performance analysis

Results of the water seepage test is shown in Figure 11. With the expansion of the fog seal material's coating area, the water permeability coefficient of the asphalt mixture decreased, and material C had the best improvement effect. This shown that the fog seal material could seal the pavement gap and fill the micro-cracks, thereby preventing the pavement from water seepage. The seepage coefficient of pavement was less than 10 mL/min when the void content was 5%, and the dose of material C was either 0.71 kg/m^2 and 0.86 kg/m^2. This value met the technical requirements of airport pavement after spraying the fog seal (Airport Department of China Civil Aviation Administration, 2010).

The fog seal material enhanced the mixture's impermeability more effectively when the void content was more less. For instance, material C improved impermeability by 100% when the void content was 5% but only by 61% when the void content was 11%. This phenomenon could be attributed to the fact that the surface voids of the dense graded low void content mixture were fewer, and thus the fog seal material could exert its full treatment effect. However,

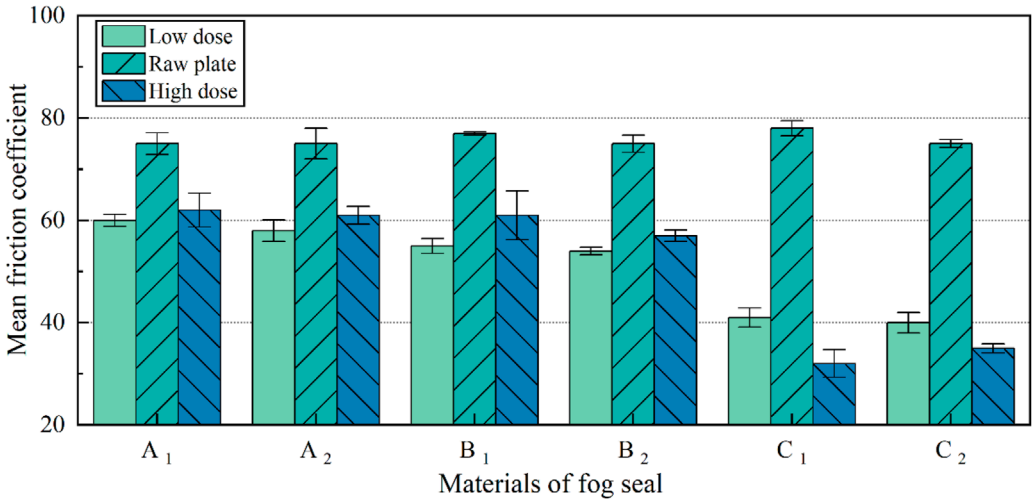

FIGURE 13
Friction coefficient at different doses.

when the road surface void content increased, the fog seal material could not fill these voids adequately, leading to poor improvement of fog seal material. Hence, the fog seal method was not recommended for treating pavement with severe damage.

The improvement of different doses is shown in Figure 12. With the increase in the dose of fog seal material, the impermeability of the mixture was improved, and the sensitivity of material C to the change of dose was the highest. The increased material dose increases viscosity, which could block more water seepage. The sensitivity of impermeability to the dose change of the three materials was different. From high to low is material C > material B > material A. The reason was that material A is based on emulsified asphalt. If there was uneven mixing, insufficient moisture, or insufficient dose, cracking might occur during drying, and its impermeability was significantly reduced. The fluidity of material B was better than that of material A, and it was easier to close the gap evenly, so the improvement effect of material B was slightly better than that of material A; material C had less fluidity and greater viscosity. The surface voids could be tightly sealed by uniform application, and it had certain toughness in the dry state, so it was not easy to crack. At the same time, when the void content was significant and the fog seal dose was small, the improvement effect of impermeability was also poor. It can be seen that when pavement damage was severe if the fog seal was used for treatment, the fog seal material could not be used in small doses.

3.4 Skid resistance performance analysis

The fog seal material reduced the pavement friction coefficient. The skid raveling resistance performance of material C-coated specimens decreased most significantly. The friction coefficient of the samples coated with material A and material C ranged from 55BPN to 60BPN, indicating a specific attenuation and meeting open traffic conditions. The main reason for attenuating the friction coefficient was that the fog seal material was directly applied to the surface of the specimen, wrapping the surface aggregate and making the surface smoother.

Friction coefficient at different doses is shown in Figure 13. The friction coefficients of materials A and B increased slightly with the dose increase, while the friction coefficient of material C decreased further. Materials A and B contained more sand when the dose increased. The sand floated on the specimen surface when the emulsion penetrated the gap. After drying, the friction coefficient increased to some extent. Material C was based on rock asphalt, which could form a thick and glossy protective film on the free surface. The sand floating on the surface was coated by material C, severely attenuating the friction coefficient. In addition, when the dose increased, although the amount of sand also increased, the sand could no longer weaken the smoothness of the surface, so when the overall dose of the material increased, the friction coefficient decreased.

4 Conclusion

This paper evaluates the improvement effect of fog seal material on the performance of asphalt mixture from four aspects.

1) Material C has the best durability. Its wear resistance and anti-stripping performance are the best. After the use of material C, the anti-stripping performance of the specimen was increased by 50%. The test results are significantly affected by the oil-stone ratio. When the void content is large, the fog seal material is easier to penetrate the gap. It can be used as a part of the binder, play a role in consolidation.
2) The influence of pore content dominates the impermeability of the material. When the gap of the mixture is too large, the fog seal material cannot be evenly covered on the road surface. The use of fog seal has little effect.
3) The influence of void content dominates the impermeability of materials. The medium dose selected in the test is recommended for construction. The fog seal material cannot be evenly covered

on the surface of the road when the gap of the road surface is too large. Therefore, if the fog seal is used when the road surface damage is severe, the fog seal material cannot be used in small doses.

4) The complete research results show that material C has achieved good treatment effect on the pavement with loose pavement and serious water seepage, and the wear resistance is stable. In the construction process, the amount of emery should be appropriately increased to not less than 0.35 kg/m^2. The improvement of material A and material B on pavement performance is limited. When it acts on looser and more serious roads, the dose can be appropriately increased to 0.9 kg/m$^{2.}$ At the same time, the amount of water should be appropriately increased to increase its flow capacity. But construction should be scheduled for the summer. In this paper, according to the characteristics of fog seal treatment, the existing standard experiments are improved. But there are still some shortcomings. This paper does not consider biological modification and other types of fog seals. The applicability of airport pavement is studied without combining the performance of fog seal material, which is also the follow-up research direction.

Data availability statement

The original contributions presented in the study are included in the article/Supplementary Material, further inquiries can be directed to the corresponding authors.

Author contributions

PL contributed to the conception and design of the study. WP participated in the writing of the first draft of the article and conducted data analysis. JM compiled the experimental data and some manuscripts. XY and ZL provided help in data analysis. LK participated in the test of experimental samples. All authors contributed to the article and approved the submitted version.

Funding

This work was supported by the National Key Research and Development Program of China (2021YFB2601000), Guangxi Key Research and Development Program (AB17292035), the National Natural Science Foundation of China (51878075), Hunan Provincial Natural Science Foundation of China (2022JJ30594), and Postgraduate Scientific Research Innovation Project of Hunan Province (QL20220189).

Conflict of interest

Author XY is employed by Hunan Hengyong Expressway Construction and Development Co., Ltd; Author LK is employed by China Construction Seventh Engineering Division Corp., Ltd.

The remaining authors declare that the research was conducted in the absence of any commercial or financial relationships that could be construed as a potential conflict of interest.

Publisher's note

All claims expressed in this article are solely those of the authors and do not necessarily represent those of their affiliated organizations, or those of the publisher, the editors and the reviewers. Any product that may be evaluated in this article, or claim that may be made by its manufacturer, is not guaranteed or endorsed by the publisher.

Supplementary material

The Supplementary Material for this article can be found online at: https://www.frontiersin.org/articles/10.3389/fmats.2023.1231461/full#supplementary-material

References

Airport Department of China Civil Aviation Administration (2010). *Technical guide for site maintenance of civil airport flight area AC-140-CA-2010-3*.

Airport Department of China Civil Aviation Administration (2020). *Fog seal material with emulsion mastic for asphalt pavement JT/T 1330—2020*.

Civil Aviation Administration of China (2017). *Specifications for asphalt pavement design of civil airports MH/T 5010-2017*. Beijing: China Civil Aviation Press.

Civil Aviation Administration of China (2019). *Specifications for asphalt pavement construction of civil airports MH/T 5011-2019*. Beijing: China Civil Aviation Press.

Cui, P., Wu, S., Xu, H., and Lv, Y. (2019). Silicone resin polymer used in preventive maintenance of asphalt mixture based on fog seal. *Polymers* 11, 1814. doi:10.3390/polym11111814

Feng, X., Guo, L., Ren, G., and Liu, S. (2019a). Research on the causes and prevention of airport pavement diseases. *Iop Conf. Ser. Earth Environ. Sci.* 330, 022042. doi:10.1088/1755-1315/330/2/022042

Feng, P., Wang, H., Zhang, X., Mohd Hasan, M. R., You, Z., and Gao, J. (2019b). Study on workability and skid resistance of bio-oil–modified fog seal with sand. *J. Test. Eval.* 48, 20190224. doi:10.1520/jte20190224

Guo, T., Wang, C., Yang, X., and Sun, X. (2017). Development and performance of sand fog seal with cooling and air purification effects. *Constr. Build. Mater.* 141, 608–618. doi:10.1016/j.conbuildmat.2017.03.003

Hu, C. C., Li, R., Zhao, J. Y., Leng, Z., and Lin, W. W. (2020). Performance of waterborne epoxy emulsion sand fog seal as a preventive pavement maintenance method: From laboratory to field. *Adv. Mater. Sci. Eng.* 2020, 1–9. doi:10.1155/2020/6425817

Huang, M., Huang, Z., and Zhu, H. (2020). Excellent stability of molecular catalyst/bivo4 photoanode in borate buffer solution. *Nano Energy* 70, 104487. doi:10.1016/j.nanoen.2020.104487

Im, J. H., and Kim, Y. R. (2013). Methods for fog seal field test with polymer-modified emulsions. *Transp. Res. Rec. J. Transp. Res. Board* 2361, 88–97. doi:10.3141/2361-11

Islam, R. M., Arafat, S., and Wasiuddin, N. M. (2017). Quantification of reduction in hydraulic conductivity and skid resistance caused by fog seal in low-volume roads. *Transp. Res. Rec.* 2657, 99–100. doi:10.3141/2657-11

Jia, Y., Wang, S., Huang, A., Gao, Y., Wang, J., and Zhou, W. (2021). A comparative long-term effectiveness assessment of preventive maintenance treatments under

various environmental conditions. *Constr. Build. Mater.* 273, 121717. doi:10.1016/j.conbuildmat.2020.121717

Jiang, Y., Fan, J., Lv, P., Yuan, K., Yi, Y., Tian, T., et al. (2021). Development of the fog seal layer characterized by durability in terms of skid resistance. *Adv. Mater. Sci. Eng.* 2021, 1–18. doi:10.1155/2021/6210875

Li, R., Karki, P., and Hao, P. (2020). Fatigue and self-healing characterization of asphalt composites containing rock asphalts. *Constr. Build. Mater.* 230, 116835. doi:10.1016/j.conbuildmat.2019.116835

Liu, F., Zheng, M., Liu, X., Ding, X., Wang, F., and Wang, Q. (2021). Performance evaluation of waterborne epoxy resin-sr composite modified emulsified asphalt fog seal. *Constr. Build. Mater.* 301, 124106. doi:10.1016/j.conbuildmat.2021.124106

Minaka, U. S., Okamura, M., and Ono, K. (2021). Verification of effectiveness and design procedure of gravel drains for liquefaction remediation. *Soils Found.* 61, 1191–1206. doi:10.1016/j.sandf.2021.06.002

Ministry of Transport of the People's Republic of China (2011). *Standard test methods of bitumen and bituminous mixtures for highway engineering JTG E20-2011*. Beijing: China Communications Press.

Ministry of Transport of the People's Republic of China (2019). *Field test methods of highway subgrade and pavement JTG 3450-2019*.

Peng, W., Li, P., Gong, W., Tian, S., Wang, Z., Liu, S., et al. (2023). Preparation and mechanism of rubber-plastic alloy crumb rubber modified asphalt with low viscosity and stabilized performance. *Constr. Build. Mater.* 388, 131687. doi:10.1016/j.conbuildmat.2023.131687

Praticò, F. G., Vaiana, R., and Iuele, T. (2015). Macrotexture modeling and experimental validation for pavement surface treatments. *Constr. Build. Mater.* 95, 658–666. doi:10.1016/j.conbuildmat.2015.07.061

Qureshi, N. A., Tran, N. H., Watson, D., and Jamil, S. M. (2013). Effects of rejuvenator seal and fog seal on performance of open-graded friction course pavement. *Maejo Int. J. Sci. Technol.* 7, 189.

Rahman, M. N., Sarkar, M. T. A., Elseifi, M. A., Mayeux, C., and Cooper, S. B. (2020). Effects of emulsion types, application rates, and crumb rubber on the laboratory performance of chip seal. *Constr. Build. Mater.* 260, 119787. doi:10.1016/j.conbuildmat.2020.119787

Sahebzamani, H., Alavi, M. Z., and Farzaneh, O. (2018). Evaluating effectiveness of polymerized pellets mix additives on improving asphalt mix properties. *Constr. Build. Mater.* 187, 160–167. doi:10.1016/j.conbuildmat.2018.07.143

Wu, T., Qiu, W., Kim, C., Chang, K., and Lu, X. (2021). Study of metabolomics in selenium deprived Przewalski's Gazelle (*Procapra przewalskii*). *Struct. Infrastructure Eng.*, 1–12. ahead-of-print. doi:10.1017/S000711452100355X

Xiao, F., Ma, D., Wang, J., Cai, D., Lou, L., and Yuan, J. (2019). Impacts of high modulus agent and anti-rutting agent on performances of airfield asphalt pavement. *Constr. Build. Mater.* 204, 1–9. doi:10.1016/j.conbuildmat.2019.01.138

Xu, L., Zhao, Z., Li, X., Yuan, J., Zhou, Q., and Xiao, F. (2021). Cracking investigation on fog seal technology with waterborne acrylate and polyurethane as a clean modification approach. *J. Clean. Prod.* 329, 129751. doi:10.1016/j.jclepro.2021.129751

Xu, L., Jiang, C., and Xiao, F. (2022). Application of fog-seal technology with waterborne thermosetting additive in asphalt pavement. *J. Mater. Civ. Eng.* 34. doi:10.1061/(asce)mt.1943-5533.0004288

Xv, L., Wang, X., Li, X., Guan, X., and Xiao, P. (2022). Effect of waterborne EmulsiononPerformance of polymer-modified FogSeal materials. *J. Tongji Univ. Nat. Sci.* 50, 1471–1481. doi:10.11908/j.issn.0253-374x.21465

You, L., Dai, Q., You, Z., Zhou, X., and Washko, S. (2020). Stability and rheology of asphalt-emulsion under varying acidic and alkaline levels. *J. Clean. Prod.* 256, 120417. doi:10.1016/j.jclepro.2020.120417

Yu, B., Gu, X., Ni, F., and Guo, R. (2015). Multi-objective optimization for asphalt pavement maintenance plans at project level: Integrating performance, cost and environment. *Transp. Res. Part D Transp. Environ.* 41, 64–74. doi:10.1016/j.trd.2015.09.016

Zhang, X., Wang, H., Hasan, M. R. M., Gao, J., and Irfan, M. (2019). Traffic open time prediction of fog seal with sand using image processing technology. *Constr. Build. Mater.* 209, 9–19. doi:10.1016/j.conbuildmat.2019.03.070

Zhang, B., Jie, J., Zhang, Z., Tang, L., Lv, Y., and Qi, G. (2023). Impact resistance of modified asphalt concrete for airport runway. *Nanjing Univ. Aeronautics Astronautics* 55, 139–145. doi:10.16356/j.1005-2615.2023.01.017

frontiers | Frontiers in Materials

TYPE Original Research
PUBLISHED 28 August 2023
DOI 10.3389/fmats.2023.1231483

OPEN ACCESS

EDITED BY
Dawei Wang,
RWTH Aachen University, Germany

REVIEWED BY
Huanan Yu,
Changsha University of Science and Technology, China
Di Wang,
Aalto University, Finland
Yue Xiao,
Chang'an University, China

*CORRESPONDENCE
Wenju Peng,
pwj1112@foxmail.com
Yanlong Han,
han18348348740@163.com

RECEIVED 30 May 2023
ACCEPTED 14 August 2023
PUBLISHED 28 August 2023

CITATION
Li P, Peng W, Han Y, Wang B, Liu Z, Li W and Wei W (2023), Effect of deicing agents on the performance of airport asphalt pavement.
Front. Mater. 10:1231483.
doi: 10.3389/fmats.2023.1231483

Effect of deicing agents on the performance of airport asphalt pavement

Ping Li[1,2], Wenju Peng[1,3]*, Yanlong Han[1]*, Bin Wang[4], Zhaohui Liu[1], Wei Li[5] and Wanfeng Wei[6,7]

[1]School of Traffic and Transportation Engineering, Changsha University of Science and Technology, Changsha, China, [2]Airport Engineering Research Center of CAAC, Beijing, China, [3]School of Civil Engineering, Hubei Engineering University, Xiaogan, China, [4]Hunan Expressway Maintenance Engineering Co, Ltd, Changsha, China, [5]Henan College of Transportation, Zhengzhou, China, [6]Guangxi Key Laboratory of Road Structure and Materials, Nanning, China, [7]Department of Civil Engineering, Chongqing Jiaotong University, Chongqing, China

Deicing agents are widely used to remove ice and snow on airport pavement, ensuring air traffic operation and safety. However, excessive spraying may affect the performance of airport pavement. The effects of different chloride deicing agents on the performance of airport asphalt and mixture have been assessed by previous studies. The three deicing agents (NaCl, KHF-1A, and NW056) were selected. Conducting various tests to examine their influence on the performance of asphalt and asphalt mixture. The tests include the DSR test, BBR test, indirect tensile test, bending test of small beam, and freeze-thaw splitting test. The results indicate that the asphalt anti-rutting factor $G^*/\sin\delta$ varies by 25%–45%, the asphalt creep stiffness increases by 15%–50%, and the anti-fatigue factor ($G^*\sin\delta$) increases by 10%–40% under the effect of the deicing agents. The splitting strength of the mixture decreases by 10%–40%, the bending stiffness modulus increases by 6%–20%, and the freeze-thaw splitting strength ratio does not change significantly under the effect of the deicing agents. NW056 deicing agent has minimal effect on the performance of airport pavement and has optimal performance. The replacement of traditional chloride deicing agents helps to prolong the service life of airport asphalt pavement.

KEYWORDS

deicing agent, airport pavement, asphalt performance, mixture performance, acetate deicing agent

1 Introduction

According to the Civil Aviation Administration of China, China had 248 domestic transport airports by the end of 2021 (Civil Aviation Administration of China, 2022). The 'National Comprehensive Three-dimensional Transportation Network Planning Outline' suggests that the number of national civil transport airports will increase to about 400 from 2021 to 2035 (Ministry of Transport of China, 2021). This means China must construct 10 new airports yearly for the next 15 years. Therefore, airport planning and construction remain a fundamental challenge at this stage. Airport runways can be made of cement or asphalt pavement materials. Asphalt pavement has become a common choice for building new airports and reconstructing old runways because of its advantages in viscoelasticity, construction, maintenance, and later paving (Qiu and Nixon, 2008; Koščák et al., 2020). However, asphalt pavement also poses a security risk for airport runway operation during ice

and snow events, affecting flight safety and efficiency. One of the effective methods to remove snow and prevent icing on airports and highways is to spray deicing agents (Hanke et al., 2019; Vignisdottir et al., 2019).

The effects of deicers on airport pavement have been widely investigated in foreign literature. For example, Nazari et al. reported that deicers could cause deterioration of asphalt performance (Nazari and Shi, 2019), such as reduced low-temperature performance and viscosity, as well as damage to aggregate and surface structure, leading to decreased pavement elasticity and skid resistance. At lower temperatures, calcium chloride and magnesium chloride were more effective than sodium chloride, but they were more difficult to handle, more expensive, and more damaging to infrastructure (Du et al., 2019). Ylva Edwards found that the duration, temperature, and concentration of deicer exposure mainly influenced the change in pavement performance (Edwards and Aurstad, 2000). Fay Laura et al. explained that the performance degradation of pavement materials caused by deicing agents was due to the physical and chemical reactions between the ions of deicing agents and the materials, resulting in alterations in the internal structure of the materials (Shi et al., 2009; Fay and Shi, 2011). The most traditional and common airport pavement deicers were chloride salts, such as sodium chloride, calcium chloride, and magnesium chloride (Hanke et al., 2019; Terry et al., 2020; Gruber et al., 2023a). Although they could ensure the safety of the pavement in winter conditions, they also caused severe corrosion to the pavement structure and airport facilities (Fischel, 2001; Fay and Shi, 2012; Peng et al., 2023). Previous studies have shown that chloride ions could penetrate the pavement, causing pavement cracking, increased permeability, and reduced compressive strength, ultimately leading to a significant decrease in pavement performance (Shi et al., 2014; Das and Pradhan, 2019; Gruber et al., 2023b). Sodium ions could reduce soil permeability and aeration, and affect plant growth, and 10%–60% of sodium chloride would accumulate in groundwater, affecting the environment (Findlay and Kelly, 2011).

Compared with highway asphalt pavement, the smoothness of airport pavement was higher, and the deicer residue lasted longer, which led to the damage and shedding of pavement structure and seriously affected the safety of aircraft taking off and landing. Because of the severe corrosion and environmental damage caused by chloride deicers to the pavement, chlorine-free deicers have been increasingly studied (Fortin et al., 2014). Among them, acetate has received considerable attention from researchers because its aqueous solution has a much lower freezing point than chloride salt solution and has minor corrosion to metal structures and pavement infrastructure (Frolova et al., 2015; Meng et al., 2023). Acetate products have been widely used as alternative deicers to control ice and snow on airport pavements and bridges (Terry et al., 2020). However, although acetate deicing agent is generally considered less damaging to asphalt than traditional chloride salt, it still has some adverse effects. So far, few studies have investigated the influence of acetate deicing agents on the overall performance of airport pavement, and the mechanism of action is far from clear (Zhang et al., 2021a). Hence, it is vital to examine the effect of acetate deicing agents on the performance of asphalt and asphalt mixture.

In this study, the commonly used chlorine salt deicer NaCl and two main acetate deicers NW056h and KHF-1A3 (the main components of the two are the same, but the types of additives and active ingredients are different, and their deicing performance is also quite different) are selected. Based on the environmental parameters of the airport asphalt pavement, the paper conducts low-temperature and fatigue performance tests of asphalt, and high-temperature, low-temperature, and water stability performance tests of the mixture. The paper aims to comprehensively and systematically study the effect of deicing agents on airport pavement, verify the feasibility of using NW056 and KHF-1A as alternatives to traditional chloride salt deicers, and provide references for selecting deicing agents for airport snow removal, thereby extending the service life of asphalt pavements.

TABLE 1 Main technical indexes of deicing agent.

Type	NaCl	NW056	KHF-1A
Appearance	White particle	Colorless liquid	Colorless liquid
PH (25°C)	6.7–7.3	9.93	9.29
Freezing point (°C)	−21	≤-28	≤- 26
Active ingredients (%)	NaCl, 99%	CH_3COOK, 58.3%	CH_3COOK, 52.2%
Solubility 20°C (%)	23.0	49.0	53.2
Density 25°C (g/cm^3)	2.165	1.282	1.260

2 Materials and methods

2.1 Materials

2.1.1 Deicing agents

The conventional chloride salt deicer NaCl was chosen as the control group for comparison with KHF-1A and NW056. The technical indexes of the deicing agents are presented in Table 1.

2.1.2 Asphalt mixture

This experiment followed the "Technical Specification for Construction of Asphalt Mixture Pavement of Civil Airport" (MH/T 5011–2019) (Civil Aviation Administration of China, 2019) and used Karamay 110 matrix asphalt and 6% Yuehua SBS modifier to prepare modified asphalt. The performance test results of the modified asphalt are shown in Table 2. The aggregate was basalt gravel, with coarse aggregate sizes of 15–10 mm and 5–10 mm and fine aggregate sizes of 0–5 mm. The mineral powder was alkaline limestone powder, and the fiber was polyacrylonitrile. The aggregate, mineral powder, and fiber properties met the specification requirements. The SMA-13 gradation range satisfies the specification requirements (Accompanying diagram 1), and the optimal oil-stone ratio is 5.9%. Table 3 presents the test results of the asphalt mixture performance.

2.2 Laboratory tests

Laboratory tests were conducted to study the deicing agents of influence on airport asphalt pavement performance, as shown in

TABLE 2 Modified asphalt performance test results.

Test items		Units	Test method (Ministry of Transport Highway Research Institute, 2011)	Technical standard (Civil Aviation Administration of China, 2019)	Test result
Penetration (25°C, 100 g, 5 s)		0.1 mm	T 0604	60–80	78.5
Softening point (universal method)		°C	T 0606	>43	49.2
Extensibility (5 cm/min, 5°C)		cm	T 0605	>40	66.1
Equivalent softening point T_{800}		°C	T 0606	>48	48.8
Equivalent brittle point $T_{1.2}$		°C	T 0606	<- 10	- 16.0
Flashpoint (COC)		°C	T 0611	>230	308
Density (15°C)		g/cm^3	T 0603	Actual	0.958
Elastic recovery (15°C)		%	T 0662	>65	94
Film-heating test 163°C/5 h	Mass loss	%	T 0610	<0.8	0.09
	Penetration ratio	%	T 0604	>60	94.9
	Extensibility (5°C)	cm	T 0605	>10	41.8

TABLE 3 Asphalt mixture performance.

Test items	Test result	Technical standard (Civil Aviation Administration of China, 2019)
Bulk Density (g/cm^3)	2.482	-
Theory Density (g/cm^3)	2.571	-
VV (%)	3.5	3–4.5
VMA (%)	17.3	≥16.5
VFA (%)	79.8	75–85
VCA_{mix} (%)	40.6	≤VCA_{DRC}
VCA_{DRC} (%)	41.3	-
Stability (kN)	10.1	≥6
Flow Value (0.1 mm)	25.6	Actual (20–40)

Figure 1. The mass fractions of the deicing agent were chosen based on the following considerations: Feng et al. suggested that when the mass fraction of the salt solution was less than 3%, the freeze-thaw process was the dominant factor for the deterioration of the mixture performance (Feng et al., 2010). When the mass fraction exceeded 3%, the salt solution was the main factor for the decline in the mixture performance. Zhang et al. indicated that the optimal mass fraction of NaCl deicing agent solution was about 10%. The maximum solubility of NaCl solution at room temperature was 35.9 g, and the corresponding mass fraction was about 26% (Zhang et al., 2014; Zhang and Zhang, 2015; Zhang et al., 2019). Therefore, 2%, 10%, 20%, and 26% were selected as the critical mass fractions for preparing the deicing agent.

The deicing agent solutions were prepared: three different deicing agents were dissolved in distilled water to obtain solutions with mass fractions of 0%, 2%, 10%, 20%, and 26%. They were stored at room temperature and covered with plastic wrap at the cup mouth to prevent leakage and evaporation of the deicing agent. Then, a laboratory test was conducted to study the effects of the deicing agent on the performance of the asphalt and asphalt mixture.

2.2.1 Asphalt performance tests

The asphalt performance test was conducted as follows: a thin film oven test was used to prepare a thin layer sample with a thickness of about 0.1 cm. Then, the deicing agent was poured over the asphalt sample until it was 1 cm above the surface, and the mixture was stirred well and left for 30 min. Next, the model was placed in the experimental environment (heat preservation/soaking) for a specific time, and then the performance of the treated specimen was tested. The laboratory test of the effect of the deicing agent on asphalt performance is shown in Table 4.

2.2.2 Asphalt mixture performance tests

The asphalt mixture was prepared according to the design gradation. The molded specimen was immersed in the deicing

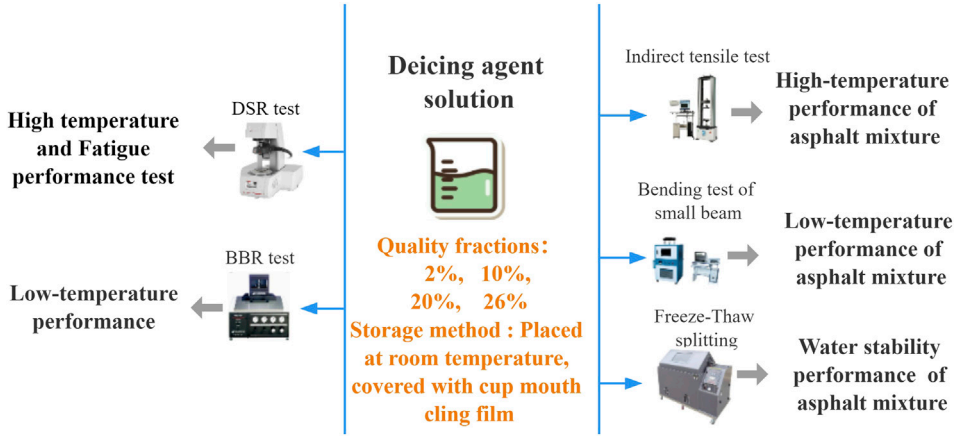

FIGURE 1
Laboratory test process.

TABLE 4 Asphalt performance laboratory test.

Test items	Test	Test method (Ministry of Transport Highway Research Institute, 2011)	Evaluation indexes	Test variables		
				Deicing agents	Temperature (°C)	Mass fractions (%)
High-temperature performance	DSR	T 0628	Rutting factor ($G^*/\sin\delta$)	3	58, 64, 70, 76	10, 26
Low-temperature performance	BBR	T 0627	Creep stiffness (S) Creep rate (m)	3	-	10, 26
Fatigue performance	DSR	T 0628	Fatigue factor ($G^*\cdot\sin\delta$)	3	25, 28, 31	10, 26

TABLE 5 Laboratory test of asphalt mixture performance.

Test items	Test	Test method (Ministry of Transport Highway Research Institute, 2011)	Evaluation indexes	Test variables			
				Deicing agents	Mass fractions (%)	Cycle number	Number of compactions
High-temperature performance	Indirect tensile	T 0716	Splitting strength	3	10, 26	10, 20	-
Low-temperature performance	Bending test of small beam	T 0715	Bending stiffness modulus	3	10, 26	10, 20	-
Water stability performance	Freeze-Thaw splitting	T 0729	Freeze-thaw splitting strength ratio	3	10, 26	-	30, 50

agent solution until the immersion was completed, and then the mixture performance test was performed. The laboratory test of the effect of the deicing agent on the mixture performance is shown in Table 5.

Several foreign research institutions, including the National Academy of Sciences, the Academy of Engineering, the Transportation Research Council, and the New Jersey Department of Transportation, conducted studies on the relationship between rutting tests and Indirect Tensile (IDT) strength. The results of these studies revealed a strong correlation between IDT strength and rutting resistance. The IDT test was recommended as a simple method to evaluate the rutting resistance of asphalt mixtures in the 2004 Traffic Research Notice titled "Simple Test Method for Asphalt Mixture Performance." This method was later included in the US "Asphalt Mixture Performance Specification" in 2016 (Button et al., 2004; Christensen et al., 2004; McCarthy et al., 2016). For Marshall specimens, the best correlation between IDT strength and rutting

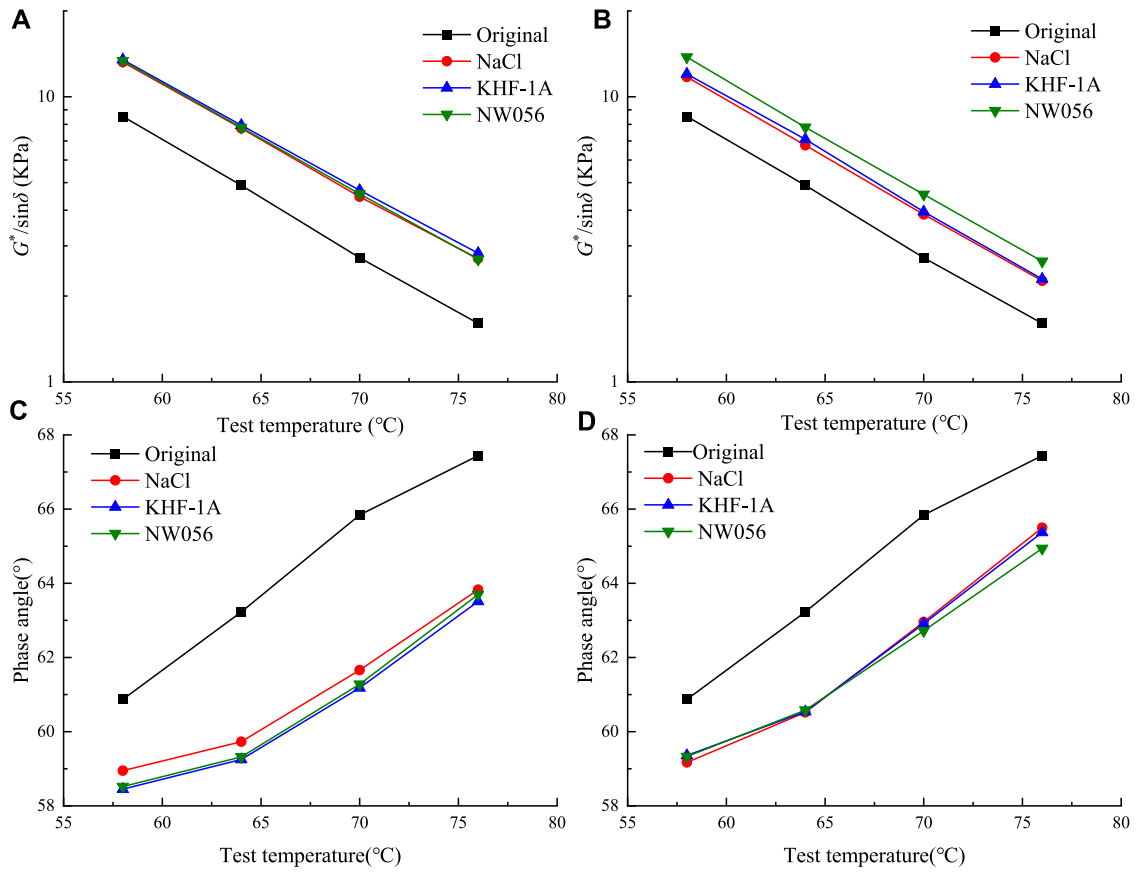

FIGURE 2
G*/sinδ and Phase angle δ under different conditions. **(A)** 10% **(B)** 26% **(C)** 10% **(D)** 26%.

results was achieved at a temperature of 40°C and a loading rate of 50 mm/min. This mechanical index could be used to evaluate the high-temperature performance of asphalt mixtures (Christensen and Bonaquist, 2002; Bennert et al., 2018).

3 Results and discussion

3.1 Effect of deicer on rheological properties of asphalt

3.1.1 High-temperature performance

DSR tested the shear rheological properties of asphalt film samples after high-temperature insulation for 96 h. The DSR test used a strain control of 10%, an angular velocity of 10 rad/s, a test plate diameter of 25 mm, and a gap of 1,000 μm. The changes of asphalt anti-rutting factor $G^*/\sin\delta$ and phase angle δ with temperature after treatment with different deicing agent solutions are shown in Figure 2.

The treatment of the deicing agent solution reduced the phase angle δ of asphalt by 1.5°–5°. It increased the anti-rutting factor $G^*/\sin\delta$ by 25%–45%, indicating that the deicing agent significantly improved the high-temperature performance of asphalt. This was because the soluble salt in the deicing agent solution penetrated the asphalt. The ions further immersed in the asphalt molecule, which reduced the content of light components in the asphalt, significantly reduced the bonding between the asphalt molecules, reduced the shear rheological properties of the asphalt, and increased the anti-rutting factor (Xiong et al., 2019; Zhang et al., 2021a; Meng et al., 2021). However, this change also enhanced the high-temperature deformation ability of the asphalt to some extent, but it significantly weakened its fatigue performance.

The influence of the acetate deicing agent on the asphalt phase angle and anti-rutting factor was greater than that of the chloride deicing agent. When the mass fraction was 10%, the asphalt phase angle was NaCl > NW056 > KHF-1A, and the anti-rutting factor was NaCl < NW056 < KHF-1A. When the mass fraction was 26%, the phase angle was NaCl > KHF-1A > NW056, and the anti-rutting factor was NaCl < NW056 < KHF-1A. This showed that NW056 and KHF-1A significantly improved the high-temperature performance of asphalt more than traditional NaCl deicing agents. In addition, the influence of different dosages of deicing agents on the high-temperature performance of asphalt was distinct. When the NW056 solution was 10% and 26%, the anti-rutting factor of asphalt was the same. In comparison, the NaCl solution decreased by 10%–20%, indicating that the influence of NW056 solution on the high-temperature performance of asphalt was less affected by a mass fraction, KHF-1A was moderate, and NaCl was most affected by a mass fraction.

The high-temperature performance of asphalt was not significantly affected by the temperature of the deicing agent. The

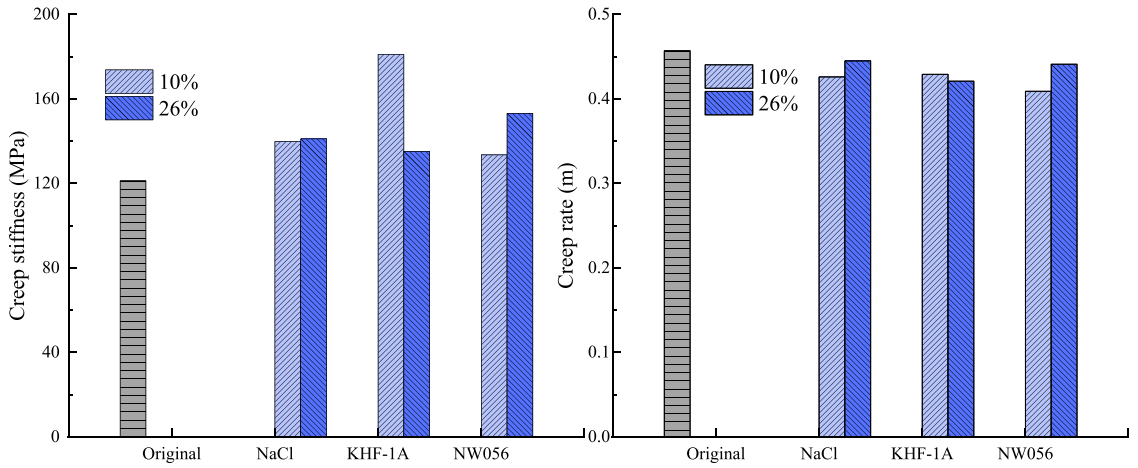

FIGURE 3
Creep stiffness and creep rate under different conditions.

variation of different deicing agents and original samples with temperature showed a similar trend.

3.1.2 Low-temperature performance

The BBR test measured the low-temperature performance of asphalt after holding at −25 °C for 96h, and the loading time was 60s. The creep stiffness (*S*) and creep rate (*m*) of asphalt treated with different deicing agent solutions are shown in Figure 3. Both met the specification requirements that the creep stiffness modulus of asphalt should not exceed 300 MPa, and the creep rate should not be less than 0.3. In fact, the higher the *S* value, the more brittle the material and the more prone to road surface cracking. The higher the m value, the better the stress relaxation ability of the material and the better the low-temperature crack resistance (Li et al., 2017).

Using the deicing agent increased the creep stiffness of asphalt by 15%–50%. It decreased the creep rate by 3%–11%, indicating that the deicing agent deteriorated the low-temperature crack resistance of asphalt, resulting in the brittleness of asphalt and the deterioration of stress relaxation ability. This is due to the significant difference in the effect of different deicers on the low-temperature performance of asphalt. Overall, acetate deicer had a more substantial impact on the creep stiffness (*S*) and creep rate (*m*) of asphalt than chloride deicer. After soaking in NaCl solution, KHF-1A solution, and NW056 solution, the creep stiffness of asphalt increased by 16%, 49%, and 26% on average, and the creep rate decreased by 3%, 6%, and 4%, respectively. The low-temperature performance of the acetate deicing agent changed significantly because the acetate solution contained a large number of lipophilic organic chains (-CH_3) and hydrophilic groups (-COO) that could act as emulsifiers in the aqueous solution and emulsify the asphalt (Pan et al., 2008). The proportion of small molecular components in the asphalt decreased, resulting in a decrease in the stress relaxation ability of the asphalt, which in turn deteriorated the low-temperature performance (Pan, 2007).

The deicing agent's mass fraction also affected asphalt's low-temperature performance. NaCl and NW056 deicing agents showed that the higher the mass fraction of the deicing agent, the more severe the deterioration of the low-temperature performance. Although both KHF-1A and NW056 were acetate deicing agents and had the same primary components, KHF-1A showed the opposite trend. This might have been because the types of additives were different, and some additives (N, P, S, Pb, and Cd) in KHF-1A caused this phenomenon.

3.1.3 Fatigue performance

DSR tested the shear rheological properties of asphalt film samples after soaking them at room temperature for 30 days. The DSR test used a strain control of 10% and an angular velocity of 10 rad/s. The changes in asphalt anti-fatigue factor ($G^*\cdot\sin\delta$) with temperature after treatment with different deicing agent solutions are shown in Figure 4. Previous studies have shown that $G^*\cdot\sin\delta$ could represent the fatigue resistance of materials, and the lower the value, the stronger the fatigue resistance (Yang et al., 2022).

The results showed that the deicer solution treatment increased the anti-fatigue factor ($G^*\cdot\sin\delta$) of asphalt by 50-200KPa, which implied that the deicer impaired the anti-fatigue performance of asphalt. This might have been attributed to the penetration of salt ions from the deicer solution into the asphalt, which disrupted the molecular bond and increased the content of solid asphaltene. Consequently, the asphalt became more brittle, reducing its fatigue performance (Zhang et al., 2021a).

The type of deicing agent significantly influenced the fatigue performance degradation of asphalt. NW056 had the most severe effect on asphalt degradation among the three deicing agents. NaCl and KHF-1A had a minor effect on the anti-fatigue factor of asphalt. The ranking of the anti-fatigue factor of asphalt at 10% mass fraction was NW056 > NaCl > KHF-1A, while at 26% mass fraction, it was KHF-1A > NW056 > NaCl. At the same temperature, the acetate deicing agent's mass fraction positively correlated with the anti-fatigue factor of asphalt. This was because the higher concentration of acetate ions penetrated the asphalt more effectively, which damaged the asphalt molecular bond faster and more extensively. This also made the asphalt more susceptible to fatigue.

10.3389/fmats.2023.1231483

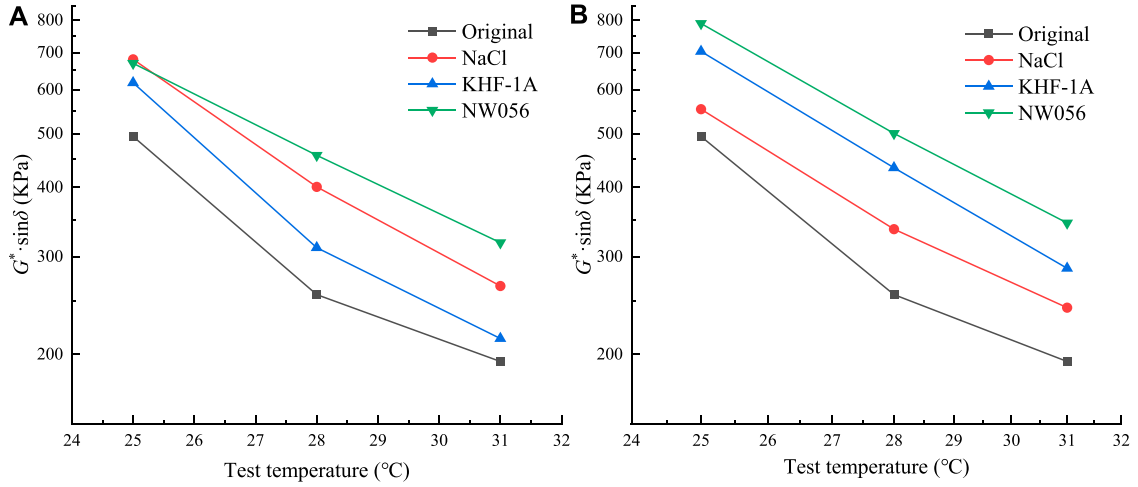

FIGURE 4
Fatigue factors G*·sinδ under different conditions. **(A)** 10% **(B)** 26%.

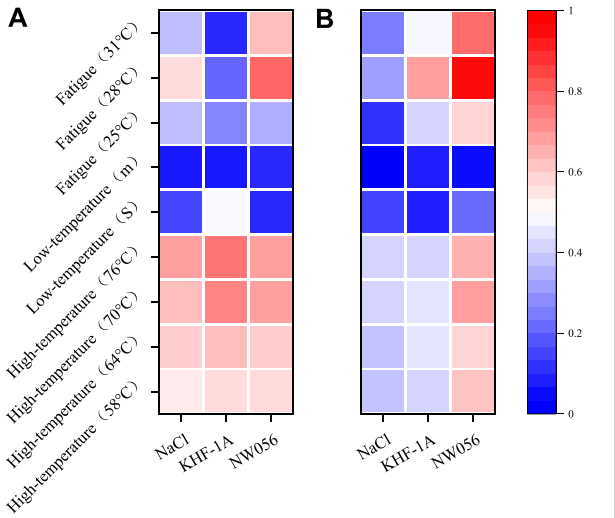

FIGURE 5
Asphalt performance evaluation index changes. **(A)** 10% **(B)** 26%.

The deicing agent's temperature had a negligible effect on the fatigue performance of asphalt. The results indicated that the three deicing agents had the same influence on the anti-fatigue factor of asphalt as the original sample. The only exception was the 10% NaCl asphalt, which showed an abnormal increase in the anti-fatigue factor. This might have been due to the rapid reaction between salt ions in NaCl solution and asphalt under NaCl's optimal deicing mass fraction.

3.1.4 Comprehensive effection for asphalt performance

The effects of different experimental parameters on asphalt performance were investigated using four key indicators: the anti-rutting factor $G^*/\sin\delta$, the creep stiffness S, the creep rate m, and the anti-fatigue factor $G^*\cdot\sin\delta$. The relative changes of these indicators for asphalt treated with different deicing agents compared to the untreated sample are shown in Figure 5.

A more pronounced effect was observed on the high-temperature performance of asphalt due to the use of deicing agents than on the low-temperature performance. The high-temperature performance was improved by more than 40%, while the low-temperature performance was reduced by less than 40%. The fatigue performance of asphalt was deteriorated by different deicing agents, and the difference was noticeable.

At 10% mass fraction, the three types of deicing agents had similar effects on the high-temperature performance of asphalt. Only KHF-1A deicing agent caused a higher creep stiffness S of asphalt at low temperatures, but the difference was insignificant. KHF-1A deicing agent had the most negligible effect and the best performance regarding asphalt fatigue degradation. At 26% mass fraction, the NW056 deicing agent had a much more substantial impact on the high-temperature performance of asphalt than the other two deicing agents. In contrast, the effects on the low-temperature performance were comparable. NW056 deicing agent also had a much stronger effect on asphalt fatigue degradation than NaCl, while KHF-1A had a moderate impact.

Based on the comprehensive evaluation of the effects of the conventional deicing agent NaCl and two acetate deicing agents, KHF-1A and NW056, on asphalt performance, KHF-1A was found to perform better than NW056. It also had similar or better performance than NaCl in some aspects.

3.2 Effect of deicing agent on mixture performance

3.2.1 High-temperature performance

The IDT test measured the splitting strength (MPa) of asphalt mixture samples after soaking them in the deicing agent for 30 min. The models had a diameter of 150 mm and a thickness of 50 mm. Figure 6 shows the results of the splitting strength test for the samples treated with different mass fractions of deicing agent solution.

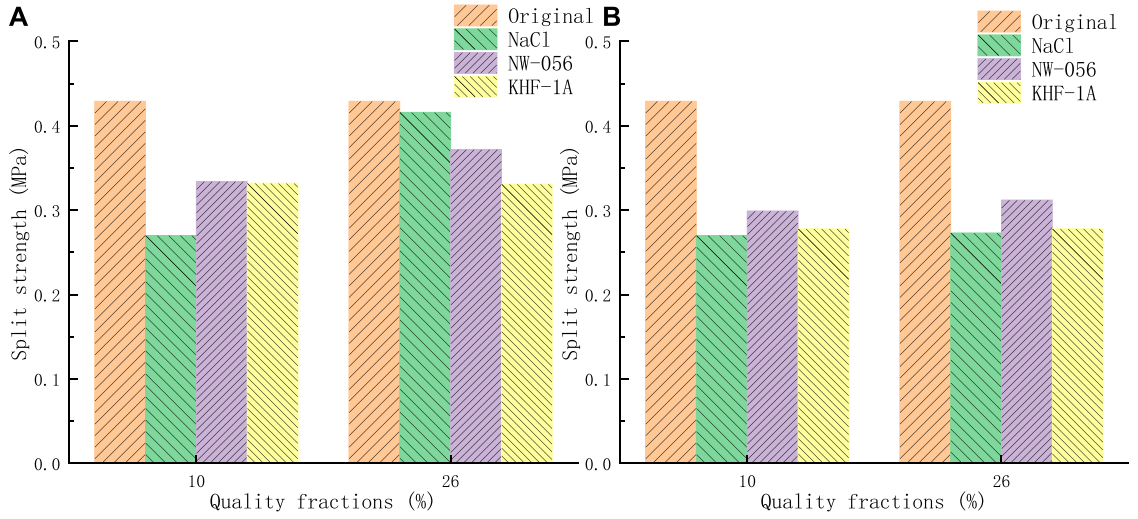

FIGURE 6
Splitting strength under different conditions. **(A)** Cycle 10 times **(B)** Cycle 20 times.

Figure 6 shows that using the deicing agent reduced the splitting strength of the asphalt mixture by 10%–40% compared to the original, indicating a significant deterioration of the high-temperature performance. NaCl solution had the most pronounced effect on the splitting strength among the three deicing agents, while NW056 and KHF-1A solutions had relatively minor effects. This might have been due to the cracking of the interface between the asphalt layer and the aggregate caused by the crystallization expansion of the deicer in the freeze-thaw environment. The cracks allowed more water to infiltrate the asphalt binder and the total, reducing the splitting strength (Meng et al., 2022).

The effect of the chloride deicing agent on the splitting strength of the mixture was seriously affected by the mass fraction and the number of cycles. The acetate deicing agent was more stable. The ranking of the deicing agents by their impact on the splitting strength was NaCl > KHF-1A > NW056. At 10% mass fraction, the mixture treated with NW056 and KHF-1A solution showed a significant decrease in splitting strength by 8.2% and 12.6%, respectively, from 10 to 20 cycles. At 26% mass fraction, the mixture treated with NaCl solution showed a drastic reduction in splitting strength by 33.3%, while the changes of NW056 and KHF-1A were relatively small. In general, the splitting force of the mixture decreased as the number of freeze-thaw cycles increased. The mass fraction significantly affected the splitting strength when the number of cycles was 10. After 20 cycles, the splitting force changed slightly with the mass fraction, all within 2%.

3.2.2 Low-temperature performance

The bending test of the beams was conducted to study the effect of the deicing agent on the mixture's low-temperature performance. The length of the test trabecular was 250 ± 2.0 mm, a width of 30 ± 2.0 mm, and a height of 35 ± 2.0 mm. After soaking in the deicing agent solution for 24 h, they were subjected to freeze-thaw cycles according to the "high-temperature performance freeze-thaw cycle test conditions." The mixture's bending stiffness modulus was measured; the results are shown in Figure 7.

The deicing agent significantly affected the low-temperature crack resistance of the asphalt mixture. Using a deicing agent increased the bending stiffness modulus of the asphalt mixture by 6%–20%, indicating a deterioration of the low-temperature crack resistance. This might have been due to the penetration of the chloride deicing agent solution into the pores of the specimen, which reduced the adhesion between the asphalt mixture components during the wet-dry cycle. As a result, the flexural tensile strength of the asphalt mixture decreased, and the bending stiffness modulus increased. Among the three deicing agents, KHF-1A had the most substantial effect on the bending stiffness modulus of the cross, followed by NaCl and NW056. The impacts of KHF-1A and NW056 deicing agent solutions on the asphalt mixture were mainly caused by emulsification. The emulsification reduced the asphalt content, lowered the flexural strength of the asphalt mixture, and raised the bending stiffness model (Zhang et al., 2021b).

The concentration of the deicing agent strongly influenced the bending stiffness modulus of the mixture, and the trend varied with different cycles of the mass fraction. At 10 cycles, the ranking of the three deicing agents by their effect on the bending stiffness modulus was KHF-1A > NaCl > NW056; the bending stiffness modulus of the mixture increased by 21%, 13.6%, and 6.8%, respectively, from 10% to 26% concentration. At 20 cycles, the increases were 19.7%, 23.2%, and 15.9%, respectively. The bending stiffness modulus of the mixture decreased as the number of freeze-thaw cycles increased. After 20 cycles, the bending stiffness modulus of the three deicing agents became more stable and approached the original value at 26% concentration.

3.2.3 Water stability performance

The freeze-thaw splitting test evaluated the water stability of the mixture. The test measured the mixture's freeze-thaw splitting strength ratio (TSR), shown in Figure 8.

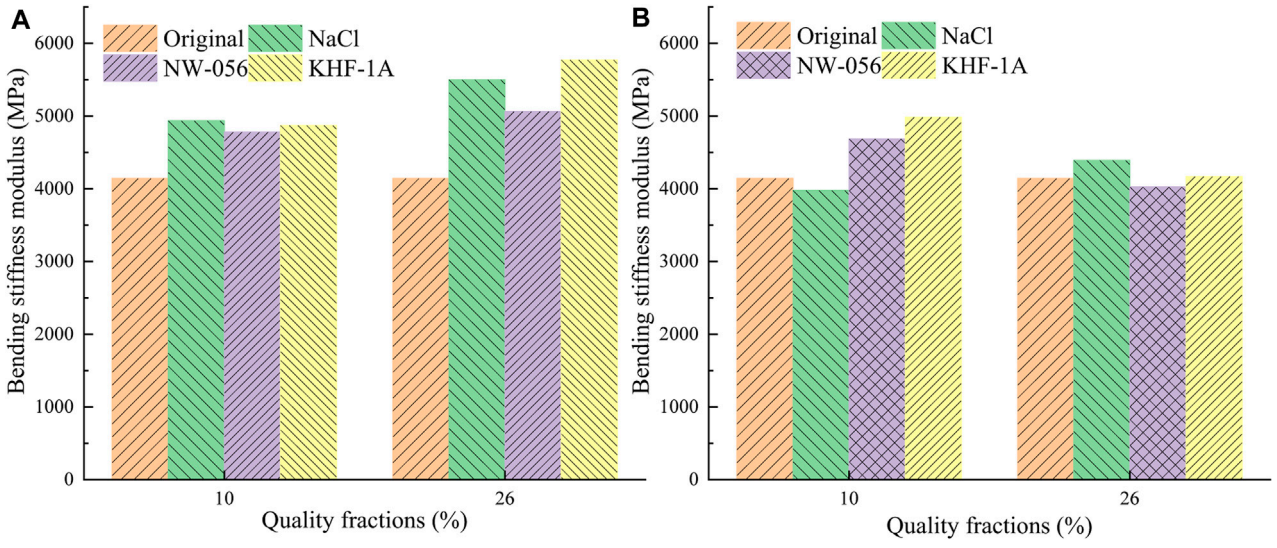

FIGURE 7
Bending stiffness modulus under different conditions. **(A)** Cycle 10 times **(B)** Cycle 20 times.

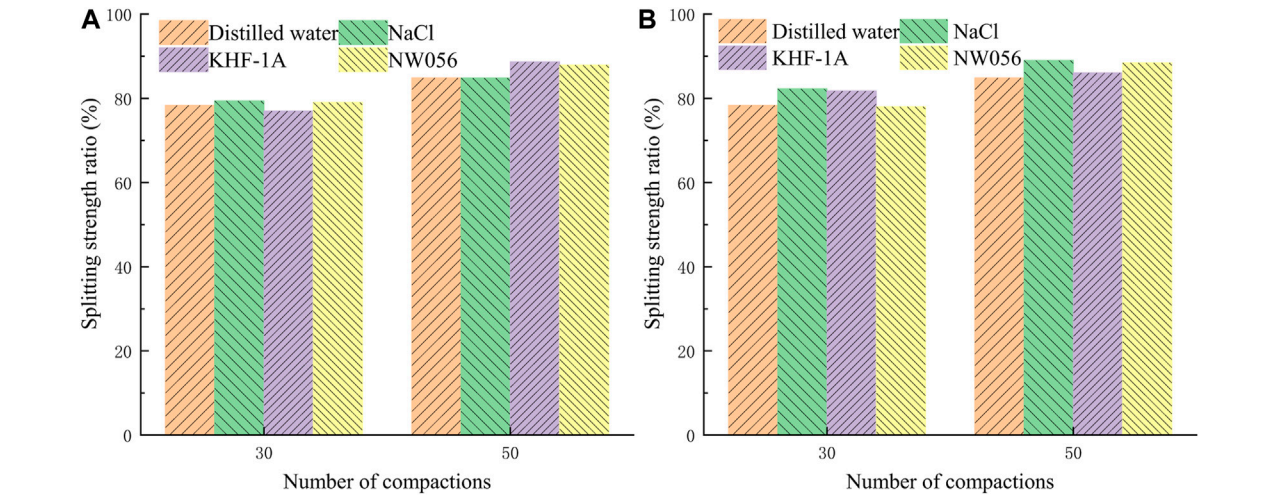

FIGURE 8
Splitting strength ratio under different conditions. **(A)** 10% **(B)** 26%.

The deicing agent had a negligible effect on the water stability of the asphalt mixture. The acetate and chloride deicing agents did not significantly affect the freeze-thaw splitting strength ratio of the mix, and some ratios were even higher than those of the water solution. This might be explained by the fact that the water volume in the pores of the asphalt mixture changed constantly during the freezing and melting processes. The addition of a deicing agent reduced the volume expansion rate of the solution when it froze (Ma et al., 2021), which in turn reduced the volume expansion of the answer in the pores of the mixture during the freeze-thaw cycle and the structural damage of the asphalt mixture.

The mixture treated with a high mass fraction deicing agent had a higher freeze-thaw splitting strength ratio because of the lower volume expansion rate of the high concentration deicing agent solution. The low mass fraction deicing agent had little effect on the freeze-thaw splitting strength ratio of the mixture. The freeze-thaw splitting strength ratio of the mixture increased with the number of compaction times. This might be because higher compaction times decreased the porosity of the mix, which reduced the reaction rate between the deicing agent and the asphalt mixture and ultimately lowered the splitting strength ratio of the mix.

3.2.4 Comprehensive evaluation of the effect on the performance of asphalt and mixture

The analysis of the effect of the deicing agent on the high and low-temperature performance of asphalt and mixture was based on

10.3389/fmats.2023.1231483

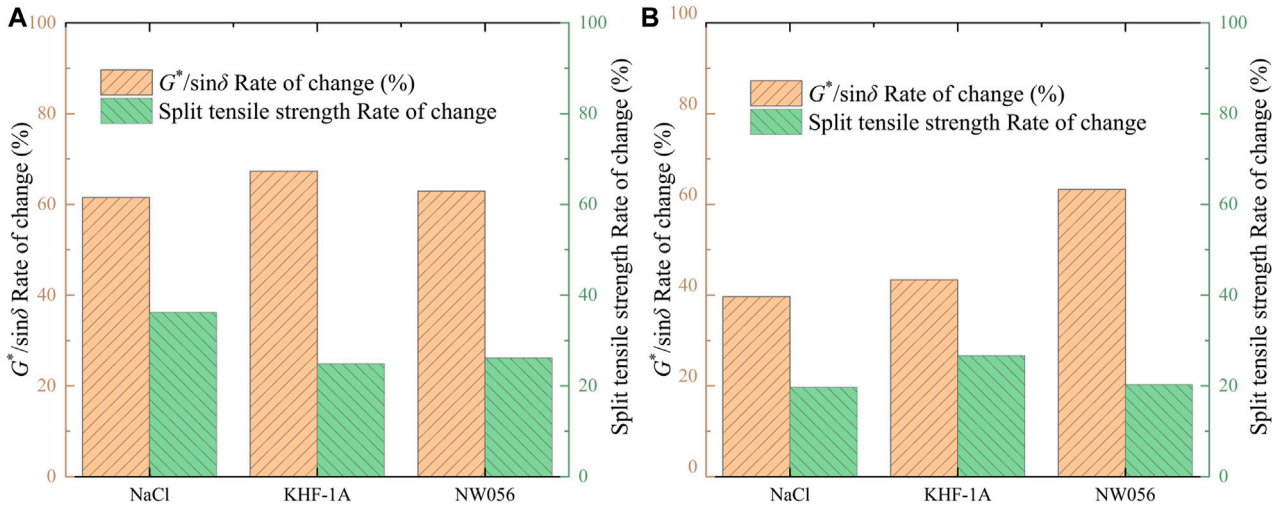

FIGURE 9
Anti-rutting factor and splitting strength change rate. **(A)** 10% **(B)** 26%.

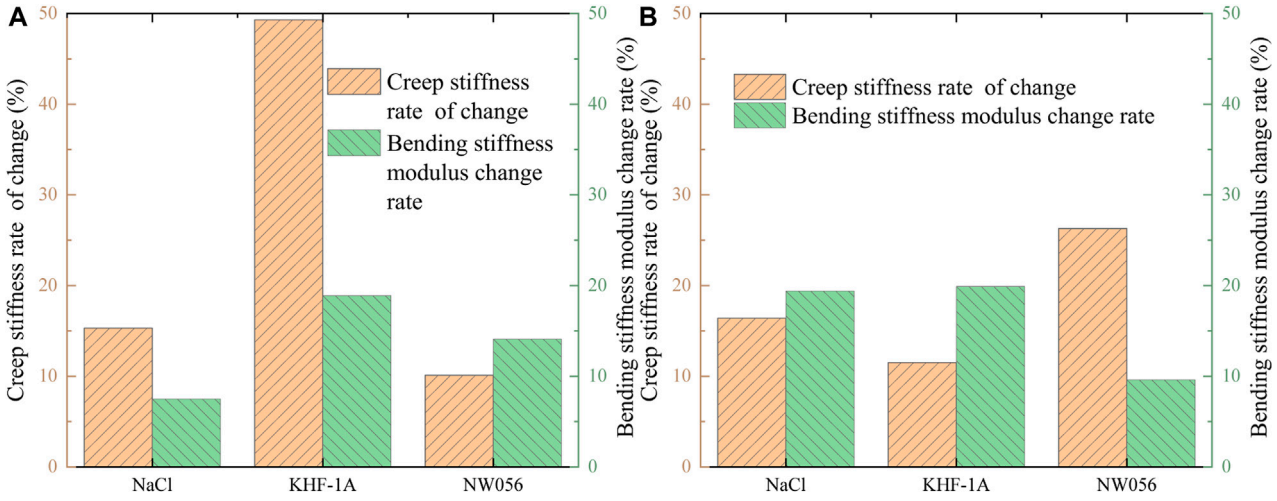

FIGURE 10
Creep stiffness and Bending stiffness modulus change rate. **(A)** 10% **(B)** 26%.

the following indicators: the anti-rutting factor $G^*/\sin\delta$ of asphalt and the splitting strength of medicine at high temperatures and the creep stiffness S and the bending stiffness modulus of the mixture at low temperatures. The relative changes of these indicators for asphalt and variety treated with deicing agents compared to the untreated samples are shown in Figure 9 and Figure 10.

The deicing agent had opposite effects on the high-temperature performance of asphalt and mixture. It improved the high-temperature performance of asphalt but reduced the mixture's high-temperature performance. Figure 9 shows that the higher the improvement of the high-temperature performance of asphalt, the lower the reduction of the mixture of high-temperature performance, indicating a negative correlation between the deicing agent and the high-temperature performance of asphalt and variety. At 10% mass fraction, KHF-1A and NW056 deicing agents improved the high-temperature performance of asphalt more than the conventional NaCl deicing agent and reduced the high-temperature performance of the mixture less. At 26% mass fraction, KHF-1A and NW056 deicing agents still improved the high-temperature performance of asphalt more than NaCl deicing agents. Still, the ranking of the deicing agents by their impact on the mixture's high-temperature performance was KHF-1A > NW056 > NaCl, with a slight difference.

The deicing agent deteriorated the low-temperature performance of asphalt and mixture. Figure 10 shows that the type of deicing agent greatly influenced its effect on the low-temperature performance of asphalt and mix. At 10% mass fraction, the KHF-1A deicing agent had a much stronger deterioration effect on the low-temperature performance of asphalt and mixture than NW056 and NaCl deicing agents. In contrast, the NaCl deicing agent had the most minor impact on

the low-temperature performance of the mix. At 26% mass fraction, the NW056 deicing agent had the most substantial reduction effect on the low-temperature performance of asphalt among the three but the weakest effect on the low-temperature performance of the mixture. NaCl and KHF-1A deicing agents had similar effects on the low-temperature performance degradation of asphalt and mix.

Based on the comprehensive evaluation of the effects of chloride deicing agent NaCl and two acetate deicing agents, KHF-1A and NW056, on the high and low-temperature performance of asphalt and mixture, NW056 deicing agent was found to have the best performance among the three.

4 Conclusion

This study used laboratory tests to investigate the effects of three deicing agents (NaCl, KHF-1A, and NW056) on airport asphalt and mixture performance. The main findings are as follows.

(1) The change in asphalt performance is greater than 10%. Although the fact that the high-temperature performance of asphalt increases by more than 25%, the low-temperature crack resistance and fatigue resistance are significantly weakened, by nearly 50%.
(2) Compared with NaCl, deicers NW056 and KHF-1A have minor effects on the performance of asphalt. Due to the emulsifying effect of acetic acid on asphalt, the low-temperature performance of NW056 and KHF-1A is slightly higher than that of NaCl.
(3) The mixture's high-temperature performance decreases by 10%–40%, and the low-temperature performance decreases by 6%–20%. Furthermore, the more significant the improvement of the high-temperature performance of the asphalt by the deicing agent, the smaller the reduction of the mixture's high-temperature performance.
(4) The two acetate deicers have better pavement performance than the NaCl deicer. Even after prolonged use, the asphalt pavement surface may be damaged, but due to the weak corrosion of the acetate deicing agent, it will not cause severe damage to the pavement. In particular, the NW056 deicing agent has a minor effect on the high and low temperatures of the mixture and is an excellent alternative material for pavement deicing.

This study investigated the effects of the combined deicing agent NaCl and the acetate deicing agents NW056 and KHF-1A on the performance of airport pavements in detail. It verified the feasibility of replacing traditional chloride deicing agents with NW056 and KHF-1A. This has a good application prospect and helps to provide a reference for selecting deicing agents for airport deicing. However, this study also has some limitations. On the one hand, due to the large variety of acetate deicing agents, this paper only selects NW056 and KHF-1A as representatives. On the other hand, the impact of deicing agents on pavement skid resistance, wear resistance, low-temperature fracture, and aggregate performance has not been considered. This is also the direction of further research in the future.

Data availability statement

The original contributions presented in the study are included in the article/Supplementary material, further inquiries can be directed to the corresponding authors.

Author contributions

PL is the experimental designer of this study and contributes to the writing and revision of the thesis. WP participated in the writing of the first draft of the article and conducted data analysis. YH participated in the test and compiled the experimental data and some manuscripts. ZL and BW participated in the experimental design and provided help in data analysis. WL participated in the test of experimental samples. WW participated in the English polishing of the final manuscript. All authors contributed to the article and approved the submitted version.

Funding

This work was supported by the National Key Research and Development Program of China (2021YFB2601000), Guangxi Key Research and Development Program (AB21220070), Airport Engineering Research Center of CAAC Program (ERCAOTP20220301), the National Natural Science Foundation of China (51878075), Hunan Provincial Natural Science Foundation of China (2022JJ30594), Postgraduate Scientific Research Innovation Project of Hunan Province (QL20220189), and Key Scientific Research Projects of Universities in Henan Province (23A580005/23B580005).

Conflict of interest

BW was employed by Hunan Expressway Maintenance Engineering Co., Ltd.

The remaining authors declare that the research was conducted in the absence of any commercial or financial relationships that could be construed as a potential conflict of interest.

The reviewer (HY) declared a shared parent affiliation with the authors (PL, WP, YH, ZL) to the handling editor at the time of the review.

Publisher's note

Supplementary material

The Supplementary Material for this article can be found online at: https://www.frontiersin.org/articles/10.3389/fmats.2023.1231483/full#supplementary-material

References

Bennert, T., Haas, E., and Wass, E. (2018). Indirect tensile test (IDT) to determine asphalt mixture performance indicators during quality control testing in New Jersey. *Transp. Res. Rec.* 2672, 394–403. doi:10.1177/0361198118793276

Button, J. W., Timothy, B. A., Ronald, C., Frank, F., Gary, L. F., Thomas, P. H., et al. (2004). *New simple performance test for asphalt mixes*. Washington, DC: Transp. Res. Board, 1–44.

Christensen, D. W., Bonaquist, R., Anderson, D. A., and Gokhale, S. (2004). "Indirect tension strength as a simple performance test," in *Transportation research circular, number E-C068*, 44–57.

Christensen, D. W., Jr, and Bonaquist, R. (2002). Use of strength tests for evaluating the rut resistance of asphalt concrete. *J. Assoc. Asphalt Paving Technol.*, 71.

Civil Aviation Administration of China (2022). 2021 statistical bulletin of civil aviation industry development. 7.

Civil Aviation Administration of China (2019). *Specifications for asphalt pavement construction of civil airports. MH/T 5011-2019*. China Civil Aviation Publishing House.

Das, J. K., and Pradhan, B. (2019). Effect of cation type of chloride salts on corrosion behaviour of steel in concrete powder electrolyte solution in the presence of corrosion inhibitors. *Constr. Build. Mater* 208, 175–191. doi:10.1016/j.conbuildmat.2019.02.153

Du, S., Akin, M., Bergner, D., Xu, G., and Shi, X. (2019). *Synthesis of material application methodologies for winter operations.*

Edwards, Y., and Aurstad, J. (2000). The influence of runway de-icing agents on the durability of asphalt concrete pavements for airfields. *Road. Mater Pavement* 1, 387–405. doi:10.1080/14680629.2000.12067152

Fay, L., and Shi, X. (2012). Environmental impacts of chemicals for snow and ice control: state of the knowledge. *Water, Air, and Soil Pollut.* 223, 2751–2770. doi:10.1007/s11270-011-1064-6

Fay, L., and Shi, X. (2011). Laboratory investigation of performance and impacts of snow and ice control chemicals for winter road service. *J. COLD Reg. Eng.* 25, 89–114. doi:10.1061/(asce)cr.1943-5495.0000025

Feng, D., Yi, J., Wang, D., and Chen, L. (2010). Impact of salt and freeze–thaw cycles on performance of asphalt mixtures in coastal frozen region of China. *COLD Reg. Sci. Technol.* 62, 34–41. doi:10.1016/j.coldregions.2010.02.002

Findlay, S. E., and Kelly, V. R. (2011). Emerging indirect and long-term road salt effects on ecosystems. *Ann. N. Y. Acad. Sci.* 1223, 58–68. doi:10.1111/j.1749-6632.2010.05942.x

Fischel, M. (2001). *Evaluation of selected deicers based on a review of the literature.*

Fortin, C., Tjaden, L., and Mulhem, N. (2014). Chloride free snow and ice control material. *Transp. Res. synthesis*.

Frolova, E. A., Kondakov, D. F., Nikolaev, V. V., Tin Gaev, O. P., and Danilov, V. P. (2015). Phase equilibria in the sodium formate–potassium formate–water system below 0° c and the anti-icing properties of salt compositions. *Theor. Found. Chem. EN+* 49, 719–720. doi:10.1134/s004057951505005x

Gruber, M. R., Hofko, B., Hoffmann, M., Stinglmayr, D., and Grothe, H. (2023a). Analysis of metal corrosion methods and identification of cost-efficient and low corrosion deicing agents. *Corros. Eng. Sci. Technol.* 58, 452–463. doi:10.1080/1478422x.2023.2200008

Gruber, M. R., Hofko, B., Hoffmann, M., Stinglmayr, D., Seifried, T. M., and Grothe, H. (2023b). Deicing performance of common deicing agents for winter maintenance with and without corrosion-inhibiting substances. *COLD Reg. Sci. Technol.* 208, 103795, 103795. doi:10.1016/j.coldregions.2023.103795

Hanke, H., Nutz, P., Maier-Farkas, H., Neuhold, J., Rizzardo, F., Jezek, P., et al. (2019). *International development of application methods of de-icing chemicals-state of the art and best practice.*

Koščák, P., Berežný, Š., Vajdová, I., Koblen, I., Ojciec, M., Matisková, D., et al. (2020). Reducing the negative environmental impact of winter airport maintenance through its model design and simulation. *Int. J. Env. Res. PUB HE* 17, 1296. doi:10.3390/ijerph17041296

Li, B., Huang, W., Tang, N., Hu, J., Lin, P., Guan, W., et al. (2017). Evolution of components distribution and its effect on low temperature properties of terminal blend rubberized asphalt binder. *Constr. Build. MATER* 136, 598–608. doi:10.1016/j.conbuildmat.2017.01.118

Ma, H., Yu, H., Tan, Y., and Da, B. (2021). Ice pressure and icing volume expansion rate of acetate-based deicers under freezing conditions. *Constr. Build. MATER* 305, 124751. doi:10.1016/j.conbuildmat.2021.124751

McCarthy, L. M., Callans, J., Quigley, R., and Scott, S. V., III (2016). *Performance specifications for asphalt mixtures.*

Meng, Y., Lai, J., Ling, L., Zhang, C., Chen, J., and Zhu, J. (2023). Preparation of an eco-friendly de-icing filler and its effects on the performance of different asphalt mastic. *Constr. Build. Mater* 364, 129967. doi:10.1016/j.conbuildmat.2022.129967

Meng, Y., Xu, R., Guo, H., Ling, L., Xi, C., Qin, Y., et al. (2021). Influences of sodium salt erosion on the self-healing ability and fatigue life of bitumen. *Constr. Build. Mater* 286, 122884. doi:10.1016/j.conbuildmat.2021.122884

Meng, Y., Zhang, C., Chen, J., Ling, L., Lai, J., Yan, T., et al. (2022). Deicing characteristics and pavement performance of eco-friendly de-icing asphalt mixture. *Constr. Build. Mater* 360, 129565. doi:10.1016/j.conbuildmat.2022.129565

Ministry of Transport Highway Research Institute (2011). *Standard test methods of bitumen and bituminous mixtures for highway engineering*. Industry Standard - Transportation.

Ministry of Transport of China (2021). *Outline of national comprehensive three-dimensional transportation network planning.*

Nazari, M. H., and Shi, X. (2019). Developing renewable agro-based anti-icers for sustainable winter road maintenance operations. *J. Mater Civ. Eng.* 31, 4019299. doi:10.1061/(asce)mt.1943-5533.0002963

Pan, T., He, X., and Shi, X. (2008). Laboratory investigation of acetate-based deicing/anti-icing agents deteriorating airfield asphalt (with discussion). *J. Assoc. Asphalt Paving Technol.*, 77773–793.

Pan, T. (2007). "Mitigation of moisture and deicer effects on asphalt thermal cracking through polymer modification," in *Prepared for the US department of transportation research and innovative Technology administration*.

Peng, W., Li, P., Gong, W., Tian, S., Wang, Z., Liu, S., et al. (2023). Preparation and mechanism of rubber-plastic alloy crumb rubber modified asphalt with low viscosity and stabilized performance. *Constr. Build. MATER* 388, 131687. doi:10.1016/j.conbuildmat.2023.131687

Qiu, L., and Nixon, W. A. (2008). Effects of adverse weather on traffic crashes: systematic review and meta-analysis. *Transp. Res. Rec.* 2055, 139–146. doi:10.3141/2055-16

Shi, X., Akin, M., Pan, T., Fay, L., Liu, Y., and Yang, Z. (2009). Deicer impacts on pavement materials: introduction and recent developments. *Open Civ. Eng. J.* 3, 16–27. doi:10.2174/1874149500903010016

Shi, X., Jungwirth, S., Akin, M., Wright, R., Fay, L., Veneziano, D. A., et al. (2014). Evaluating snow and ice control chemicals for environmentally sustainable highway maintenance operations. *J. Transp. Eng.* 140, 5014005. doi:10.1061/(asce)te.1943-5436.0000709

Terry, L. G., Conaway, K., Rebar, J., and Graettinger, A. J. (2020). Alternative deicers for winter road maintenance—a review. *Water, Air, Soil Pollut.* 231, 394–429. doi:10.1007/s11270-020-04773-x

Vignisdottir, H. R., Ebrahimi, B., Booto, G. K., O'Born, R., Brattebø, H., Wallbaum, H., et al. (2019). A review of environmental impacts of winter road maintenance. *COLD Reg. Sci. Technol.* 158, 143–153. doi:10.1016/j.coldregions.2018.10.013

Xiong, R., Jiang, W., Yang, F., Li, K., Guan, B., and Zhao, H. (2019). Investigation of voids characteristics in an asphalt mixture exposed to salt erosion based on CT images. *MATERIALS* 12, 3774. doi:10.3390/ma12223774

Yang, K., Li, R., Underwood, B. S., and Castorena, C. (2022). Effect of laboratory oxidative aging on dynamic shear rheometer measures of asphalt binder fatigue cracking resistance. *Constr. Build. MATER* 337, 127566. doi:10.1016/j.conbuildmat.2022.127566

Zhang, K., Li, W., and Han, F. (2019). Performance deterioration mechanism and improvement techniques of asphalt mixture in salty and humid environment. *Constr. Build. MATER* 208, 749–757. doi:10.1016/j.conbuildmat.2019.03.061

Zhang, K., and Zhang, Z. (2015). Deterioration of mechanical properties of asphalt mixture in salty and humid environment. *J. South China Univ. Technol. Sci. Ed.* 43, 106–112. doi:10.3969/j.issn.1000-565X.2015.08.016

Zhang, K., Zhang, Z., Yi, F., Montserrat, N., Hishida, T., Esteban, C. R., et al. (2014). Direct conversion of human fibroblasts into retinal pigment epithelium-like cells by defined factors. *J. WUHAN Univ. Technol.* 36, 48–58. doi:10.1007/s13238-013-0011-2

Zhang, Q., Wu, D., Zhang, X., Chang, K., and Wang, Y. (2021a). Effect of organic deicing agents on asphalt rheology and analysis of the mechanism. *Constr. Build. MATER* 284, 122649. doi:10.1016/j.conbuildmat.2021.122649

Zhang, X., Chen, H., and Hoff, I. (2021b). The mutual effect and reaction mechanism of bitumen and de-icing salt solution. *Constr. Build. MATER* 302, 124213. doi:10.1016/j.conbuildmat.2021.124213

Frontiers in Materials

Investigates the discovery and design of materials for future application

A multidisciplinary journal that explores the breadth of materials science, engineering and mechanics - from carbon-based materials to smart materials.

Discover the latest Research Topics

See more →

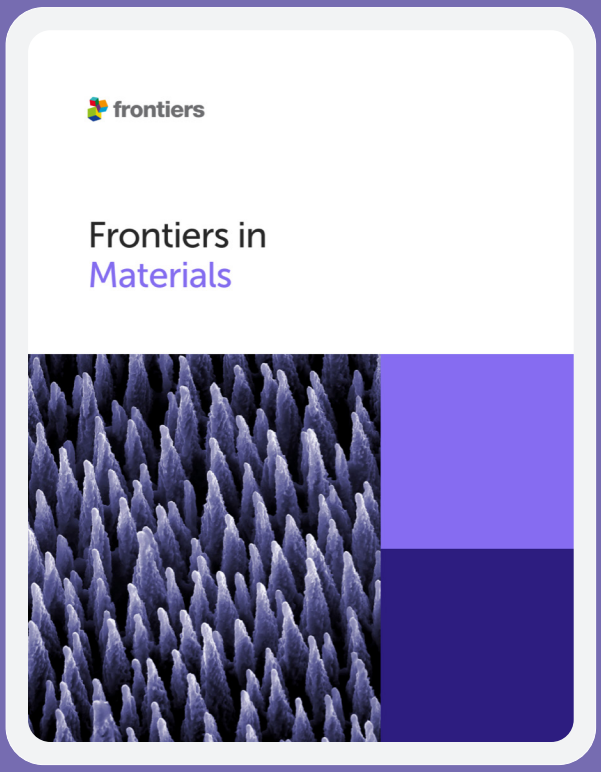

Frontiers

Avenue du Tribunal-Fédéral 34
1005 Lausanne, Switzerland
frontiersin.org

Contact us

+41 (0)21 510 17 00
frontiersin.org/about/contact